Universitat
de Girona

SUPRAMOLECULAR NANOCAPSULES AS PLATFORMS FOR MOLECULAR RECOGNITION AND REACTIVITY IN CONFINED SPACES

Carles Fuertes Espinosa

Per citar o enllaçar aquest document:
Para citar o enlazar este documento:
Use this url to cite or link to this publication:

http://hdl.handle.net/10803/674186

ADVERTIMENT. L'accés als continguts d'aquesta tesi doctoral i la seva utilització ha de respectar els drets de la persona autora. Pot ser utilitzada per a consulta o estudi personal, així com en activitats o materials d'investigació i docència en els termes establerts a l'art. 32 del Text Refós de la Llei de Propietat Intel·lectual (RDL 1/1996). Per altres utilitzacions es requereix l'autorització prèvia i expressa de la persona autora. En qualsevol cas, en la utilització dels seus continguts caldrà indicar de forma clara el nom i cognoms de la persona autora i el títol de la tesi doctoral. No s'autoritza la seva reproducció o altres formes d'explotació efectuades amb finalitats de lucre ni la seva comunicació pública des d'un lloc aliè al servei TDX. Tampoc s'autoritza la presentació del seu contingut en una finestra o marc aliè a TDX (framing). Aquesta reserva de drets afecta tant als continguts de la tesi com als seus resums i índexs.

ADVERTENCIA. El acceso a los contenidos de esta tesis doctoral y su utilización debe respetar los derechos de la persona autora. Puede ser utilizada para consulta o estudio personal, así como en actividades o materiales de investigación y docencia en los términos establecidos en el art. 32 del Texto Refundido de la Ley de Propiedad Intelectual (RDL 1/1996). Para otros usos se requiere la autorización previa y expresa de la persona autora. En cualquier caso, en la utilización de sus contenidos se deberá indicar de forma clara el nombre y apellidos de la persona autora y el título de la tesis doctoral. No se autoriza su reproducción u otras formas de explotación efectuadas con fines lucrativos ni su comunicación pública desde un sitio ajeno al servicio TDR. Tampoco se autoriza la presentación de su contenido en una ventana o marco ajeno a TDR (framing). Esta reserva de derechos afecta tanto al contenido de la tesis como a sus resúmenes e índices.

WARNING. Access to the contents of this doctoral thesis and its use must respect the rights of the author. It can be used for reference or private study, as well as research and learning activities or materials in the terms established by the 32nd article of the Spanish Consolidated Copyright Act (RDL 1/1996). Express and previous authorization of the author is required for any other uses. In any case, when using its content, full name of the author and title of the thesis must be clearly indicated. Reproduction or other forms of for profit use or public communication from outside TDX service is not allowed. Presentation of its content in a window or frame external to TDX (framing) is not authorized either. These rights affect both the content of the thesis and its abstracts and indexes.

DOCTORAL THESIS

SUPRAMOLECULAR NANOCAPSULES AS PLATFORMS FOR MOLECULAR RECOGNITION AND REACTIVITY IN CONFINED SPACES

Carles Fuertes Espinosa

2020

Doctoral programme in Chemistry

Supervised by: Dr. Xavi Ribas Salamaña

Tutor: Dr. Xavi Ribas Salamaña

This manuscript has been presented to opt for the doctoral degree from the University of Girona

Universitat
de Girona

Dr. Xavi Ribas Salamaña from the University of Girona declare:

That the thesis entitled "Supramolecular nanocapsules as platforms for molecular recognition and reactivity in confined spaces", presented by Carles Fuertes Espinosa to obtain a doctoral degree, has been completed under my supervision and meets the requirements to opt for an international Doctorate.

For all intents and purposes, I whereby sign this document.

Dr. Xavi Ribas Salamaña

Girona, March 05, 2020

FULL LIST OF PUBLICATIONS

This thesis is based on a compendium of the following publications:

Chapter III

Supramolecular Fullerene Sponges as Catalytic Masks for Regioselective Functionalization of C_{60}. **Fuertes-Espinosa, C**.; Garcia-Simon, C.; Pujals, M.; Garcia-Borras, M.; Gomez, L.; Parella, T.; Juanhuix, J.; Imaz, I.; Maspoch, D.; Costas, M. and Ribas, X. *Chem.* **2020**, 6, 169-186. (impact factor: 18.20, multidisciplinary, 1st quartile)

Chapter IV

A Copper-based Supramolecular Nanocapsule that Enables Straightforward Purification of Sc_3N-based Endohedral Metallofullerenes Soots. **Fuertes-Espinosa, C**.; García-Simón, C.; Catro, E.;Costas, M.; Echegoyen, L. and Ribas, X. *Chemistry - A European Journal*, **2017**, 15, 3553–3557. (impact factor: 5.16, multidisciplinary, 1st quartile)

Chapter V

Purification of Uranium-based Endohedral Metallofullerenes (EMFs) by Selective Supramolecular Encapsulation and Release. **Fuertes-Espinosa, C**.; Gómez-Torres, A.; MoralesMartínez, R.; Rodríguez-Fortea, A.; García-Simón, C.; Gándara, F.; Imaz, I.; Juanhuix, J.; Maspoch, D.; Poblet, J.M.; Echegoyen, L. and Ribas, X. *Angew. Chem., Int. Ed.,* **2018**, 57, 11294–11299. (impact factor: 12.25, multidisciplinary, 1st quartile)

Chapter VI

Highly Selective Encapsulation and Purification of U-based C_{78}-EMFs within a Supramolecular Nanocapsule. **Fuertes-Espinosa, C**.; Murillo, J.; Soto, M.; Ceron, M.; MoralesMartínez, R.; Rodríguez-Fortea, A.; Poblet, J.M.; Echegoyen, L. and Ribas, X. *Nanoscale* **2019**, 11, 23035-23041 (impact factor: 6.97, multidisciplinary, 1st quartile)

LIST OF ABBREVIATIONS

AcO	Acetate
[C60]PCBM	Phenyl-C61-butyric acid methyl ester)
2D	Bidimensional
3D	Three-dimensional
Å	Angstroms
BArF	Tetrakis [3,5-bis(trifluoromethyl)phenyl] borane
OTf	Trifluoromethanesulfonate (triflate)
CNT	Carbon Nanotubes
CPP	Cycloparaphenylenes
DCM	Dichloromethane
DFT	Density Functional Theory
DMF	Dimethylformamide
DMSO	Dimethyl Sulfoxide
DOSY	Diffusion Order Spectroscopy
Equiv	Equivalent
HRMS	High Resolution Mass Spectrometry
ESI-MS	ElectroSpray Ionization Mass Spectrometry
G	Guest
H	Host
h	hours
K_{as}	Association Constant
Kcal	Kilocalorie
L	Ligand
M	Metal
MDS	Molecular Dynamics Simulations
min	Minute
MOF	Metal Organic Framework
MW	Molecular Weight
NMR	Nuclear Magnetic Resonance
p.	Page
Porph	Porphyrin
Ref.	References

r.t.	Room Temperature
T	Temperature
TBA	Tetrabutylamonium
TCE	Trichloroethane
TEA	Triethylamine
TON	Turn Over Number
UV-Vis	Ultraviole-Visible spectroscopy
XRD	X-Ray Diffraction Data

LIST OF FIGURES

ACKNOWLEDGEMENTS

This work would not have been possible without the following collaborations:

- Serveis Tècnics de Recerca from Universitat de Girona for technical support
- Dr.Marc Garcia Borràs from the Institut de Química Computacional i Catàlisi from Universitat de Girona for the MDS
- Dr. Josep Maria Poblet, Dr. Antonio Rodríguez and Roser Morales from Universitat Rovira i Virgili de Tarragona for the DFT calculations
- Dr. Daniel Maspoch, Dr. Inhar Imar and Dr. Judith Juanhuix from Institut Català de Nanocència and ALBA synchrotron, for the XRD data.
- Dr. Felipe Gándara from Universidad Complutense de Madrid, for the crystal data refinement
- Dr. Teodor Parella from Universitat Autònoma de Barcelona for the NMR data.
- Dr. Luis Echegoyen from University of Texas at El Paso, for hosting a scientific visit and the collaborative research in the purification of EMFs.
- Generalitat de Catalunya for the PhD grant “Beques predoctorals per a la formació de personal investigador (FI- DGR 2012)”.
- Universitat de Girona for the mobility grant “Beques per a estades de recerca a l’estranger (BE-DGR 2017)”
- X.R. Icrea Acadèmia award 2010 (9111087).

GRAPHICAL ABSTRACT

Summary

Chapter I. General Introduction

Chapter II. Objectives

Chapter III. Supramolecular Fullerene Sponges as Catalytic Masks for Regioselective Functionalization of C_{60}

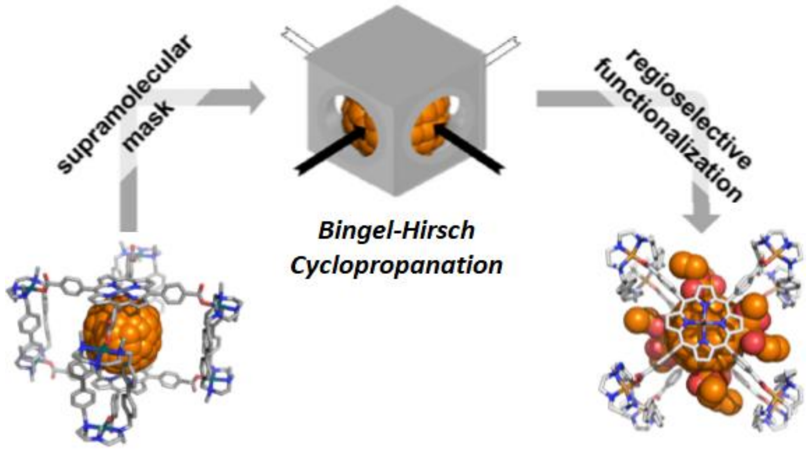

Chapter IV. A Copper-based Supramolecular Nanocapsule that Enables Straightforward Purification of Sc_3N-based Endohedral Metallofullerenes Soots.

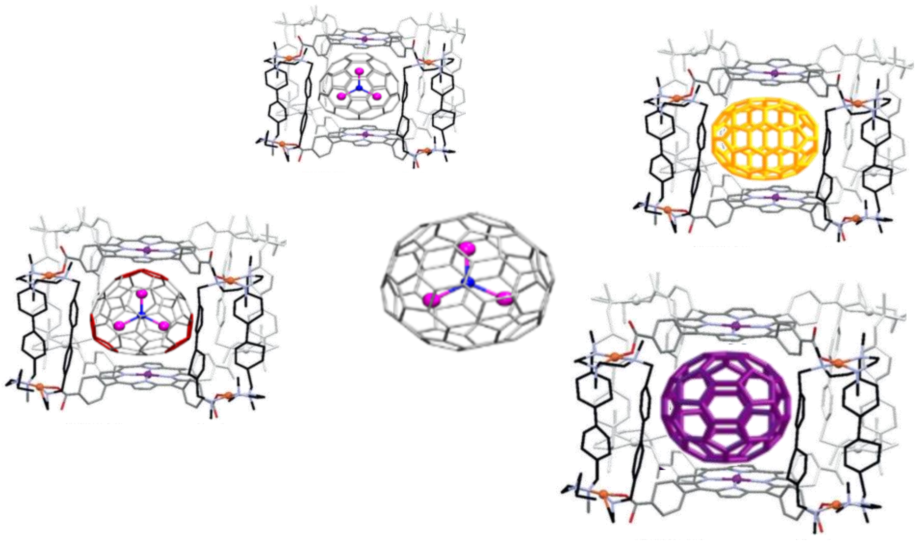

Chapter V. Purification of Uranium-based Endohedral Metallofullerenes (EMFs) by Selective Supramolecular Encapsulation and Release.

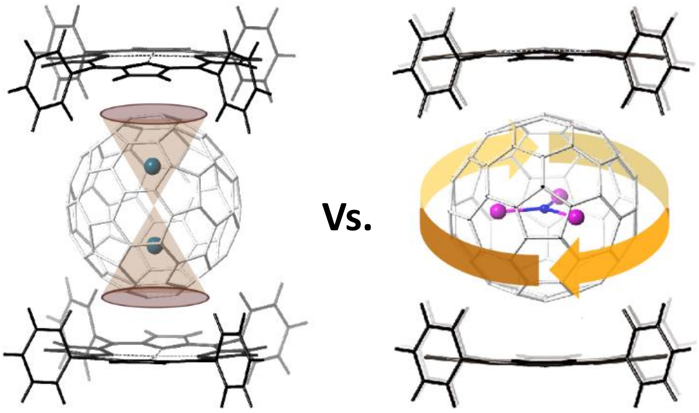

Chapter VI. Highly Selective Encapsulation and Purification of U-based C_{78}-EMFs within a Supramolecular Nanocapsule

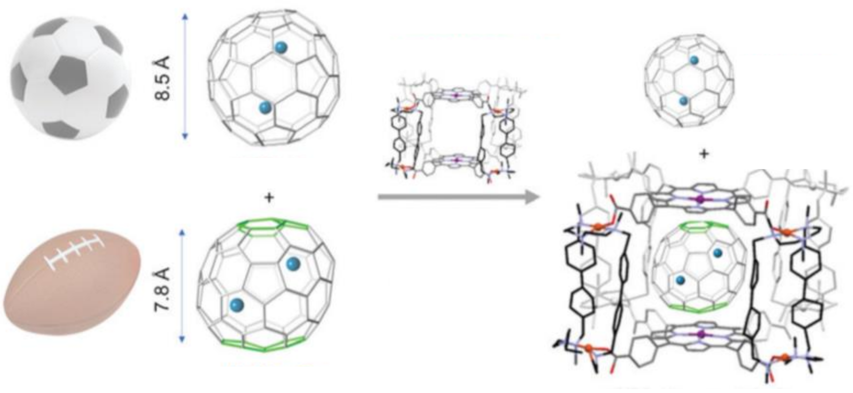

Chapter VII. Results and Discussion

Chapter VIII. General Conclusions

Annex

TABLE OF CONTENTS

SUMMARY

The use of self-assembly to bring simple building blocks together into complex product, has led to the preparation of an increasing number of sophisticated and functional 3D supramolecular nanocapsules. By understanding the selectivity of these different coordinative bond-forming reactions and interactions between the subcomponents, complex supramolecular scaffolds by design are cleanly generated from simple building blocks. Important prospective applications of metal-organic capsules are the development of low-energy methodologies for chemical separations and purification of target molecules, and the reactivity modulation of confined guests for the efficient and selective production of valuable compounds.

In the first part, this thesis builds upon expanding the capabilities of **1a**·(BArF)$_8$ (Pd(II)-based tetragonal prismatic nanocapsule) as a supramolecular mask, to gain full regio-functionalization control and modulate the reactivity of Bingel cyclopropanation reactions on confined fullerene C_{60}. The confinement effect not only allows a very precise control of the regiochemistry in the synthesis of poly-functionalized C_{60} adducts, but also, completely precludes the over-reactivity commonly observed without mask. In this manner, fully equatorial bis-, tris- and tetrakis- homo- and heteroadducts have been synthesized for the first time, as well as hekakis-heteroadducts.

Afterwards, the Cu(II)-based tetragonal prismatic nanocapsule **5·**(OTf)$_8$, analogue of the **1a**·(BArF)$_8$, was prepared and fully characterized. As a consequence of the inherent lability of the Cu(II)-carboxylate coordinative bonds present in the metal nodes of **5·**(OTf)$_8$, this nanocapsule is able to reversibly encapsulate large fullerenes and EMFs in homogeneous and heterogeneous (host in solid and guest in solution) systems. The different affinities displayed by **5·**(OTf)$_8$ towards the species present in a Sc_3N-based soot, allows for the straightforward purification of $Sc_3N@C_{80}$ in a single step.

Then, **5·**(OTf)$_8$ nanocapsule was derivatized by exchanging its OTf^- counter-anions by $BArF^-$, yielding **1b**·(BArF)$_8$. We investigated the ability of **1b**·(BArF)$_8$ as a selective host in the purification of U/Sc-based EMF soots. The very precise and divergent selectivity shown by **1b**·(BArF)$_8$ towards $U_2@C_{80}$ and unprecedented $Sc_2CU@C_{80}$ guests allows their sequential and selective uptake in a single and operationally simple step. The obtained results demonstrate that **1b**·(BArF)$_8$ is able to discriminate EMFs bearing exactly the same carbon cage and differing exclusively in the endohedral clusters.

In the final part of this thesis, the ability of **1b**·(BArF)$_8$ to purify challenging EMFs directly from complex mixtures has been further exemplified by the selective encapsulation and purification of U-based C_{78} EMFs in the presence of U-based C_{80} ones. The molecular recognition events observed in the heterogeneous (host in solid and guest in solution) host-guest systems, were dictated by the enhanced electrostatic interactions between the host and the EMFs guests possessing ellipsoidal fullerene cages, such as U-based C_{78} EMFs, compared to spherical C_{80} species. Moreover, further host-guest experiments demonstrate that **1b**·(BArF)$_8$ is able to distinguish among EMF with very similar endohedral clusters, i.e. $U_2@D_{3h}\text{-}C_{78}$ versus $U_2C@D_{3h}\text{-}C_{78}$.

RESUM

L'ús de reaccions d'autoensamblatge ha facilitat la preparació de nombroses càpsules supramoleculars 3D. La comprensió d'aquestes reaccions, permet dissenyar i sintetitzar de manera selectiva aquestes estructures supramoleculars usant subcomponents senzills. Aquestes càpsules d'alta complexitat, mostren un gran potencial en el desenvolupament de metodologies de separació/purificació de productes químics, així com, en la síntesi millorada de productes d'alt valor afegit, gràcies al confinament dels precursors sintètics en les cavitats internes de les càpsules i la peculiar reactivitat que es dóna en aquests espais confinats.

La primera part d'aquesta tesi doctoral es focalitza en l'expansió de les capacitats de **1a**·$(BArF)_8$ (càpsula tetragonal prismàtica basada en Pd (II)) com a màscara supramolecular, per exercir un control total de la regioselectivitat i la reactivitat en reaccions de ciclopropanació en el ful·lerè C_{60}, mitjançant el seu confinament. Aquest confinament del substrat, no només permet controlar de manera precisa la regioselectivitat durant la formació de derivats poli-funcionalitzats de C_{60}, sinó que també exerceix un control de la quimioselectivitat del procés. D'aquesta manera, s'han sintetitzat per primera vegada bis-, trista i tetrakis- homo- i heteroadductos completament equatorials, així com hekakis-heteroadductos.

Posteriorment, es va preparar i caracteritzar una nova càpsula de Cu (II) (**5**·$(OTf)_8$), anàloga a **1a**·$(BArF)_8$. Gràcies a la inherent labilitat dels enllaços de coordinació present en els nodes metàl·lics d'aquesta estructura, es va aconseguir encapsular de manera reversible ful·lerens i EMFs de grans dimensions (usant **5**·$(OTf)_8$ en solució o en estat sòlid). Gràcies a l'afinitat divergent que mostra **5**·$(OTf)_8$ davant les diferents espècies presents en un cru de reacció de EMFs basats en clústers de "Sc3N", es va aconseguir purificar en un sol pas de reacció el compost $Sc_3N@C_{80}$.

El següent pas en aquesta tesi doctoral, va ser derivatitzar la càpsula **5**·$(OTf)_8$ mitjançant l'intercanvi del seu contra-anió (OTf- per BArF-), generant la càpsula **1b**·$(BArF)_8$. Seguidament, es van estudiar les capacitats que mostrava **1b**·$(BArF)_8$ per encapsular les diferents espècies presents en un cru de reacció d'EMFs basats en clústers de "U/Sc", amb l'objectiu de purificar-lo. Gràcies a la gran selectivitat que mostra **1b**·$(BArF)_8$ cap $U_2@C_{80}$ i $Sc_2CU@C_{80}$, es va aconseguir encapsular de manera seqüencial i selectiva aquests dos EMFs, finalment purificant-los en un sol pas de reacció. Els resultats obtinguts en aquest projecte van evidenciar la capacitat de **1b**·$(BArF)_8$ per distingir entre espècies d'EMFs que únicament difereixen en els seus clústers interns, mostrant exactament la mateixa caixa de carboni.

A la part final d'aquesta tesi, les capacitats de **1a**·$(BArF)_8$ per purificar espècies d'EMFs directament de crus de reacció, va ser clarament evidenciada amb l'encapsulació selectiva i purificació d'uns nous EMFs basats en U i caixes de carboni C_{78}. Cal destacar, que l'afinitat de **1b**·$(BArF)_8$ per a aquests nous EMFs, és encara més gran que l'observada per $U_2@C_{80}$. Els esdeveniments de reconeixement molecular que mostra **1b**·$(BArF)_8$ en sistemes heterogenis (**1b**·$(BArF)_8$ en estat sòlid i els EMFs en solució), són dirigits per les interaccions electroestàtiques de major eficiència que es donen entre **1b**·$(BArF)_8$ i els EMFs que posseeixen caixes de carboni el·lipsoidals (com ara els EMFs basats en urani i caixes de carboni C_{78}), en comparació amb aquelles caixes de carboni més esfèriques (com el C_{80}). A més, l'estudi de reconeixement molecular que es va dur a terme va demostrar que **1b**·$(BArF)_8$ es pot distingir entre EMFs amb clústers interns molt similars, tal com $U_2@D_{3h}\text{-}C_{78}$ versus $U_2C@D_{3h}\text{-}C_{78}$.

RESUMEN

El uso de reacciones de autoensamblaje ha facilitado la preparación de numerosas cápsulas supramoleculares 3D. La comprensión de dichas reacciones, permite diseñar y sintetizar de manera selectiva estas estructuras supramoleculares usando subcomponentes sencillos. Dichas cápsulas de alta complejidad, muestran un gran potencial en el desarrollo de metodologías de separación/purificación de productos químicos, así como, en la síntesis mejorada de productos de alto valor añadido, gracias al confinamiento de los precursores sintéticos de las cavidades internas de las cápsulas y la peculiar reactividad que se da en estos espacios confinados.

La primera parte de esta tesis doctoral se focaliza en la expansión de las capacidades de **1a**·(BArF)$_8$ (cápsula tetragonal prismática basada en Pd(II)) como máscara supramolecular, para ejercer un control total de la regioselectividad y la reactividad en reacciones de ciclopropanación en el ful·lereno C_{60} mediante su confinamiento. Dicho confinamiento del sustrato, no solo permite controlar de manera precisa la regioselectividad durante la formación de derivados poli-funcionalizados de C_{60}, sino que también ejerce control en la quimioselectividad del proceso. De esta manera, se han sintetizado por primera vez bis-, tris- y tetrakis- homo- y heteroadductos completamente ecuatoriales, así como hekakis-heteroadductos.

Posteriormente, se preparó y caracterizó una nueva cápsula de Cu(II) (**5·**(OTf)$_8$), análoga a **1a**·(BArF)$_8$. Gracias a la inherente labilidad de los enlaces de coordinación presente en los nodos metálicos de dicha estructura, se consiguió encapsular de manera reversible fulerenos y EMFs de gran tamaño (usando **5·**(OTf)$_8$ en solución o en estado sólido). Gracias a la afinidad divergente que muestra **5·**(OTf)$_8$ enfrente las diferentes especies presentes en un crudo de reacción de EMFs basados en clústeres de "Sc_3N", se consiguió purificar en un solo paso de reacción el compuesto $Sc_3N@C_{80}$.

El siguiente paso en esta tesis doctoral, fue derivatizar la cápsula **5·**(OTf)$_8$ mediante el intercambio de su contra-anión (OTf$^-$ por BArF$^-$), generando la cápsula **1b**·(BArF)$_8$. Seguidamente, se estudiaron las capacidades que mostraba **1b**·(BArF)$_8$ para encapsular las diferentes especies presentes en un crudo de reacción de EMFs basados en clústeres de "U/Sc", con el objetivo de purificar dicho crudo. Gracias a la gran selectividad que muestra **1b**·(BArF)$_8$ hacia $U_2@C_{80}$ y $Sc_2CU@C_{80}$, se consiguió encapsular de manera secuencial y selectiva estos dos EMFs, consiguiendo finalmente su purificación en un solo paso de reacción. Los resultados obtenidos en este proyecto evidenciaron la capacidad de **1b**·(BArF)$_8$ para distinguir entre especies de EMFs que únicamente difieren en sus clústeres internos, mostrando exactamente la misma caja de carbono.

En la parte final de esta tesis, las capacidades de **1b**·(BArF)$_8$ para purificar especies de EMFs directamente de crudos de reacción, fue claramente evidenciada con la encapsulación selectiva y purificación de unos nuevos EMFs basados en U y cajas de carbono C_{78}. Cabe destacar, que la afinidad de **1b**·(BArF)$_8$ para estos nuevos EMFs, es aún mayor que la observada para $U_2@C_{80}$. Los eventos de reconocimiento molecular que muestra **1b**·(BArF)$_8$ en sistemas heterogéneos (**1b**·(BArF)$_8$ en estado sólido y los EMFs en solución), son dirigidos por las interacciones electrostáticas de mayor eficiencia que se dan entre **1b**·(BArF)$_8$ y los EMFs que poseen cajas de carbono elipsoidales (tales como los EMFs basados en uranio y cajas de carbono C_{78}), en comparación con aquellas cajas de carbono más esférica (como el C_{80}). Además, el estudio de reconocimiento molecular que se llevó a cabo demostró que **1b**·(BArF)$_8$ puede distinguir entre EMFs con clústeres internos muy similares, tal como $U_2@D_{3h}\text{-}C_{78}$ versus $U_2C@D_{3h}\text{-}C_{78}$.

Chapter I.

General Introduction

I.1. The chemistry of fullerenes

I.1.1. Carbon allotropes

In 1985, during a series of experiments directed to understand how long-chain carbon molecules were formed in space, the group of Kroto, Smalley and Curl detected for the first time fullerene C_{60} by laser vaporization of amorphous carbon and proposed its unprecedented truncated icosahedral structure.[1] The unexpected groundbreaking finding of C_{60} deserved the Nobel Prize in Chemistry in 1996,[2] boosting the discovery and development of many other carbon nanostructures till nowadays (Figure I.1), [3] such as carbon nanotubes,[4] carbon nanohorns,[5] graphene,[6] nanoonions[7] and other combined carbon nanostructures like carbon peapods.[8]

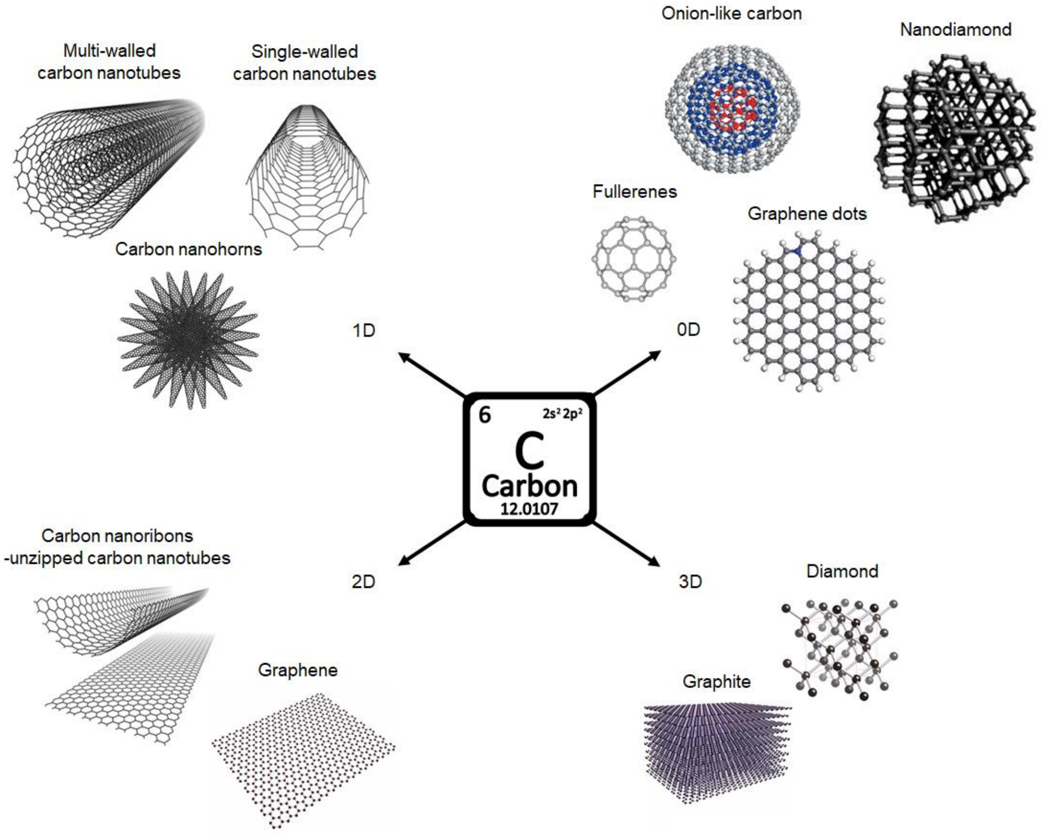

Figure I.1. Allotropic forms of carbon and their classification according to dimensionality

I.1.2. Fullerenes: spherical carbon nanostructures

I.1.2.1. Structural properties

Fullerenes are spherical-like discrete molecules which contain a defined even number of carbon atoms, forming a cage like fused-ring polycyclic system of 5-membered and 6-membered rings.[1] These spherical carbon nanostructures mainly consist of networks of sp^2 carbon atoms arranged in different shapes and sizes, what impacts into their electronic and physicochemical properties. The smallest stable and most abundant fullerene is C_{60}, followed by C_{70} and higher fullerenes. The stability of fullerenes is dictated by the so-called isolated pentagon rule (IPR), proposed by Kroto two years after the discovery of fullerenes.[9] This rule states that fullerenes with all pentagons surrounded by hexagons are more stable than those containing contiguous pentagons. Therefore, the structural organization of IPR fullerene cages consists in 12 pentagons and increasing number of hexagons. The reason for such structural disposition is that the bonds shared by two pentagons increase local strain, giving rise to less stable carbon cages.[10] Stabilization of non-IPR fullerenes can be achieved by releasing the strain generated by fused pentagons through exohedral chemical functionalization or by endohedral inclusion of metals or metal clusters in their hollow inner cavity (EMFs), as depicted in Figure I.2.[11]

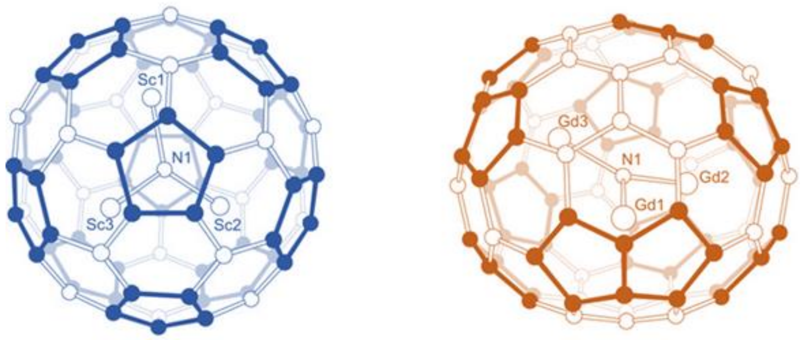

Figure I.2. Example of IPR EMF Sc_3N@*Ih*-C_{80} (left) and example of non-IPR EMF Gd_3N@*(51665)*C_{80} (right)

I.1.2.2 Production

The next breakthrough beyond the discovery of C_{60} was the multiple gram scale production of fullerenes by Krätschmer and Huffman in 1990, which was achieved by resistive heating of graphite in helium atmosphere.[12] A modified version of Krätschmer-Huffman fullerene reactor, using a plasma induced by an electric arc discharge between graphite electrodes, was developed by Smalley soon after has become the most common method used for the production of fullerenes. (Figure I.3).[13] Temperature reaches thousands of degrees at the center of the arc and a decreasing gradient of temperature provides cooler temperatures (> 1000 ºC) where the fullerenes are formed.

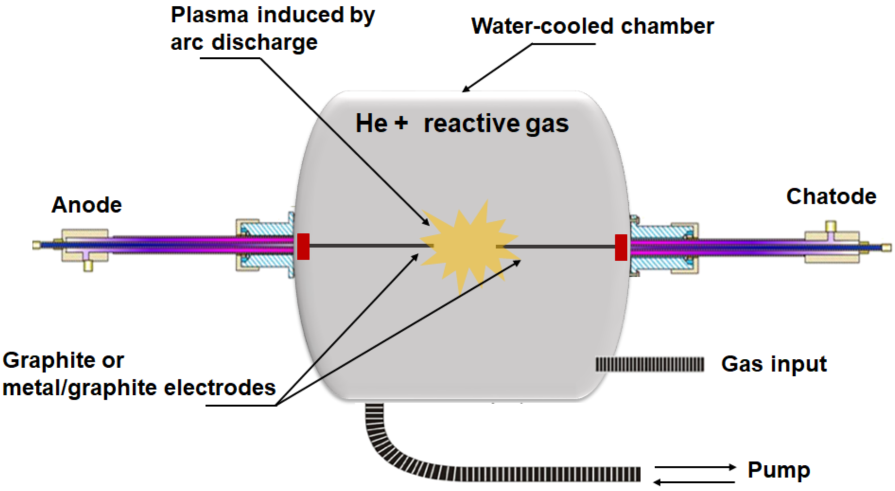

Figure I.3. Graphical representation of Krätschmer-Huffman reactor inducing the plasma by an electric arc discharge

The crude soot product generated from the evaporation/condensation of graphite rods contains mixtures of different-size fullerenes, as well as carbon nanotubes and amorphous carbon. However, the mixtures obtained need to be purified, and large efforts have geared during the last decades towards the design of efficient purification strategies. The first approaches were based on controlled sublimation of soot,[14] extraction with organic solvents (Soxhlet extraction),[15] crystallization[16] and chromatographic separation techniques[17,18]. Nowadays, High Performance Liquid Chromatography (HPLC) is the most extensively used methodology for the purification of fullerenes. Although a judicious combination of the methodologies mentioned above is in general efficient, protocols are tedious, energy and time-consuming, and generally lack versatility.

I.1.3. Endohedral metallofullerenes (EMFs)

One of the unique structural characteristic of fullerenes is their hollow inner cavity, and this rapidly triggered intuitive inspiration to entrap atoms or even small molecules inside carbon cages. In 1991, this hypothesis was confirmed experimentally by Smalley and coworkers, producing the first solvent-extractable EMF.[19] Analogously to the production of empty fullerenes, EMFs are synthesized using the arc-discharge reactor. Typically, a target rod composed of metal-oxide/graphite mixture is arced under direct current conditions, generating a carbon-rich plasma under He or Ar inert gas atmosphere and the appropriate reactive gas (H_2, N_2, NH_3, among others).[20] Further details of EMF synthesis, classification and their selective separation techniques are discussed in section I.2.

I.1.4. Encapsulation of fullerenes

Fullerene recognition in supramolecular entities is a hot topic of research as a purification tool and as a strategy to study their reactivity at the confined space. Many supramolecular receptors for fullenes have been reported and are very briefly discussed in this section.

I.1.4.1. Metal-ligand directed self-assembly

Nature is a source of inspiration for chemists working towards the construction of sophisticated and highly complex architectures using supramolecular interactions. Nevertheless, as the scale and the complexity of target molecules increases, the assembly of small molecules into larger aggregates turns into an increasingly impeded process, and often low yielding. This is mainly due to the difficulty of fully controlling the directionality of the traditional weak supramolecular interactions. As a response to these limitations, coordination-driven self-assembly has emerged as a powerful tool to regain control over supramolecular synthesis for the straightforward construction of highly complex molecules. The facile formation of metal-ligand coordination bonds provides easy access to a large variety of supramolecules, which structures are predictable and defined by the metal geometries and the nature of the subcomponent linkers (Figure I.4).[21] Especially interesting are supramolecular hosts since they possess inner cavities that can be exploited for performing chemistry at the confined space.[22] Depending on the type of molecular synthons used, bi-dimensional and tri-dimensional entities can be obtained and the size and shape of the cavities can be tailored.

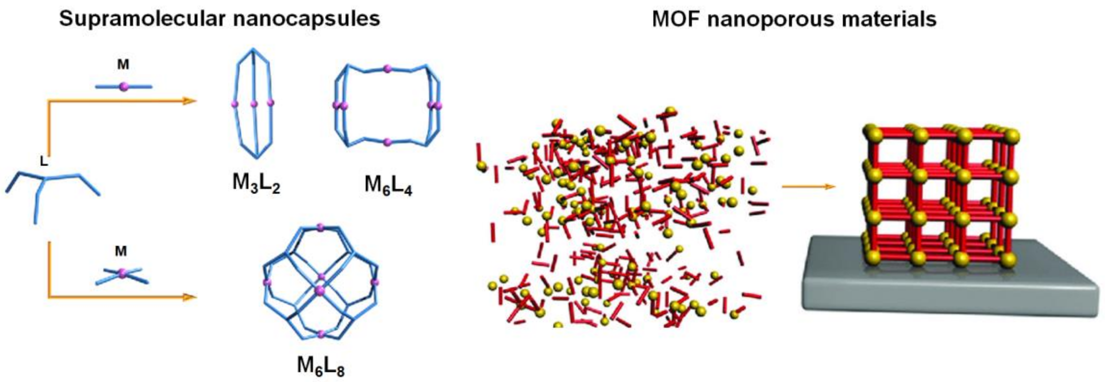

Figure I.4. Graphical representation of the metal-ligand directed self-assembly reactions yielding: a set of supramolecular nanocapsules (left) and nanoporous materials, such as MOFs (right).

I.1.4.2. 3D supramolecular host

The application of supramolecular hosts is diverse, being their use as nanoscale reactors one of the highlighted. Importantly, hydrophobic effects, effective concentration and protection against decomposition of the encapsulated species allows catalytic processes with genuine regioselectivities[23] and enhanced enantioselectivities,[24,25,26,27] in an analogous manner as the spatial constraints imposed by enzyme active sites.[28] On the other hand, supramolecular hosts featuring extended π-systems such as porphyrins have been extensively used in recognition host-guest experiments of all kinds of molecules (aromatics guests, anion recognition, etc.).

In this context, over the past years, supramolecular nanocapsules and nanoporous materials with nanometer-sized cavities have been reported.[29, 30] Such supramolecular structures have found widespread use in fullerene chemistry, highlighting their performance in molecular recognition, separation, purification and promoting unusual reaction outcomes in confined guests, among other applications. In this line, molecular receptors containing extended π-systems have been designed due to their affinity towards the sphere-like unsaturated structure of fullerenes. On the other hand, large efforts have been devoted to release the entrapped guest molecules, aiming the selective liberation of the encapsulated fullerenes or fullerene derivatives without affecting the integrity of the host.[31] More details of reactivity at the confined cavites of supramolecular compounds are given in Section I.1.5.3.

I.1.5. Synthesis of fullerene derivatives

I.1.5.1. Inherent reactivity of C_{60}

The increasing attention for carbon nanostructures and specially fullerenes over the last two decades is not only motivated by their fascinating nature, but also because of their potential applications in the next generation of functional materials in a wide range of fields, such as energy conversion/photovoltaics,[32] and biomedicine (sensing, imaging, drug delivery…).[33] However, fullerenes need to be derivatized to convert them into functional molecules by design.

Among all carbon nanostructures, fullerenes and EMFs are the only discrete molecular forms of carbon, thus having good solubility in a variety of organic solvents and also allowing their chemical modification. Although at the beginning C_{60} was considered aromatic, crystallographic data showed that it is more correctly described as a polyene, forming a conjugated π-system which contains alternately single ([5,6] bonds) and double bonds ([6,6] bonds) (Figure I.5).[34] Consequently, the [6,6] bonds in C_{60} behave like an electron-deficient olefins, thus experiencing analogous reactions. In addition, due to the spherical shape of C_{60} the C-C bonds are considerably strained, featuring a high degree of pyramidalization and consequently showing rich reactivity. When reacting with nucleophiles, the two C_{sp2} atoms involved become sp^3-hybridized, causing a release of strain that favors the reaction to occur. In this context, a variety of synthetic routes concerning the functionalization of fullerenes has been established since the early days of fullerene chemistry at the very beginning of the 1990s.[34]

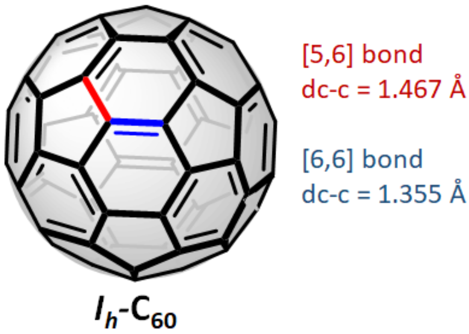

Figure I.5. Structure of C_{60} with different classes of bonds depicted.

I.1.5.2 Poly-functionalization of C_{60} in bulk solution

Since it can be produced in large scale, C_{60} has been the most exploited fullerene. However, the spherical nature of C_{60} containing 30 equivalent double bonds with almost identical reactivity, compromises the control of the regiochemistry in multiple additions, which is still a challenge in today's fullerene chemistry. Starting from a given mono-adduct, 8 different bis-adduct isomers can result by the addition of a second identical and symmetric addend (Figure I.6).[35] A third addition of another identical and symmetric group will potentially form 46 different tris-adduct products.[36] The regioisomeric mixtures of C_{60} derivatives require tedious (and often unsuccessful) chromatographic purification and subsequent spectroscopic characterization, fact that limits the complete exploitation of these functional materials. Nevertheless, highly functionalized fullerene derivatives are considered very attractive materials for practical applications,[37] and many efforts have been devoted to achieve the desired adducts in a selective manner.[38] In this line, different strategies for the selective production of multiple substituted fullerenes have been pursued, generally involving the initial stoichiometric modification of the fullerene with directing groups.

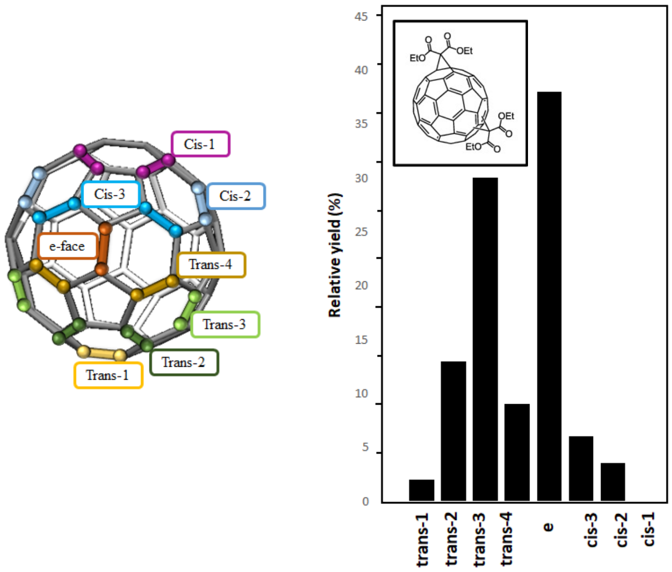

Figure I.6. C_{60} structure and depicted possible Bingel bis-regioisomers formed upon the addition of a second identical symmetric addend. On the right, histogram representing the abundance of each bis-regioisomer formed in bulk solution.

I.1.5.2.1. Removable Diels-Alder template addends

The use of removable template addends was introduced by Hirsch and co-workers in 1995.[39] The authors used a slightly modified protocol for Bingel cyclopropanations, adding 9,10-dimethyl anthracene (DMA) to the reaction mixture. Reversible Diels Alder (DA) [4+2] cycloaddition of DMA moieties, which act as a labile template agent activating the equatorial bonds of the C_{60} framework, allows for the efficient and selective production of a cyclopropanated T_h symmetric hexakis-adduct, in a one pot reaction. An analogous strategy was developed by Kräutler and coworkers (so-called "orthogonal transposition"), taking advantage of the selective formation of *trans*-1 anthracene bisadducts in the solid state to then synthesize equatorial cyclopropanated *e,e,e,e*-tetrakis-adduct under complete regiochemical control (Figure I.7).[40] The retro-DA is achieved thermally (180ºC) in the solid state.

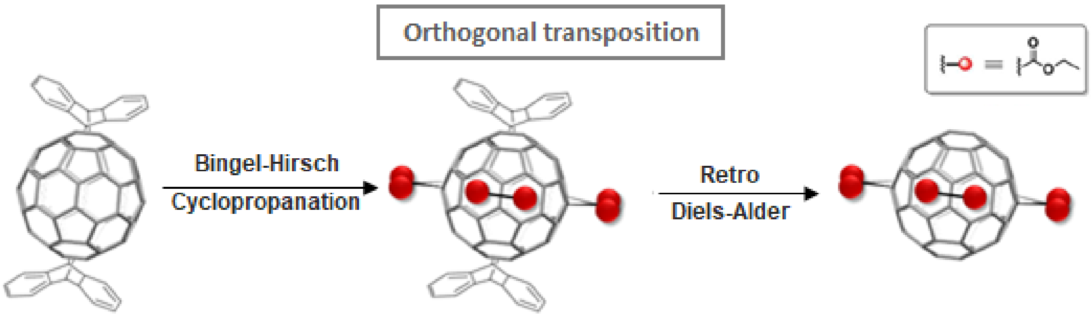

Figure I.7. Orthogonal transposition strategy via reversible DA adduct formation for the regioselective synthesis of equatorial cyclopropanated e,e,e,e-tetrakis-C_{60} derivative.

I.1.5.2.2. Tethered remote functionalization

Another well-known regioselective strategy is the "tether-directed remote functionalization", which allows the synthesis of bis-, tris-, pentakis- and hexakis-adducts with excellent regiochemistry. This concept was firstly introduced by Diederich and co-workers in 1994 and consists in the addition of multiple addends bridged together with a tether functionality (Figure I.8).[41, 42] The length and nature of the tether moiety direct the successive addition to a specific [6,6] bond of C_{60}. The tether strategy is mainly used for Bingel cyclopropanations and has been extensively applied for the regiocontrolled bis- and tris-additions. Importantly, the tether moiety is not removable, which is an evident drawback. On the other hand, the Diels Alder adduct as a templating agent (see section I.1.5.2.1) is not a versatile strategy, since it requires high temperatures and long times (hours) for the retro-Diels Alder. Arguably, all methods for regioselective functionalization of fullerenes mentioned above, are tedious, limited in scope, and overall lack of the versatility and practical utility required to boost the applicability of fullerene derivatives.

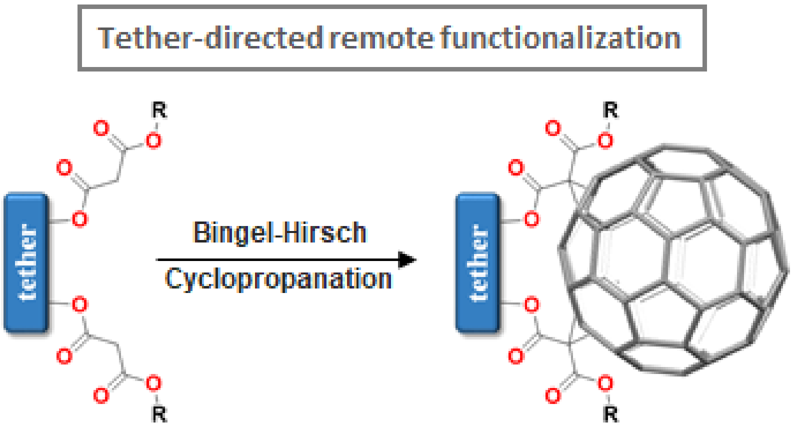

Figure I.8. Tether-directed remote functionalization strategy to control the regiochemistry during the synthesis of C_{60} bis-adduct cyclopropanated derivatives

I.1.5.3. Chemoselective functionalization of confined C_{60}

I.1.5.3.1. Chemoselective formation of bis-adducts

Despite hundreds of molecular receptors for fullerene or fullerene derivatives have been reported in the literature during the last decades,[31] the reactivity modulation of C_{60} by confinement remains very scarce and is limited to Diels-Alder (DA) reactions.

From this perspective, Nitschke and coworkers reported in 2016 the first example of functionalization of a fullerene within the inner void space of a supramolecular cage.[43] They focused on the synthesis of Diels Alder C_{60} derivatives, aiming at the selective formation of bis-adducts directed by the inherent steric constrains of confined C_{60} (see Figures I.9 and I.10). The authors hypothesized that the incorporation of electron-poor perfluorophenylene groups into a cage framework could optimize the binding of fullerene derivatives. Consequently, an electron-deficient cubic framework **Supra-1** was synthesized, consisting of a tetrakis-(perfluorophenylene)Ni-porphyrin core bearing four triazolyl-pyridine chelating groups (**Porph-1**, see Figure I.9). Guest encapsulation within **Supra-1** was proven using ^{19}F-NMR spectroscopy, whereby the chemical shifts of the inward-facing fluorine atoms were observed to act as probes of their chemical environments. It is well known that large container molecules are able to recognize small molecules due to favorable Coulombic interactions; however, during the host-guest experiments performed with large anions (such as $Mo_6O_{19}^{2-}$, $B_{12}F_{12}^{2-}$, BPh_4^-, etc.) no evidences for the encapsulation were observed. In addition, encapsulation of C_{60}, C_{70}, or any of the higher fullerenes present in fullerene soot was not observed, either. By Rebek's 55% rule,[44] the 3183 Å^3 cavity volume of **Supra-1** should optimally encapsulate guests having volumes around 1750 Å^3. The authors reasoned that, whereas spherical guest such as unsubstituted fullerenes would be expected to favor high occupancy ratios, no effective interactions were present with the inner cavity of the receptor.

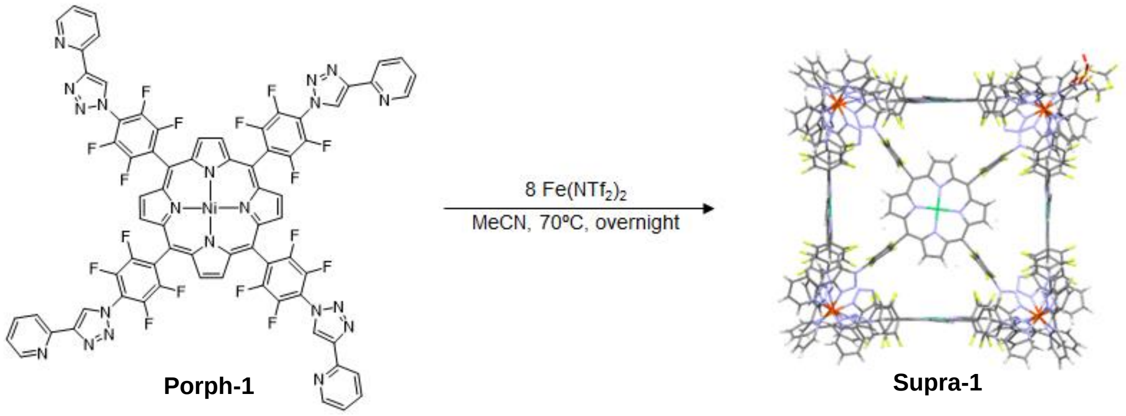

Figure I.9. Formation of **Supra-1** based on the self-assembly of ligand **Porph-1** and Fe(II) triflimide complex. The crystal structure of **Supra-1** is depicted at right. Counteranions and disorder are omitted for clarity.

Conversely, the authors hypothesized that the functionalization of fullerenes should lead to molecules which, once encapsulated, would exhibit stacking interactions with the inner cavity walls. To confirm the hypothesis, the host-guest properties of **Supra-1** using C_{60} indene-derivatives as guests were investigated (Figure I.10, top). Therefore, excess of mono- (C_{60}Ind), bis-indene-C_{60} (C_{60}Ind$_2$) and pristine C_{60} were added to a solution of **Supra-1** in acetonitrile and the mixture was heated at 70ºC for 16h. The reaction crude was analyzed by NMR and electrospray ionization mass spectrometry (ESI-MS) and encapsulation of C_{60}Ind$_2$ (isomeric mixture) was solely observed. The selective encapsulation of the bis-adduct derivative in the presence of mono-adduct and pristine C_{60} prompted the authors to explore whether a general trend was present, and the study of the selectivity of **Supra-1** towards anthracene (Diels Alder) was performed. Preliminar host-guest studies with purified mono- (C_{60}An$_1$) and bis-anthracene-C_{60} (C_{60}An$_2$) adducts yielded results identical to those obtained with the indene-derivatives, observing specific binding of bis-adducts. In a proof-of-concept study, the authors combined **Supra-1**, C_{60} and anthracene in acetonitrile and heated the mixture to 50ºC overnight (Figure I.10, bottom). The ESI-MS experiments of the reaction crude revealed the selective formation of C_{60}An$_2$$\subset$**Supra-1** host-guest adduct. However, the weakly associated anthracene moieties, which was present in excess, gave rise to the formation of undesired C_{60}An$_1$$\subset$**Supra-1** and C_{60}An$_3$$\subset$**Supra-1** (due to retro-DA side reactions) under the conditions employed to record the mass spectrum. It is worth to note that, cage **Supra-1** enabled reaction between species that individually are not suitable for encapsulation to form products that have a favorable size and shape for encapsulation.

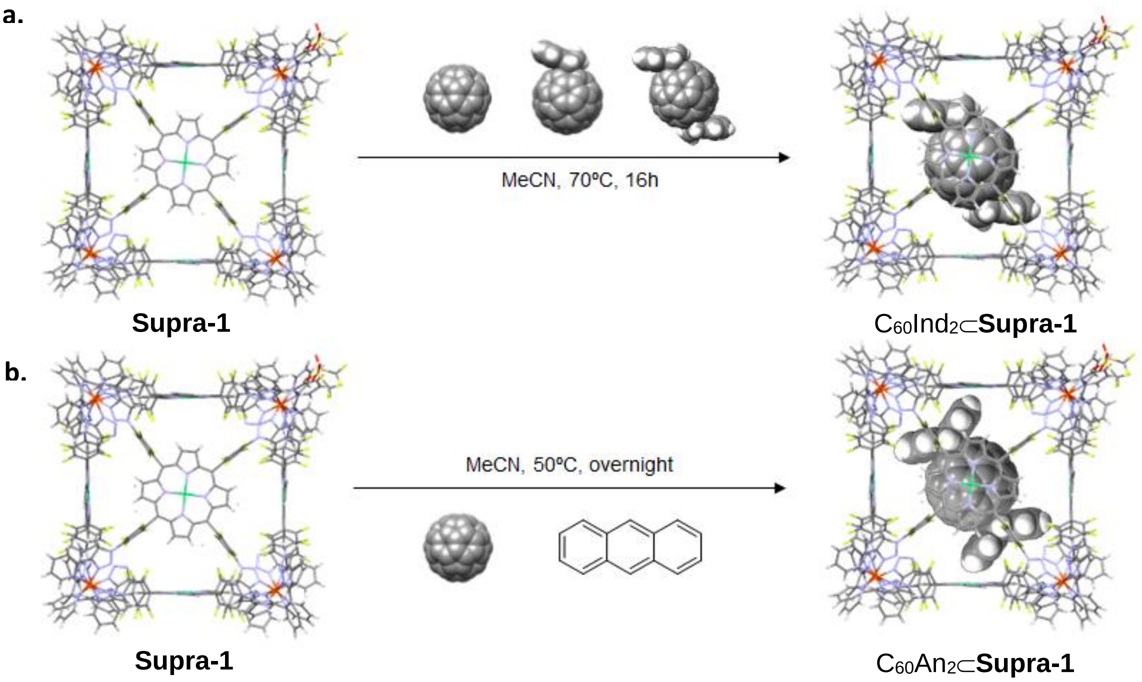

Figure I.10. a) Selectivity of cage Supra-1 towards bis-adducts when subjected to a sample containing the crude mixture of a Diels Alder reaction between C_{60} and indene (top). b) in situ reaction between C_{60} and anthracene inside **Supra-1** and preferential formation of $C_{60}An_2$⊂**Supra-1**. In both representations, only one isomer of the bis-adducts is shown for clarity.

Inspired by the work of Nitschke (Figure I.10), Zhou group attempted to apply the same concept to MOFs, aiming at turning the selective production of fullerene derivatives in confined spaces into a catalytic methodology.[45] The authors hypothesized that the functionality of the cage **Supra-1** (Figure I:9) could be transferred to a 3D framework by synthesizing a structurally analogous MOF scaffold, in terms of size, shape and electronic features of the internal void cavity (Figure I.11). The authors observed that by replacing the triazolyl-pyridine chelating groups of the **Porph-1** ligand (Figure I.9) by a pyrazolidine ring, an extended 3D-network instead of a discrete supramolecular entity was formed (Figure I.11). Furthermore, the high stability and insolubility of pyrazolide-based MOFs, turned them into promising candidates for the development of recyclable heterogeneous catalysts. From that perspective, the electron-deficient MOF **PCN-624** was obtained as a crystalline powder by mixing nickel acetate, 5,10,15,20-tetrakis(2,3,5,6-tetrafluoro-4-(1H-pyrazol-4-yl)phenyl)-porphyrin (**Porph-3**) and deionized water in DMF (Figure I.11, bottom) under solvothermal conditions (120ºC, 24h). UV-vis monitoring of the encapsulation of $C_{60}An_2$ (isomer mixture) in PCN-624 afforded a 86% uptake after 36h. Host-guest experiments with pristine C_{60} and $C_{60}An$ were conducted under the same conditions, however, no evidence of the inclusion compounds was observed. The authors attributed these findings to low occupancy ratios of C_{60} and $C_{60}An$ (size/shape mismatching). The **PCN-624** network contained cubic cages with highly electron-deficient surface, which has an inner void volume of 3243 Å^3 (almost the same volume than **Supra-1** cage, Figure I.9). According to the Rebek's rule,[44] this framework could selectively encapsulate guest molecules with volume of 1783 Å^3. Compared with other fullerene adducts, the bis-anthracene-C_{60} ($C_{60}An_2$) adducts, which has a volume of 1802 Å^3, is the optimum guest among numerous fullerene derivatives tested. Furthermore, the aperture size (6.6 x 14.5 Å^2) of **PCN-624** was large enough to accommodate the entry and exit of the ellipsoidal $C_{60}An_2$ (minor diameter 6.4 Å and major diameter 11 Å), which is a requirement for the purification and the catalytic production of these

C_{60} derivatives. Interestingly, using the fluorine-free analogue **PCN-602** MOF, no evidences for the capture of $C_{60}An_2$ were observed (Figure I.11). These evidences suggested that the supramolecular recognition present on this host-guest complex is mainly governed by the C-F···π interactions[46] promoted by the inward-facing fluorine atoms present in the void cavity of **PCN-624** and $C_{60}An_2$. Therefore, the combination of suitable void volume (size/shape complementarity) and electron-deficient inner surface in the cavity of **PCN-624** (electronic complementarity) afforded efficient molecular recognition of the target fullerene derivative.

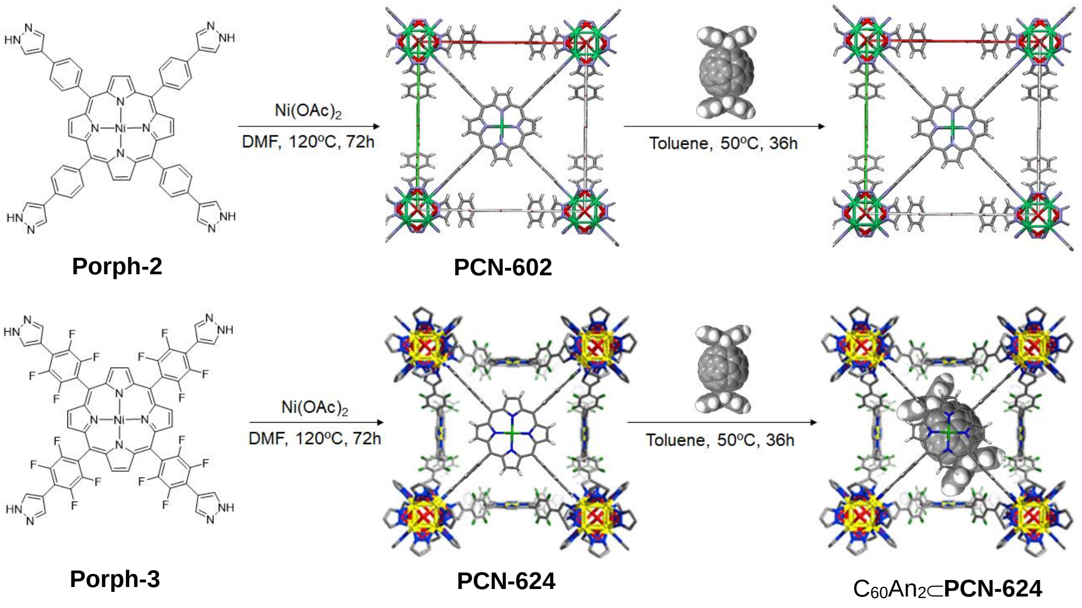

Figure I.11. Synthesis of MOFs **PCN-602** (top) and **PCN-624** (bottom), based on the assembly of ligands **Porph-2** and **Porph-3** (respectively) and nickel(II) acetate, and schematic diagram of the host-guest affinity of **PCN-602** and **PCN-624** towards $C_{60}An_2$. Only **PCN-624** is able to encapsulate $C_{60}An_2$. (Crystal structures depicted omitting hydrogens for clarity; only one isomer of the Diels Alder bis-adducts is shown for clarity).

Encouraged by the selective binding of $C_{60}An_2$, the authors further attempted to employ this framework as nanoreactor to selectively produce $C_{60}An_2$ (Figure I.12). The DA reaction between C_{60} and anthracene was conducted in acetonitrile at 50ºC during 12h, in the presence of **PCN-624**. After filtration, the isolated **PCN-624** was soaked in toluene, the resulting solution was filtered and analyzed by HPLC. The HPLC measurements revealed that $C_{60}An_2$ was selectively generated as a single product. The same reaction conditions were reproduced without **PCN-624** and no $C_{60}An_2$ was formed, which was attributed to the low solubility of C_{60} in CH_3CN. On the other hand, the reaction performed in toluene without the MOF led to the formation of a mixture of mono-, bis- and tris-adducts. Finally, the authors studied the recyclability of the nanoreactor, aiming a cyclic performance of the heterogeneous catalyst. Interestingly, **PCN-624** could be easily separated and recovered from the reaction crude by filtration and solvent washing. The regenerated **PCN-624** could be subjected up to five cycles and the catalyst still retained its crystallinity and porosity, showcasing its performance as heterogeneous catalyst.

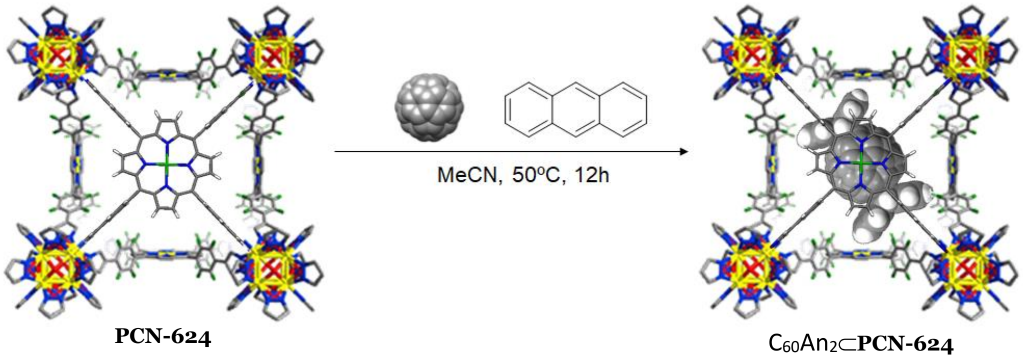

Figure I.12. Selective production of $C_{60}An_2$ using **PCN-624** as a nanoreactor (only one isomer of the Diels Alder bis-adducts is shown for clarity).

I.1.5.3.2. Chemoselective formation of mono-adducts

Early in 2019, Clever and coworkers reported a modular system based on molecular pillars (**L₁** and **L₂**) self-assembled with two Palladium(II)-coordinating units, producing **Supra-2** capsule and unprecedented **Supra-3** bowl-like supramolecular scaffolds (Figure I.13).[47] Heating **L¹** and $[Pd(CH_3CN)_4](BF_4)_2$ (2:1 molar ratio) in CH_3CN at 70ºC for 24h resulted in the quantitative formation of cage **Supra-2** (Figure I.13b), unambiguously characterized by X-ray diffraction. Interestingly, **Supra-2** is selective towards the encapsulation of C_{60}, since no uptake of C_{70} was observed (Figure I.13b). They attributed this selectivity to the good match in terms of shape (spherical C_{60} vs ellipsoidal C_{70}) and size (572 $Å^3$ void cavity vs 547 $Å^3$ van-der-Waals volume of C_{60} and 646 $Å^3$ for C_{70}) for the confined space of **Supra-2**. The average distances from the ligand benzene ring centroid to the center of C_{60}, clearly verify that the concave inner surface of **Supra-2** cavity can serve as a fullerene receptor through strong π···π interactions. Furthermore, the dihedral angle between two pyridine arms of the same ligand was completely different depending whether the C_{60} is encapsulated or not. Hence, uptake of the fullerene guest led to a conformational change of the cage geometry indicating an induced-fit structural adaptation. On the other hand, prolonged heating of **L₂** and $[Pd(CH_3CN)_4](BF_4)_2$ (2:1 molar ratio) in CH_3CN unexpectedly yielded a bowl-shaped scaffold **Supra-3**, containing two Pd nodes and three quinolone-based ligands **L₂** (Figure I.13c). The X-ray diffraction analysis of **Supra-3** unambiguously verified its bowl's open geometry. The authors hypothesized that the bowl-shaped nanocapsule could act as a supramolecular protecting group for fullerene guests to modify the reaction outcome of a DA reaction. As observed in the crystal structure of C_{60}⊂**Supra-3**, only 25% of the total C_{60} surface area of the guest was exposed and susceptible to be functionalized. In order to elucidate this hypothesis, the C_{60}⊂**Supra-3** adduct was subjected to a DA reaction conditions using anthracene. The system allowed the selective production of anthracene mono-adduct (with no traces of bis-adduct) when C_{60}⊂**Supra-3** was treated with up to 50 equivalents of anthracene at 50ºC in CH_3CN during 12h (Figure I.13d). In addition, the crystal structure of $C_{60}An$⊂**Supra-3** clearly showed indeed that a second anthracene DA cyclization was not possible for steric reasons. Furthermore, this structure represented the first crystallographic report of a C_{60}–Anthracene mono-adduct. The versatility of the system is further exemplified by dimerization of the two **Supra-3** bowls into pill-shaped assemblies, by replacing the CH_3CN groups that are coordinated to the Pd nodes by terephthalate bridges (Figure I.13e). Dimerization could be shown for both the empty **Supra-3** and its C_{60}/C_{70} complexes, as demonstrated by spectroscopic and spectrometric techniques. Furthermore, the pill-shaped dimer is able to bind two fullerenes (C_{60} or C_{70}) (Figure I.13e).

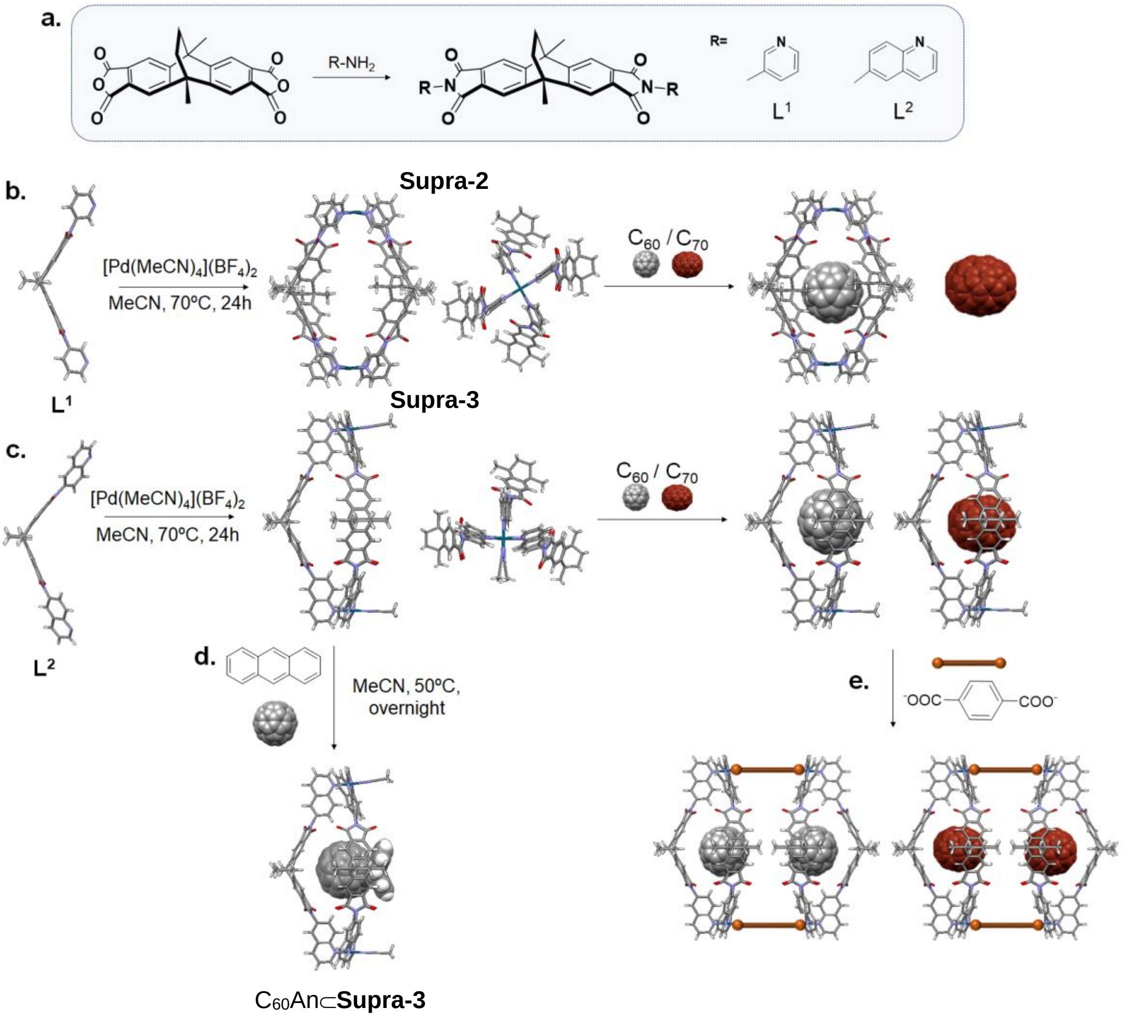

Figure I.13. Ligand and cage synthesis. a) Preparation of ligands **L^1** and **L^2**; b) Ligand **L^1** assembles with Pd^{II} cations to form cage **Supra-2**, which is capable of binding C_{60} selectively; c) Ligand **L^2** assembles with Pd^{II} cations to form cage **Supra-3**, which is capable of binding C_{60} and C_{70}; d) Diels-Alder reaction between anthracene and confined C_{60} within **Supra-2**. e) Dimerization of host-guest adducts formed between cage **Supra-3** and C_{60} or C_{70}, though reaction with terephthalate bridges.

I.1.6. Synthesis of EMFs derivatives

I.1.6.1. Inherent regioselectivity dictated by the internal cluster

On the other hand, the examples of chemical modification of EMFs are scarce when compared with their empty analogs. The first example of EMFs functionalization was reported by Akasaka and coworkers in 1995.[48] The authors produced an exohedral mono-adduct derivative of La@C_{82} through photochemical attachment of disilirane functional group (disilacyclopropane). However, most of the chemistry behind EMFs has been developed over the last 15 years. The reactivity of EMFs changes significantly as compared with empty fullerenes, since electron transfer processes from the internal metal or metal cluster to the carbon cage dramatically disturb its electronic structure and inherently controls the regiochemistry of successive additions (Figure I.14). [49,50]

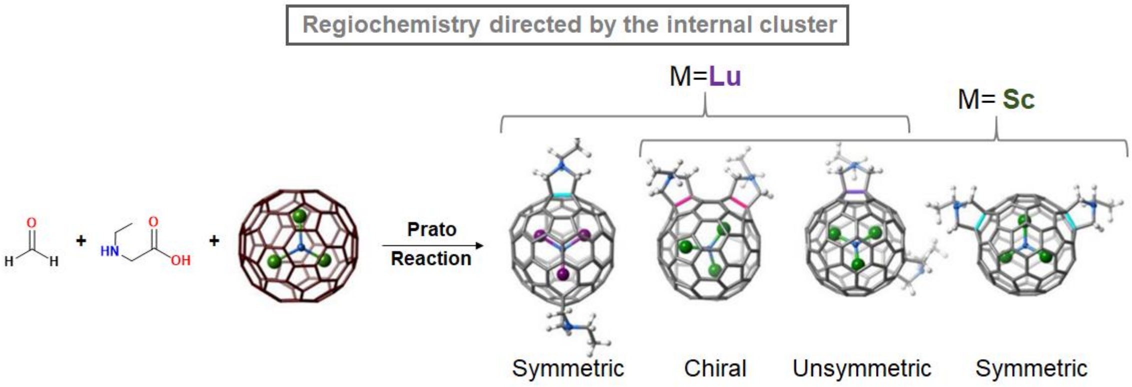

Figure I.14. Representation of the selective formation of specific bis-adducts depending on the metal cluster present on the $M_3N@C_{80}$ EMFs

The scarcity of examples of EMF functionalization, when compared with pristine fullerenes, is directly related to the very limited access to pure samples, which is extensively discussed in the following section.

I.2. Endohedral Metallofullerenes: embedding metals in hollow fullerenes

I.2.1 Discovery and structural properties

Soon after the discovery of C_{60}, the feasibility of hosting Lanthanum (La) atoms into the void cavity of fullerene cages was hypothesized on the basis of mass spectrometric detection of $La@C_{60}$.[51] In 1991, the first solvent extractable EMF $La@C_{82}$ was experimentally produced. [19] The unprecedented properties of $La@C_{82}$ revealed a three electron transfer from the endohedral metal to the carbon cage, formally $La^{3+}@C_{82}^{3-}$. The intramolecular charge transfer, which can vary depending on the metal in the cavity, renders EMFs with unique electronic and/or magnetic properties, making them very intriguing materials.[52]

A breakthrough in the EMF field occurred in 1999, when $Sc_3N@C_{80}$ was discovered via introducing nitrogen gas into the Krätschmer-Huffman reactor during the vaporization of graphite rods containing scandium oxide (Sc_2O_3).[53] The very high yield of $Sc_3N@C_{80}$ compared to all other EMFs produced previously, was a groundbreaking achievement in this field. Besides, from the point of view of the molecular structure, the $(Sc_3N)^{6-}$ cluster is unstable as a single species, existing only in the microenvironment provided by the fullerene cage. In addition, the icosahedral C_{80} carbon cage is unstable as an empty fullerene, being a clear example of a specific mutual stabilization of the inner metal cluster and the outer fullerene cage specifically.[54, 55]

I.2.2 Classification and applications

Following these advances, during the past two decades the family of EMFs has been considerably extended by different type of entrapped metal clusters. On the basis of the composition of the internal metallic species, EMFs can be categorized in nine classes: monometallic endohedrals (mono-EMFs),[19] dimetallic endohedrals (di-EMFs),[56] metal nitride clusterfullerenes (NCFs),[53] metal carbide clusterfullerenes (CCFs),[57] metal oxide clusterfullerenes (OCFs),[58] metal sulfide clusterfullerenes (SCFs),[59] metal cyanide clusterfullerenes (CYCFs),[60] metal hydrocarbide clusterfullerenes (HCCFs),[61] metal carbonitride clusterfullerenes (CNCFs)[62] and metal-mixed clusterfullerenes (MMCFs)[63] (Figure I.15). Thus, the clusterfullerene family represents nowadays the most variable and intriguing branch in the field.

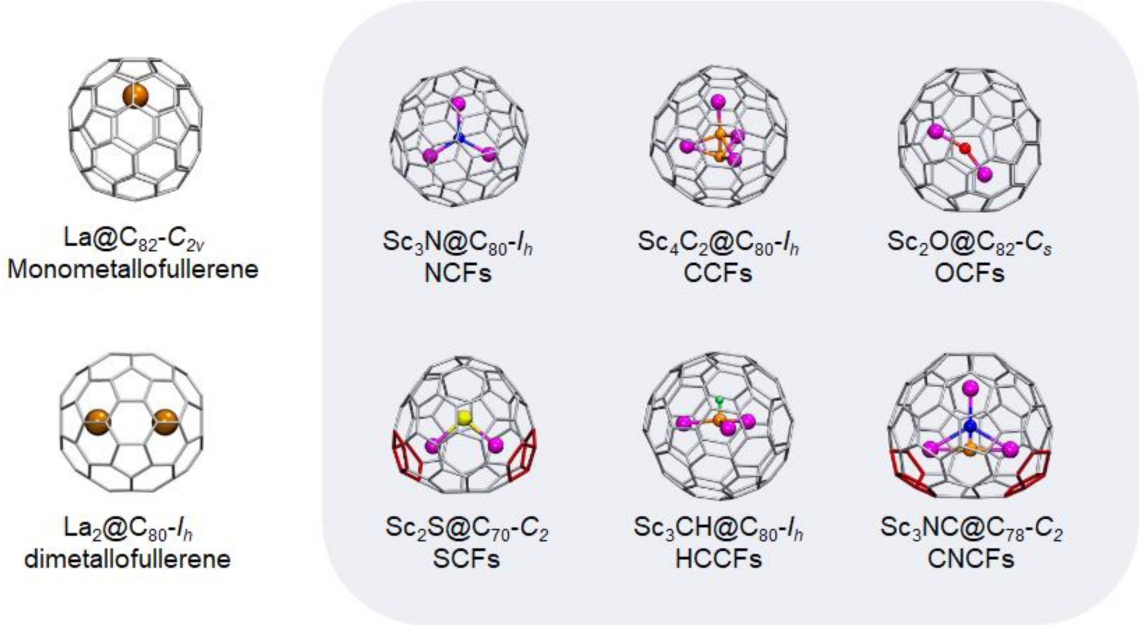

Figure I.15. Molecular structures of the most representative classes of EMFs.

Shielding of the entrapped metals or metal clusters by the fullerene cage, confers high stability to the metal/metal cluster-cage hybrid EMF structures, making them excellent candidates for electro-active materials (new acceptors/electron transporting materials for organic photovoltaic devices,[64] donor-acceptor dyads,[65] photoelectrochemical cells,[66] high-density storage devices,[67] etc), for magnetic properties (Single Molecule Magnets)[52] and for biomedical applications due to their low toxicity (contrast agents,[68] radiopharmaceuticals,[69] antitumor[70] and antimicrobial[71] drugs, etc). However, all these applications have not been fully exploited owing to the limitations of the purification methods reported so far.

I.2.3 Purification and separation techniques

I.2.3.1 Chromatographic techniques

The Direct-Current (DC) arc-discharge method is the most used for production of EMFs due to its simplicity and cost-effectivity.[20] However, it is a rather harsh process which does not allow taking in situ probes of the formed product. Furthermore, no selectivity is observed towards the production of the desired EMFs species, yielding complex mixtures of different-size empty fullerenes and EMFs, nanotubes and amorphous carbon. High performance liquid chromatography (HPLC) is by far the most powerful technique used for the isolation of fullerenes and EMFs. Although efficient columns for the HPLC separation of EMFs are available, their purification via chromatographic techniques faces serious difficulties due to the large variety of the species in the crude soot and the similar size and shape of the carbon cages, together with the very limited content of EMFs in the raw soot.[72] This dramatically hinders the purification of these carbon materials, even when running in multi-step or recycling HPLC modes. To circumvent these limitations, some chemical and electrochemical separation methodologies have been developed targeting the isolation of EMFs.

I.2.3.2 Non-Chromatographic techniques

Pioneering electrochemical studies of fullerenes revealed a substantial difference on the oxidation potential of fullerene isomer cages. Accordingly, in 2005 Echegoyen and coworkers accomplished for the first time the separation of $Sc_3N@I_h\text{-}C_{80}$ and $Sc_3N@D_{5h}\text{-}C_{80}$ isomers by selective chemical oxidation.[73] In the same year, Dorn and coworkers followed a different strategy by taking advantage of the kinetic chemical stability of NCFs compared to empty fullerenes in Diels-Alder (DA) reactions (Figure I.16, left). Using a cyclopentadiene-functionalized resin, one-step separation of a series of $M_3N@C_{80}$ was accomplished.[74] In light of such different reactivity, in 2008 the same group reported the separation of NCFs by a chemical reaction of congeners with 9-methyl-anthracene (Figure I.16, right). The higher DA reactivity of fullerenes and some EMFs compared with the inertness of NCFs, promote the selective formation of functionalized derivatives, which can be easily removed due to the orthogonal solubility between these derivatives and NCFs.[75]

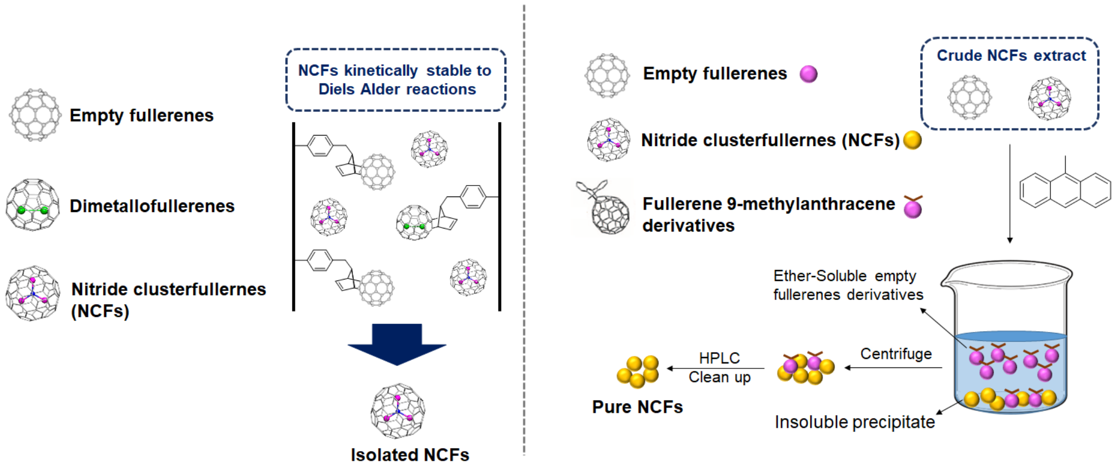

Figure I.16. Schematic representation of NCFs purification strategies reported by Dorn and coworkers. Both strategies are based on the kinetic chemical stability of NCFs towards DA reactions compared to empty fullerenes and dimetallofullerenes in Diels-Alder reactions.

Following an analogous strategy, Stevenson *et al.* proposed a method named "SAFA" (Stir And Filter Approach) (Figure I.17). Without any chromatographic equipment, the authors achieved the selective immobilization of empty fullerenes and non-NCFs in a cyclopentadienyl- and amino-functionalized silica, while the relatively inert NCFs remained in solution and could be directly isolated by filtration.[76] Later on, the same group accomplished the separation of $Sc_3N@I_h\text{-}C_{80}$ and $Sc_3N@D_{5h}\text{-}C_{80}$ by applying this methodology.[77] It is worth to note that fullerenes and EMFs immobilized on the silica phase during the "SAFA" protocol, were previously discarded as a waste due to the lack of a recovery strategy. In 2014, a novel recovery method by adding CS_2 to functionalized silica containing trapped EMFs, resulted in the release of these absorbed carbon cages (i.e. Er- and Gd-based EMFs).[78]

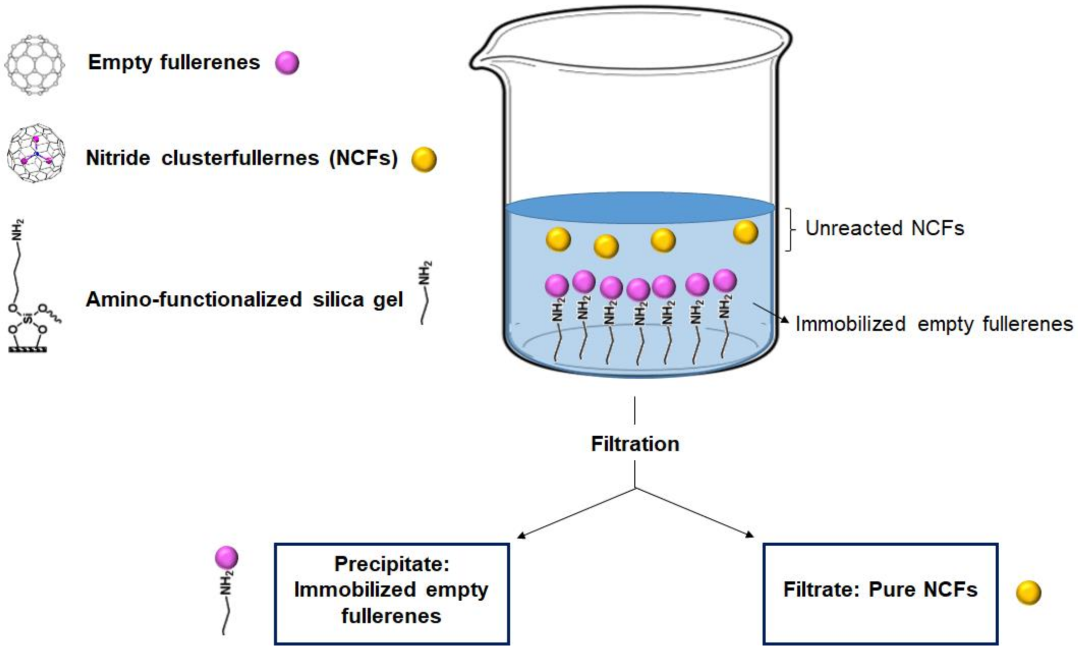

Figure I.17. Schematic representation of NCFs purification strategies reported by Stevenson and coworkers. The strategy so called SAFA (stir and filter approach) immobilize selectively the empty fullerenes in a functionalized silica and NCFs are isolated by filtering the suspension

Another popular alternative EMF purification strategy is the selective precipitation of NCFs by complexation with Lewis acids (Figure I.18). Stevenson and coworkers found that NCFs and OCFs react faster with an array of Lewis acids (such as $AlCl_3$ and $FeCl_3$), whereas empty fullerenes are mostly unreactive. The Lewis acid-EMF adduct is treated with H_2O and extracted with CS_2 to recover the EMF. Rate constants determined experimentally exhibited a linear correlation to the electrochemical band gaps of the corresponding EMFs, resulting finally in the selective precipitation and purification of $Sc_3N@I_h\text{-}C_{80}$.[79] Manipulation of Lewis acids according to the different reactivity towards different EMFs is nowadays one of the most used and versatile non-chromatographic purification strategies, suitable for the isolation of many type of EMFs, such as mono- and dimetallofullerenes,[80] and metal mixed nitride clusterfullerenes (MMNCFs),[81] among others.

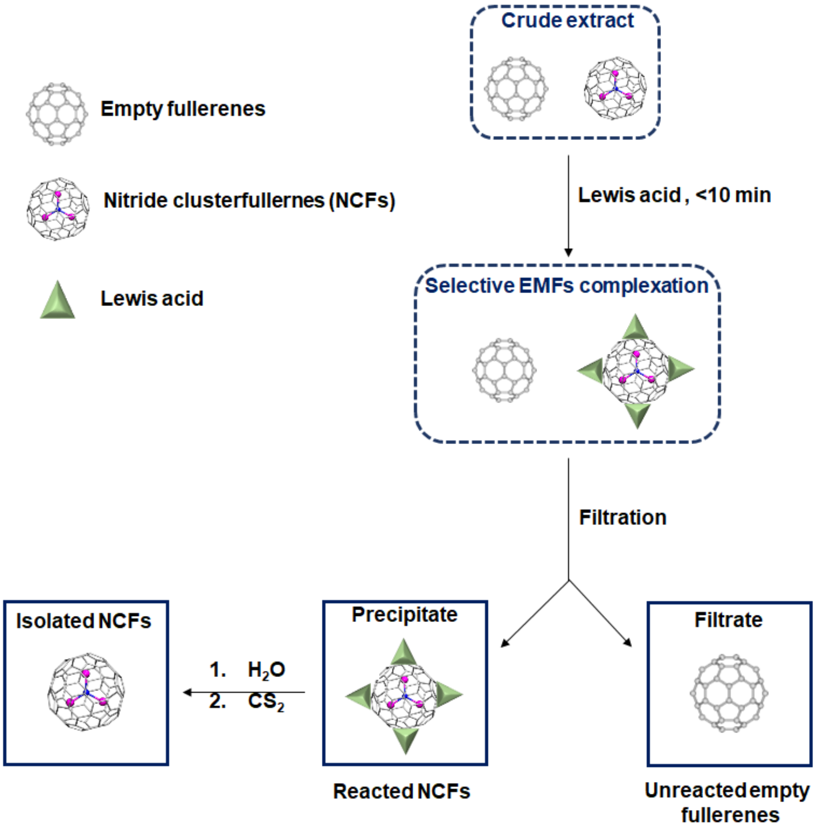

Figure I.18. Schematic representation of NCFs purification strategy reported by Stevenson and coworkers, based on the selective complexation and precipitation of NCFs with Lewis acids, in the presence of other fullerenes

I.2.4 Molecular recognition of EMFs

I.2.4.1 Macrocyclic platforms and non-porphyrinic receptors

In 1992 Ringsdorf and co-workers reported the first example of a molecular receptor for hosting hollow fullerenes,[82] just two years after the discovery of multigram production of these spherical-like carbon allotropes.[20] Since then, the use of molecular receptors for fullerene separation has emerged as an attractive strategy allowing potential selectivity, non-requirement of specific equipment and ideally, recyclability of hosts by design.[31] On the other hand, examples of molecular receptors for recognition of EMFs remains scarce to date. Since chromatographic HPLC isolation of EMFs is tedious and not suitable for high-throughput and large scale separation,[72] non-chromatographic methods were thus explored.

The ability of fullerenes to form supramolecular assemblies by complexation with crown ether-like macrocyclic compounds was reported back in 2006 (ref 84).[83] EMFs are intrinsically different from hollow fullerenes, exhibiting unique electronic properties derived from their metal-to-cage electron transfer.[84] Their distinctive characteristics directly influence the non-covalent forces involved in their molecular recognition with supramolecular receptors.

In this context, in 2006, Akasaka and coworkers studied for the first time the complexation behavior of EMFs with azacrown ether macrocycles, achieving their selective isolation from soots.[85] The preferential extraction of La@C_{82} from raw soot using nitrogen-containing solvents , such as pyridine, led to enriched samples of La@C_{82}, facilitating the study of its 1:1 supramolecular complexes formed with azacrown ethers **3-5** and acyclic polyamine **2** (Figure I.19). The authors observed a close correlation between the number of heteroatoms in the azacrown macrocycle and the stability of the supramolecular complex formed with La@C_{82}. On the other hand, the low affinity of acyclic polyamine **2** towards La@C_{82} in comparison to azacrown **5** was rationalized through the importance of the macrocyclic shape of the receptor in the complexation events. The significant differences in the complexation behavior between fullerenes and EMFs prompted the authors to attempt the purification of La-based EMFs from mixtures contained in extracts of soot. The addition of **3** to a toluene solution of the extract afforded a precipitate, which was collected by filtration and sonicated in CS_2. Remarkably, the HPLC and the LDI-TOF analysis of the CS_2 solution confirmed that the La-based EMFs were selectively extracted from the initial soot. The facile electron transfer (characteristic of EMFs with low reduction potential) was pointed to be at the basis of the highest affinity of azacrown ether macrocycles towards La@C_{82} in comparison to C_{60} and C_{70}.

To gain further information on the non-covalent forces directing the complexation of La@C_{82}, in 2006, the same authors developed a new series of sulfur-based crown thioether derivatives **6-10** for EMF complexation (Figure I.19)**.**[86] Unsaturated crowns were included, due to their known ability to exhibit a rigid structure and restricted directionality of the sulfur atoms pointing towards the inner side of the ring. Vis-NIR spectroscopy indicated that crown thioethers **7-10** formed 1:1 complexes with La@C_{82} in solution. Interestingly, whereas unsaturated thiacrown ether **10** exhibited the largest binding constant, its saturated analogue did not exhibit effective complexation, thus highlighting the importance of the olefinic moiety. Furthermore, it was demonstrated for the first time that the complexation strength towards La@C_{82} depends on the size of the host molecules (shape/size complementary), suggesting the formation of the first inclusion complexes with EMFs.

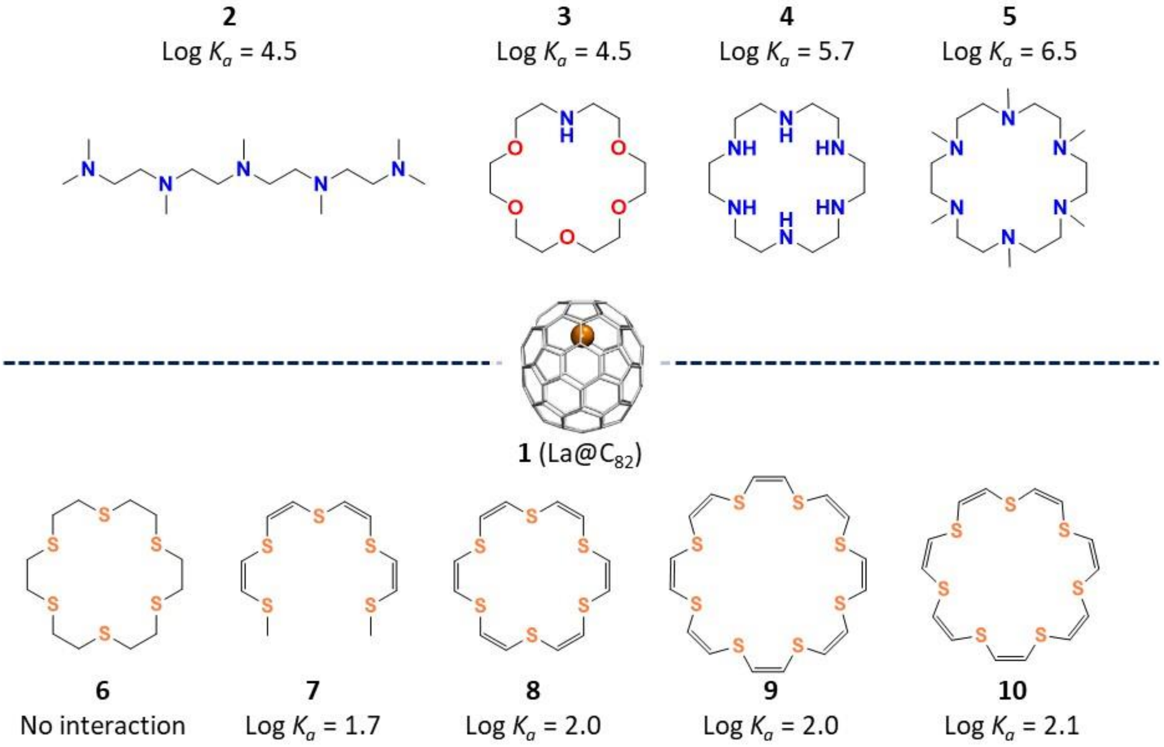

Figure I.19. Macrocyclic receptors designed to study the host-guest complexation of La@C_{82}. Ka values calculated in nitrobenzene

In analogy to these examples, Fukuzumi and coworkers observed a very strong complexation of Li@C_{60} using benzo- and dithiabenzo- crown ether functionalized monopyrrolotetrathia derivatives, namely **Fulvalene-1** and **Fulvalene-2** (Figure I.20).[87] Binding constants were much higher than those obtained with pristine C_{60} (100 times fold, in benzonitrile). The different stability was attributed to the enhanced electrostatic interactions between the endohedral Li^+ ion and the oxygen (**Fulvalene-1**) or sulfur atoms (**Fulvalene-2**) present on the macrocyclic derivatives. In order to gain insight into the nature of these interactions, Li@C_{60} was treated separately with tetrathiafulvalene and 4'-nitrobenzene[24]crown-8 ether, observing complexation only with the crown ether (Figure I.20). In addition, the authors observed that the higher was the number of the sulfur atoms on the scaffold, the lower the stability of the supramolecular complexes. The lower affinity of these derivative towards Li@C_{60} were rationalized through the large size of the sulfur atoms, which displaced further away the fullerene cage from the crown ether.

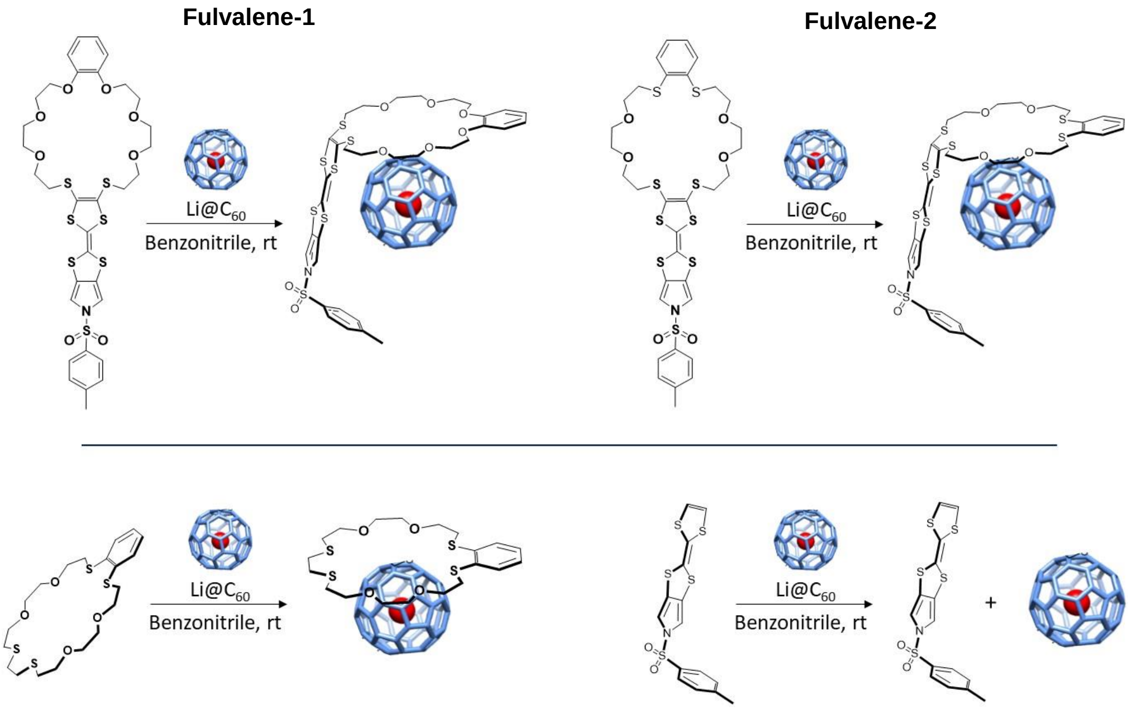

Figure I.20. On the top, thiabenzo- crown ethers functionalized with monopyrrolotetrathiafulvalene derivatives, synthesized by Fukuzumi and coworkers, and graphical representation of the corresponding host-guest complexes with Li@C_{60}. On the bottom, Li@C_{60} was treated separately with tetrathiafulvalene and 4'-nitrobenzene[24]crown-8 ether, observing complexation only with the crown ether.

Later in 2014, the same group reported the first example of a rigid receptor for EMFs (**Tweezer-1**), consisting in a tweezer-type pentiptycene-based bis(crown ether) host (Figure I.21).[88] In analogy to the previous example, the absence of complexation with pristine C_{60} revealed that the Li^+ ion present in Li@C_{60} played a very important role on the molecular recognition processes. In addition, the strong electron donor character of the receptor led to a photoinduced electron-transfer to the trapped Li@C_{60}. Furthermore, photo-excitation of the supramolecular complex monitored by time resolved transient absorption analysis reveals a very efficient formation of a long-lived charge-separated excited state. In line with these results, they demonstrate the feasibility to use Li@C_{60} in combination with electron donor hosts for applications in organic electronics and solar energy conversion, thus upgrading EMFs as better alternatives than pristine fullerenes.

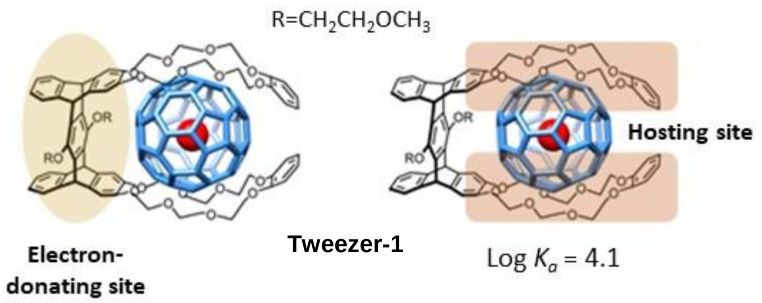

Figure I.21. Molecular representation of the complex formed between a tweezer-type pentiptycene-based bis (crown ether) host and Li@C$_{60}$ as guest. Ka values calculated in benzonitrile

Although the efficiency of the crown ether-like derivatives for the selective molecular recognition of EMFs in the presence of pristine fullerenes was proven, none of the strategies discussed above achieved the discrimination of EMFs between them.[83] For the purification of a targeted EMF directly from an arc-produced soot, mainly two critical hurdles have to be overcome: A) a single EMF must be separated from empty fullerenes (EMFs-selective), and b) from other EMFs with different carbon cages (size-selective). In this context, Itami, Shinohara and coworkers relied on the use of extended π-conjugated systems to fulfill these requirements.[89] They hypothesized that EMFs, which comprise negatively charged carbon cages (electron transfer from the internal metal cluster to the fullerene cage), interact with π-conjugated molecules stronger than their empty analogs. On the other hand, to attain size selectivity, they decided to use a host-guest system with a hoop-shaped π-conjugated macrocycle. In this regard, cycloparaphenylene (CPP) carbon nanorings were chosen as a suitable host for EMFs. The size-selectivity of [11]CPP towards EMFs based in C$_{82}$ carbon cages was achieved and confirmed by ^{1}H-NMR. The authors observed a downfield shift of the [11]CPP signal upon the addition of Lu$_2$@C$_{82}$. Interestingly, no changes in ^{1}H NMR were observed with [12]CPP, indicating that the diameter of CPP has to be compatible with the size of the carbon cage (Figure I.22). The UV-Vis spectroscopic titrations and fluorescent experiments using different C$_{82}$-based EMFs (Gd@C$_{82}$ Ka=1.8 ± 0.1 x 10^6 M^{-1}, Tm@C$_{82}$ Ka=1.8 ± 0.2 x 10^6 M^{-1} and Lu$_2$@C$_{82}$ Ka=1.8 ± 0.2 x 10^6 M^{-1}, in CHCl$_3$) and [11]CPP indicated the same affinity, regardless of the nature and the number of encapsulated metal atoms (Figure I.22). The authors demonstrated that the complexation of Gd@C$_{82}$ with [11]CPP can be applied to the extraction and enrichment of this EMF directly form complex crude mixtures.

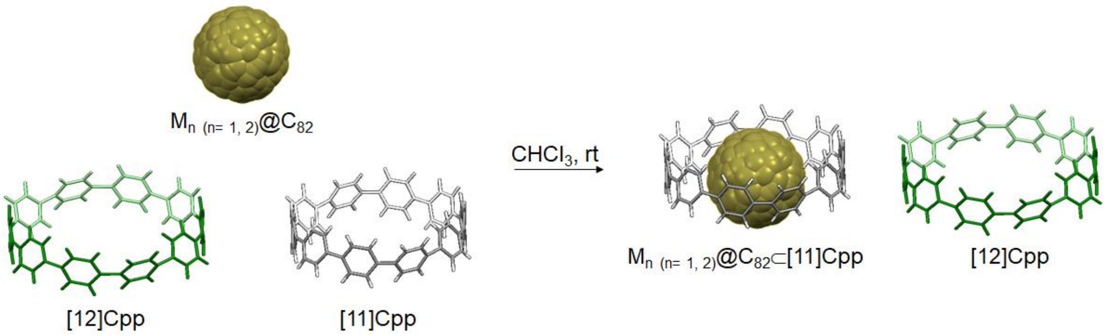

Figure I.22. Molecular representation of the selective complexation of M$_{n\ (n=1,2)}$ @C$_{82}$ EMFs with [11]CPP (M = Gd, Lu, Tm).

As a general trend, the larger the carbon cage of a fullerene or EMFs, the higher is the number of possible isomers formed.[20] The low solubility of these carbon materials in organic solvents makes their isolation and characterization a very challenging task. Furthermore, the lack of hydrogen atoms on their structure precludes their study by ^{1}H-NMR. Consequently, ^{13}C-NMR is the most extensively used technique for the direct identification of fullerene isomers, although the low sensitivity of this technique together with the low solubility of these compounds hinders their full spectroscopic characterization. Aiming a straightforward identification of fullerene and EMFs isomers, in 2014 Chiu and coworkers reported the preparation of a fully covalent nanocapsule **Cov-1** that formed hemicarceplexes with $Sc_3N@C_{80}$ (under solvent-free conditions) (Figure I.23), being the first example of a complex molecular receptor for the recognition of EMFs that does not contain porphyrin units on its structure.[90] Nanocapsule **Cov-1** increased the solubility of $Sc_3N@C_{80}$ (I_h- and D_{5h}- isomer mixture) in TCE up to 50-fold upon encapsulation. To further increase the solubility of the host-guest adduct to attain a full spectroscopic characterization of the system, the authors synthesized a more soluble cage **Cov-2** (Figure I.23) containing three succinic diester linkages, increasing the solubility of $Sc_3N@C_{80}$ in TCE by 200-fold. The spectroscopic study of the host-guest complex $Sc_3N@C_{80}\subset$**Cov-2** allowed the authors to identify and distinguish the two isomers, $Sc_3N@D_{5h}$-C_{80} and $Sc_3N@I_h$-C_{80}.

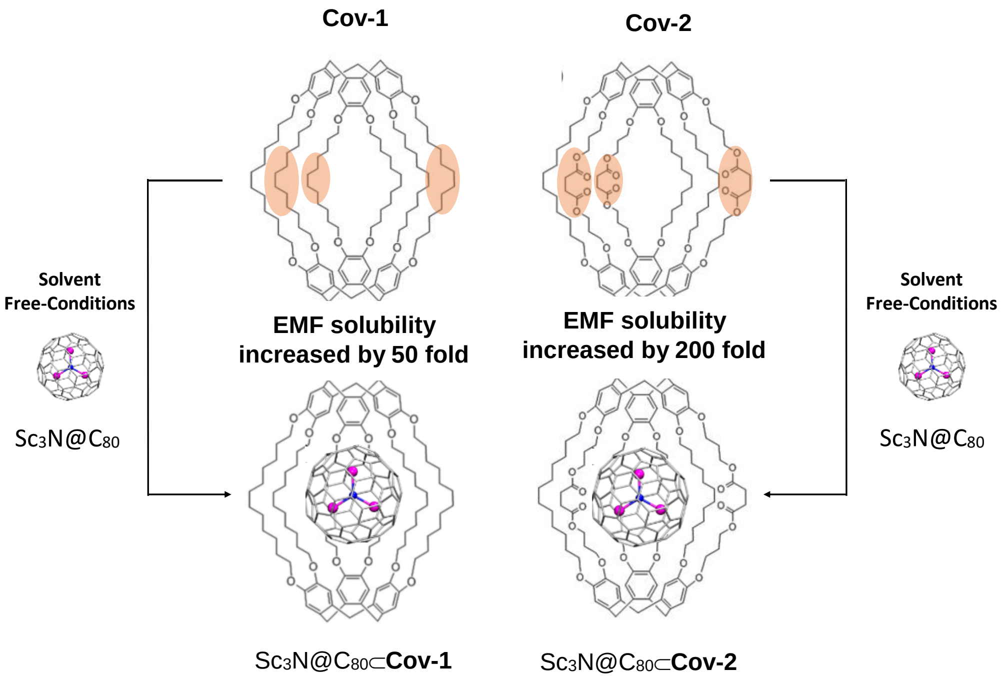

Figure I.23. Chemical structure of the two **Cov-1** and **Cov-2**-based hemicarceplexes synthesized by Chiu and coworkers, and representation of the corresponding inclusion complexes with $Sc_3N@D_{5h}$-C_{80} and $Sc_3N@I_h$-C_{80}

I.2.4.2 Metalloporphyrin containing receptors

First evidences of strong fullerene- and EMF interactions with porphyrin units were discovered in the cocrystallization with porphyrin units in 1997.[91] In this context, among the wide range of receptors for fullerenes and EMFs reported in the literature,[31] those based on porphyrins display the highest binding affinities.[92, 93] Nevertheless, molecular receptors containing only one porphyrin unit are usually not efficient receptors for the selective molecular recognition of these compounds. In this line, several examples of well-defined scaffolds containing two or more metalloporphyrin units have been reported in the literature during the last decades as hosts for fullerenes and EMFs, aiming at the enhancement of the strength of the host-guest interactions.[31, 92, 93]

The first example of host-guest complexation of EMFs using a metalloporphyrin-based receptor was reported by Anderson and coworkers in 2010.[94] The authors hypothesized that a well-defined triangular porphyrin trimer **Cov-3** (Figure I.24), in which the three porphyrins were preorganized to chelate to the same guest, might provide very strong bindings. The molecular scaffold was synthesized through intramolecular Sonogashira coupling between 3,4-iodophenethylamine and the corresponding alkyne-terminated linear porphyrin trimer. The affinity of the trimeric molecular receptor, featuring a trigonal-shaped cavity, for C_{60} was studied by UV-vis titration in a wide range of solvents, showing an association constant in toluene of 1.6 (±0.7) · 10^6 M^{-1}. On the other hand, the inclusion complex formed with C_{70} was two orders of magnitude more stable (K_a (C_{70}) = 1.6 (±0.7) · 10^8 M^{-1}), while C_{86}⊂**Cov-3** and La@C_{82}⊂**Cov-3** complexes were too stable to be measured ($K_a > 10^9$ M^{-1}), even with fluorescence spectroscopy. K_a value for C_{60} was notably higher than the ones reported previously with analogous porphyrin dimers, indicating that the presence of the third porphyrin moiety on the receptor structure had a positive effect on the binding of C_{60}. The cooperative effect of the third porphyrin became more pronounced with the larger C_{70}, C_{86} and La@C_{82}, enabling better interactions with the three walls of the receptor. Interestingly, in parallel to size/shape complementary between La@C_{82} and the molecular receptor, the authors pointed that the electronic polarization of the La@C_{82}, which donates three valence electrons to the carbon sphere, also contributed towards the strong binding exhibited.[95]

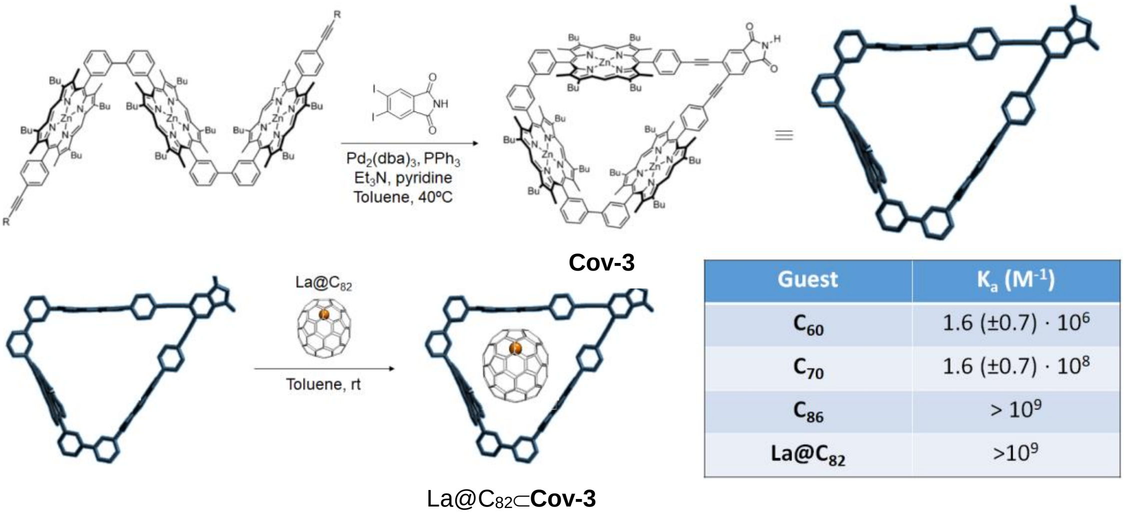

Cov-3

La@C_{82}⊂**Cov-3**

Guest	K_a (M^{-1})
C_{60}	1.6 (±0.7) · 10^6
C_{70}	1.6 (±0.7) · 10^8
C_{86}	> 10^9
La@C_{82}	>10^9

Figure I.24. Molecular structure and graphical representation of the cyclic porphyrin trimer synthesized by Anderson and coworkers (top) and graphical representation of the corresponding host-guest adduct with La@C_{82}.

Also in 2010, Shinohara, Tagmatarchis and coworkers reported a tweezer-type di-porphyrin scaffold (**Cov-4**), in which the porphyrin units are bridged through an isophthaloyl-bridges (Figure I.25).[96] The molecular receptor formed a 1:1 host-guest complex with La@C$_{82}$ at room temperature in CH_2Cl_2/CS_2 solvent mixture (Figure I.25). UV-vis titration measurements indicated moderate association forces (K_a (La@C$_{82}$) = 6.3 (±0.3) · 10^4 M^{-1}). Conversely to the previous example in Figure I.24, photoluminescence and EPR studies suggested that no charge transfer from the photoexcited porphyrin moiety to the La@C$_{82}$ occurred. Consequently, the authors concluded that despite of the photoactive character of the porphyrin moiety, the complexation of La@C$_{82}$ is exclusively driven by the structural non-covalent interactions between the porphyrin rings and the EMF.

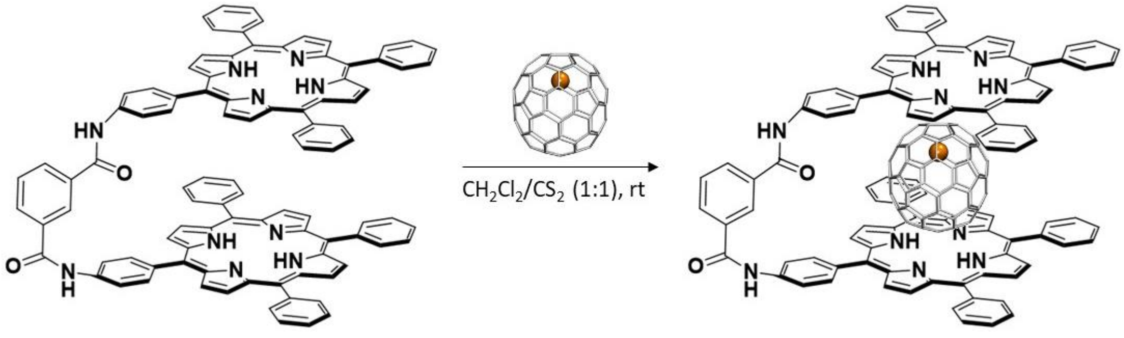

Cov-4 La@C$_{82}\subset$**Cov-4**

Figure I.25. Chemical structure of the tweezer-type di-porphyrin scaffold **Cov-4** reported by Shinohara, Tagmatarchis and coworkers. In the presence of La@C$_{82}$, the inclusion complex with the tweezer receptor is formed (graphical representation on the right).

Three new cyclic covalent di-porphyrin receptors were reported by Aida group in 2011, which were based on copper(II), zinc(II) and metal-free porphyrins (Figure I.26).[97] The interesting feature of **Cyclo-Cu**, **Cyclo-Zn** and **Cyclo-H** was that they contained functional groups (olefins) susceptible to undergo post assembly modification (PAM) reactions. When the cyclic porphyrin dimers were subjected to ring-closing olefin metathesis of its side-chain olefinic termini, they were quantitatively transformed into the caged form analog **Cage-Cu**, **Cage-Zn** and **Cage-H** (Figure I.26). **Cyclo-Cu** receptor formed highly stable host-guest complexes with La@C$_{82}$ in toluene at room temperature (K_a (La@C$_{82}\subset$**Cyclo-Cu**) = 1.5 (±0.6) · 10^6 M^{-1}) (Figure I.26a). Subsequently, La@C$_{82}\subset$**Cyclo-Cu** supramolecular complex was subjected to ring-closing olefin metathesis reaction, obtaining 20% yield of La@C$_{82}\subset$**Cage-Cu** (low yield due to release of the guest during the PAM reactions). Remarkably, the authors found that the metal-free analog La@C$_{82}\subset$**Cyclo-H** can be metathesized to give better yields (40%) of its cage form (La@C$_{82}\subset$**Cage-H**), which was attributed to a 10-fold higher affinity constant of La@C$_{82}$ with **Cyclo-Cu** (K_a (La@C$_{82}\subset$**Cyclo-H**) = 1.5 (±0.8) · 10^7 M^{-1}). Complex La@C$_{82}\subset$**Cage-H** was then quantitatively converted into La@C$_{82}\subset$**Cage-Cu** by metalation with $Cu(OAc)_2$. In order to explore the possibility of ferromagnetic spin coupling, the authors measured electron spin resonance and the electron spin transient nutation spectra of the mentioned above supramolecular complexes and their specific components. After a thorough study, the authors concluded that the paramagnetic La@C$_{82}$ is ferromagnetically coupled with the copper(II) metal centers in La@C$_{82}\subset$**Cyclo-Cu** of the porphyrin units of the host component, being the first example of this ferromagnetic interaction involving La@C_{82}. Furthermore, the interaction turned ferrimagnetic within its caged analog La@C_{82}⊂**Cage-Cu** (Figure I.26b).

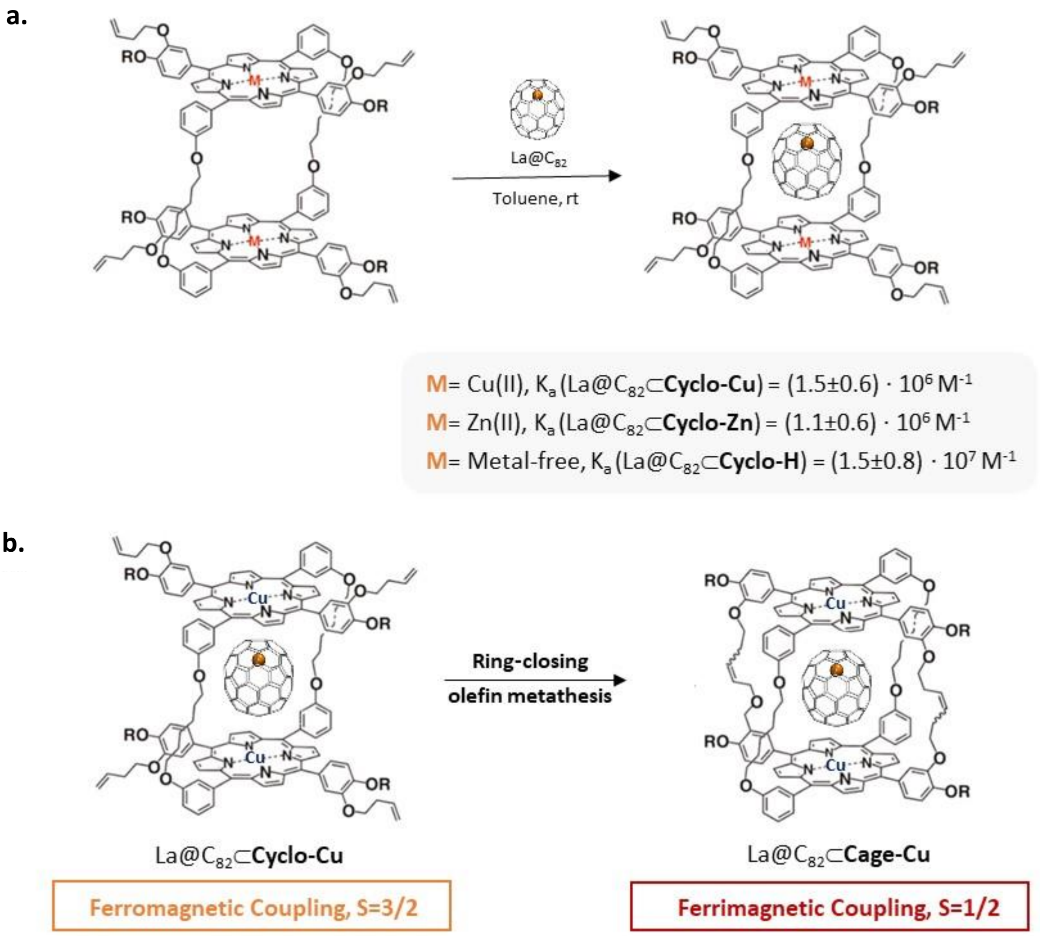

Figure I.26. a) Chemical structure of the inclusion complex formed between La@C_{82} and **Cyclo-M** porphyrin dimer, and b) host-guest adducts La@C_{82}⊂**Cyclo-Cu** and La@C_{82}⊂**Cage-Cu** featuring ferromagnetic and ferromagnetic properties, respectively.

A similar strategy was used by Ballester, Echegoyen and coworkers, who reported a cyclic covalent receptor synthesized through dimerization of two β-pyrrole unsubstituted meso-tetraphenyl bisporphyrins yielding the porphyrin dimer **Cov-5** (Figure I.27a).[98] Analogous to the example described in Figure I.26, **Cov-5** is susceptible to PAM reactions. Consequently, hydrogenation of alkyne moieties in highly rigid **Cov-5** scaffold (expanded form) afforded the more flexible dimeric receptor **Cov-6** (collapsed form) (Figure I.27a). Interestingly, the loss of rigidity of the linkers notably affected the shape and the flexibility of the receptor, modifying their affinity towards different fullerene and EMFs guests. Both expanded (**Cov-5**) and collapsed (**Cov-6**) forms of the receptor afforded 1:1 host-guest complexes with C_{60} and C_{70} (Figure I.27b). The more rigid receptor **Cov-5**, which contained fully unsaturated spacers, presented a relatively weak interaction with C_{70} (K_a ~10^4 M^{-1}, in toluene at room temperature) and unobservable interaction with C_{60} ($K_a < 10^4$ M^{-1}). On the other hand, the more flexible receptor **Cov-6**, containing fully saturated linkers, formed more stable complexes with C_{60} (K_a ~10^4 M^{-1}) and C_{70} (K_a ~10^5 M^{-1}). The higher flexibility of the spacers with the collapsed form of the receptor (**Cov-6**) allowed a better adaptability of the receptor to the guest and enhanced size/shape complementarity between them. Both receptors were also able to form inclusion complexes with $Sc_3N@I_h$-C_{80} ($K_a \sim 10^5\ M^{-1}$) (Figure I.27b). The larger size of $Sc_3N@I_h$-C_{80} compared to C_{60} and C_{70}, enabled better interactions with the two porphyrins moiety of the rigid receptor **Cov-5**, endowing the corresponding inclusion complex with very similar stability than the one observed for the flexible hydrogenated receptor (**Cov-6**). It is worth noting that crystal structures of an EMF bound to molecular bis-porphyrin receptor were obtained for the first time (Figure I.27c).

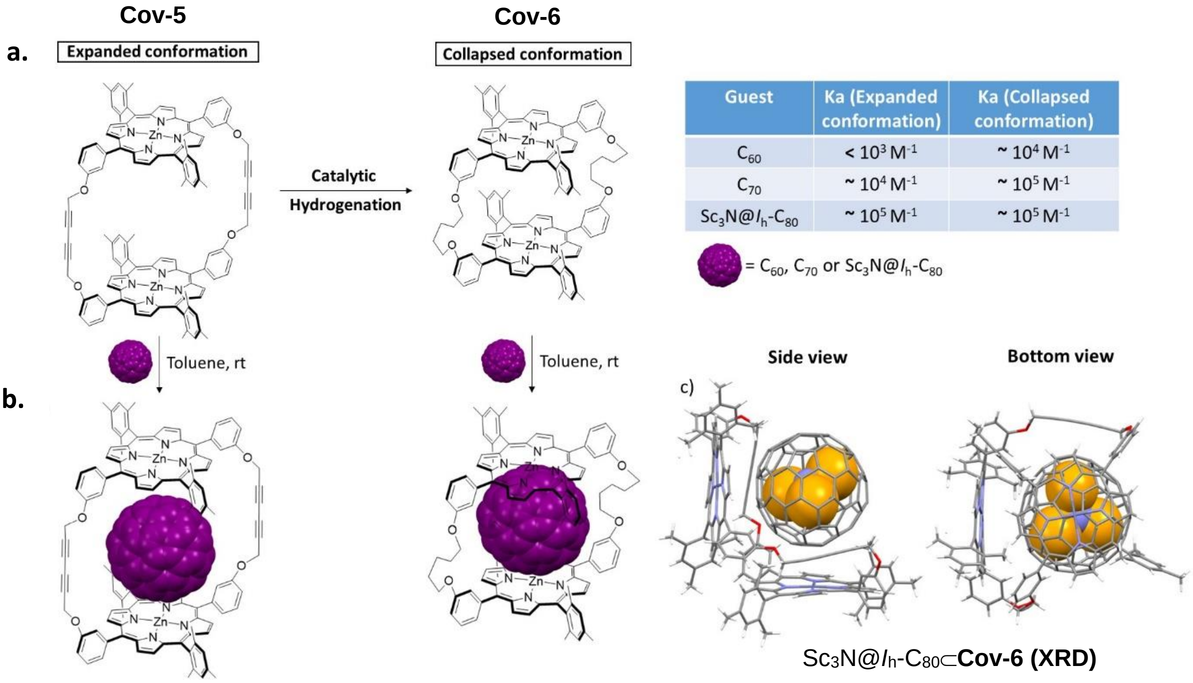

Guest	Ka (Expanded conformation)	Ka (Collapsed conformation)
C_{60}	$< 10^3\ M^{-1}$	$\sim 10^4\ M^{-1}$
C_{70}	$\sim 10^4\ M^{-1}$	$\sim 10^5\ M^{-1}$
$Sc_3N@I_h$-C_{80}	$\sim 10^5\ M^{-1}$	$\sim 10^5\ M^{-1}$

● = C_{60}, C_{70} or $Sc_3N@I_h$-C_{80}

Figure I.27. a) Molecular structure of the covalent porphyrin dimer in its expanded (**Cov-5**, left) and collapsed conformation (**Cov-6**, right), synthesized by Ballester, Echegoyen and coworkers. b) Graphical representation of the host-guest complexes formed with C_{60}, C_{70} and $Sc_3N@I_h$-C_{80} in both conformation of the porphyrin dimer. d) X-ray crystal structure of the inclusion complex formed between the expanded **Cov-6** host and $Sc_3N@C_{80}$.

I.3. References

(1) Kroto, H. W.; Heath, J. R.; O'Brien, S. C.; Curl, R. F.; Smalley, R. E. *Nature* **1985**, *318*, 162.

(2) Krueger, A. Carbon Nanotubes and Related Structures Carbon Nanotube Reinforced Composites Carbon Nanotube Devices Advanced Nanomaterials Nanomaterials for the Life Sciences Reliability of MEMS. *Ed. Wiley-VCH: Weinheim,* **2010**.

(3) Georgakilas, V.; Perman, J. A.; Tucek, J.; Zboril, R. *Chem. Rev.* **2015**, *115* (11), 4744.

(4) Iijima, S. *Nature* **1991**, *354*, 56.

(5) Iijima, S.; Yudasaka, M. **1999**, Núm. August, 165.

(6) Ortiz Balbuena, J.; Tutor De Ureta, P.; Rivera Ruiz, E.; Mellor Pita, S. *Med. Clin. (Barc).* **2016**, *146* (2), 93.

(7) Fuhrman, Jed; McCallum, Kirk; Davis, A. *Nature* **1992**, *359*, 710.

(8) Speed, M. P. *Nature* **1998**, *396* (6709), 323.

(9) Kroto, H. W. *Nature* **1987**, *329* (6139), 529.

(10) Albertazzi, E.; Domene, C.; Fowler, P. W.; Heine, T.; Seifert, G.; Van Alsenoy, C.; Zerbetto, F. *Phys. Chem. Chem. Phys.* **1999**, *1* (12), 2913.

(11) Tan, Y. Z.; Xie, S. Y.; Huang, R. Bin; Zheng, L. S. *Nat. Chem.* **2009**, *1* (6), 450.

(12) Krätschmer, W.; Lamb, L. D.; Fostiropoulos, K.; Huffman, D. R. *Nature* **1990**, *347* (6291), 354.

(13) Haufler, R. E.; Conceicao, J.; Chibante, L. P. F.; Chai, Y.; Byrne, N. E.; Flanagan, S.; Haley, M. M.; O'Brien, S. C.; Pan, C.; Xiao, Z.; Billups, W. E.; Ciufolini, M. A.; Hauge, R. H.; Margrave, J. L.; Wilson, L. J.; Curl, R. F.; Smalley, R. E. *J. Phys. Chem.* **1990**, *94* (24), 8634.

(14) Yeretzian, C.; Wiley, J. B.; Holczer, K.; Su, T.; Nguyen, S.; Kaner, R. B.; Whetten, R. L. *J. Phys. Chem.* **1993**, *97* (39), 10097.

(15) Ajie, H.; Alvarez, M. M.; Anz, S. J.; Beck, R. D.; Diederich, F.; Fostiropoulos, K.; Huffman, D. R.; Krätschmer, W.; Rubin, Y.; Schriver, K. E.; Sensharma, D.; Whetten, R. L. *J. Phys. Chem.* **1990**, *94* (24), 8630.

(16) Doome, R. J.; Fonseca, A.; Richter, H.; Nagy, J. B.; Thiry, P. A.; Lucas, A. A. *J. Phys. Chem. Solids* **1997**, *58* (11), 1839.

(17) Trimethoxysilylmethyl, S.; Sherstyannikova, L. V; Voronkov, M. G. **2004**, *74*, 551.

(18) Johnson, R. D.; Meijer, G.; Bethune, D. S. *J. Am. Chem. Soc.* **1990**, *112* (24), 8983.

(19) Chai, Y.; Guo, T.; Jin, C.; Haufler, R. E.; Chibante, L. P. F.; Fure, J.; Wang, L.; Alford, J. M.; Smalley, R. E. *J. Phys. Chem.* **1991**, *95* (20), 7564.

(20) Popov, A. A.; Yang, S.; Dunsch, L. *Chem. Rev.* **2013**, *113* (8), 5989.

(21) Caulder, D. L.; Raymond, K. N. *Acc. Chem. Res.* **1999**, *32* (11), 975.

(22) Rizzuto, F. J.; von Krbek, L. K. S.; Nitschke, J. R. *Nat. Rev. Chem.* **2019**, *3* (4), 204.

(23) Fiedler, D.; Leung, D. H.; Bergman, R. G.; Raymond, K. N. *Acc. Chem. Res.* **2005**, *38* (4),

349.

(24) Brown, C. J.; Bergman, R. G.; Raymond, K. N. *J. Am. Chem. Soc.* **2009**, *131* (48), 17530.

(25) Bellini, R.; Chikkali, S. H.; Berthon-Gelloz, G.; Reek, J. N. H. *Angew. Chemie - Int. Ed.* **2011**, *50* (32), 7342.

(26) García-Simón, C.; Gramage-Doria, R.; Raoufmoghaddam, S.; Parella, T.; Costas, M.; Ribas, X.; Reek, J. N. H. *J. Am. Chem. Soc.* **2015**, *137* (7), 2680.

(27) Gadzikwa, T.; Bellini, R.; Dekker, H. L.; Reek, J. N. H. *J. Am. Chem. Soc.* **2012**, *134* (6), 2860.

(28) Koblenz, T. S.; Wassenaar, J.; Reek, J. N. H. *Chem. Soc. Rev.* **2008**, *37* (2), 247.

(29) Zhang, D.; Ronson, T. K.; Nitschke, J. R. *Acc. Chem. Res.* **2018**, *51* (10), 2423.

(30) Percástegui, E. G.; Jancik, V. *Coord. Chem. Rev.* **2020**, *407*, 213165.

(31) García-Simón, C.; Costas, M.; Ribas, X. *Chem. Soc. Rev.* **2016**, *45* (1), 40.

(32) Collavini, S.; Delgado, J. L. *Sustain. Energy Fuels* **2018**, *2* (11), 2480.

(33) Panwar, N.; Soehartono, A. M.; Chan, K. K.; Zeng, S.; Xu, G.; Qu, J.; Coquet, P.; Yong, K. T.; Chen, X. *Chem. Rev.* **2019**, *119* (16), 9559.

(34) Liu, S.; Lu, Y.; Kappes, M. M.; Ibers, J. A. **1974**, *254* (16), 3.

(35) Kordatos, K.; Bosi, S.; Da Ros, T.; Zambon, A.; Lucchini, V.; Prato, M. *J. Org. Chem.* **2001**, *66* (8), 2802.

(36) Hirsch, A.; Lamparth, I.; Karfunkel, H. R. *Angew. Chemie Int. Ed. English* **1994**, *33* (4), 437.

(37) Paquin, F.; Rivnay, J.; Salleo, A.; Stingelin, N.; Silva, C. *J. Mater. Chem. C* **2015**, *3*, 10715.

(38) Hirsch, A.; Brettreich, M. *Fullerenes: Chemistry and Reactions*; 2005.

(39) Diederich, F.; Kessinger, R. *Acc. Chem. Res.* **1999**, *32* (6), 537.

(40) Schwenninger, R.; Mu, T.; Kra, B.; Innsbruck, A.-. **1997**, *2* (9 mL), 9317.

(41) Thilgen, C.; Sergeyev, S.; Diederich, F. **2005**, 1.

(42) Zhou, Z.; Wilson, S. *Curr. Org. Chem.* **2005**, *9* (8), 789.

(43) Brenner, W.; Ronson, T. K.; Nitschke, J. R. *J. Am. Chem. Soc.* **2017**, *139* (1), 75.

(44) Mecozzi, S.; Rebek, J. *Chem. - A Eur. J.* **1998**, *4* (6), 1016.

(45) Huang, N.; Wang, K.; Drake, H.; Cai, P.; Pang, J.; Li, J.; Che, S.; Huang, L.; Wang, Q.; Zhou, H. C. *J. Am. Chem. Soc.* **2018**, *140* (20), 6383.

(46) Takezawa, H.; Murase, T.; Resnati, G.; Metrangolo, P.; Fujita, M. *J. Am. Chem. Soc.* **2014**, *136* (5), 1786.

(47) Chen, B.; Holstein, J. J.; Horiuchi, S.; Hiller, W. G.; Clever, G. H. *J. Am. Chem. Soc.* **2019**, *141* (22), 8907.

(48) Akasaka, T.; Kato, T.; Kobayashi, K.; Nagase, S.; Yamamoto, K.; Funasaka, H.; Takahashi, T. *Nature*. 1995, p 600-601.

(49) Garcia-Borràs, M.; Romero-Rivera, A.; Osuna, S.; Luis, J. M.; Swart, M.; Solà, M. *J. Chem. Theory Comput.* **2012**, *8* (5), 1671.

(50) Garcia-Borràs, M.; Osuna, S.; Luis, J. M.; Swart, M.; Solà, M. *Chem. Soc. Rev.* **2014**, *43* (14), 5089.

(51) Heath, J. R.; O'Brien, S. C.; Liu, Q. Z. Y.; Curl, R. F.; Tittel, F. K.; Smalley, R. E.; Kroto, H. W. *J. Am. Chem. Soc.* **1985**, *107* (25), 7779.

(52) Liu, F.; Spree, L.; Krylov, D. S.; Velkos, G.; Avdoshenko, S. M.; Popov, A. A. *Acc. Chem. Res.* **2019**, *52* (10), 2981.

(53) Stevenson, S.; Rice, G.; Glass, T.; Harich, K.; Cromer, F.; Jordan, M. R.; Craft, J.; Dorn, H. C. *Nature* **1999**, *80*, 80.

(54) Dunsch, L.; Yang, S. *Small* **2007**, *3* (8), 1298.

(55) Dunsch, L.; Yang, S. *Phys. Chem. Chem. Phys.* **2007**, *9* (24), 3067.

(56) Umemoto, H.; Ohashi, K.; Inoue, T.; Fukui, N.; Sugai, T.; Shinohara, H. *Chem. Commun.* **2010**, *46* (31), 5653.

(57) Wang, C. R.; Kai, T.; Tomiyama, T.; Yoshida, T.; Kobayashi, Y.; Nishibori, E.; Takata, M.; Sakata, M.; Shinohara, H. *Angew. Chemie - Int. Ed.* **2001**, *40* (2), 397.

(58) Stevenson, S.; Mackey, M. A.; Stuart, M. A.; Phillips, J. P.; Easterling, M. L.; Chancellor, C. J.; Olmstead, M. M.; Balch, A. L. *J. Am. Chem. Soc.* **2008**, *130* (36), 11844.

(59) Dunsch, L.; Yang, S.; Zhang, L.; Svitova, A.; Oswald, S.; Popov, A. A. *J. Am. Chem. Soc.* **2010**, *132* (15), 5413.

(60) Liu, F.; Gao, C. L.; Deng, Q.; Zhu, X.; Kostanyan, A.; Westerström, R.; Wang, S.; Tan, Y. Z.; Tao, J.; Xie, S. Y.; Popov, A. A.; Greber, T.; Yang, S. *J. Am. Chem. Soc.* **2016**, *138* (44), 14764.

(61) Krause, M.; Ziegs, F.; Popov, A. A.; Dunsch, L. *ChemPhysChem* **2007**, *8* (4), 537.

(62) Wang, T. S.; Feng, L.; Wu, J. Y.; Xu, W.; Xiang, J. F.; Tan, K.; Ma, Y. H.; Zheng, J. P.; Jiang, L.; Lu, X.; Shu, C. Y.; Wang, C. R. *J. Am. Chem. Soc.* **2010**, *132* (46), 16362.

(63) Brandenburg, A.; Krylov, D. S.; Beger, A.; Wolter, A. U. B.; Büchner, B.; Popov, A. A. *Chem. Commun.* **2018**, *54* (76), 10683.

(64) Ross, R. B.; Cardona, C. M.; Guldi, D. M.; Sankaranarayanan, S. G.; Reese, M. O.; Kopidakis, N.; Peet, J.; Walker, B.; Bazan, G. C.; Van Keuren, E.; Holloway, B. C.; Drees, M. *Nat. Mater.* **2009**, *8* (3), 208.

(65) Pinzón, J. R.; Plonska-Brzezinska, M. E.; Cardona, C. M.; Athans, A. J.; Gayathri, S. S.; Guldi, D. M.; Herranz, M. Á.; Martín, N.; Torres, T.; Echegoyen, L. *Angew. Chemie - Int. Ed.* **2008**, *47* (22), 4173.

(66) Yang, S.; Fan, L.; Yang, S. *J. Phys. Chem. B* **2004**, *108* (14), 4394.

(67) Jaros, A.; Bonab, F.; Straka, M.; Foroutan-Nejad, C. **2019**.

(68) Fatouros, P. P.; Corwin, F. D.; Chen, Z. J.; Broaddus, W. C.; Tatum, J. L.; Kettenmann, B.; Ge, Z.; Gibson, H. W.; Russ, J. L.; Leonard, A. P.; Duchamp, J. C.; Dorn, H. C. *Radiology* **2006**, *240* (3), 756.

(69) Zhang, J.; Ye, Y.; Chen, Y.; Pregot, C.; Li, T.; Balasubramaniam, S.; Hobart, D. B.; Zhang,

Y.; Wi, S.; Davis, R. M.; Madsen, L. A.; Morris, J. R.; Laconte, S. M.; Yee, G. T.; Dorn, H. C. *J. Am. Chem. Soc.* **2014**, *136* (6), 2630.

(70) Chen, C.; Xing, G.; Wang, J.; Zhao, Y.; Li, B.; Tang, J.; Jia, G.; Wang, T.; Sun, J.; Xing, L.; Yuan, H.; Gao, Y.; Meng, H.; Chen, Z.; Zhao, F.; Chai, Z.; Fang, X. *Nano Lett.* **2005**, *5* (10), 2050.

(71) McCluskey, D. M.; Smith, T. N.; Madasu, P. K.; Coumbe, C. E.; MacKey, M. A.; Fulmer, P. A.; Wynne, J. H.; Stevenson, S.; Phillips, J. P. *ACS Appl. Mater. Interfaces* **2009**, *1* (4), 882.

(72) Yang, S.; Wei, T.; Jin, F. *Chem. Soc. Rev.* **2017**, *46* (16), 5005.

(73) Elliott, B.; Yu, L.; Echegoyen, L. *J. Am. Chem. Soc.* **2005**, *127* (31), 10885.

(74) Ge, Z.; Duchamp, J. C.; Cai, T.; Gibson, H. W.; Dorn, H. C. *J. Am. Chem. Soc.* **2005**, *127* (46), 16292.

(75) Angeli, C. D.; Cai, T.; Duchamp, J. C.; Reid, J. E.; Singer, E. S.; Gibson, H. W.; Dorn, H. C. *Chem. Mater.* **2008**, *20* (15), 4993.

(76) Stevenson, S.; Harich, K.; Yu, H.; Stephen, R. R.; Heaps, D.; Coumbe, C.; Phillips, J. P. *J. Am. Chem. Soc.* **2006**, *128* (27), 8829.

(77) Stevenson, S.; Mackey, M. A.; Coumbe, C. E.; Phillips, J. P.; Elliott, B.; Echegoyen, L. *J. Am. Chem. Soc.* **2007**, *129* (19), 6072.

(78) Stevenson, S.; Rottinger, K. A.; Fahim, M.; Field, J. S.; Martin, B. R.; Arvola, K. D. *Inorg. Chem.* **2014**, *53* (24), 12939.

(79) Stevenson, S.; Mackey, M. A.; Pickens, J. E.; Stuart, M. A.; Confait, B. S.; Phillips, J. P. *Inorg. Chem.* **2009**, *48* (24), 11685.

(80) Akiyama, K.; Hamano, T.; Nakanishi, Y.; Takeuchi, E.; Noda, S.; Wang, Z.; Kubuki, S.; Shinohara, H. *J. Am. Chem. Soc.* **2012**, *134* (23), 9762.

(81) Stevenson, S.; Thompson, H. R.; Arvola, K. D.; Ghiassi, K. B.; Olmstead, M. M.; Balch, A. L. *Chem. - A Eur. J.* **2015**, *21* (29), 10362.

(82) Effing, J.; Jonas, U.; Jullien, L.; Plesnivy, T.; Ringsdorf, H.; Diederich, F.; Thilgen, C.; Weinstein, D. *Angew. Chemie Int. Ed. English* **1992**, *31* (12), 1599.

(83) Moreira, L.; Illescas, B. M.; Martín, N. *J. Org. Chem.* **2017**, *82* (7), 3347.

(84) Lu, X.; Feng, L.; Akasaka, T.; Nagase, S. *Chem. Soc. Rev.* **2012**, *41* (23), 7723.

(85) Tsuchiya, T.; Sato, K.; Kurihara, H.; Wakahara, T.; Nakahodo, T.; Maeda, Y.; Akasaka, T.; Ohkubo, K.; Fukuzumi, S.; Kato, T.; Mizorogi, N.; Kobayashi, K.; Nagase, S. *J. Am. Chem. Soc.* **2006**, *128* (20), 6699.

(86) Tsuchiya, T.; Kurihara, H.; Sato, K.; Wakahara, T.; Akasaka, T.; Shimizu, T.; Kamigata, N.; Mizorogi, N.; Nagase, S. *Chem. Commun.* **2006**, *1* (34), 3585.

(87) Supur, M.; Kawashima, Y.; Larsen, K. R.; Ohkubo, K.; Jeppesen, J. O.; Fukuzumi, S. *Chem. - A Eur. J.* **2014**, *20* (43), 13976.

(88) Supur, M.; Kawashima, Y.; Ma, Y. X.; Ohkubo, K.; Chen, C. F.; Fukuzumi, S. *Chem. Commun.* **2014**, *50* (99), 15796.

(89) Nakanishi, Y.; Omachi, H.; Matsuura, S.; Miyata, Y.; Kitaura, R.; Segawa, Y.; Itami, K.;

Shinohara, H. *Angew. Chemie - Int. Ed.* **2014**, *53* (12), 3102.

(90) Ku, M. Y.; Huang, S. J.; Huang, S. L.; Liu, Y. H.; Lai, C. C.; Peng, S. M.; Chiu, S. H. *Chem. Commun.* **2014**, *50* (79), 11709.

(91) Sun, Y.; Drovetskaya, T.; Bolskar, R. D.; Bau, R.; Boyd, P. D. W.; Reed, C. A. *J. Org. Chem.* **1997**, *62* (11), 3642.

(92)

(93) Tashiro, K.; Aida, T. *Chem. Soc. Rev.* **2007**, *36* (2), 189.

(94) Gil-Ramírez, G.; Karlen, S. D.; Shundo, A.; Porfyrakis, K.; Ito, Y.; Briggs, G. A. D.; Morton, J. J. L.; Anderson, H. L. *Org. Lett.* **2010**, *12* (15), 3544.

(95) Xiao, J.; Savina, M. R.; Martin, G. B.; Francis, A. H.; Meyerhoff, M. E. *J. Am. Chem. Soc.* **1994**, *116* (20), 9341.

(96) Pagona, G.; Economopoulos, S. P.; Aono, T.; Miyata, Y.; Shinohara, H.; Tagmatarchis, N. *Tetrahedron Lett.* **2010**, *51* (45), 5896.

(97) Hajjaj, F.; Tashiro, K.; Nikawa, H.; Mizorogi, N.; Akasaka, T.; Nagase, S.; Furukawa, K.; Kato, T.; Aida, T. *J. Am. Chem. Soc.* **2011**, *133* (24), 9290.

(98) Hernández-Eguía, L. P.; Escudero-Adán, E. C.; Pinzón, J. R.; Echegoyen, L.; Ballester, P. *J. Org. Chem.* **2011**, *76* (9), 3258.

Chapter II.

Objectives

Preceding pages of this thesis have covered relevant properties of fullerenes and EMFs, and methods for their controlled functionalization and selective isolation. On the other hand, we have discussed the ability of supramolecular entities to host fullerenes and EMFs in their inner cavities. The frame of this thesis will be circumscribed to the study of fullerene and EMF encapsulation in supramolecular tetragonal prismatic nanocapsules bearing porphyrin panels. In view of the precedents exposed, together with the solid experience of our research group in the field of supramolecular chemistry, we set the objectives of the present thesis.

Objective 1: Chemo- and Regioselective functionalization of C_{60} in confined spaces (Chapter III)

Previously reported methodologies for the functionalization of fullerenes are tedious and have a very limited substrate scope. Therefore, developing new protocols to efficiently prepare C_{60} poly-adduct derivatives under chemo- and regioselective control is highly desirable. Chapter 3 deals with the functionalization of confined C_{60} by one of the most used and versatile fullerene derivatization reactions, i.e. Bingel-Hirsch cyclopropanation. Although some examples of Diels Alder reactions involving C_{60} confined in the inner cavity of supramolecular scaffolds have been reported, the ability to control the chemo- and the regioselectivity of cyclopropanation reactions has never been studied. Taking into account these considerations, the first objective of this thesis will concern the synthesis of a Pd(II)- and Cu(II)-based tetragonal prismatic nanocapsules and prove their ability to act as supramolecular masks for the regioselective poly-functionalization of C_{60}.

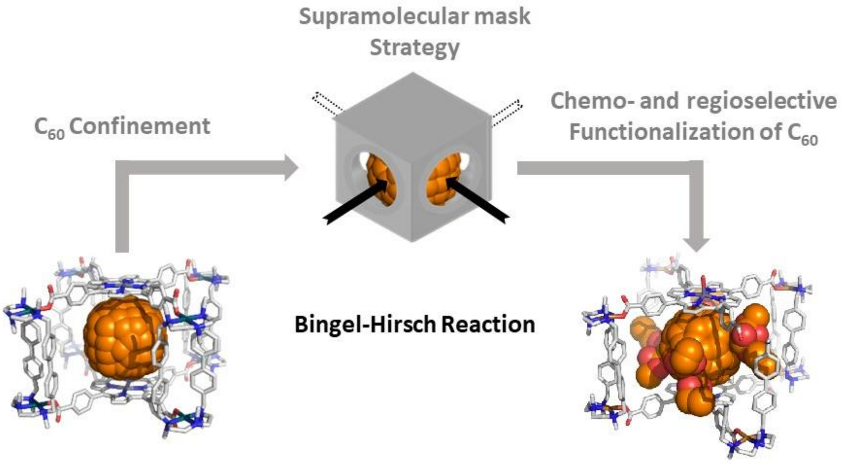

Objective 2: Selective molecular recognition of EMFs for their straightforward purification (Chapters IV, V and VI)

The availability of EMFs is severely limited by their extensive, time consuming and sometimes unattainable chromatographic purification. Therefore, the development of novel purification strategies facilitating the access to EMFs and boosting their applicability is mandatory. Chapters 4, 5 and 6 in this thesis will be devoted to the second objective of this thesis, which consist in the development of straightforward and non-chromatographic purification protocols for the isolation of EMFs via selective encapsulation in a novel supramolecular Cu(II)-based tetragonal prismatic nanocapsule.

Objective 2 was carried out in collaboration with the research group of Dr. Luis Echegoyen, within the framework of a pre-doctoral stay in his laboratories at the University of Texas at El Paso (UTEP). We aimed at facilitating the purification of challenging Uranium-based EMFs species using our supramolecular nanocapsules.

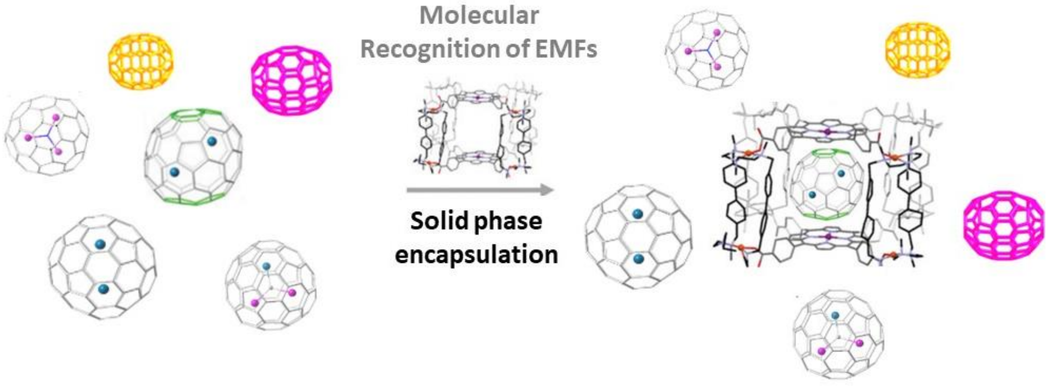

From a general point of view, Objectives 1 and 2 rely on the preparation of supramolecular tetragonal prismatic nanocapsules and the investigation of their properties as molecular vessels. The preparation of macrocyclic complexes based on Cu(II) (analogous to the Pd(II) based ones previously developed in the group) as pillar molecular clips will allow for the self-assembly with tetracarboxylated substituted metalloporphyrins to obtain novel 3D tetragonal prismatic capsules.

Building blocks

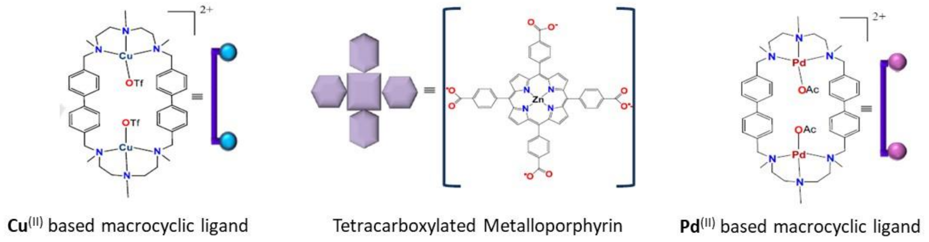

Self-Assembly of 3D tetragonal prismatic nanocapsules

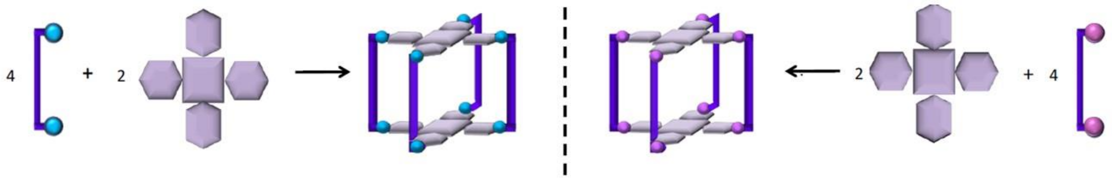

Chapter III.

Supramolecular Fullerene Sponges as Catalytic Masks for Regioselective Functionalization of C_{60}.

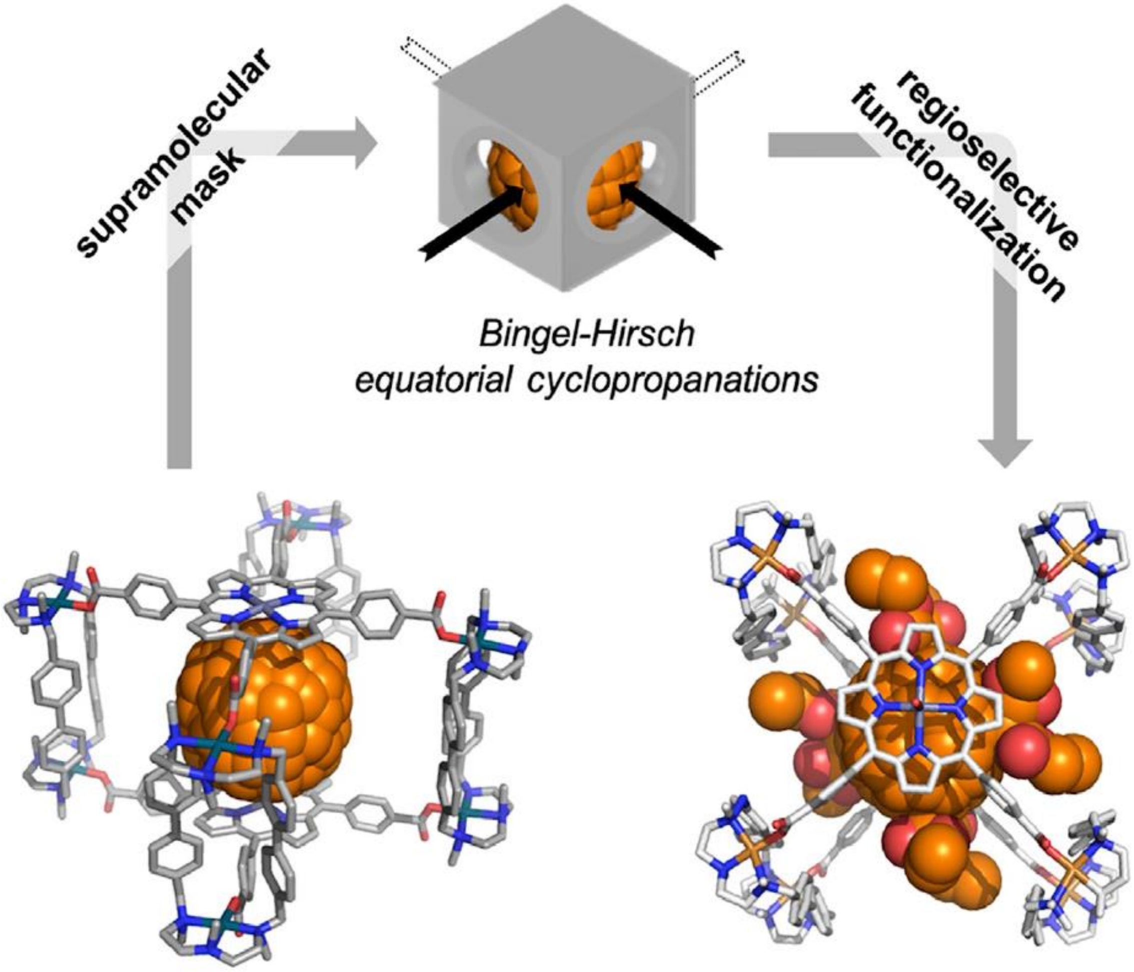

This chapter corresponds to the following publication:

Fuertes-Espinosa, C.; Garcia-Simon, C.; Pujals, M.; Garcia-Borras, M.; Gomez, L.; Parella, T.; Juanhuix, J.; Imaz, I.; Maspoch, D.; Costas, M. and Ribas, X. *Chem.* **2020**, 6, 169-186.

Reprinted with permission from Cell Press editorial

Chem

CellPress

Article

Supramolecular Fullerene Sponges as Catalytic Masks for Regioselective Functionalization of C_{60}

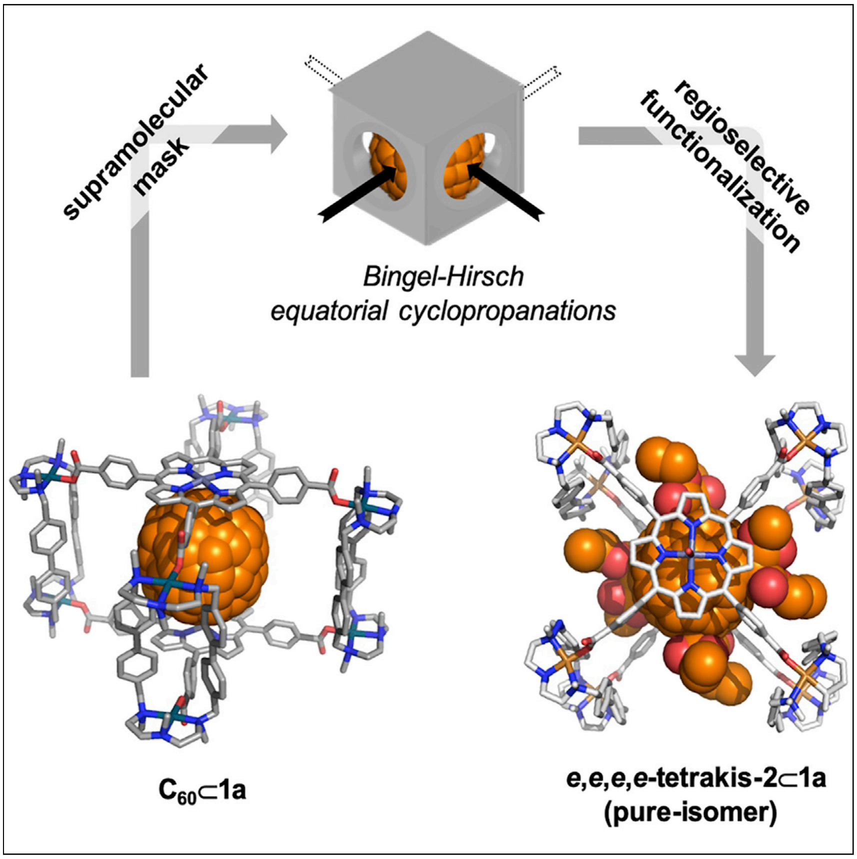

Carles Fuertes-Espinosa, Cristina García-Simón, Míriam Pujals, ..., Daniel Maspoch, Miquel Costas, Xavi Ribas

xavi.ribas@udg.edu

HIGHLIGHTS

Synthesis of pure equatorial tetrakis-C_{60} adduct via supramolecular mask strategy

Crystallographic proof of encapsulated equatorial tetrakis-C_{60} adduct

One-pot synthesis of equatorial hetero-tetrakis- and hetero-hexakis-C_{60} adducts

Biphasic protocol for the catalytic synthesis of an equatorial homo-tetrakis-adduct

An unprecedented and straightforward supramolecular mask strategy to prepare exclusively equatorial bis-, tris-, and tetrakis-cyclopropanated-C_{60} Bingel-Hirsch derivatives is reported. By taking advantage of the high affinity for fullerene of tetragonal prismatic supramolecular cages, a highly stable $C_{60}\subset$**1a**·(BArF)$_8$ host-guest complex is submitted to Bingel-Hirsch cyclopropanation reaction conditions. Regioselectivity is strictly dictated by the four cross-shaped apertures of the nanocapsule in a controlled fashion. Moreover, stepwise-cyclopropanated adducts up to tetrakis additions are obtained in excellent yields and purities.

3 GOOD HEALTH AND WELL-BEING

7 AFFORDABLE AND CLEAN ENERGY

Fuertes-Espinosa et al., Chem 6, 1–18
January 9, 2020 © 2019 Elsevier Inc.
https://doi.org/10.1016/j.chempr.2019.10.010

Please cite this article in press as: Fuertes-Espinosa et al., Supramolecular Fullerene Sponges as Catalytic Masks for Regioselective Functionalization of C_{60}, Chem (2019), https://doi.org/10.1016/j.chempr.2019.10.010

Chem

CellPress

Article

Supramolecular Fullerene Sponges as Catalytic Masks for Regioselective Functionalization of C_{60}

Carles Fuertes-Espinosa,[1] Cristina García-Simón,[1] Míriam Pujals,[1] Marc Garcia-Borràs,[1] Laura Gómez,[2] Teodor Parella,[3] Judit Juanhuix,[4] Inhar Imaz,[5] Daniel Maspoch,[5,6] Miquel Costas,[1] and Xavi Ribas[1,7,*]

SUMMARY

Isomer-pure poly-functionalized fullerenes are required to boost the development of fullerene chemistry in all fields. On a general basis, multi-adduct mixtures with uncontrolled regioselectivity are obtained, and the use of chromatographic purification is prohibitively costly and time consuming, especially in the production of solar cells. Single-isomer poly-functionalized fullerenes are only accessible via stoichiometric, multistep paths entailing protecting-unprotecting sequences. Herein, a nanocapsule is used as a supramolecular tetragonal prismatic mask to exert full control on the reactivity and the equatorial regioselectivity of Bingel-Hirsch cyclopropanation reactions of a confined C_{60} guest. Thus, equatorial bis-, tris-, and tetrakis-C_{60} homo-adducts are exclusively obtained in a stepwise manner. Furthermore, isomer-pure equatorial hetero-tetrakis-adducts or hetero-*Th*-hexakis-adducts are synthesized at will in one-pot synthesis for the first time. This work provides a synthetically valuable path to produce a plethora of new pure-isomer poly-functionalized C_{60}-based compounds as candidates for testing in solar cell devices and biomedical applications.

INTRODUCTION

From the early stages of their discovery, fullerene species have gained increasing interest in several fields including biomedical chemistry,[1–4] material science,[5] solar energy conversion,[6–8] and energy storage.[9] A variety of synthetic routes concerning the functionalization of fullerenes have been established to improve their solubility and modify their physicochemical properties.[10,11] To date, C_{60} fullerene, which has a highly symmetric structure and can be produced in large scale, has been the most exploited substrate. In 2013, C_{60} fullerene and its derivatives were introduced into perovskite solar cells (PSCs),[8,12–14] demonstrating that their use in the perovskite layers plays an important role in passivating the charge traps at the surface and grain boundaries of the thin film, leading to higher device performance (power conversion efficiencies [PCEs] above 20%).[15] Easily accessible mono-adduct $PC_{60}BM$ (and also $PC_{70}BM$) is mainly used as electron transport layers (ETLs) in solar cell devices due to the hampered accessibility to pure-isomer poly-adduct derivatives.[7,12,16] It is generally accepted that the regio-controlled multiple functionalization is the Achilles' heel of fullerene-derivative preparation, which heavily impacts many fields and solar cells in particular.[8,13] This was clearly shown by Grätzel in the enhanced PCE (20.8%) and better stability of PSCs when pure α-bis-$PC_{60}BM$ was utilized in the generation of the perovskite thin layer compared to standard mono-functionalized $PC_{60}BM$ (19.9%).[6] In line with this, Imahori clearly demonstrated the

The Bigger Picture

The supramolecular mask protocol is a significant step forward for the regioselective functionalization of fullerenes. The exquisite ability to form pure-isomer poly-functionalized C_{60} adducts, overcoming tedious and non-practical chromatographic separations, allows for their direct testing in solar cell prototypes. Furthermore, the supramolecular mask strategy can be applied to C_{70} or higher fullerenes, opening a plethora of poly-functionalized fullerene derivatives to be synthesized and tested. Moreover, apart from the nucleophilic cyclopropanations reported herein, the protocol is currently being expanded to Diels-Alder (DA), 1,3-dipolar cycloadditions and $PC_{60}BM$-type cyclopropanations, thus enabling a variety of regioselective functionalization reactions. This supramolecular mask strategy can help the discovery of the next generation of improved solar cells (organic or perovskite based) or new drug candidates.

Please cite this article in press as: Fuertes-Espinosa et al., Supramolecular Fullerene Sponges as Catalytic Masks for Regioselective Functionalization of C_{60}, Chem (2019), https://doi.org/10.1016/j.chempr.2019.10.010

detrimental use of regioisomer mixtures compared to pure isomers in organic photovoltaics (OPVs).[16] Therefore, synthetic access to novel, precisely poly-functionalized fullerenes is needed to unravel structure-property relationships and drive the design of improved solar cell devices.[14] Generally, the spherical nature of C_{60} containing several double bonds with almost identical reactivity compromises the controlled synthesis of site-selective[17] and regioselective[18] multiple adducts of these species. Thus, purification of poly-functionalized fullerene mixtures usually involves tedious and time-consuming chromatographic separation protocols, hampering the full exploitation of these derivatives.[18] To address this shortcoming, different strategies for the selective production of multiple substituted fullerenes have been pursued, generally involving the initial stoichiometric modification of the fullerene with directing groups. Highlighted is the "tether-directed remote functionalization" strategy for the synthesis of bis-, tris-, pentakis-, and hexakis-adducts under regiocontrol, firstly developed by Diederich in 1994 (Figure 1A),[19–23] and the "orthogonal transposition" synthetic strategy developed by Kräutler in 1997 (Figure 1B)[24] for the production of the equatorial-cyclopropanated tetrakis-diethylmalonate-C_{60} adduct (Bingel-Hirsch reaction), which is used for further functionalization on the available axial positions.[25] On the other hand, the modulation of the C_{60} regiochemical reactivity by confinement in supramolecular receptors remains scarce. Cubic[26] and a bowl-shaped[27] coordination cages and a metal-organic framework[28] had been used as supramolecular hosts, all limited to DA reactions and leading to formation of mono- or bis-adducts. Arguably, all methods for regioselective functionalization of fullerenes reported to date,[26,29,30] albeit elegant, are tedious and limited in scope, and overall lack the versatility and practical utility required to boost the applicability of fullerenes. In a broad sense, the regioselective poly-functionalization of fullerenes showcases the general problem of exerting selectivity in a large spherical-like molecule, a challenging question in organic synthesis.

Here, we present an unprecedented straightforward supramolecular mask strategy to prepare exclusively equatorial bis-, tris-, and tetrakis-cyclopropanated-C_{60} Bingel-Hirsch derivatives. By taking advantage of the high affinity of porphyrin-based tetragonal prismatic supramolecular nanocapsules (Pd-based **1a**·$(BArF)_8$ and Cu-based **1b**·$(BArF)_8$) for fullerenes,[31,32] a highly stable $C_{60}\subset$**1a**·$(BArF)_8$ host-guest complex is submitted to Bingel-Hirsch cyclopropanation reaction conditions. Regioselectivity is strictly dictated by the four cross-shaped apertures of the supramolecular tetragonal prismatic container in a controlled fashion. Moreover, the usually observed overreactivity that commonly drives the formation of poly-adducts is cancelled upon confinement of C_{60}, and clean, stepwise-cyclopropanated adducts up to tetrakis additions are obtained in excellent yields and purities.

RESULTS AND DISCUSSION

Synthesis and Characterization of Equatorial Tetrakis-adducts

In general, the regiochemistry of exohedral poly-functionalization of fullerenes remains a standing problem. In order to gain control over these reactions, C_{60} was encapsulated within **1a**·$(BArF)_8$, taking advantage of the complementary size and high affinity between the host and the guest.[32] To test the strategy shown in Figure 1C, we first subjected $C_{60}\subset$**1a**·$(BArF)_8$ to standard conditions commonly used for Bingel-Hirsch reactions. Accordingly, diethyl bromomalonate (4 equiv, nucleophile A) and NaH (4 equiv) were added into a solution of $C_{60}\subset$**1a**·$(BArF)_8$ in pure acetonitrile, and the resulting mixture was stirred for 2 h. Electrospray ionization-high resolution mass spectrometry (ESI-HRMS) monitoring of the reaction crude revealed a stepwise formation of a single product corresponding to the encapsulated

[1]Institut de Química Computacional i Catàlisi and Departament de Química, Universitat de Girona, Campus Montilivi, 17003 Girona, Catalonia, Spain

[2]Serveis Tècnics de Recerca (STR), Universitat de Girona, Parc Científic i Tecnològic, 17003 Girona, Catalonia, Spain

[3]Servei de RMN and Departament de Química, Facultat de Ciències, Universitat Autònoma de Barcelona (UAB), Campus UAB, 08193 Bellaterra, Catalonia, Spain

[4]ALBA Synchrotron, Cerdanyola del Vallès, 08290 Barcelona, Catalonia, Spain

[5]Catalan Institute of Nanoscience and Nanotechnology (ICN2), CSIC and the Barcelona Institute of Science and Technology, Campus UAB, 08193 Bellaterra, Barcelona, Catalonia, Spain

[6]ICREA, Pg. Lluís Companys 23, 08010 Barcelona, Catalonia, Spain

[7]Lead Contact

*Correspondence: xavi.ribas@udg.edu

https://doi.org/10.1016/j.chempr.2019.10.010

Please cite this article in press as: Fuertes-Espinosa et al., Supramolecular Fullerene Sponges as Catalytic Masks for Regioselective Functionalization of C_{60}, Chem (2019), https://doi.org/10.1016/j.chempr.2019.10.010

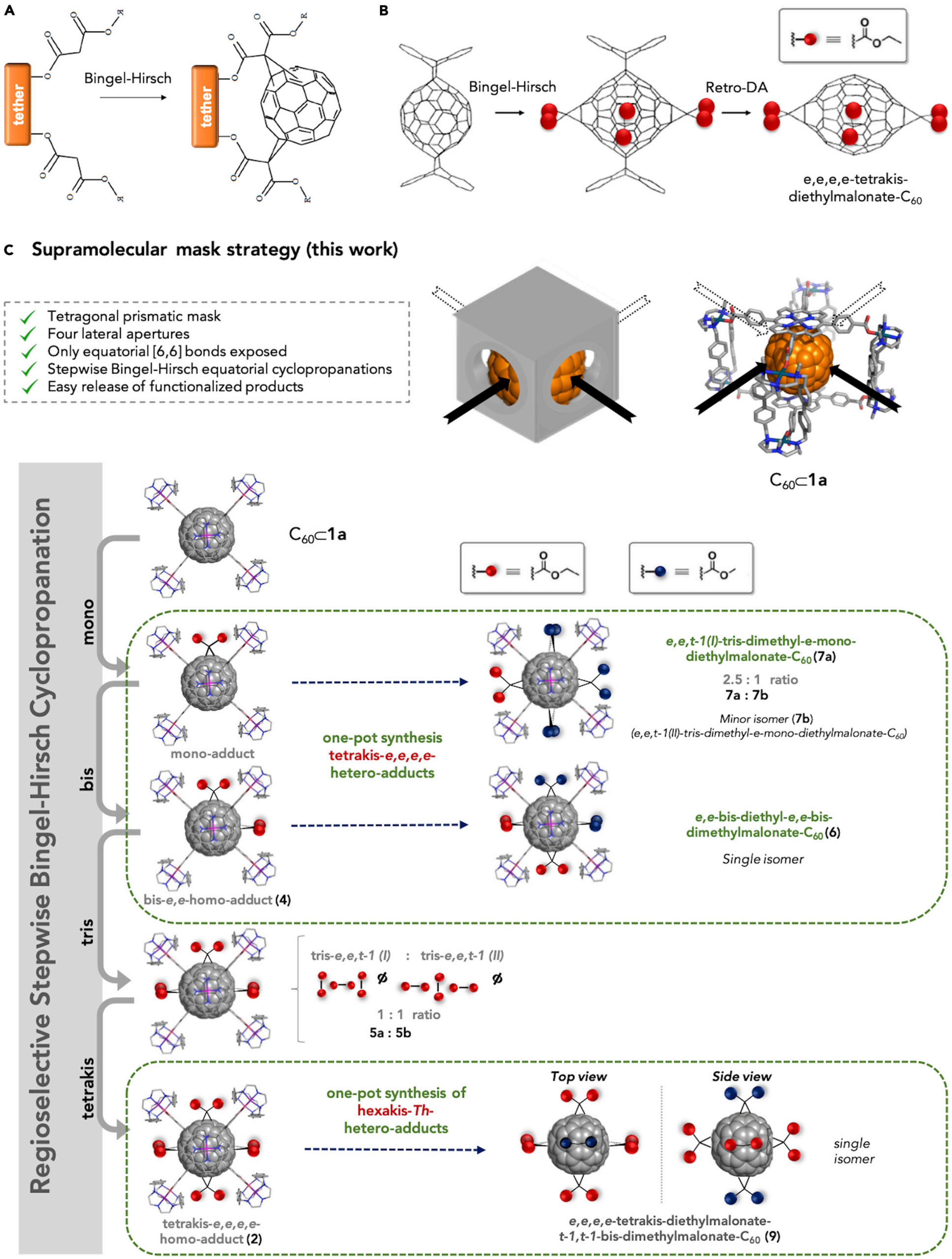

Please cite this article in press as: Fuertes-Espinosa et al., Supramolecular Fullerene Sponges as Catalytic Masks for Regioselective Functionalization of C_{60}, Chem (2019), https://doi.org/10.1016/j.chempr.2019.10.010

Figure 1. Synthetic Strategies Aiming at Regioselective Functionalization of C_{60}
(A) Tether-directed bis-adduct functionalization.
(B) Topochemically controlled orthogonal transposition to obtain fully equatorial tetrakis-adducts, involving Diels-Alder (DA), Bingel-Hirsch, and retro-DA steps.
(C) Supramolecular mask strategy (this work) using encapsulated C_{60} in tetragonal prismatic nanocapsule **1a**·$(BArF)_8$, to synthesize equatorial tetrakis-cyclopropanated-C_{60} homo- and hetero-derivatives as well as hexakis-hetero-derivatives (all functionalized adducts are named as non-encapsulated compounds for clarity).

tetrakis-diethylmalonate-C_{60} adduct **2** (Figures 1C, 2, and 3). ^{1}H-NMR spectrum and high-performance liquid chromatography (HPLC) showed only peaks corresponding to a single, regioisomerically pure, tetrakis-adduct in >99.5% purity and 99% yield

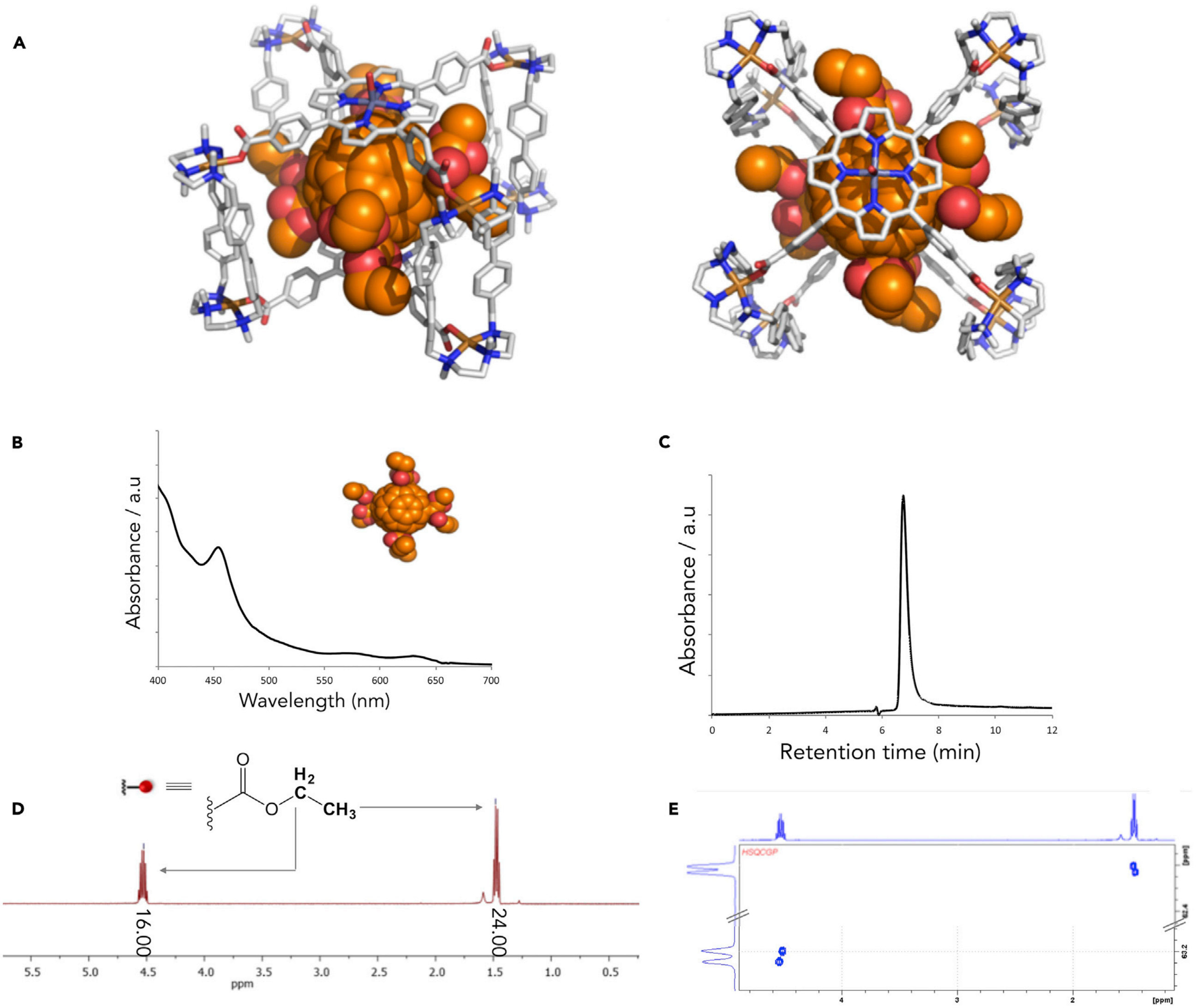

Figure 2. Full Characterization of *e,e,e,e*-Tetrakis-adduct (2)
(A) X-ray crystal structure of **2**⊂**1b**·$(BArF)_8$ (side and apical view), depicting the tetrakis-adduct **2** docked in the nanocapsule **1b**·$(BArF)_8$ (solvent, anions, and H atoms are removed for clarity).
(B) UV-vis spectrum (298 K, toluene).
(C) HPLC chromatogram (BuckyPrep M, 0.5 mL/min, 320 nm, toluene).
(D) ^{1}H-NMR spectrum (500 MHz, 298 K, $CDCl_3$).
(E) 2D ^{1}H-^{13}C spectral-aliased heteronuclear single quantum correlation (HSQC) spectrum (500 MHz, 298 K, $CDCl_3$) of isolated tetrakis-adduct **2**.
See also Table S1.

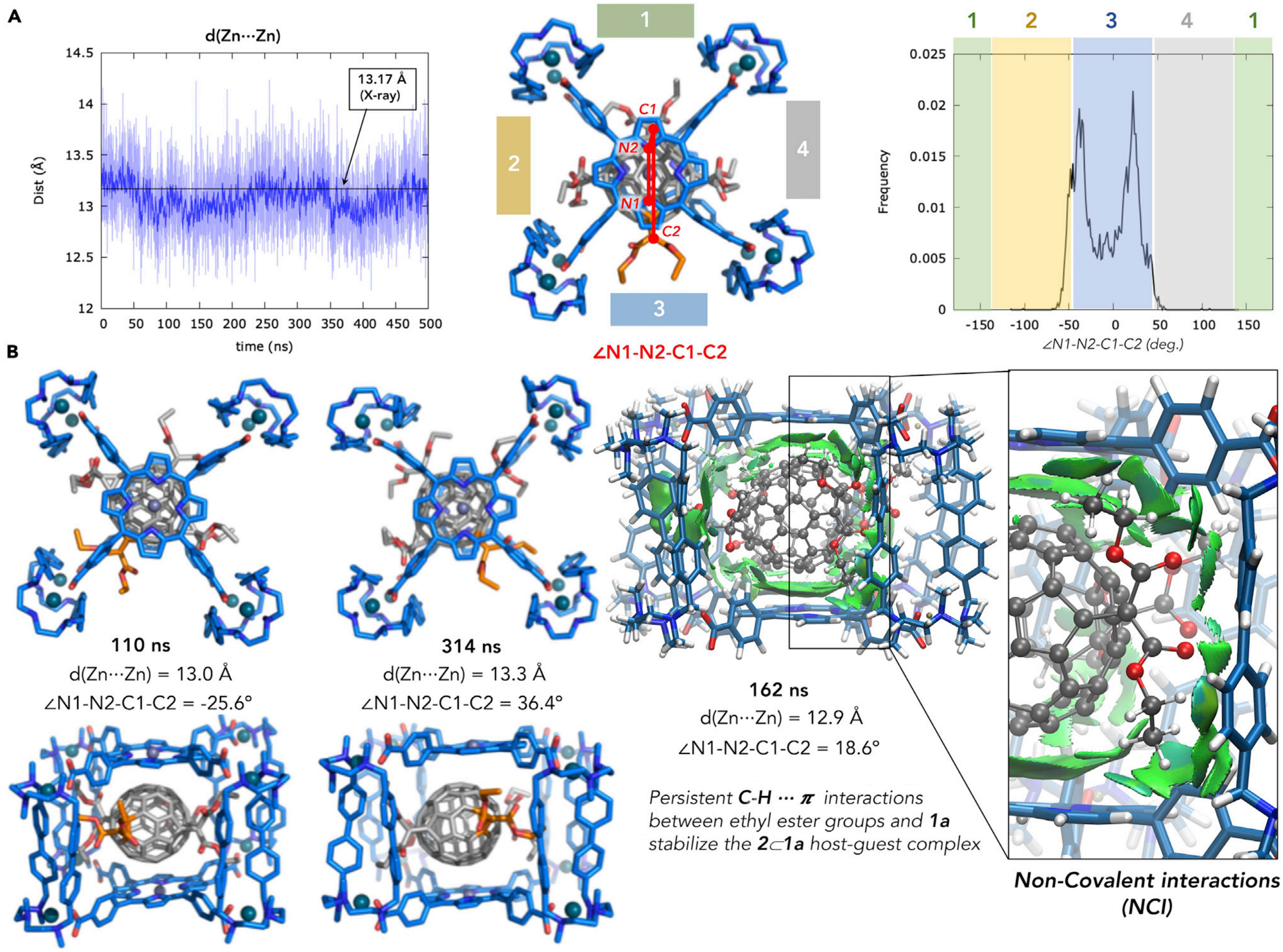

Figure 3. Molecular Dynamics (MD) Simulations of 2⊂1a·(Cl)$_8$ Complex

(A) Analysis of geometric features of **2**⊂**1a**·(Cl)$_8$ complex from 500 ns MD simulations (distances are given in Å and dihedral angles in degrees).

(B) Snapshots of **2**⊂**1a** (Cl)$_8$ complex from the MD trajectory showing different representative orientations of the encapsulated substrate **2**. Non-covalent interaction analysis (NCI) revealed the appearance of persistent C–H···π interactions (stabilizing interactions shown as green surfaces) between ester alkyl and the aromatic rings of the nanocapsule.

See also Figures S8, S9, and S10 and Video S1.

(Figures 1 and 2). Further analysis by NMR showed two overlapped quadruplets at 4.51 and 4.54 ppm and two overlapped triplets at 1.46 and 1.48 ppm corresponding to the ethyl ester groups oriented vertical or horizontal with respect to the equatorial belt. Moreover, ultraviolet-visible (UV-vis) analysis (the addition pattern rather than the nature of the addend can be used as a fingerprint for the identification of a regioisomer)[33,34] matched perfectly with previously reported equatorial tetrakis-adducts, and therefore altogether unambiguously allowed the assignment of the tetrakis-adduct **2** to a D_{2h}-symmetric *e*,*e*,*e*,*e*-regioisomer (Figure 2). Remarkably, this tetrakis-adduct **2** could be released from the nanocapsule either by exchange with pristine C_{60} or by disassembling the nanocapsule, which could be further reassembled and re-used.[32]

To evaluate the influence of nanocapsule **1a**·(BArF)$_8$, we reproduced the Bingel-Hirsch reaction using free C_{60}. Under these conditions, no reaction took place presumably due to the very poor solubility of C_{60} in acetonitrile. For this reason, we

Please cite this article in press as: Fuertes-Espinosa et al., Supramolecular Fullerene Sponges as Catalytic Masks for Regioselective Functionalization of C_{60}, Chem (2019), https://doi.org/10.1016/j.chempr.2019.10.010

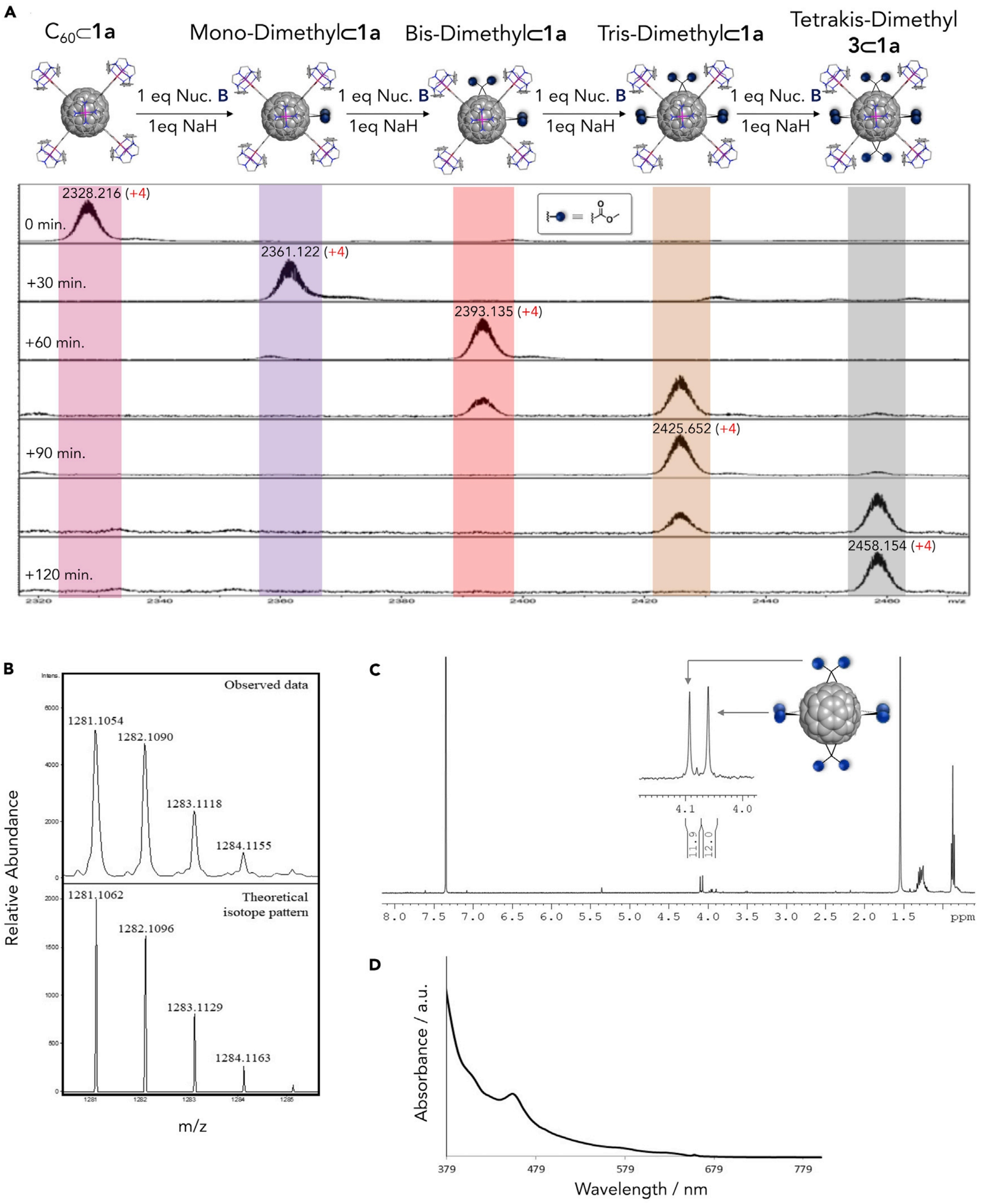

Figure 4. Synthesis of Equatorial *e,e,e,e*-Tetrakis-dimethylmalonate-C_{60} (3)

(A) Mass spectrum monitoring the formation of 3⊂1a·$(BArF)_8$ by sequential addition of nucleophile B (dimethyl bromomalonate) (electrospray ionization mass spectrometry [ESI-MS], positive ion mode, CH_3CN).

(B) Experimental and theoretical isotope pattern of high resolution ESI-MS of **3** (M + Na) (ESI-MS, positive ion mode, CH_2Cl_2:MeOH).

(C) ^{1}H-NMR spectrum of adduct **3** (500 MHz, 298 K, $CDCl_3$), showing two singlets at 4.06 and 4.09 ppm corresponding to the two types of methyl ester groups.

(D) UV-vis absorption spectrum of tetrakis-diethylmalonate-C_{60} adduct **3** (298 K, toluene).

Please cite this article in press as: Fuertes-Espinosa et al., Supramolecular Fullerene Sponges as Catalytic Masks for Regioselective Functionalization of C_{60}, Chem (2019), https://doi.org/10.1016/j.chempr.2019.10.010

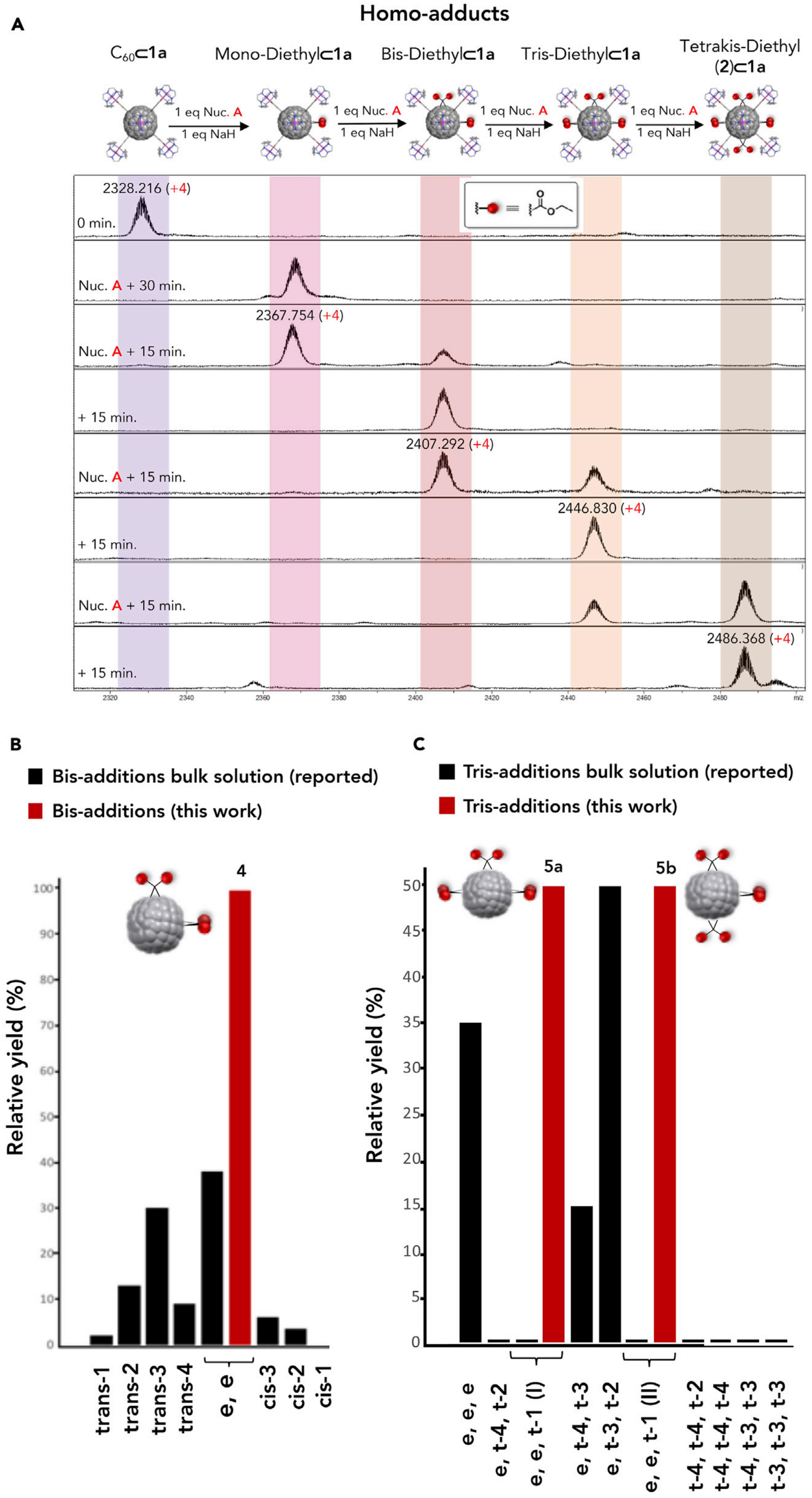

Figure 5. Stepwise Formation of Bis-, Tris-, and Tetrakis-Equatorial Diethylmalonate-C_{60} Adducts
(A) ESI-HRMS monitoring of the formation of the different adducts upon the sequential addition of nucleophile and base (positive ion mode, CH_3CN).

Please cite this article in press as: Fuertes-Espinosa et al., Supramolecular Fullerene Sponges as Catalytic Masks for Regioselective Functionalization of C_{60}, Chem (2019), https://doi.org/10.1016/j.chempr.2019.10.010

Figure 5. *Continued*

(B and C) Comparison between C_{60} regioisomers obtained in bulk solution and using the supramolecular confinement strategy for bis-adducts (B) and for tris-adducts (nucleophile A, diethyl bromomalonate) (C).
See also Figures S1 and S2.

repeated this reaction in toluene where C_{60} is soluble. In toluene, bis- to hexakis-adducts were produced even at short reaction times (30 min), whereas up to 60% of starting C_{60} remained unreacted (Figure S6). Altogether, these results suggested that the confinement of C_{60} in the nanocapsule completely modifies not only its reactivity in acetonitrile but also the reaction outcome, directing the nucleophilic attacks exclusively toward the equatorial [6,6] bonds of the fullerene.

Slow diffusion of Et_2O into a solution of **2**$\subset$**1b**$\cdot(BArF)_8$ in CH_2Cl_2 containing 5% of CH_3CN (**1b**$\cdot(BArF)_8$ is the Cu-based analog of the Pd-based **1a**$\cdot(BArF)_8$) provided X-ray quality single crystals suitable for diffraction analysis under synchrotron radiation. Single-crystal X-ray diffraction (XRD) analysis of **2**$\subset$**1b**$\cdot(BArF)_8$ revealed that each diethylmalonate group of the docked tetrakis-adduct **2** was pointing toward the four apertures of nanocapsule **1b**$\cdot(BArF)_8$ (Figure 2). The short Zn$\cdots$Zn distance (13.17 Å) indicated an important degree of adaptability of **1b**$\cdot(BArF)_8$ to maximize the porphyrin-fullerene interactions. The fact that tetrakis-adduct **2** could be observed in the XRD analysis strongly suggested that rotation of the guest inside the nanocapsule was severely restricted. The latter was confirmed by molecular dynamics (MD) simulations of **2**$\subset$**1a**$\cdot Cl_8$, showing that motion of each diethylmalonate adduct is totally restricted within a single aperture of the nanocapsule due to their size (Figure 3), although malonate groups do not stay fixed in the center of the open gates, and they orient closer to the nanocapsule walls establishing persistent C–H$\cdots\pi$ interactions between alkyl ester and the aromatic rings of the nanocapsule. Indeed, the mean Zn$\cdots$Zn distance in the MD (13.1 Å) reproduced perfectly (see Video S1) the one found by XRD, and it is also in line with the distance measured in our previously reported density functional theory (DFT)-optimized $C_{60}\subset$**1a**$\bullet Cl_8$ structure.[32]

As expected, using other nucleophiles such as dimethyl bromomalonate (nucleophile B), the D_{2h}-symmetric *e*,*e*,*e*,*e*-regioisomer of tetrakis-dimethylmalonate-C_{60} adduct (**3**) was obtained in one step following the same procedure (Figure 4).

Stepwise Synthesis of Equatorial Bis- and Tris-adducts

It is known that functionalized C_{60} adducts are more prone to nucleophilic attacks than pristine C_{60}.[35] However, this overreactivity was completely suppressed when C_{60} was encapsulated in **1a**$\cdot(BArF)_8$, observing a smooth stepwise formation of mono-, bis-, tris-, and tetrakis-adducts (see Figures 1 and 5). Following the herein reported supramolecular mask strategy, the single bis-adduct (**4**) was selectively produced by using sodium acetate as a weaker base (NaH was not used to totally exclude the formation of *trans-1* bis-adduct)[36–38] and controlling the number of equivalents of nucleophile added (Figures 5 and S1). 1D and 2D NMR, HPLC, and UV-vis analyses of released **4** indicated the exclusive formation of C_s-symmetric *e*,*e*-regioisomer, contrasting with the seven bis-regioisomers obtained in bulk solution (Figure 5B). No trace of *trans-1* bis-adduct was detected either, which could be related to the enhanced reactivity in the equatorial bonds adjacent to the first addend.[38]

Additionally, the equatorial tris-adduct was also attained (Figure 1C), obtaining equimolar amounts of two non-chiral isomers **5a** and **5b**, which corresponded to a

Please cite this article in press as: Fuertes-Espinosa et al., Supramolecular Fullerene Sponges as Catalytic Masks for Regioselective Functionalization of C_{60}, Chem (2019), https://doi.org/10.1016/j.chempr.2019.10.010

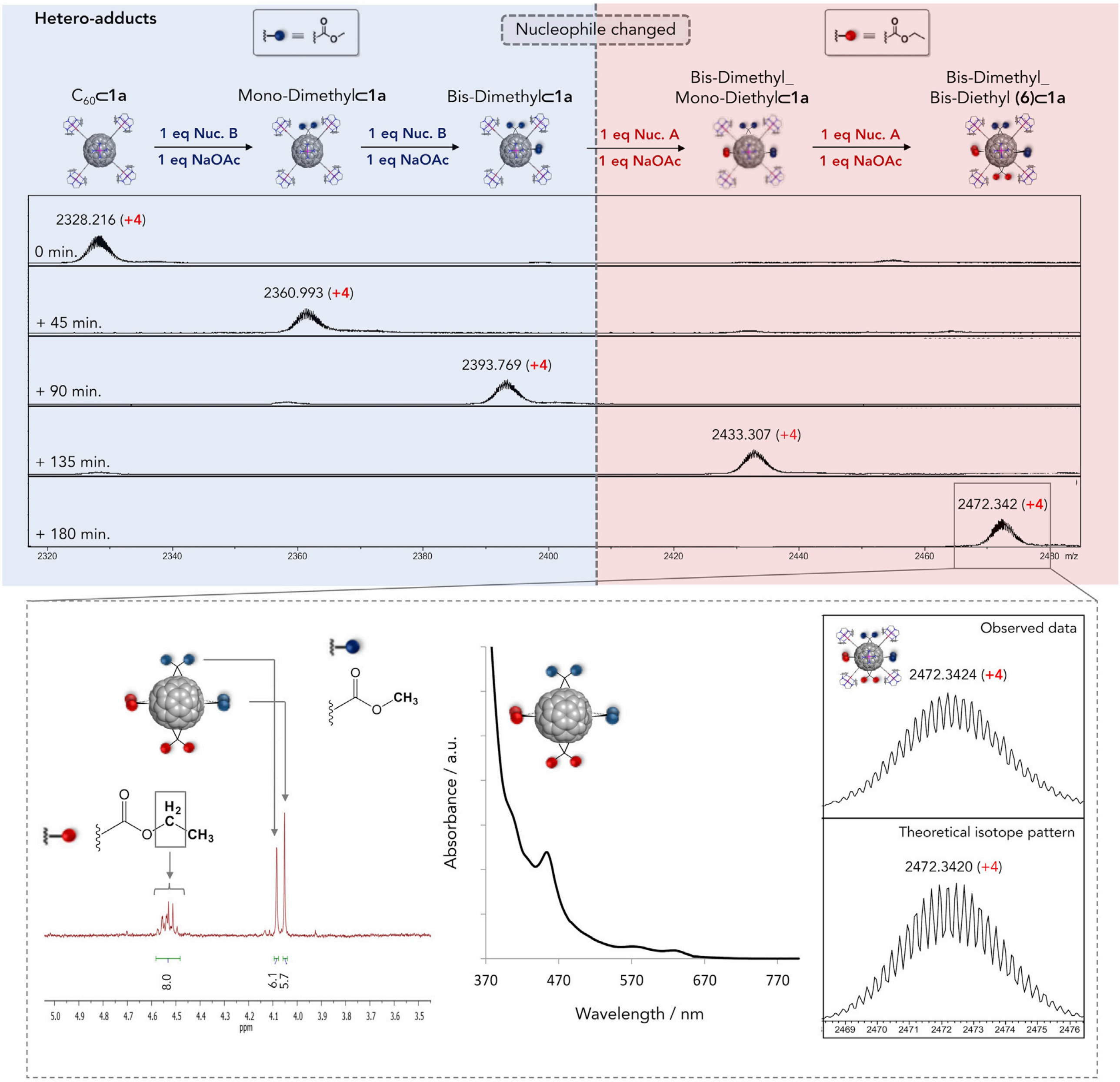

Figure 6. Stepwise Synthesis of Hetero-tetrakis-adduct *e,e*-Bis-diethyl-*e,e*-bis-dimethylmalonate-C_{60} 6 (Nucleophile B, Dimethyl Bromomalonate)

ESI-HRMS monitoring of the formation of **6** by sequential addition of the two different A and B nucleophiles. Inset shows the ^{1}H-NMR (500 MHz, 298 K, $CDCl_3$), highlighting the multiplet corresponding to the methylene region (4.55 [2H], 4.54 [2H], and 4.52 [4H]) and the singlets corresponding to the methyl esters (4.090 [3H], 4.087 [3H], and 4.05 [6H]); UV-vis (298 K, toluene) and ESI-MS (experimental and theoretical isotopic pattern for z = +4) characterization for **6**.

See also Figure S3.

C_s-symmetric *e,e,t-1* (*I*) and *e,e,t-1* (*II*),[39] as ascertained by 1D and 2D NMR (Figure S2). Remarkably, both *e,e,t-1* (*I*) and *e,e,t-1* (*II*) equatorial regioisomers have never been detected in bulk solution (Figure 5C). The steric constrains of the encapsulated bis-adduct **4** prevent free rotation as ascertained by MD simulations (see Video S3), exposing the two remaining equatorial sites to the nanocapsule apertures, being both equally suitable to further react forming tris-adducts **5a** and **5b**.

Please cite this article in press as: Fuertes-Espinosa et al., Supramolecular Fullerene Sponges as Catalytic Masks for Regioselective Functionalization of C_{60}, Chem (2019), https://doi.org/10.1016/j.chempr.2019.10.010

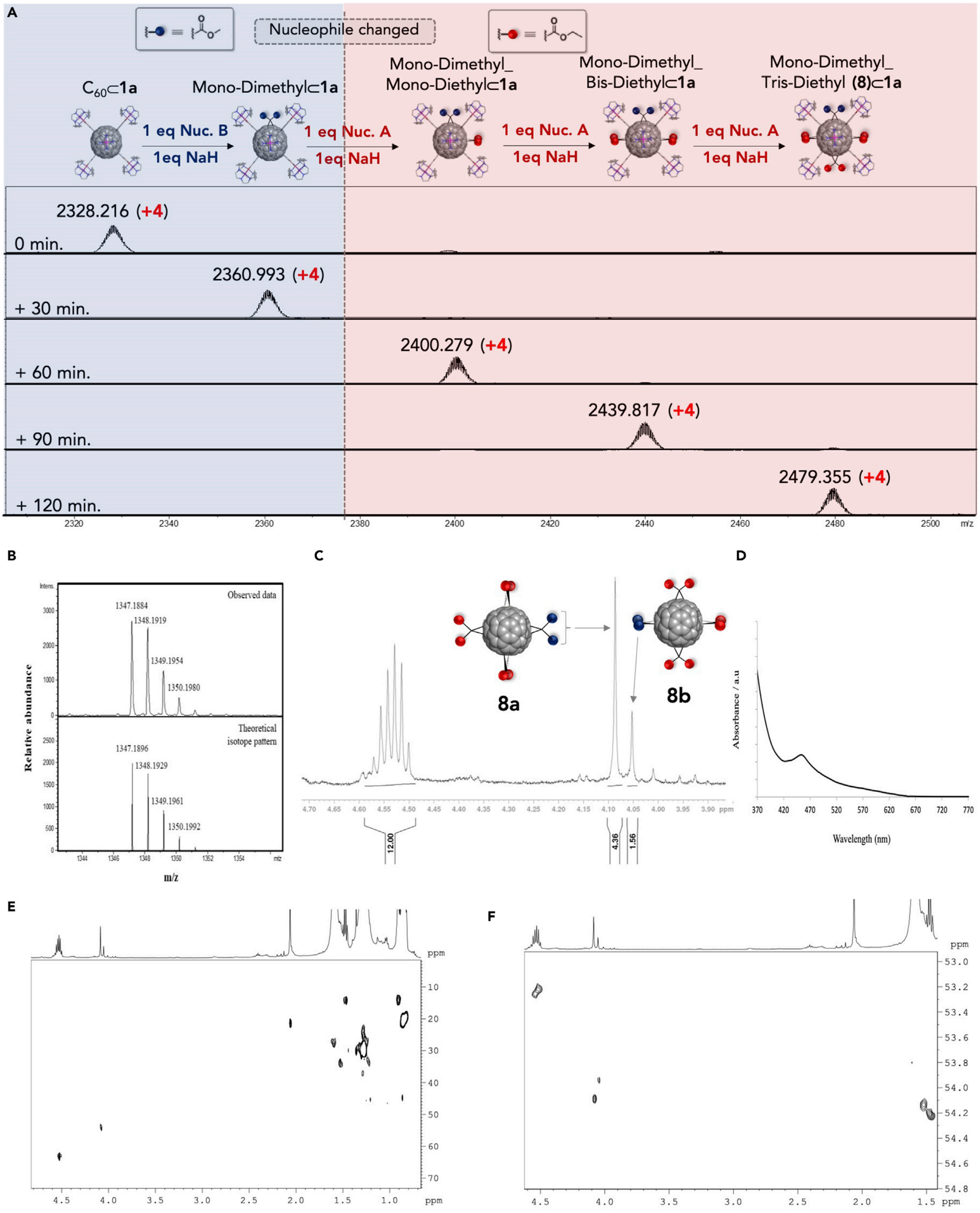

Please cite this article in press as: Fuertes-Espinosa et al., Supramolecular Fullerene Sponges as Catalytic Masks for Regioselective Functionalization of C_{60}, Chem (2019), https://doi.org/10.1016/j.chempr.2019.10.010

Figure 7. Synthesis of *e,e,t-1(I)*-Tris-diethyl-*e*-mono-dimethylmalonate-C_{60} (8a) and *e,e,t-1(II)*-Tris-diethyl-*e*-mono-dimethylmalonate-C_{60} (8b) (8a:8b Ratio 2.8:1)

(A) Mass spectrum monitoring the formation of (**8a**/**8b**)⊂**1a**·(BArF)$_8$ (nucleophile A, diethyl bromomalonate; and nucleophile B, dimethyl bromomalonate) (ESI-MS, positive ion mode, CH_3CN).

(B) Experimental and theoretical isotope pattern of high resolution ESI-MS of **8a**/**8b** (M + Na) (ESI-MS, positive ion mode, CH_2Cl_2:MeOH).

(C) ^{1}H-NMR spectrum of adduct **8a**/**8b** (500 MHz, 298 K, $CDCl_3$), highlighting the singlet at 4.08 ppm corresponding to the methyl esters of **8a** and the singlet at 4.06 ppm for **8b** (integration area is in agreement with an **8a**:**8b** ratio of 2.8:1).

(D) UV-vis absorption spectrum of adduct **8a**/**8b** (298 K, toluene).

(E) 2D ^{1}H-^{13}C HSQC spectrum of adduct **8a**/**8b** (500 MHz, 298 K, $CDCl_3$).

(F) 2D ^{1}H-^{13}C spectral-aliased HSQC spectrum of adduct **8a**/**8b** (500 MHz, 298 K, $CDCl_3$).

One-Pot Synthesis of Equatorial Hetero-tetrakis-adducts

Given the versatility of platform **1a**·(BArF)$_8$, we pursued the development of a synthetic route to produce equatorial hetero-tetrakis-adducts in a one-pot protocol. Noteworthy, it was required to use a single isomer as the precursor molecule to obtain a single tetrakis-regioisomer. The smooth and stepwise formation of cyclopropanated fullerene equatorial adducts when C_{60} is confined in **1a**·(BArF)$_8$ allowed *in operando* synthesis of the *e*,*e*-dimethyl-bis-adduct. The subsequent addition of 2 equiv of diethyl bromomalonate and 2 equiv of sodium acetate on the reaction crude afforded the fully equatorial hetero-D_{2h}-tetrakis-adduct *e*,*e*-bis-diethyl-*e*,*e*-bis-dimethylmalonate-C_{60} (**6**) (Figures 6 and S3), as a single isomer in high purity and excellent yield (97% yield). The same synthetic strategy was followed changing the nucleophile once mono-diethylmalonate-C_{60} adduct was obtained. The fully equatorial hetero-tetrakis-adduct *e*,*e*,*t-1*(*I*)-tris-dimethyl-*e*-mono-diethylmalonate-C_{60} (**7a**) was formed upon the addition of 3 equiv of dimethyl bromomalonate and 3 equiv of sodium hydride on the reaction crude (Figure 1C). UV-vis spectrum indicated that a fully equatorial compound was obtained. However, careful 1D and 2D NMR analysis showed that the isomer **7b** (*e*,*e*,*t-1*(*II*)-tris-dimethyl-*e*-mono-diethylmalonate-C_{60}) was also present in a minor amount (2.5:1 **7a**:**7b**) (Figure S4). To better understand the parameters governing this preferential formation, the same synthetic strategy was followed using mono-dimethylmalonate-C_{60} adduct as the precursor and adding 3 equiv of diethyl bromomalonate. Again, a mixture of hetero-tetrakis-adduct *e*,*e*,*t-1*(*I*)-tris-diethyl-*e*-mono-dimethylmalonate-C_{60} (**8a**) and *e*,*e*,*t-1*(*II*)-tris-diethyl-*e*-mono-dimethylmalonate-C_{60} (**8b**) was obtained in a similar ratio (2.8:1 **8a**:**8b**) (Figure 7). MD simulations showed totally restricted gate-to-gate motion of bis-adducts, as opposite to the mono-adducts, which can also spin around the cyclopropane axis (Figures 8 and S8–S13; Videos S2 and S3). Taken together, these results suggested that a preferential orientational attack of the second nucleophile fixed the fullerene molecule to produce **7a** and **8a** in higher ratios and that the preference of this second addition might be related to the non-covalent interactions between alkyl ester and the aromatic rings of the nanocapsule observed by MD (Figures S12 and S15).

One-Pot Synthesis of Hetero-hexakis-adducts

In a further twist in the preparation of hetero-poly-adducts, we discovered that by adding more equivalents (3 equiv) of a different malonate (i.e., dimethylbromomalonate) after the synthesis of *e*,*e*,*e*,*e*-tetrakis-diethylmalonate-C_{60} adduct (**2**) inside the nanocapsule, a pure single isomer of the *Th*-hexakis-hetero-adduct, namely *e*,*e*,*e*,*e*-tetrakis-diethylmalonate-*t-1*,*t-1*-bis-diethylmalonate-C_{60} (**9**), was obtained (Figures 1 and 9).[18] Given the multiple options described in Figure 1C, the present supramolecular mask strategy can be potentially used to obtain all possible combinations of *Th*-hexakis hetero-adducts with two different addends ([6:0], [5:1], type I [1:5], type I [4:2], type II [4:2], type I [2:4], type II [2:4], and type II [3:3]), with the exception of type I [3:3]).[2,18] Notably, diffusion coefficients (diffusion-ordered

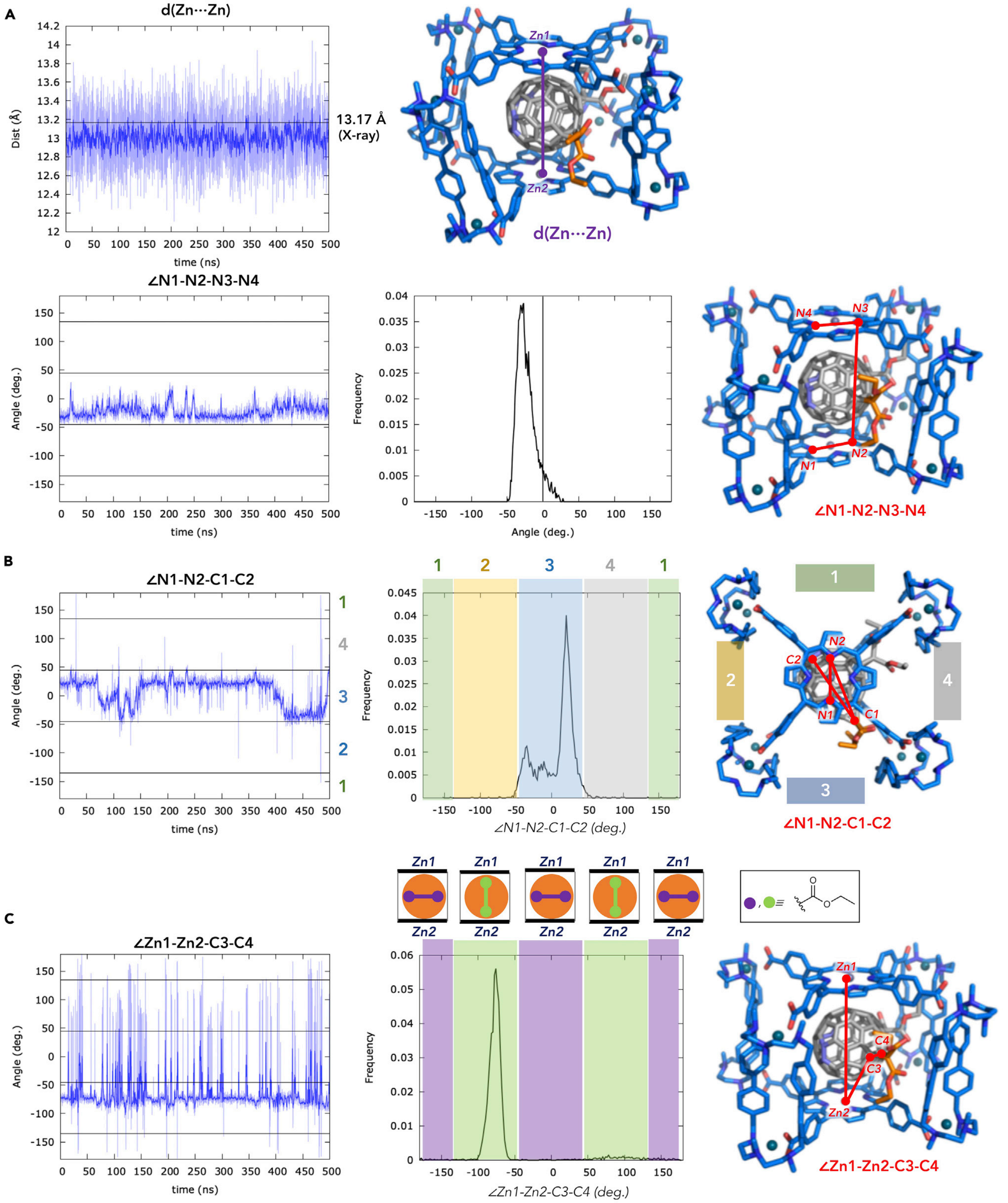
A
d(Zn···Zn)
Dist (Å)
14.2
14
13.8
13.6
13.4
13.2
13
12.8
12.6
12.4
12.2
12
0 50 100 150 200 250 300 350 400 450 500
time (ns)
13.17 Å
(X-ray)
Zn1
Zn2
d(Zn···Zn)
∠N1-N2-N3-N4
Angle (deg.)
150 100 50 0 -50 -100 -150
time (ns)
Frequency
0.04 0.035 0.03 0.025 0.02 0.015 0.01 0.005 0
-150 -100 -50 0 50 100 150
Angle (deg.)
N4
N3
N1
N2
∠N1-N2-N3-N4
B
∠N1-N2-C1-C2
1
4
3
2
1
Angle (deg.)
time (ns)
1 2 3 4 1
Frequency
0.045 0.04 0.035 0.03 0.025 0.02 0.015 0.01 0.005 0
-150 -100 -50 0 50 100 150
∠N1-N2-C1-C2 (deg.)
1
2
4
3
N2
C2
N1
C1
∠N1-N2-C1-C2
C
Zn1 Zn1 Zn1 Zn1 Zn1
Zn2 Zn2 Zn2 Zn2 Zn2
●, ● ≡
O
O
∠Zn1-Zn2-C3-C4
Angle (deg.)
time (ns)
Frequency
0.06 0.05 0.04 0.03 0.02 0.01 0
-150 -100 -50 0 50 100 150
∠Zn1-Zn2-C3-C4 (deg.)
Zn1
C4
C3
Zn2
∠Zn1-Zn2-C3-C4

Please cite this article in press as: Fuertes-Espinosa et al., Supramolecular Fullerene Sponges as Catalytic Masks for Regioselective Functionalization of C_{60}, Chem (2019), https://doi.org/10.1016/j.chempr.2019.10.010

Figure 8. Conformational Analysis of $4 \subset 1a\cdot(Cl)_8$ (Bis-*e*,*e*-adduct) Host-Guest Complex from 500 ns of Molecular Dynamics (MD) Trajectories in Explicit CH_3CN Solvent

(A) Zn···Zn distance and ∠N1-N2-N3-N4 dihedral angle measured along the MD trajectory. ∠N1-N2-N3-N4 dihedral angle describes the torsion of the nanocapsule: the larger deviation from ∠N1-N2-N3-N4 = 0 angle, the more twisted the capsule. Most visited angle values are shown in the histogram plot (frequency versus angle value).

(B) ∠N1-N2-C1-C2 dihedral angle measured along the MD trajectory. ∠N1-N2-C1-C2 angle describes the relative rotation of the encapsulated fullerene with respect to the capsule, and most visited angle values are shown in the histogram plot (frequency versus angle value). Different capsule windows (labeled as 1, 2, 3, and 4 in the figure) correspond to different ranges of explored angle values.

(C) ∠Zn1-Zn2-C3-C4 dihedral angle measured along the MD trajectory. ∠Zn1-Zn2-C3-C4 angle describes the relative orientation of the cyclopropane ring with respect to the capsule. ∠Zn1-Zn2-C3-C4 values around 0° and ±180° indicate that the cyclopropane ring stays perpendicular to the porphyrins, while values around ±90° indicate that the cyclopropane ring stays in a parallel conformation with respect to the porphyrins. Distances and angles are given in angstroms (Å) and degrees (°), respectively.

See also Figures S11–S13 and Videos S2 and S3.

NMR spectroscopy [DOSY-NMR]) of bis-, tris-, tetrakis- and hexakis-adducts were in agreement with the increasing bulkiness of the molecules (Figure S5).

Biphasic Protocol for the Catalytic Synthesis of Tetrakis-adduct 2

Finally, the supramolecular mask concept was upgraded to a synthetically useful catalytic methodology by implementing a reversible phase transfer protocol. First, we sought confirmation that the nanocapsule (with and without cargo) could be cleanly transferred by anion metathesis from the organic phase (toluene:CH_2Cl_2, 1:1) to the aqueous phase (H_2O:DMSO, 9:1) after the addition of 5 equiv of $(n\mathrm{Bu}_4\mathrm{N})_2(\mathrm{SO}_4)$, and vice versa after the addition of 10 equiv of NaBArF (Figures 10A and S7). Once this was ensured, the catalytic system was set up dissolving 1 equiv. of $\mathbf{1a}\cdot(\mathrm{BArF})_8$ and 20 equiv of C_{60} in the organic layer. Then, by the addition of 5 equiv of $(n\mathrm{Bu}_4\mathrm{N})_2(\mathrm{SO}_4)$, the cage and the cargo were transferred to the aqueous layer ($C_{60}\subset\mathbf{1a}\cdot(\mathrm{SO}_4)_4$), triggering simultaneously the Bingel-Hirsch reaction (diethyl bromomalonate as the nucleophile and NaOAc as the base). This reaction required 24 h due to the low solubility of diethyl bromomalonate in the aqueous phase (10% DMSO was added to enhance its solubility while maintaining the double phase). After completion, addition of 10 equiv of NaBArF brought the encapsulated tetrakis-adduct (i.e., $\mathbf{2}\subset\mathbf{1a}\cdot(\mathrm{BArF})_8$) into the organic phase, which contained excess of C_{60} (19 equiv). In this situation, simple stirring for 30 min allowed the ejection of **2** (*e*,*e*,*e*,*e*-tetrakis-diethylmalonate-C_{60}) into the organic phase by encapsulation of pristine C_{60}, which has a ~25-fold higher affinity than the tetrakis-adduct **2** (K_a (**2**) = 1.4 (±0.3)·10^6 M^{-1}; K_a (C_{60}) = 3.6 (±0.2)·10^7 M^{-1} in CH_2Cl_2:toluene 1:1) (Figures 10B–10D). The excess of C_{60} was used to ensure a rapid exchange with **2**. Further addition of 5 equiv of $(n\mathrm{Bu}_4\mathrm{N})_2(\mathrm{SO}_4)$ started the second cycle of the protocol. Repetition of 10 complete cycles afforded quantitative formation of **2**, which was dried and separated from the remaining excess of C_{60} by flash chromatography and analyzed by HLPC to confirm its purity (48% global yield, >97% yield with respect to consumed C_{60}, 10 TON, 9.7 equiv, and 10.2 mg). Alternatively, the excess of C_{60} can be removed by the addition of a precise amount of $\mathbf{1a}\cdot(\mathrm{BArF})_8$ to exclusively form $C_{60}\subset\mathbf{1a}\cdot(\mathrm{BArF})_8$ owing to its higher affinity. The process was catalytic in nanocapsule $\mathbf{1a}\cdot(\mathrm{BArF})_8$, no decomposition of the supramolecular host was detected after 10 cycles, and its efficiency was kept quantitative provided C_{60} was found in excess with respect to the tetrakis-adduct. Moreover, since the Bingel-Hirsch reaction is confined at the aqueous phase, the tetrakis-adduct can be accumulated in the organic phase with any sign of overreaction thus avoiding one of main drawbacks in fullerene functionalization. The protocol meets the fullerene-derivative scale (tens of milligrams) requirements for PSC device preparation[6] and might be easily scalable. All attempts to improve the practicality of the catalytic system by turning it to a heterogeneous catalysis have failed because of loss of regioselectivity (in pure CH_3CN) or loss of reactivity

Please cite this article in press as: Fuertes-Espinosa et al., Supramolecular Fullerene Sponges as Catalytic Masks for Regioselective Functionalization of C_{60}, Chem (2019), https://doi.org/10.1016/j.chempr.2019.10.010

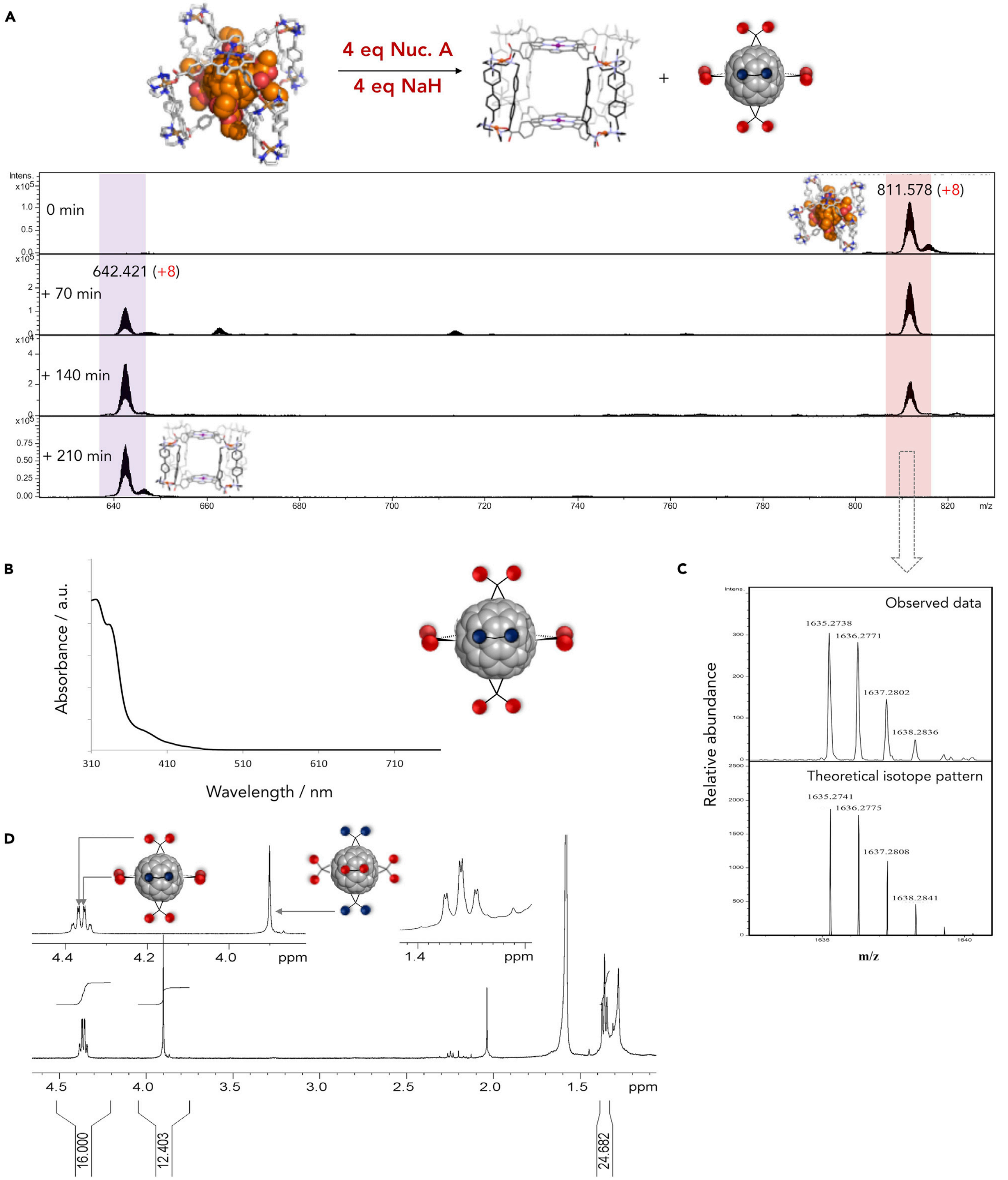

Figure 9. Synthesis of *Th*-Hexakis-hetero-adduct *e,e,e,e*-Tetrakis-diethylmalonate-*t-1,t-1*-bis-diethylmalonate-C_{60} (9)

(A) HRMS monitoring for the formation of **9** from $\mathbf{2}\subset\mathbf{1a}\cdot(\mathrm{BArF})_8$. Adduct **2** was released from $\mathbf{1a}\cdot(\mathrm{BArF})_8$ upon the addition of nucleophile B, forming adduct **9** outside the capsule thus observing the formation of empty cage (nucleophile B, dimethyl bromomalonate).

(B) UV-vis absorption spectrum of adduct **9** (298 K, toluene).

Please cite this article in press as: Fuertes-Espinosa et al., Supramolecular Fullerene Sponges as Catalytic Masks for Regioselective Functionalization of C_{60}, Chem (2019), https://doi.org/10.1016/j.chempr.2019.10.010

Figure 9. *Continued*

(C) ESI-MS of **9**, positive ion mode, CH_3CN.

(D) ^{1}H-NMR spectrum of adduct **9** (500 MHz, 298 K, $CDCl_3$), showing two overlapped quadruplets at 4.35 and 4.36 ppm and two overlapped triplets at 1.358 and 1.361 ppm corresponding to the ethyl ester groups oriented vertical or horizontal with respect to the equatorial region, and one singlet at 3.90 ppm corresponding to the methyl esters located at the axial positions of the *Th*-hexakis-adduct.

(in pure nitromethane) in the Bingel-Hirsch cyclopropanation reaction (Figure S14). Collectively, the present supramolecular one-pot mask protocol allows potential access to a plethora of new single regioisomer poly-functionalized C_{60}-based compounds, which are candidates for testing in solar cell devices and other technological and biomedicinal applications.

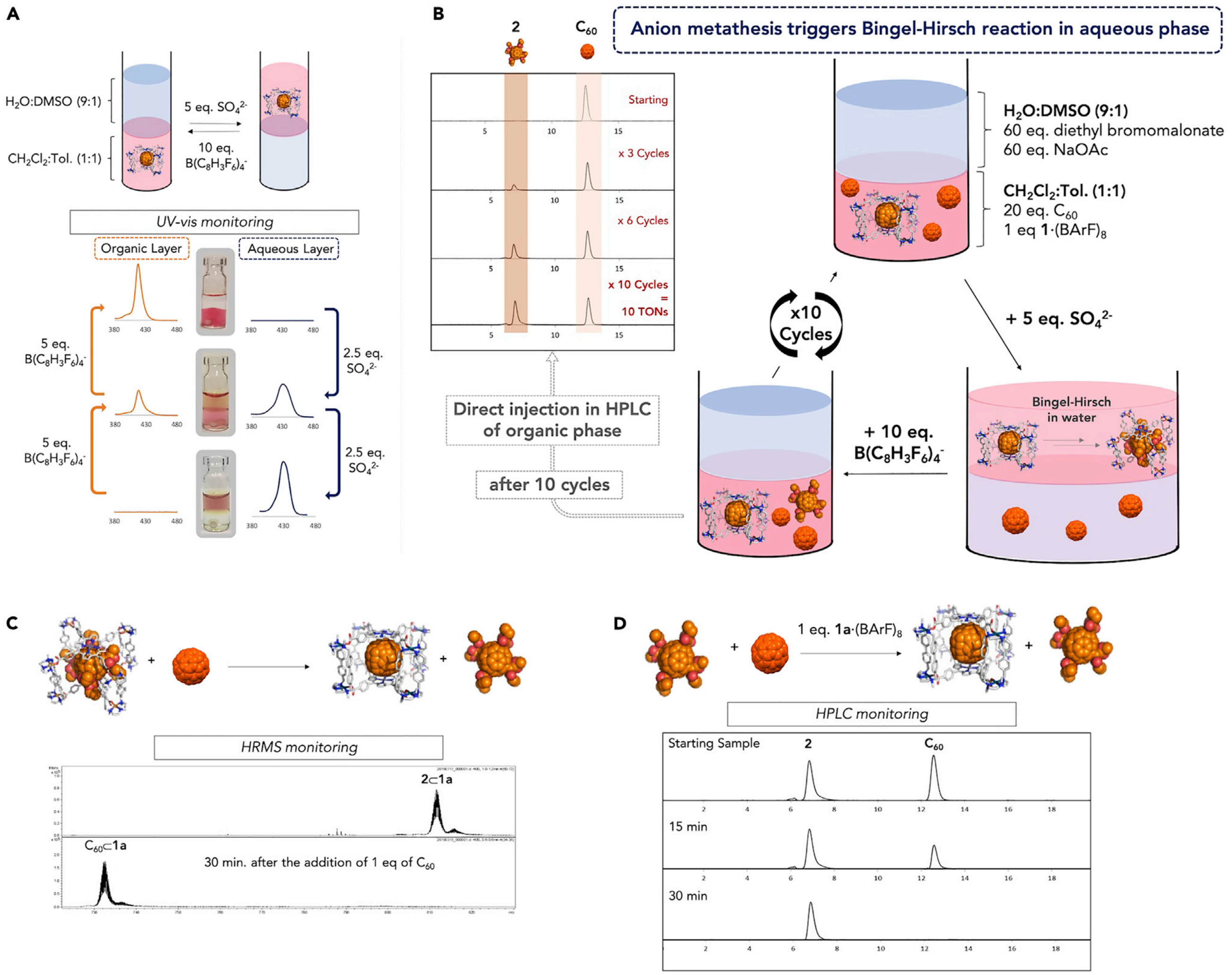

Figure 10. Biphasic Catalytic Protocol for the Synthesis of the Equatorial Tetrakis-adduct 2

(A) Reversible phase transfer of $C_{60}\subset$**1a** from the organic to the aqueous phase and vice versa, including the UV-vis monitoring upon anion metathesis.

(B) Design of biphasic methodology for the synthesis of equatorial tetrakis-adduct **2** using 10 mol % catalytic loadings of nanocapsule **1a**·(BArF)$_8$ (up to 10 tons with no signs of decomposition of **1a**).

(C) Control ESI-MS experiment for the exchange of encapsulated **2** ([$C_{60}\subset$**1a**] = 2.07×10^{-3} M) by an equimolar amount of C_{60} after 30 min (toluene: CH_3CN 9:1).

(D) Control experiment showing the higher affinity of nanocapsule **1a**·(BArF)$_8$ for C_{60} in toluene only with equimolar amounts of **2** and C_{60}, as deduced from HPLC monitoring ([$C_{60}\subset$**1a**] = [C_{60}] = 2.07×10^{-3} M).

See also Figure S7.

In conclusion, a tetragonal prismatic supramolecular nanocapsule is used as a supramolecular mask to exert full control on the reactivity and equatorial regioselectivity of Bingel-Hirsch cyclopropanation reactions of confined C_{60} fullerene. The four cross-shaped open windows featured by the supramolecular mask are key to gain full control on the functionalization of encapsulated C_{60} in terms of exclusive equatorial regioselectivity and stepwise formation of the bis-, tris-, and tetrakis-C_{60} homo-adducts. Moreover, isomer-pure equatorial hetero-tetrakis-adducts or hetero-*Th*-hexakis-adducts are synthesized at will in one-pot synthesis for the first time. To upgrade this strategy into a catalytic regime, a synthetically useful biphasic protocol is designed to achieve selective and quantitative formation of exclusively tetrakis-adducts, by using anion metathesis and catalytic amounts of the nanocapsule. In comparison to recent examples of functionalization of C_{60} in bowl-shaped cavities limited to DA mono-adducts,[27] the supramolecular mask strategy reported here represents a dramatic extension of the regioselective approach. Indeed, this work provides a synthetically valuable path to produce unprecedented pure-isomer poly-functionalized C_{60}-based compounds, which are candidates for testing in solar cell devices and biomedical applications.

EXPERIMENTAL PROCEDURES

Full experimental procedures can be found in the Supplemental Information.

DATA AND CODE AVAILABILITY

The accession number for the crystal structure CIF reported in this paper is CCDC: 1913118.

SUPPLEMENTAL INFORMATION

Supplemental Information can be found online at https://doi.org/10.1016/j.chempr.2019.10.010.

A video abstract is available at https://doi.org/10.1016/j.chempr.2019.10.010#mmc5.

ACKNOWLEDGMENTS

This work was supported by grants from MINECO-Spain (CTQ2016-77989-P to X.R., RTI2018-095622-B-100 to D.M. and I.I., PGC2018-095808-B-I00 to T.P., and JdC contract IJCI-2017-33411 to M.G.-B.), Generalitat de Catalunya (2017SGR264 and a PhD grant to C.F.-E.), and the Severo Ochoa Center of Excellence Program (ICN2, grant SEV-2017-0706). X.R. and M.C. also thank ICREA-Acadèmia awards. M.P. thanks UdG for a PhD grant, and we thank QBIS-CAT research group and STR-UdG for technical support.

AUTHOR CONTRIBUTIONS

C.F.-E., C.G.-S., and M.P. performed all synthetic experiments and isolated all products. M.G.-B. performed all molecular dynamics simulations and computational modeling analyses. L.G. provided technical assistance on the HRMS studies. T.P. performed all NMR characterization analyses. J.J., I.I., and D.M. technically assisted, performed, and solved the XRD structure of $\mathbf{2}\subset\mathbf{1b}\cdot(\mathrm{BArF})_8$ at ALBA synchrotron. M.C. and X.R. wrote the manuscript. X.R. directed the project.

Please cite this article in press as: Fuertes-Espinosa et al., Supramolecular Fullerene Sponges as Catalytic Masks for Regioselective Functionalization of C_{60}, Chem (2019), https://doi.org/10.1016/j.chempr.2019.10.010

DECLARATION OF INTERESTS

The authors declare no competing interests.

Received: July 29, 2019
Revised: September 17, 2019
Accepted: October 13, 2019
Published: November 11, 2019

REFERENCES AND NOTES

1. Castro, E., Hernandez Garcia, A.H., Zavala, G., and Echegoyen, L. (2017). Fullerenes in biology and medicine. J. Mater. Chem. B *5*, 6523–6535.
2. Hirsch, A., and Vostrowsky, O. (2001). C60 Hexakisadducts with an octahedral addition pattern – A new structure motif in organic chemistry. Eur. J. Org. Chem. *2001*, 829–848.
3. Muñoz, A., Sigwalt, D., Illescas, B.M., Luczkowiak, J., Rodríguez-Pérez, L., Nierengarten, I., Holler, M., Remy, J.S., Buffet, K., Vincent, S.P., et al. (2016). Synthesis of giant globular multivalent glycofullerenes as potent inhibitors in a model of Ebola virus infection. Nat. Chem. *8*, 50–57.
4. Nierengarten, J.F. (2017). Fullerene hexa-adduct scaffolding for the construction of giant molecules. Chem. Commun. (Camb.) *53*, 11855–11868.
5. Krätschmer, W., Lamb, L.D., Fostiropoulos, K., and Huffman, D.R. (1990). Solid C60: a new form of carbon. Nature *347*, 354–358.
6. Zhang, F., Shi, W., Luo, J., Pellet, N., Yi, C., Li, X., Zhao, X., Dennis, T.J.S., Li, X., Wang, S., et al. (2017). Isomer-pure bis-PCBM-assisted crystal engineering of perovskite solar cells showing excellent efficiency and stability. Adv. Mater. *29*, 28240401.
7. Lenes, M., Wetzelaer, G.-J.A.H., Kooistra, F.B., Veenstra, S.C., Hummelen, J.C., and Blom, P.W.M. (2008). Fullerene bisadducts for enhanced open-circuit voltages and efficiencies in polymer solar cells. Adv. Mater. *20*, 2116–2119.
8. Castro, E., Murillo, J., Fernandez-Delgado, O., and Echegoyen, L. (2018). Progress in fullerene-based hybrid perovskite solar cells. J. Mater. Chem. C *6*, 2635–2651.
9. Friedl, J., Lebedeva, M.A., Porfyrakis, K., Stimming, U., and Chamberlain, T.W. (2018). All-fullerene-based cells for nonaqueous redox flow batteries. J. Am. Chem. Soc. *140*, 401–405.
10. Vidal, S. (2016). Glycofullerenes: sweet fullerenes vanquish viruses. Nat. Chem. *8*, 4–6.
11. Liu, G.F., Filipović, M., Ivanović-Burmazović, I., Beuerle, F., Witte, P., and Hirsch, A. (2008). High catalytic activity of dendritic C60 monoadducts in metal-free superoxide dismutation. Angew. Chem. Int. Ed. Engl. *47*, 3991–3994.
12. Umeyama, T., Igarashi, K., Sakamaki, D., Seki, S., and Imahori, H. (2018). Unique cohesive nature of the β1-isomer of [70]PCBM fullerene on structures and photovoltaic performances of bulk heterojunction films with PffBT4T-2OD polymers. Chem. Commun. *54*, 405–408.
13. Umeyama, T., Miyata, T., Jakowetz, A.C., Shibata, S., Kurotobi, K., Higashino, T., Koganezawa, T., Tsujimoto, M., Gélinas, S., Matsuda, W., et al. (2017). Regioisomer effects of [70]fullerene mono-adduct acceptors in bulk heterojunction polymer solar cells. Chem. Sci. *8*, 181–188.
14. Gatti, T., Menna, E., Meneghetti, M., Maggini, M., Petrozza, A., and Lamberti, F. (2017). The Renaissance of fullerenes with perovskite solar cells. Nano Energy *41*, 84–100.
15. Chiang, C.-H., Nazeeruddin, M.K., Grätzel, M., and Wu, C.-G. (2017). The synergistic effect of H2O and DMF towards stable and 20% efficiency inverted perovskite solar cells. Energy Environ. Sci. *10*, 808–817.
16. Umeyama, T., and Imahori, H. (2019). Isomer effects of fullerene derivatives on organic photovoltaics and perovskite solar cells. Acc. Chem. Res. *52*, 2046–2055.
17. Canevet, D., Pérez, E.M., and Martín, N. (2011). Wraparound hosts for fullerenes: tailored macrocycles and cages. Angew. Chem. Int. Ed. Engl. *50*, 9248–9259.
18. Yan, W., Seifermann, S.M., Pierrat, P., and Bräse, S. (2015). Synthesis of highly functionalized C60 fullerene derivatives and their applications in material and life sciences. Org. Biomol. Chem. *13*, 25–54.
19. Isaacs, L., Haldimann, R.F., and Diederich, F. (1994). Tether-directed remote functionalization of buckminsterfullerene: regiospecific Hexaadduct Formation. Angew. Chem. Int. Ed. Engl. *33*, 2339–2342.
20. Beuerle, F., Chronakis, N., and Hirsch, A. (2005). Regioselective synthesis and zone selective deprotection of [60]fullerene tris-adducts with an e,e,e addition pattern. Chem. Commun. (Camb.) *29*, 3676–3678.
21. Ioannou, C.P., and Chronakis, N. (2013). The first one-pot synthesis of a chiral pentakis-adduct of C60 utilising an opened-structure malonate tether. Chem. Commun. (Camb.) *49*, 10611–10613.
22. Isaacs, L., Diederich, F., and Haldimann, R.F. (1997). Multiple Adducts of C60 by tether-directed remote functionalization and synthesis of soluble derivatives of new carbon allotropes Cn(60+5). Helv. Chim. Acta *80*, 317–342.
23. Maxouti, K.L., and Hirsch, A. (2018). Sequential tether-directed synthesis of Pentakis-adducts of C60 with a mixed [3:2] octahedral addition pattern. Eur. J. Org. Chem. *2018*, 2579–2586.
24. Schwenninger, R., Müller, T., and Kräutler, B. (1997). Concise route to symmetric multiadducts of [60]fullerene: preparation of an equatorial tetraadduct by orthogonal transposition. J. Am. Chem. Soc. *119*, 9317–9318.
25. Castro, E., Azmani, K., Garcia, A.H., Aghabali, A., Liu, S., Metta-Magana, A.J., Olmstead, M.M., Rodríguez-Fortea, A., Poblet, J.M., and Echegoyen, L. (2017). Unusual C2h-symmetric trans-1-(bis-pyrrolidine)-tetra-malonate hexa-adducts of C60: the unexpected regio- and stereocontrol mediated by malonate–pyrrolidine interaction. Chemistry *23*, 15937–15944.
26. Brenner, W., Ronson, T.K., and Nitschke, J.R. (2017). Separation and selective formation of fullerene adducts within an MII8L6 cage. J. Am. Chem. Soc. *139*, 75–78.
27. Chen, B., Holstein, J.J., Horiuchi, S., Hiller, W.G., and Clever, G.H. (2019). Pd(II) coordination sphere engineering: pyridine cages, quinoline bowls, and heteroleptic pills binding one or two fullerenes. J. Am. Chem. Soc. *141*, 8907–8913.
28. Huang, N., Wang, K., Drake, H., Cai, P., Pang, J., Li, J., Che, S., Huang, L., Wang, Q., and Zhou, H.C. (2018). Tailor-made Pyrazolide-based metal–organic frameworks for selective catalysis. J. Am. Chem. Soc. *140*, 6383–6390.
29. Bottari, G., Trukhina, O., Kahnt, A., Frunzi, M., Murata, Y., Rodríguez-Fortea, A., Poblet, J.M., Guldi, D.M., and Torres, T. (2016). Regio-, stereo-, and atropselective synthesis of C60 fullerene bisadducts by supramolecular-directed functionalization. Angew. Chem. Int. Ed. Engl. *55*, 11020–11025.
30. Xu, Y., Kaur, R., Wang, B., Minameyer, M.B., Gsänger, S., Meyer, B., Drewello, T., Guldi, D.M., and von Delius, M. (2018). Concave–convex π–π template approach enables the synthesis of (10). J. Am. Chem. Soc. *140*, 13413–13420.
31. Rizzuto, F.J., von Krbek, L.K.S., and Nitschke, J.R. (2019). Strategies for binding multiple guests in metal–organic cages. Nat. Rev. Chem. *3*, 204–222.
32. García-Simón, C., Garcia-Borràs, M., Gómez, L., Parella, T., Osuna, S., Juanhuix, J., Imaz, I., Maspoch, D., Costas, M., and Ribas, X. (2014). Sponge-like molecular cage for purification of fullerenes. Nat. Commun. *5*, 5557.
33. Schick, G., Hirsch, A., Mauser, H., and Clark, T. (1996). Opening and closure of the fullerene cage in cis-bisimino adducts of C60: the

Please cite this article in press as: Fuertes-Espinosa et al., Supramolecular Fullerene Sponges as Catalytic Masks for Regioselective Functionalization of C_{60}, Chem (2019), https://doi.org/10.1016/j.chempr.2019.10.010

influence of the addition pattern and the addend. Chem. Eur. J. *2*, 935–943.

34. Hirsch, A., Lamparth, I., and Karfunkel, H.R. (1994). Fullerene chemistry in three dimensions: isolation of seven regioisomeric bisadducts and chiral trisadducts of C60 and di(ethoxycarbonyl)methylene. Angew. Chem. Int. Ed. Engl. *33*, 437–438.

35. Hirsch, A., and Brettreich, M. (2005). Fullerenes, Chemistry and Reactions. Nucleophilic Additions (Wiley-VCH), pp. 73–99.

36. Hawkins, J.M., Meyer, A., Lewis, T.A., Bunz, U., Nunlist, R., Ball, G.E., Ebbesen, T.W., and Tanigaki, K. (1992). Regiochemistry of the bisosmylation of fullerene C60: Ortho, meta, and para in three dimensions. J. Am. Chem. Soc. *114*, 7954–7955.

37. Djojo, F., Herzog, A., Lamparth, I., Hampel, F., and Hirsch, A. (1996). Regiochemistry of twofold additions to [6,6] bonds in C60: influence of the addend-independent cage distortion in 1,2-monoadducts. Chem. Eur. J *2*, 1537–1547.

38. Hirsch, A., and Brettreich, M. (2005). Fullerenes, Chemistry and Reactions (Wiley-VCH Verlag).

39. Djojo, F., Hirsch, A., and Grimme, S. (1999). The addition patterns of C60 trisadducts involving the positional relationships e and trans-n (n = 2–4): isolation, properties, and determination of the absolute configuration of tris(malonates) and tris[bis(oxazolines)]. Eur. J. Org. Chem. *1999*, 3027–3039.

Chapter IV.

A Copper-based Supramolecular Nanocapsule that Enables Straightforward Purification of Sc_3N-based Endohedral Metallofullerene Soots

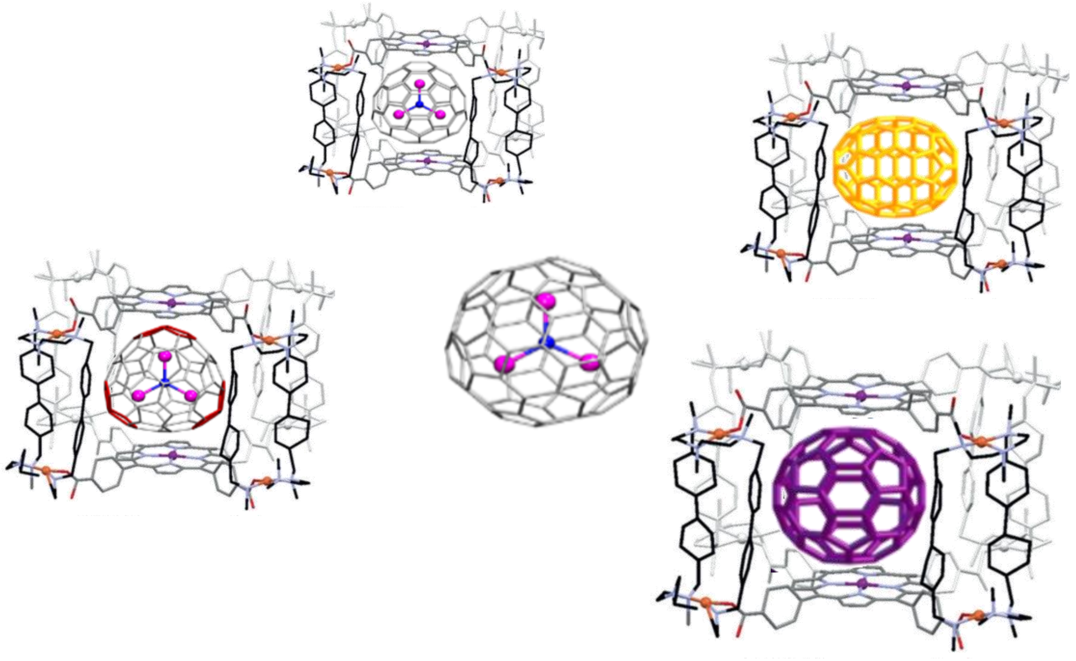

This chapter corresponds to the following publication:

Fuertes-Espinosa, C.; García-Simón, C.; Catro, E.;Costas, M.; Echegoyen, L. and Ribas, X. *Chemistry - A European Journal*, **2017**, 15, 3553–3557.

Reprinted with permission from Wiley editorial.

ChemPubSoc Europe

DOI: 10.1002/chem.201700046

CHEMISTRY
A European Journal
Communication

Supramolecular Chemistry

A Copper-based Supramolecular Nanocapsule that Enables Straightforward Purification of Sc_3N-based Endohedral Metallofullerene Soots

Carles Fuertes-Espinosa,[a] Cristina García-Simón,[a] Edison Castro,[b] Miquel Costas,*[a]
Luis Echegoyen,*[b] and Xavi Ribas*[a]

Abstract: A self-assembled Cu^{II}-based nanocapsule enables efficient and straightforward isolation of $Sc_3N@C_{80}$ from arc-processed raw soot. The newly designed Cu^{II}-based supramolecular nanocapsule **5**·$(OTf)_8$ was used to effectively entrap fullerenes and endohedral metallofullerenes (EMFs) with different affinities depending on their size and shape. Moreover, we took advantage of the sharply different entrapment abilities of the **5**·$(OTf)_8$ cage in the solid state versus in solution to encapsulate all the species with the exception of $Sc_3N@C_{80}$ (both I_h and D_{5h} isomers), which remains pure in solution. HPLC quantification determined that up to 85 % of the total $Sc_3N@C_{80}$ content in the initial mixture was recovered in very high purity (> 99.5 %). The complete release of the encapsulated species with an orthogonal solvent-washing strategy regenerates **5**·$(OTf)_8$ ready to be re-used. This approach opens new opportunities for EMFs purification.

EMFs are intriguing fullerene-based nanomaterials due to their unique electronic properties.[1,2] The small band gap of endohedral metallofullerenes (EMFs) (compared to those of empty fullerenes) places them as promising candidates for solar cells. Shielding of the entrapped metals or molecules by the fullerene cage confers high stability and low toxicity to EMFs, and are excellent materials for electronic and biomedical applications, such as in diagnostic radiology.[3] However, applications of EMFs have not been fully exploited mainly because of the very high cost of these materials, due to extensive and time-consuming HPLC procedures required for their purification.[2,4] The large variety of species present in soot mixtures and their low solubility further complicates the purification of EMFs by standard HPLC.[4] Several alternative non-chromatographic methods have been developed to purify EMF crude soots,[4] most of them mainly based on the different chemical behavior of EMFs in comparison with empty fullerenes. Those include 2-aminoethanol extraction,[5] the specific reactivity of EMFs with Lewis acids,[6] functionalized silica[7] or resins[8] or the combination of both strategies by successive precipitation of EMFs with Lewis acids, followed by treatment with amino-functionalized silica gel (SAFA, stir and filter approach).[9] In addition, the different redox properties between EMFs belonging to the same family and their selective exohedral functionalization can also be exploited to facilitate their separation.[10]

Alternatively, the use of polyaromatic molecular receptors to incarcerate EMFs has also been investigated by different groups. In 2011, Ballester's and Echegoyen's groups reported the encapsulation of $Sc_3N@C_{80}$ in a receptor based on two cyclic β-pyrrole unsubstituted *meso*-tetraphenylbisporphyrins.[11] Chiu's group synthesized a cyclotriveratrylene-based hemicarceplexe capsule, able to host $Sc_3N@C_{80}$ within its inner cavity.[12] Shinohara's group developed a size-selective host–guest complexation with cycloparaphenylene (CPP) to render mixtures enriched in $Gd@C_{82}$ from crude soot.[13] However, to our knowledge, selective purification of EMFs from crude soots mediated by coordination nanocapsules have not been described yet.

In this context, in 2014 some of us reported the synthesis of a Pd^{II}-based tetragonal prismatic supramolecular nanocapsule (**4**·$(BArF)_8$, Figure 1 a) capable of entrapping fullerenes (from C_{60} to C_{84}) and to release them in a selective manner, offering a promising platform for their purification.[14] Herein, we describe a novel Cu^{II}-based tetragonal prismatic nanocapsule **5**·$(OTf)_8$ (Figure 1 a) that enables isolation of highly pure (> 99.5 %) $Sc_3N@C_{80}$ from crude soot by selective host–guest complexation. The new nanocapsule shows enhanced encapsulation/release properties in comparison with **4**·$(BArF)_8$, and its preparation is simpler. The inherently more labile nature of Cu^{II}-carboxylate coordination bonds in **5**·$(OTf)_8$ compared to Pd^{II} in **4**·$(BArF)_8$ are thought to be the reason for its enhanced performance, allowing easier access/release of the guests.

Nanocapsule **5**·$(OTf)_8$ was synthesized by self-assembly of a tetracarboxylate Zn^{II}-porphyrin and a Cu^{II}-based molecular clip [**Cu-1 b**]$(OTf)_4$ (Figure 1 a). The [**Cu-1 b**]$(OTf)_4$ molecular clip

---

[a] C. Fuertes-Espinosa, Dr. C. García-Simón, Dr. M. Costas, Dr. X. Ribas
Institut de Química Computatcional i Catàlisi (IQCC) and Departament de Química
Universitat de Girona, Campus Montilivi, 17003
Girona, Catalonia (Spain)
E-mail: miquel.costas@udg.edu
xavi.ribas@udg.edu

[b] E. Castro, L. Echegoyen
Department of Chemistry
University of Texas at El Paso, 500 West University Avenue
El Paso, Texas 79968 (USA)
E-mail: echegoyen@utep.edu

Supporting information and the ORCID identification number(s) for the author(s) of this article can be found under http://dx.doi.org/10.1002/chem.201700046.

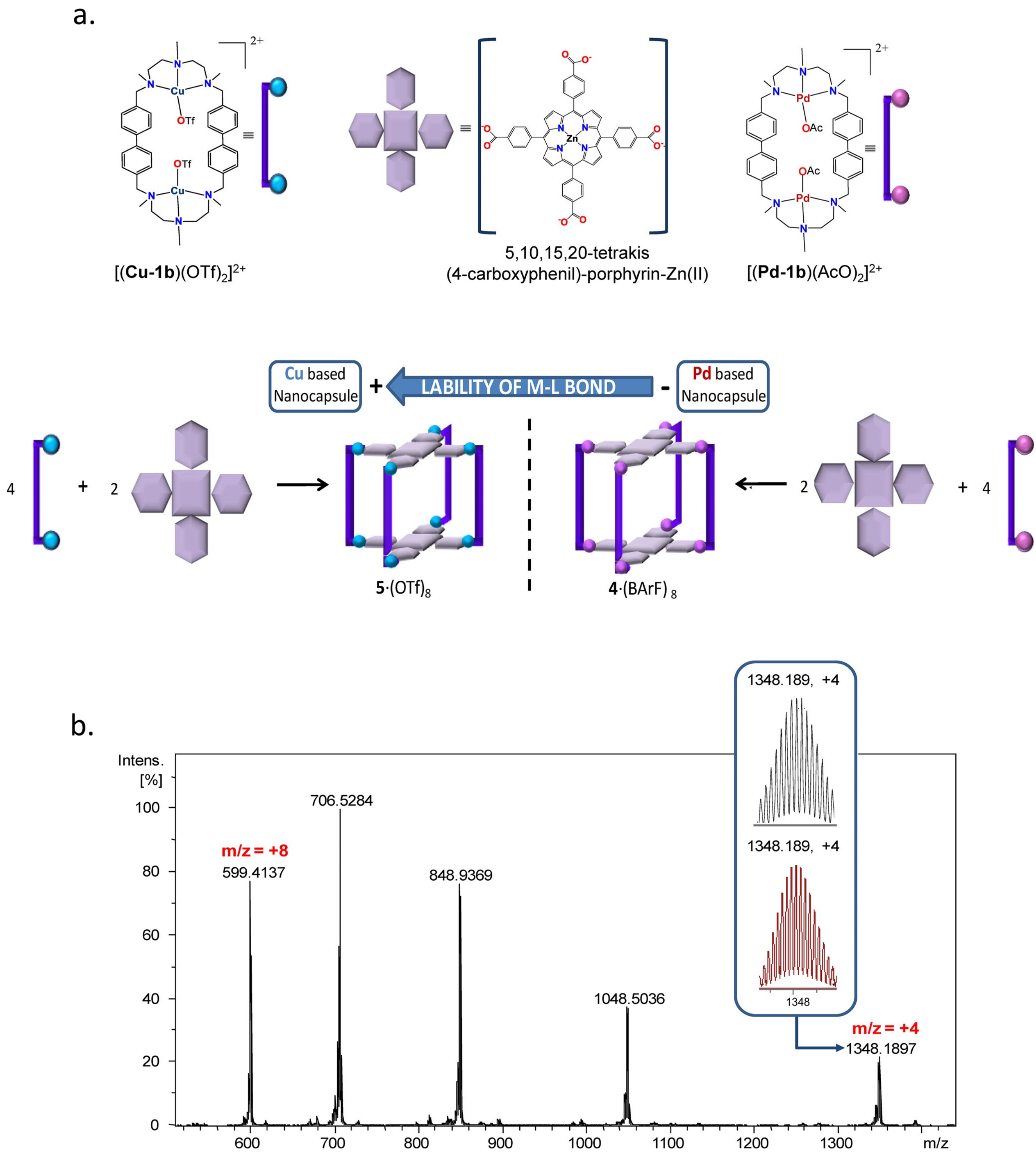

Figure 1. a) Schematic representation of the building blocks (top) used for the self-assembly of molecular clips [**Cu-1 b**]·(OTf)$_4$ or [**Pd-1 b**]·(AcO)$_2$ and tetracarboxylated Zn^{II}-porphyrin to form the supramolecular nanocapsules **5**·(OTf)$_8$ (bottom left) or **4**·(BArF)$_8$ (bottom right). b) HRMS spectrum of **5**·(OTf)$_8$ (simulated spectrum of selected peaks is shown in red).

was synthesized analogously to the previously reported Pd clip,[14] and characterized by high resolution mass spectrometry (HRMS), ultraviolet-visible spectroscopy (UV/Vis), infrared spectroscopy (FT-IR) (Supporting Information Figures S1–S3) and combustion analysis. Nanocapsule **5**·(OTf)$_8$ shows better solubility in acetonitrile than its Pd analogue **4**·(OTf)$_8$; therefore, counteranion exchange with BArF is not required to enhance its solubility in acetonitrile (Figure 1 a).[14] The HRMS (Figure 1 b) and the UV/Vis spectrum (Supporting Information Figure S4) strongly suggest that nanocapsule 5·(OTf)$_8$ retains its integrity in solution. 5·(OTf)$_8$ was also characterized by FT-IR (Supporting Information Figure S5).

We first explored the ability of $\mathbf{5}\cdot(\mathrm{OTf})_8$ to act as a host for the encapsulation/release of fullerenes. Immediate inclusion of C_{60} occurred after mixing an acetonitrile solution of $\mathbf{5}\cdot(\mathrm{OTf})_8$ with a toluene solution of C_{60}, in a 1:1 molar ratio. UV/Vis titration experiments indicated the formation of a 1:1 adduct $C_{60}\subset\mathbf{5}\cdot(\mathrm{OTf})_8$ ($K_a=3.53(\pm0.4)\times10^6\,\mathrm{M}^{-1}$, Supporting Information Figure S6). In addition, HRMS analysis showed exclusively the peaks corresponding to the $C_{60}\subset\mathbf{5}\cdot(\mathrm{OTf})_8$ complex (Figure 2 a).

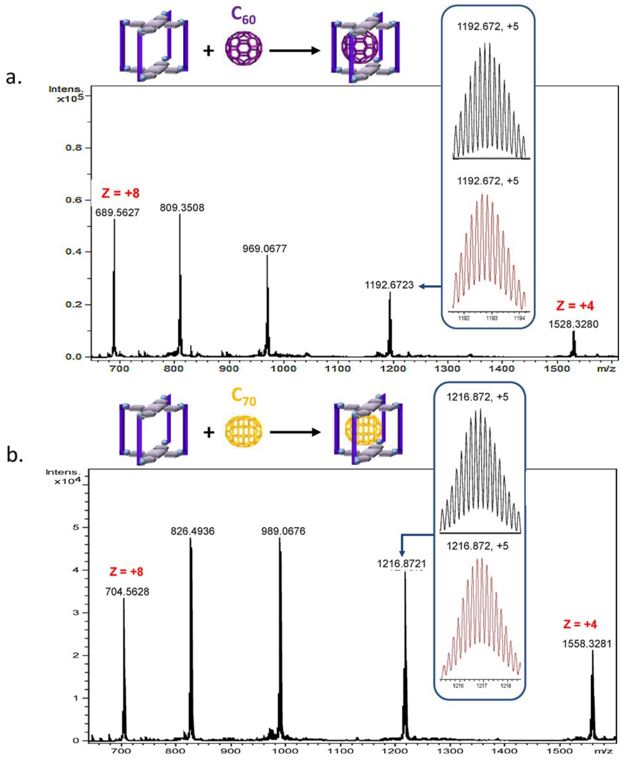

Figure 2. a) HRMS spectrum of $C_{60}\subset\mathbf{5}\cdot(\mathrm{OTf})_8$ host–guest adduct generated in solution (9:1, toluene/acetonitrile). Simulated spectrum of selected peaks is shown in red. b) HRMS spectrum of $C_{70}\subset\mathbf{5}\cdot(\mathrm{OTf})_8$ host–guest adduct generated in solution (9:1, toluene/acetonitrile). Simulated spectrum of selected peaks is shown in red.

Analogously, the $C_{70}\subset\mathbf{5}\cdot(\mathrm{OTf})_8$ complex was instantaneously formed upon mixing $\mathbf{5}\cdot(\mathrm{OTf})_8$ with C_{70} ($K_a=1.76(\pm0.7)\times10^7\,\mathrm{M}^{-1}$, see Figures S7 (Supporting Information) and Figure 2 b). The inclusion of higher fullerenes was also observed by HRMS by using fullerene extract (C_{60} 70%, C_{70} 28%, higher fullerenes 2%) (Supporting Information Figure S8a).

Subsequently, the release of the entrapped fullerenes was attempted. As previously reported, by applying a solvent washing protocol, which exploits the orthogonal solubility of the nanocapsule and fullerenes, the latter can be easily recovered.[14] Gratifyingly, the complete release of C_{60} and C_{70} from $\mathbf{5}\cdot(\mathrm{OTf})_8$ was successfully achieved using this methodology, fully recovering $\mathbf{5}\cdot(\mathrm{OTf})_8$ after the process (confirmed by HRMS) (Figure 3 and Supporting Information Figure S9). The latter is remarkable because C_{70} could not be released from $\mathbf{4}\cdot(\mathrm{BArF})_8$.[14] Presumably, the lability of metal-coordination bonds (Cu-carboxylate) endows $\mathbf{5}\cdot(\mathrm{OTf})_8$ with some degree of structural flexibility in regard to the intramolecular porphyrin–porphyrin distance ("breathing ability") that enables the remarkable fast binding and release of the fullerenes.

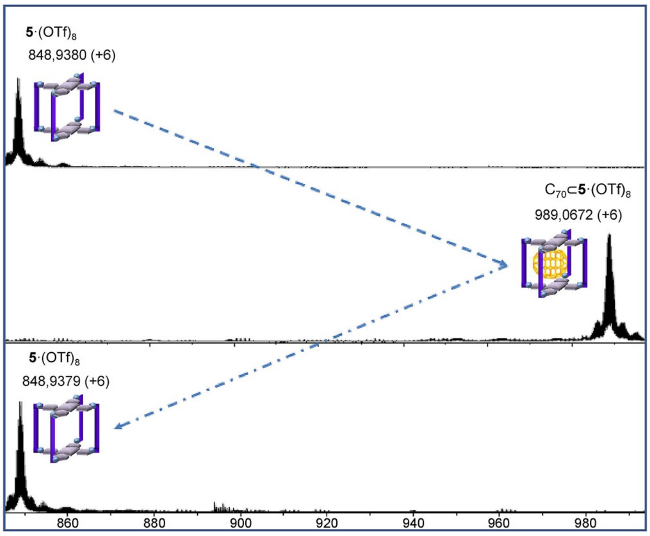

Figure 3. Solid-state extraction of fullerene C_{70} from $\mathbf{5}\cdot(\mathrm{OTf})_8$. HRMS monitoring of the C_{70} extraction-washing protocol using pure C_{70} in $\mathbf{5}\cdot(\mathrm{OTf})_8$ in solid phase.

The ability of $\mathbf{5}\cdot(\mathrm{OTf})_8$ to bind EMFs from EMF-based soots was explored. The species present in a Sc_3N-based soot were first determined by HPLC (Supporting Information Figure S10). A toluene solution of the soot was then mixed with a solution of $\mathbf{5}\cdot(\mathrm{OTf})_8$ in acetonitrile (1:1 molar ratio, assuming that all the species are $Sc_3N@C_{80}$, final mixture 9:1 toluene/acetonitrile). The HRMS of the inclusion compounds exhibited the ion peaks corresponding to $C_{60}\subset\mathbf{5}\cdot(\mathrm{OTf})_8$, $C_{70}\subset\mathbf{5}\cdot(\mathrm{OTf})_8$, $Sc_3N@C_{68}\subset\mathbf{5}\cdot(\mathrm{OTf})_8$, $Sc_3N@C_{78}\subset\mathbf{5}\cdot(\mathrm{OTf})_8$ and $Sc_3N@C_{80}\subset\mathbf{5}\cdot(\mathrm{OTf})_8$ (major peak) (Supporting Information Figure S11). In parallel, UV/Vis titration experiments of $\mathbf{5}\cdot(\mathrm{OTf})_8$ with $Sc_3N@(I_h)\text{-}C_{80}$ in toluene/acetonitrile (9:1) demonstrated the formation of a 1:1 host–guest adduct, $Sc_3N@C_{80}\subset\mathbf{5}\cdot(\mathrm{OTf})_8$, with a high association constant of $K_a=2.02(\pm0.6)\times10^7\,\mathrm{M}^{-1}$ (Supporting Information Figure S12). Remarkably, all the entrapped species can be completely released by applying our previously reported solvent washing protocol (Supporting Information Figure S13).

The versatility of the cage was further exploited by soaking a solid sample of $\mathbf{5}\cdot(\mathrm{OTf})_8$ in a toluene solution of fullerene extract (10:1 fullerene extract/$\mathbf{5}\cdot(\mathrm{OTf})_8$ molar ratio, assuming that all the fullerenes are C_{60}). The HRMS of the solid (isolated and dissolved in acetonitrile) showed $C_{60}\subset\mathbf{5}\cdot(\mathrm{OTf})_8$ and $C_{70}\subset\mathbf{5}\cdot(\mathrm{OTf})_8$ as the unique signals (with preference for C_{60} in a 4:1 ratio, Supporting Information Figure S8b). On the other hand, in the encapsulation performed in solution the ion peak corresponding to $C_{70}\subset\mathbf{5}\cdot(\mathrm{OTf})_8$ was detected as the main species by HRMS (Supporting Information Figure S8a). These results showed that $\mathbf{5}\cdot(\mathrm{OTf})_8$ preferentially encapsulated the smaller fullerenes in the solid state, in contrast to the results obtained in solution (K_a for $C_{70}>K_a$ for C_{60}, see above). This different selectivity behavior exhibited by the nanocapsule in solution or in solid phase might be rationalized by a higher structural rigidity of the capsule in the solid state, making its internal cavity more restricted and selective for smaller fullerenes. In contrast, when the nanocapsule is used in solution, the flexibility of its structure increases, making its internal cavity more accessible for larger fullerenes.

Based on these observations and aiming at circumventing a tedious work-up that must result from the similar K_a of the different species in solution, we hypothesized that the Sc_3N-based EMF soot could be purified by encapsulating smaller species using **5**·(OTf)$_8$ in the solid state. To evaluate this hypothesis, two parallel experiments were performed. First, sub-stoichiometric amounts of solid **5**·(OTf)$_8$ were mixed with a toluene solution of Sc_3N-based soot (Figure 4). As expected, preferential encapsulation of the smaller species was observed compared to the experiment with the nanocapsule in solution. With these results in hand, an excess of solid **5**·(OTf)$_8$ was added to a toluene solution of Sc_3N-based soot (6:1 **5**·(OTf)$_8$/soot molar ratio, assuming that all the species are $Sc_3N@C_{80}$). The supernatant was increasingly enriched in $Sc_3N@C_{80}$ over time, being the unique species in solution at the end of the experiment. The encapsulation process was monitored by HPLC analysis of the supernatant (Figure 5). At the end of the experiment (after 5 h stirring), we observed that the species remaining in the supernatant corresponded uniquely to $Sc_3N@C_{80}$ (also analyzed by MALDI, Supporting Information Figure S14).

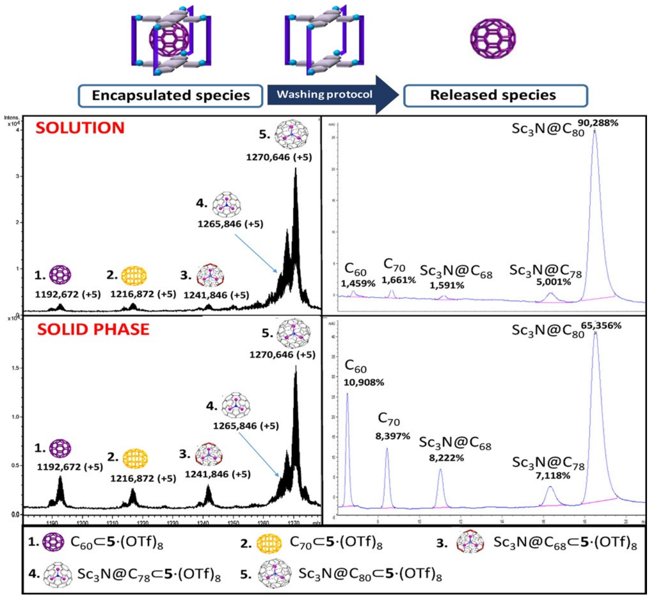

Figure 4. HRMS spectrum of Sc-based crude soot⊂**5**·(OTf)$_8$ host–guest complex generated (top left) in solution (9:1, toluene/acetonitrile) and (bottom left) in solid phase of **5**·(OTf)$_8$. HPLC chromatogram of the species released through our solvent-washing protocol from the Sc-based crude soot⊂**5**·(OTf)$_8$ host–guest complex generated in solution (top right) and in the solid phase (bottom right). The molar ratio soot:**5**·(OTf)$_8$ was 4:1, assuming that all the species are $Sc_3N@C_{80}$. The drawing of EMFs are reprinted with permission from reference [4]; Copyright (2013) American Chemical Society.

Strikingly, fractions of $Sc_3N@C_{80}$ with up to 99.5% purity were obtained in a single and operationally simple step. On the other hand, HPLC analysis of the purified fraction determined that the ratio between the two isomers of $Sc_3N@C_{80}$ (I_h and D_{5h}) remains essentially unaltered, indicating that the nanocapsule **5**·(OTf)$_8$ does not discriminate between the isomeric $Sc_3N@C_{80}$ cages (Figure 6). The quantification by HPLC of the purified fraction determined that approximately 60% of $Sc_3N@C_{80}$ contained in the initial soot was recovered. The species encapsulated in **5**·(OTf)$_8$ were completely released by a solvent-washing procedure and empty **5**·(OTf)$_8$ was ready to be re-used (see Supporting Information Figure S15).

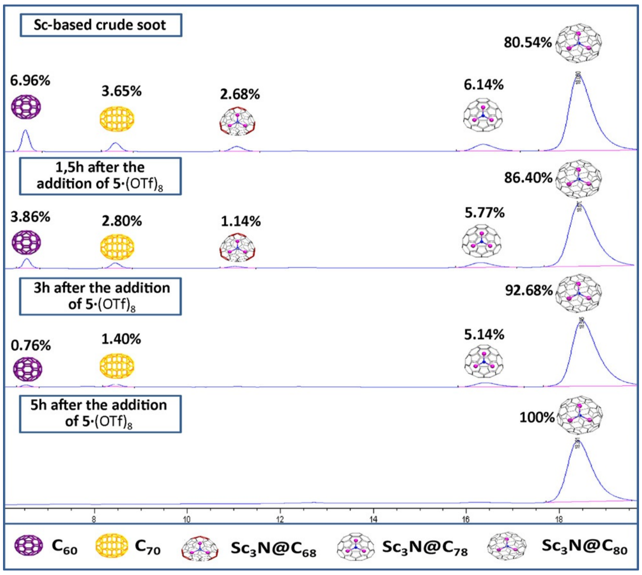

Figure 5. Sc_3N-based soot purification protocol using **5**·(OTf)$_8$ in the solid phase, by HPLC monitoring of the remaining supernatant.

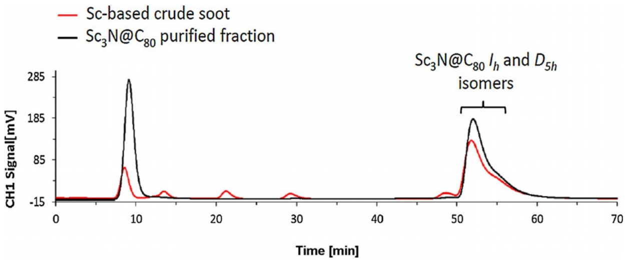

Figure 6. HPLC chromatograms of Sc-based crude soot and $Sc_3N@C_{80}$ purified fraction, from which I_h and D_{5h} isomers cannot be separated. Experimental conditions: 1.8×10^{-4} M in toluene, approximate concentration assuming that all the species are $Sc_3N@C_{80}$; HPLC separation using a 5-PBB column (ϕ=4.6 ID×250 mm); flow: 1.2 mL min^{-1}.

To further explore this different selectivity, an excess of solid nanocapsule was added to an equimolar mixture of C_{60}, C_{70} and $Sc_3N@C_{80}$ (I_h–D_{5h} mixture) in toluene (6:1:1:1 **5**·(OTf)$_8$/C_{60}/C_{70}/$Sc_3N@C_{80}$ molar ratio). The encapsulation process was monitored by HPLC analysis, clearly showing selective uptake of C_{60} and C_{70}, leaving the $Sc_3N@C_{80}$ (I_h–D_{5h} mixture) in solution after 11 hours in a single step (Figure 7). The mass recovery of $Sc_3N@C_{80}$ was 85% as determined by HPLC quantification.

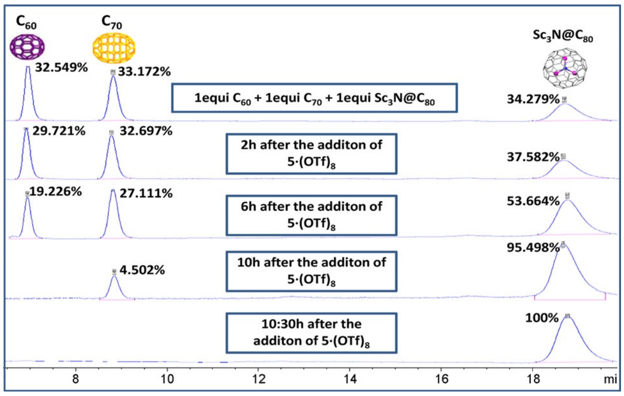

Figure 7. Purification process of an equimolar mixture of C_{60}, C_{70} and $Sc_3N@C_{80}$ (I_h–D_{5h} mixture) using **5**·(OTf)$_8$ in the solid phase (1:6 C_{60}:**5**·(OTf)$_8$, molar ratio) by HPLC monitoring of the remaining supernatant.

In summary, a Cu^{II}-based supramolecular nanocapsule **5**·(OTf)$_8$ has been prepared and enables efficient and simple purification of $Sc_3N@C_{80}$ contained in a Sc_3N-based fullerene soot. Simply by soaking a solid sample of the Cu^{II}-based supramolecular nanocapsule **5**·(OTf)$_8$ in a toluene solution of Sc_3N-based EMF soot, only $Sc_3N@C_{80}$ (I_h–D_{5h} mixture, >99.5%) is obtained in a single step. Furthermore, up to 85% recovery of the total amount of $Sc_3N@C_{80}$ from the initial mixture was attained. The species encapsulated during the process can be released and the nanocapsule can be easily recovered and directly re-used. To the best of our knowledge, this is the first EMF soot purification protocol mediated by a coordination nanocapsule. Further development of supramolecular versatile platforms for EMFs soot purification is currently being pursued in our laboratories,[15] and the exploitation of the distinctive encapsulation of the nanocapsules in the solid state is thought to offer new opportunities in fullerene and EMF purification.

Acknowledgements

We acknowledge financial support from MINECO-Spain for project CTQ2013-43012-P to X.R., CTQ2013-50306-EXP to M.C., and 2014 SGR 862 to M.C. L.E. thanks the US National Science Foundation (NSF) for generous support of this work under the NSF-PREM program (DMR-1205302) and CHE-1408865. The Robert A. Welch Foundation is also gratefully acknowledged for an endowed chair to LE (Grant AH-0033). X.R. and M.C. are also grateful for ICREA-Acadèmia awards.

Conflict of interest

The authors declare no conflict of interest.

Keywords: copper · fullerenes · scandium nitride · soot purification · supramolecular nanocapsules

[1] J. R. Heath, S. C. O'Brien, Q. Zhang, Y. Liu, R. F. Curl, F. K. Tittel, R. E. Smalley, *J. Am. Chem. Soc.* **1985**, *107*, 7779–7780.
[2] M. N. Chaur, F. Melin, A. L. Ortiz, L. Echegoyen, *Angew. Chem. Int. Ed.* **2009**, *48*, 7514–7538; *Angew. Chem.* **2009**, *121*, 7650–7675.
[3] a) R. B. Ross, C. M. Cardona, D. M. Guldi, S. G. Sankaranarayanan, M. O. Reese, N. Kopidakis, J. Peet, B. Walker, G. C. Bazan, E. Van Keuren, B. C. Holloway, M. Drees, *Nat. Mater.* **2009**, *8*, 208–212; b) A. Svitova, K. Braun, A. A. Popov, L. Dunsch, *Chem. Open* **2012**, *1*, 207–210.
[4] A. A. Popov, S. Yang, L. Dunsch, *Chem. Rev.* **2013**, *113*, 5989–6113.
[5] E. A. Sarina, B. Q. Mercado, J. U. Franco, C. J. Thompson, M. L. Easterling, M. M. Olmstead, A. L. Balch, *Chem. Eur. J.* **2015**, *21*, 17035–17043.
[6] a) S. Stevenson, M. A. Mackey, J. E. Pickens, M. A. Stuart, B. S. Confait, J. P. Phillips, *Inorg. Chem.* **2009**, *48*, 11685–11690; b) K. Akiyama, T. Hamano, Y. Nakanishi, E. Takeuchi, S. Noda, Z. Wang, S. Kubuki, H. Shinohara, *J. Am. Chem. Soc.* **2012**, *134*, 9762–9767.
[7] S. Stevenson, K. Harich, H. Yu, R. R. Stephen, D. Heaps, C. Coumbe, J. P. Phillips, *J. Am. Chem. Soc.* **2006**, *128*, 8829–8835.
[8] Z. Ge, J. C. Duchamp, T. Cai, H. W. Gibson, H. C. Dorn, *J. Am. Chem. Soc.* **2005**, *127*, 16292–16298.
[9] S. Stevenson, K. D. Arvola, M. Fahim, B. R. Martin, K. B. Ghiassi, M. M. Olmstead, A. L. Balch, *Inorg. Chem.* **2016**, *55*, 62–67.
[10] a) B. Elliott, L. Yu, L. Echegoyen, *J. Am. Chem. Soc.* **2005**, *127*, 10885–10888; b) M. R. Cerón, M. Izquierdo, N. Alegret, J. A. Valdez, A. Rodriguez-Fortea, M. M. Olmstead, A. L. Balch, J. M. Poblet, L. Echegoyen, *Chem. Commun.* **2016**, *52*, 64–67.
[11] L. P. Hernández-Eguía, E. C. Escudero-Adán, J. R. Pinzón, L. Echegoyen, P. Ballester, *J. Org. Chem.* **2011**, *76*, 3258–3265.
[12] M.-Y. Ku, S.-J. Huang, S.-L. Huang, Y.-H. Liu, C.-C. Lai, S.-M. Peng, S.-H. Chiu, *Chem. Commun.* **2014**, *50*, 11709–11712.
[13] Y. Nakanishi, H. Omachi, S. Matsuura, Y. Miyata, R. Kitaura, Y. Segawa, K. Itami, H. Shinohara, *Angew. Chem. Int. Ed.* **2014**, *53*, 3102–3106; *Angew. Chem.* **2014**, *126*, 3166–3170.
[14] C. García-Simón, M. Garcia-Borràs, L. Gómez, T. Parella, S. Osuna, J. Juanhuix, I. Imaz, D. Maspoch, M. Costas, X. Ribas, *Nat. Commun.* **2014**, *5*, 5557.
[15] Longer reaction experiments (from 5 h to 4 days) using substoichiometric amounts of solid **5**·(OTf)$_8$ (4:1 Sc_3N-based soot/**5**·(OTf)$_8$ molar ratio, assuming that all the species are $Sc_3N@C_{80}$) showed a preferential encapsulation of $Sc_3N@C_{68}$ and $Sc_3N@C_{78}$ (Supporting Information Figure S16). Additional experiments will be performed in order to further explore and understand the selectivity of the **5**·(OTf)$_8$ nanocapsule toward these EMFs.

Manuscript received: January 4, 2017
Accepted Article published: January 30, 2017
Final Article published: February 20, 2017

Chapter V.

Purification of Uranium-based Endohedral Metallofullerenes (EMFs) by Selective Supramolecular Encapsulation and Release

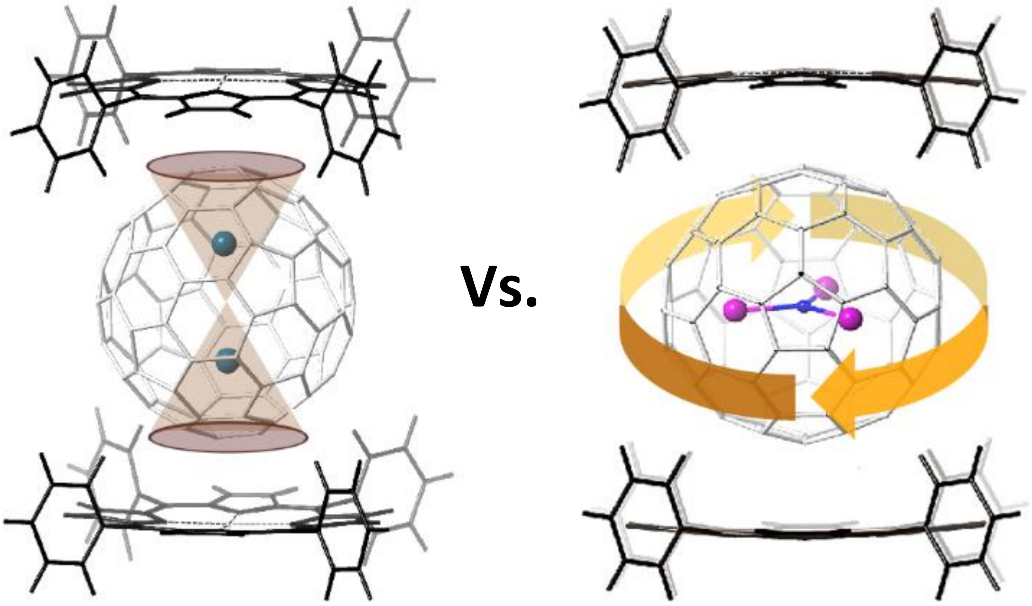

This chapter corresponds to the following publication:

Fuertes-Espinosa, C.; Gómez-Torres, A.; MoralesMartínez, R.; Rodríguez-Fortea, A.; García-Simón, C.; Gándara, F.; Imaz, I.; Juanhuix, J.; Maspoch, D.; Poblet, J.M.; Echegoyen, L. and Ribas, X. *Angew. Chem., Int. Ed.,* **2018**, 57, 11294–11299.

Reprinted with permission from Wiley editorial

Metallofullerenes

International Edition: DOI: 10.1002/anie.201806140
German Edition: DOI: 10.1002/ange.201806140

Purification of Uranium-based Endohedral Metallofullerenes (EMFs) by Selective Supramolecular Encapsulation and Release

Carles Fuertes-Espinosa, Alejandra Gómez-Torres, Roser Morales-Martínez, Antonio Rodríguez-Fortea, Cristina García-Simón, Felipe Gándara, Inhar Imaz, Judith Juanhuix, Daniel Maspoch, Josep M. Poblet, Luis Echegoyen, and Xavi Ribas**

Abstract: *Supramolecular nanocapsule* $\mathbf{1}\cdot(BArF)_8$ *is able to sequentially and selectively entrap recently discovered* $U_2@C_{80}$ *and unprecedented* $Sc_2CU@C_{80}$*, simply by soaking crystals of* $\mathbf{1}\cdot(BArF)_8$ *in a toluene solution of arc-produced soot. These species, selectively and stepwise absorbed by* $\mathbf{1}\cdot(BArF)_8$*, are easily released, obtaining highly pure fractions of* $U_2@C_{80}$ *and* $Sc_2CU@C_{80}$ *in one step.* $Sc_2CU@C_{80}$ *represents the first example of a mixed metal actinide-based endohedral metallofullerene (EMF). Remarkably, the host–guest studies revealed that* $\mathbf{1}\cdot(BArF)_8$ *is able to discriminate EMFs with the same carbon cage but with different encapsulated cluster and computational studies provide support for these observations.*

The development of novel compounds with unprecedented properties and new potential applications, together with the ability to accommodate unstable metal clusters into their carbon cages, are the main motivations boosting the progress of endohedral metallofullerene (EMF) science.[1] Endohedral metallofullerene science is mainly focused on lanthanide-based compounds, whereas actinide endohedral metallofullerenes remain poorly explored.[1a,2] In 1992, Smalley detected spectrometrically a series of uranium-based endohedral metallofullerenes, such as $U@C_{2n}$ ($2n=28$–72) and $U_2@C_{2n}$ ($2n=50$–60) for the first time.[3] However, it was not until 2017 that the successful synthesis and complete structural characterization of monometallic actinide endohedral metallofullerenes were reported ($Th@C_{3v}(8)$-C_{82}, $U@D_{3h}$-C_{74}, $U@C_2(5)$-C_{82} and $U@C_{2v}(9)$-C_{82}),[4] and very recently Chen and Echegoyen reported the first dimetallic $U_2@I_h(7)$-C_{80}.[5] However, no examples of mixed-metal cluster fullerenes (MMCFs) based on actinides have been reported to date.[1a]

Generally, the study of novel endohedral metallofullerenes is hampered by their limited availability. High performance liquid chromatography (HPLC) is by far the most powerful and used technique for the isolation of endohedral metallofullerenes.[1a,6] Nevertheless, the low production efficiency of these compounds by arc-discharge methods limits their purification by chromatography, resulting in time-consuming and expensive procedures. Commonly, these drawbacks are even more pronounced for the purification of mixed-metal cluster fullerenes crude soot,[1a] because they contain mixtures of species with the same size and isomeric carbon cages (only differentiated by the internal cluster). Moreover, their low abundance in soot extracts dramatically hinders the purification of these materials by HPLC, even when running in multi-step or recycling modes.

To circumvent the limitations of HPLC purification, some chemical and electrochemical separation methods have been developed for the isolation of endohedral metallofullerenes.[1a,7] To date, the only non-chromatographic strategy attainable for the purification of mixed-metal cluster fullerenes was reported by Stevenson et al.,[8] and it was successfully applied in the separation of $CeLu_2N@C_{80}$ by combining two chemical methods of purification: successive precipitation of endohedral metallofullerenes with a Lewis acid, followed by a stir and filter approach (SAFA). Still, several steps and long reaction times are required. On the

---

[*] C. Fuertes-Espinosa, Dr. C. García-Simón, Dr. X. Ribas
QBIS-CAT group, IQCC and Dept. Química
Universitat de Girona
Campus de Montilivi, 17003 Girona, Catalonia (Spain)
E-mail: xavi.ribas@udg.edu

A. Gómez-Torres, Prof. L. Echegoyen
Department of Chemistry
University of Texas at El Paso
500 West University Avenue, El Paso, TX 79968 (USA)
E-mail: echegoyen@utep.edu

R. Morales-Martínez, Dr. A. Rodríguez-Fortea, Prof. J. M. Poblet
Departament de Química Física i Inorgánica, Universitat Rovira i Virgili
C/Marcel·lí Domingo 1, 43007 Tarragona, Catalonia (Spain)

Dr. F. Gándara
Materials Science Factory, Instituto de Ciencia de Materiales de Madrid (ICMM), Consejo Superior de Investigaciones Científicas (CSIC)
Calle Sor Juana Inés de la Cruz, 3, 28049 Madrid (Spain)

Dr. I. Imaz, Prof. D. Maspoch
Catalan Institute of Nanoscience and Nanotechnology (ICN2), CSIC and BIST
Campus UAB, Bellaterra, 08193 Barcelona, Catalonia (Spain)

Dr. J. Juanhuix
ALBA Synchrotron
Carrer de la llum 2–26, 08290 Cerdanyola del Vallès, Barcelona, Catalonia (Spain)

Prof. D. Maspoch
ICREA
Pg. Lluís Companys 23, 08010 Barcelona, Catalonia (Spain)

Supporting information and the ORCID identification number(s) for the author(s) of this article can be found under: https://doi.org/10.1002/anie.201806140. A data set collection of computational results is available in the ioChem-BD repository and can be accessed via https://doi.org/10.19061/iochem-bd-2-26.

other hand, encapsulation of endohedral metallofullerenes using self-assembled supramolecular nanocapsules is emerging as a topic of great interest.[9] The design of supramolecular platforms for selective host-guest complexation of endohedral metallofullerenes is a potential alternative to HPLC. Recently, our group reported the first example of a supramolecular nanocapsule that allowed the efficient and simple purification of $Sc_3N@C_{80}$ by selective host-guest complexation.[10]

Herein we report the straightforward selective purification of dimetallic and mixed metallic U-based endohedral metallofullerenes from a crude soot by host–guest encapsulation in a Cu^{II}-based tetragonal prismatic nanocapsule **1**·$(BArF)_8$.[10] The sequential selective encapsulation of the desired endohedral metallofullerenes enables isolation of $U_2@I_h$-C_{80} and $Sc_2CU@I_h$-C_{80} from arc-produced soot in sequential single steps. Host-guest studies revealed that nanocapsule **1**·$(BArF)_8$ is sensitive to the content inside the fullerene cage, being able to distinguish between endohedral metallofullerenes with the same carbon cage but different internal clusters.

The supramolecular nanocapsule used in the present study was constructed by self-assembly of a dinuclear Cu^{II}-based macrocyclic synthon and commercially available tetracarboxylate Zn^{II}-porphyrin, to yield the 3D tetragonal prismatic metal-organic nanocapsule **1**·$(OTf)_8$, which after anion exchange yielded **1**·$(BArF)_8$ as a crystalline material. Supramolecular nanocapsule **1**·$(BArF)_8$ was characterized by high resolution mass spectrometry (HRMS), FT-IR, UV/Vis and single-crystal X-ray diffraction (SCXRD) (Figures S1–S4 in the Supporting Information). As expected,[11] its crystal structure confirmed the formation of a slightly distorted tetragonal prismatic nanocapsule, which is constructed from the two parallel tetracarboxylated Zn^{II}-porphyrins linked by four dinuclear Cu^{II} macrocycles (see Figure 1, Figure S4 and Table S1).

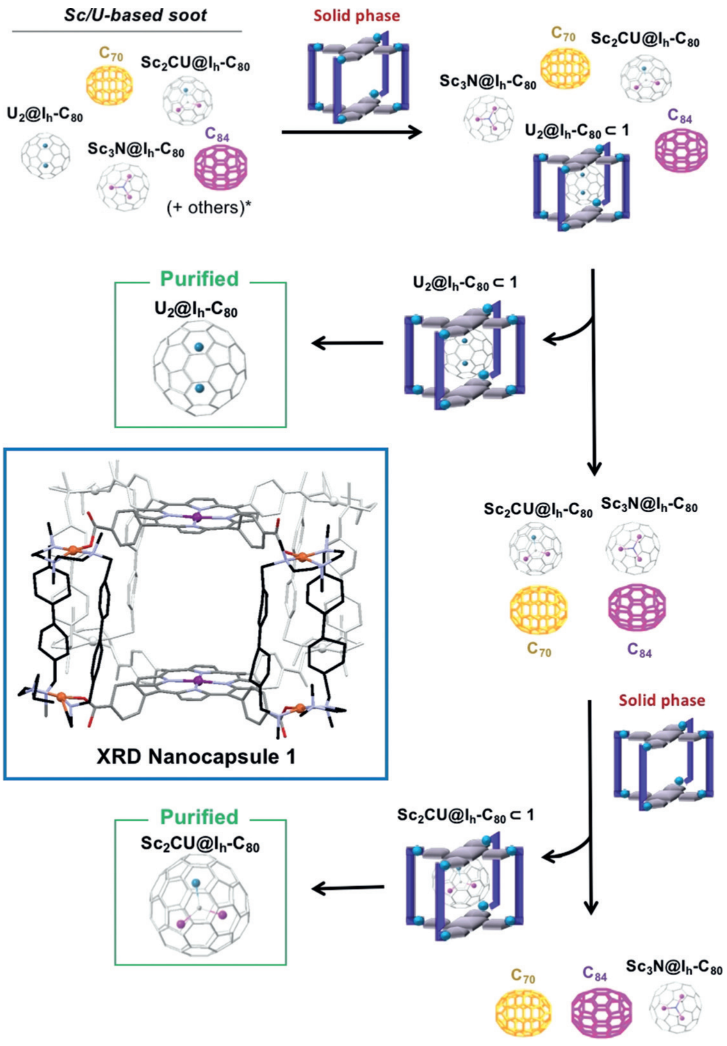

Figure 1. Straightforward purification method for selective and sequential encapsulation of $U_2@C_{80}$ and $Sc_2CU@C_{80}$ from raw soot using nanocapsule **1**·$(BArF)_8$ (*other endohedral metallofullerenes are present in the soot in small amounts, see Figure 2a). Inset shows a representation of $\mathbf{1}^{8+}$ extracted from SCXRD. Cu orange, Zn purple. (CCDC 1845202 contain the supplementary crystallographic data for this paper. These data can be obtained free of charge from The Cambridge Crystallographic Data Centre.). Endohedral atoms U blue, Sc pink.

Soot containing U-based endohedral metallofullerenes was produced by vaporization of cored graphite rods containing a mixture of U_3O_8/Sc_2O_3 in an arc-discharge reactor under a He/H_2 atmosphere. The resulting soot was extracted with CS_2 (Soxhlet) during 6 h. After removal of CS_2 under vacuum, the dry U/Sc-based soot extract was dissolved in toluene. LDI-TOF (laser desorption/ionization–time of flight) analysis of the soot showed a complex mixture containing empty fullerenes (mainly C_{70}), U-based endohedral metallofullerenes, unknown mixed-metallic compound Sc_2UC_{81} (spectroscopic and theoretical studies indicate that this compound corresponds to $Sc_2CU@I_h$-C_{80}, see below) and a family of Sc-based endohedral metallofullerenes (Figure 2a).[12]

Owing to the enhanced encapsulation selectivity of nanocapsule **1**·$(OTf)_8$ towards empty fullerenes and Sc-based fullerenes in solution or solid state,[10] crystals of **1**·$(BArF)_8$ were soaked in a toluene solution of the soot extract. The host–guest complexation reaction was monitored over time by LDI-TOF analysis of the supernatant solution (Figure 2 and Figure S5). To our surprise, the host–guest reaction resulted in the selective complexation of $U_2@C_{80}$, as indicated by an intensity decrease over time of the $U_2@C_{80}$ peak only. After 6 h no $U_2@C_{80}$ was detected by LDI-TOF, while the rest of the fullerenes and endohedral metallofullerenes remained in solution (Figure 2b). Taking advantage of the fact that $U_2@C_{80}$ was absorbed in soaked crystals of **1**·$(BArF)_8$, the host–guest complex was easily isolated by filtration. In addition, a HRMS analysis of the isolated crystals (dissolved in CH_3CN) showed the peaks corresponding to $U_2@C_{80}$⊂**1**·$(BArF)_8$, confirming the selective binding of $U_2@C_{80}$ (Figure S6). Subsequently, the release of the selectively entrapped diuranium endohedral metallofullerene was achieved by applying our previously reported solvent-washing protocol (using a 1:1 CS_2:*o*-DCB solvent mixture),[11] exploiting the

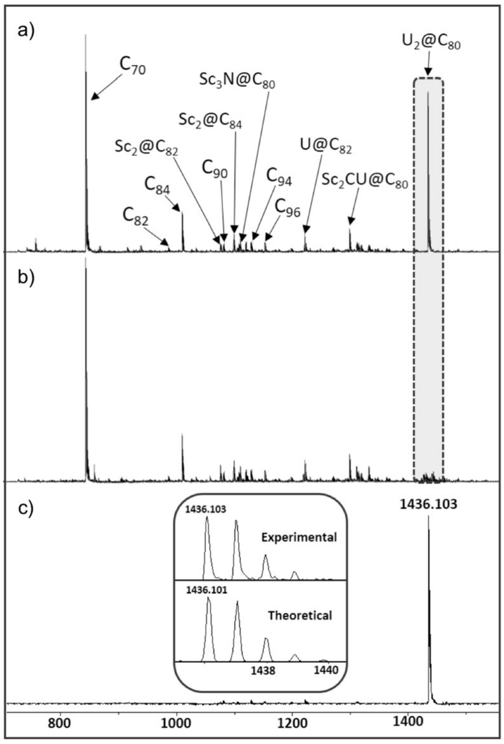

Figure 2. LDI-TOF monitoring of the selective complexation of $U_2@C_{80}$ within crystals of **1**·(BArF)$_8$ soaked in raw Sc/U soot extract solution in toluene. a) Spectrum of the starting raw Sc/U soot extract solution; b) spectrum of the remaining supernatant solution after soaking crystals of **1**·(BArF)$_8$ for 6 h; and c) spectrum of the pure $U_2@C_{80}$ released from **1**·(BArF)$_8$.

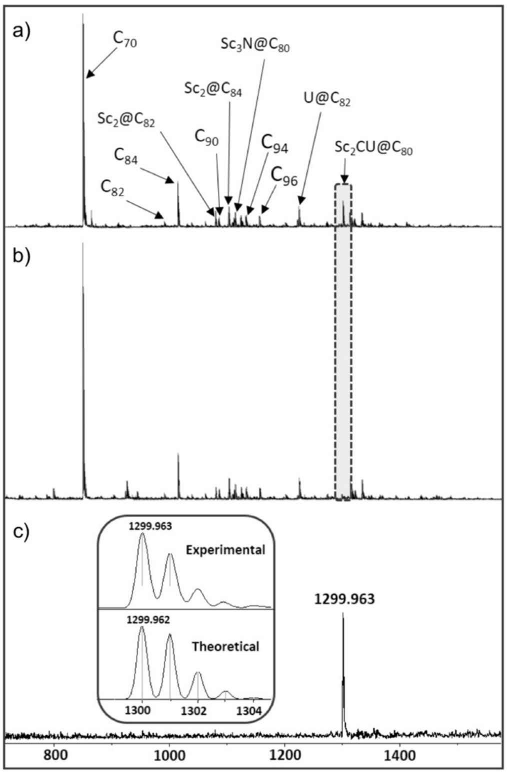

Figure 3. LDI-TOF monitoring of the remaining supernatant solution during the selective complexation of $Sc_2CU@C_{80}$ within crystals of **1**·(BArF)$_8$ soaked in Sc/U remaining soot (after the complete removal of $U_2@C_{80}$) in toluene. a) Spectrum of the remaining Sc/U soot solution; b) spectrum of the remaining supernatant solution after 1.5 h of soaking crystals of **1**·(BArF)$_8$; and c) spectrum of the pure $Sc_2CU@C_{80}$ released from **1**·(BArF)$_8$.

orthogonal solubility of **1**·(BArF)$_8$ and $U_2@C_{80}$. The LDI-TOF analysis of the released species showed a single peak at *m*/*z* 1436.103, corresponding to $U_2@C_{80}$, with an observed isotopic distribution which agrees with the theoretical predictions (Figure 2c). Therefore, highly pure $U_2@C_{80}$ was obtained in a single, rapid and operationally simple step, being selectively encapsulated in the presence of many other fullerenes and endohedral metallofullerenes.

After the complete removal of $U_2@C_{80}$ from the soot solution mixture, the subsequent encapsulation of $Sc_2CU@C_{80}$ was targeted in order to explore whether a general trend for the selective guest recognition of C_{80} Uranium-based endohedral metallofullerenes existed. An analogous strategy to that employed for the purification of $U_2@C_{80}$ was performed, and fresh crystals of **1**·(BArF)$_8$ were added to the toluene solution containing the remaining mixture of compounds (Figure 2b and Figure 3a). LDI-TOF analysis revealed a progressive decrease of the peak attributed to $Sc_2CU@C_{80}$ (Figure S7), until its complete disappearance after 1.5 h (Figure 3b). Confirmation of the selective binding of $Sc_2CU@C_{80}$ within **1**·(BArF)$_8$ was obtained by HRMS of the isolated host–guest adduct, showing the corresponding peaks for $Sc_2CU@C_{80}\subset$**1**·(BArF)$_8$ (Figure S8). The guest selectively absorbed within the crystals of **1**·(BArF)$_8$ was liberated by applying the solvent-washing method (using a 1:1 CS_2:*o*-DCB solvent mixture), and LDI-TOF analysis of the guest released from **1**·(BArF)$_8$ showed a single peak at *m*/*z* 1299.963, corresponding to $Sc_2CU@C_{80}$ (Figure 3c). The separation of this mixed-metallic species is remarkable considering that it could not be isolated by HPLC techniques due to its very low concentration and essentially the same retention time to that of $Sc_3N@C_{80}$ (Figure S9).

The UV/Vis spectrum of $Sc_2CU@C_{80}$ was rather featureless except for two minor absorption peaks at 600 nm and 680 nm (Figure S10). The spectral onset is located at around 900 nm, which indicates a band gap of 1.36 eV. Interestingly, these absorption features are very similar to those of $U_2@I_h$-C_{80},[5] further suggesting an identical cage symmetry and charge transfer (in line with DFT calculations, see below), being the internal cluster the only distinctive feature between the two. It thus follows that the selectivity of **1**·(BArF)$_8$ is in response to the nature of the different internal clusters within the carbon cages. Aiming at unraveling the origin of the observed selectivity, crystals of **1**·(BArF)$_8$ were added to a toluene solution containing an equimolar mixture of $U_2@I_h$-C_{80} and $Sc_3N@I_h$-C_{80}. These two species were selected because their only difference is the internal cluster. The host-guest complexation was monitored by LDI-TOF analysis of the supernatant over time, clearly showing the selective uptake of $U_2@I_h$-C_{80}, leaving $Sc_3N@I_h$-C_{80} in solution after 5 h (Figure 4). LDI-TOF analysis of the released species by

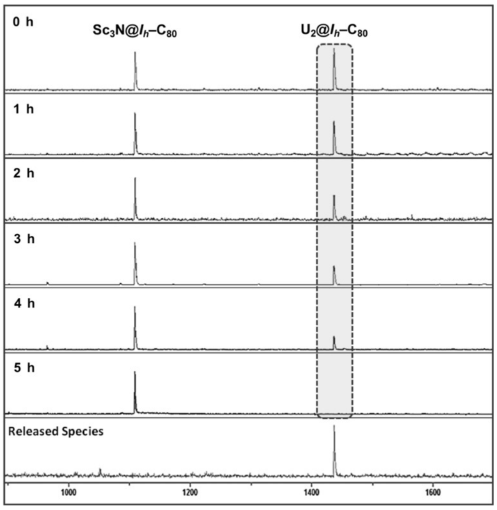

Figure 4. LDI-TOF monitoring of the remaining supernatant solution during the selective encapsulation of U$_2$@I_h-C$_{80}$ from an equimolar mixture of U$_2$@I_h-C$_{80}$ and Sc$_3$N@I_h-C$_{80}$ using crystals of **1**·(BArF)$_8$. Spectrum at the bottom corresponds to the released pure U$_2$@I_h-C$_{80}$ from **1**·(BArF)$_8$.

solvent-washing further confirmed the selective binding of U$_2$@I_h-C$_{80}$ (Figure 4, bottom).

Finally, the divergent affinity for Sc$_2$CU@I_h-C$_{80}$ with respect to Sc$_3$N@I_h-C$_{80}$ was also explored by LDI-TOF. Crystals of **1**·(BArF)$_8$ were soaked in a toluene solution containing one equivalent of Sc$_2$CU@C$_{80}$ and one equivalent of Sc$_3$N@I_h-C$_{80}$. The host-guest encapsulation was followed over time by LDI-TOF analysis of the supernatant, exhibiting a progressive decrease of the peak attributed to Sc$_2$CU@C$_{80}$ (Figure 5). After 3 h no Sc$_2$CU@I_h-C$_{80}$ was detected. Characterization by LDI-TOF of the species liberated from **1**·(BArF)$_8$ exclusively shows a single peak corresponding to Sc$_2$CU@I_h-C$_{80}$, unambiguously indicating the selective formation of complex Sc$_2$CU@I_h-C$_{80}$$\subset$**1**·(BArF)$_8$ (Figure 5, bottom).

Insight about the structure and electronic properties of unreported Sc$_2$UC$_{81}$ compound was gained by computational investigations carried out at the DFT/BLYP/TZP(D3) level. Given that its UV/Vis spectrum is similar to those endohedral metallofullerenes possessing a C$_{80}$-I_h cage and by analogy with Lu$_2$TiC@I_h-C$_{80}$, reported by Popov and co-workers,[2] the internal cluster was assumed to be Sc$_2$CU which has a planar structure. As expected, the oxidation state of U is 4+ and therefore there is a formal electron transfer between host and guest of six electrons. Note that the U–C bond length is computed to be 2.070 Å, a very short distance essentially identical to the X-ray bond length found very recently for a diuranium carbide cluster (U=C=U) stabilized inside C$_{80}$ (2.03 Å).[13] The analysis of the highest occupied orbitals for Sc$_2$CU@I_h-C$_{80}$ corroborates that there is a double bond between U and C (Figure 6 and Figure S12). The U–C distance is comparable to those found for uranium methylidene complexes H$_2$C=UHX (X = F, Cl and Br)[14] and longer than those found for uranium methylidyne molecules HC≡UX$_3$ (X = F, Cl and Br) with C≡U triple bonds (1.90–1.94 Å, see also Table S2).[15] The average Sc-C distance, 2.024 Å, is comparable to that found in the μ_3-carbido Sc$_2$CTi@I_h-C$_{80}$,[16] and somewhat smaller than those in other butterfly-shaped Sc$_2$C$_2$ clusterfullerenes.[17]

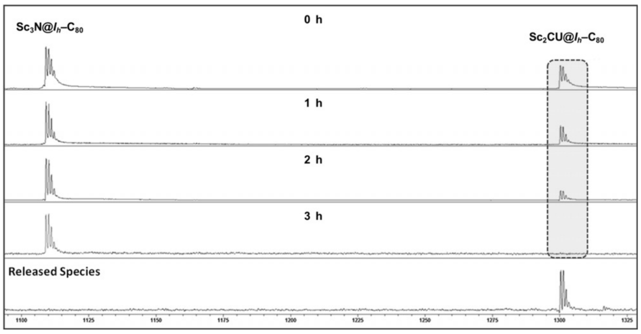

Figure 5. LDI-TOF monitoring of the remaining supernatant during the selective encapsulation of Sc$_2$CU@I_h-C$_{80}$ from an equimolar mixture of Sc$_2$CU@I_h-C$_{80}$ and Sc$_3$N@I_h-C$_{80}$ using crystals of **1**·(BArF)$_8$. Spectrum at the bottom corresponds to the released pure Sc$_2$CU@I_h-C$_{80}$ from **1**·(BArF)$_8$.

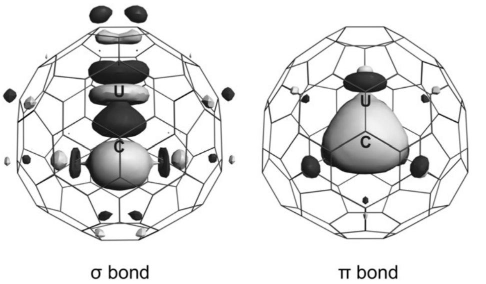

Figure 6. Occupied molecular orbitals for Sc$_2$CU@I_h-C$_{80}$ that describe the U=C double bond in the Sc$_2$CU cluster.

Previous DFT studies of the encapsulation of empty fullerenes by a Pd-based nanocapsule showed that there is a strong interaction between the fullerene and the porphyrin.[11] In an effort to understand the basis for the binding selectivity, DFT calculations were performed for simplified model systems to evaluate how endohedral fullerenes U$_2$@I_h-C$_{80}$ and Sc$_3$N@I_h-C$_{80}$ interact with the nanocapsule (see Supporting Information for computational details). As depicted in Figure 7, the computed U$_2$@I_h-C$_{80}$ fullerene shows the lowest energy orientation with respect to the two porphyrins of the nanocapsule. The two U ions are almost perfectly aligned with the Zn cations of the porphyrins.[5] When the U ions are in a perpendicular orientation the system is destabilized by 1.3 kcal mol^{-1} (see Figure S13). Note that whereas in C$_{60}$ and C$_{70}$ the carbon atoms are neutral, in Sc$_3$N@I_h-C$_{80}$ and U$_2$@I_h-C$_{80}$ there is a formal electron transfer of 6 electrons between the host and the guest, thus the electron density distribution can play a significant role.[18] The alignment of the two U ions with the porphyrin Zn cations in U$_2$@I_h-C$_{80}$ seems to be favored by the higher negative charge present on carbon atoms closer to the U^{3+} ions (see Figure 7 and Figure S14). Therefore, the preferential capture of icosahedral C$_{80}$ when it possesses two encapsulated U ions

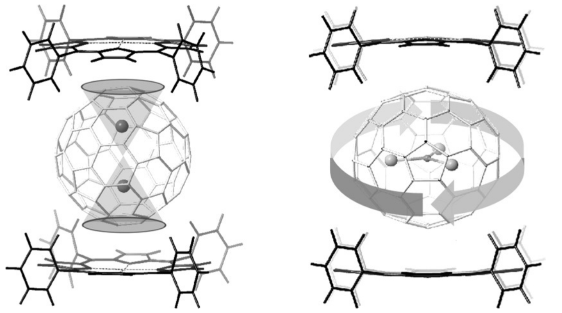

Figure 7. The lowest energy orientation of $U_2@I_h\text{-}C_{80}$ (left) and $Sc_3N@I_h\text{-}C_{80}$ (right) in a simplified two tetraphenyl-porphyrin (Zn-TPP) model. The electronic density distribution shows a linear double-conical interaction for $U_2@C_{80}$, whereas a diffuse, unspecific equatorial belt is found for $Sc_3N@I_h\text{-}C_{80}$. See Figure S14 for charge distributions and Bader charges on each pentagon.

seems to be related to the linear double-conical symmetry of the electron density induced by the presence of the guest ions (Figure 7, left). For $Sc_3N@I_h\text{-}C_{80}$, the electron density is averaged over an equatorial belt and thus it interacts less efficiently with the porphyrin units (Figure 7, right). In line with this, the energy differences among several orientations of the Sc_3N cluster and the fullerene with respect to the porphyrins are much smaller, differing only by 0.3 kcal mol^{-1} between the perpendicular and parallel cluster orientations (Figure S15). (Computed structures are given in the Supporting Information and a data set collection of computational results is available in the ioChem-BD repository[19] and can be accessed via https://doi.org/10.19061/iochem-bd-2-26.)

The computed binding energies (BE) between the carbon cage and the porphyrins for a series of fullerenes are compiled in Table S3. These values clearly indicate that the porphyrin-fullerene interaction is higher for $Sc_3N@I_h\text{-}C_{80}$ and $U_2@I_h\text{-}C_{80}$ endohedral metallofullerenes. Hence, while the interaction energies for the empty cages range between −43.1 and −51.5 kcal mol^{-1}, depending on the cage and orientation of the fullerene (Table S3 and Figures S16), they decrease down to −57.2 kcal mol^{-1} for $Sc_3N@I_h\text{-}C_{80}$ and down to −58.9 kcal mol^{-1} for $U_2@I_h\text{-}C_{80}$ (Figure S17). Thermodynamic stabilities extracted from the DFT calculations are aligned with the experimental observations, though it is worth mentioning that kinetic contributions must be relevant in the selection process of one or another endohedral metallofullerene, especially those involved in the diffusion of endohedral metallofullerenes in the solid phase.

This work describes a straightforward non-chromatographic purification methodology for the selective isolation of $U_2@I_h\text{-}C_{80}$ and $Sc_2CU@I_h\text{-}C_{80}$ contained in Sc/U-based arc-produced crude soot. This new strategy overcomes the tedious and time-consuming limitations of HPLC techniques applied for purifying endohedral metallofullerenes, and successfully distinguishes endohedral metallofullerenes with identical fullerene cages that differ only by the internal cluster. Our approach consists in a sequential and selective uptake of $U_2@I_h\text{-}C_{80}$ and $Sc_2CU@I_h\text{-}C_{80}$, simply by soaking crystals of the nanocapsule **1**·$(BArF)_8$ in a toluene solution of crude soot. $Sc_2CU@I_h\text{-}C_{80}$ is a new type of uranium endohedral metallofullerene, being the first example of a mixed-metallic actinide-based endohedral metallofullerene. DFT studies suggest that a highly directional electron-density distribution is the basis to explain the different selectivity. Compound **1**·$(BArF)_8$ provides a rapid and efficient purification method for endohedral metallofullerenes via strong π–π stacking interactions. No time-consuming work-up is needed for the isolation of the host–guest complex formed and the liberation of highly pure endohedral metallofullerenes is further facilitated by the orthogonal solubility between host and guest.

Acknowledgements

We acknowledge financial support from GenCat (2017 SGR 264 and 2017 SGR 629) and MINECO-Spain (CTQ2016-77989-P and CTQ2017-87269-P). L.E. thanks the US National Science Foundation (NSF) for generous support of this work under the NSF-PREM program (DMR-1205302) and CHE-1408865. The Robert A. Welch Foundation is also gratefully acknowledged for an endowed chair to L.E. (Grant AH-0033). ICN2 acknowledges the support of the Spanish MINECO through the Severo Ochoa Centers of Excellence Program under Grant SEV-2013-0295. X.R. and J.M.P. are also grateful to ICREA foundation for ICREA-Acadèmia awards. We acknowledge Prof. M. Costas for helpful discussions. F.G. acknowledges MINECO for funding through the "Ramón y Cajal" program.

Conflict of interest

The authors declare no conflict of interest.

Keywords: endohedral metallofullerenes · separation · supramolecular capsules · uranium

How to cite: *Angew. Chem. Int. Ed.* **2018**, *57*, 11294–11299
Angew. Chem. **2018**, *130*, 11464–11469

[1] a) S. Yang, T. Wei, F. Jin, *Chem. Soc. Rev.* **2017**, *46*, 5005–5058; b) M. D. Shultz, J. C. Duchamp, J. D. Wilson, C.-Y. Shu, J. Ge, J. Zhang, H. W. Gibson, H. L. Fillmore, J. I. Hirsch, H. C. Dorn, P. P. Fatouros, *J. Am. Chem. Soc.* **2010**, *132*, 4980–4981.

[2] A. L. Svitova, K. B. Ghiassi, C. Schlesier, K. Junghans, Y. Zhang, M. M. Olmstead, A. L. Balch, L. Dunsch, A. A. Popov, *Nat. Commun.* **2014**, *5*, 3568.

[3] T. Guo, M. D. Diener, Y. Chai, M. J. Alford, R. E. Haufler, S. M. McClure, T. Ohno, J. H. Weaver, G. E. Scuseria, R. E. Smalley, *Science* **1992**, *257*, 1661–1664.

[4] a) Y. Wang, R. Morales-Martínez, X. Zhang, W. Yang, Y. Wang, A. Rodríguez-Fortea, J. M. Poblet, L. Feng, S. Wang, N. Chen, *J. Am. Chem. Soc.* **2017**, *139*, 5110–5116; b) W. Cai, R. Morales-Martínez, X. Zhang, D. Najera, E. L. Romero, A. Metta-Magana, A. Rodríguez-Fortea, S. Fortier, N. Chen, J. M. Poblet, L. Echegoyen, *Chem. Sci.* **2017**, *8*, 5282–5290.

[5] X. Zhang, Y. Wang, R. Morales-Martínez, J. Zhong, C. de Graaf, A. Rodríguez-Fortea, J. M. Poblet, L. Echegoyen, L. Feng, N. Chen, *J. Am. Chem. Soc.* **2018**, *140*, 3907–3915.

[6] M. N. Chaur, F. Melin, A. L. Ortiz, L. Echegoyen, *Angew. Chem. Int. Ed.* **2009**, *48*, 7514–7538; *Angew. Chem.* **2009**, *121*, 7650–7675.

[7] a) E. A. Sarina, B. Q. Mercado, J. U. Franco, C. J. Thompson, M. L. Easterling, M. M. Olmstead, A. L. Balch, *Chem. Eur. J.* **2015**, *21*, 17035 – 17043; b) S. Stevenson, M. A. Mackey, J. E. Pickens, M. A. Stuart, B. S. Confait, J. P. Phillips, *Inorg. Chem.* **2009**, *48*, 11685 – 11690; c) S. Stevenson, K. Harich, H. Yu, R. R. Stephen, D. Heaps, C. Coumbe, J. P. Phillips, *J. Am. Chem. Soc.* **2006**, *128*, 8829 – 8835; d) B. Elliott, L. Yu, L. Echegoyen, *J. Am. Chem. Soc.* **2005**, *127*, 10885 – 10888; e) S. Stevenson, K. D. Arvola, M. Fahim, B. R. Martin, K. B. Ghiassi, M. M. Olmstead, A. L. Balch, *Inorg. Chem.* **2016**, *55*, 62 – 67; f) M. R. Cerón, F. F. Li, L. Echegoyen, *Chem. Eur. J.* **2013**, *19*, 7410 – 7415; g) Z. Ge, J. C. Duchamp, T. Cai, H. W. Gibson, H. C. Dorn, *J. Am. Chem. Soc.* **2005**, *127*, 16292 – 16298.

[8] S. Stevenson, H. R. Thompson, K. D. Arvola, K. B. Ghiassi, M. M. Olmstead, A. L. Balch, *Chem. Eur. J.* **2015**, *21*, 10362 – 10368.

[9] a) L. P. Hernández-Eguía, E. C. Escudero-Adán, J. R. Pinzón, L. Echegoyen, P. Ballester, *J. Org. Chem.* **2011**, *76*, 3258 – 3265; b) M.-Y. Ku, S.-J. Huang, S.-L. Huang, Y.-H. Liu, C.-C. Lai, S.-M. Peng, S.-H. Chiu, *Chem. Commun.* **2014**, *50*, 11709 – 11712.

[10] C. Fuertes-Espinosa, C. García-Simón, E. Castro, M. Costas, L. Echegoyen, X. Ribas, *Chem. Eur. J.* **2017**, *23*, 3553 – 3557.

[11] C. García-Simón, M. Garcia-Borràs, L. Gómez, T. Parella, S. Osuna, J. Juanhuix, I. Imaz, D. Maspoch, M. Costas, X. Ribas, *Nat. Commun.* **2014**, *5*, 5557.

[12] The $Sc_3N@C_{80}$ observed in the initial soot is formed presumably due to traces of nitrogen in the arcing chamber.

[13] X. Zhang, W. Li, L. Feng, X. Chen, A. Hansen, S. Grimme, S. Fortier, D.-C. Sergentu, T. J. Duignan, J. Autschbach, S. Wang, Y. Wang, G. Velkos, A. A. Popov, N. Aghdassi, S. Duhm, X. Li, J. Li, L. Echegoyen, W. H. E. Schwarz, N. Chen, *Nat. Commun.* **2018**, *9*, 2753 (DOI: 10.1038/s41467-018-05210-8).

[14] J. T. Lyon, L. Andrews, *Inorg. Chem.* **2006**, *45*, 1847 – 1852.

[15] J. T. Lyon, H.-S. Hu, L. Andrews, J. Li, *Proc. Natl. Acad. Sci. USA* **2007**, *104*, 18919 – 18924.

[16] K. Junghans, K. B. Ghiassi, N. A. Samoylova, Q. Deng, M. Rosenkranz, M. M. Olmstead, A. L. Balch, A. A. Popov, *Chem. Eur. J.* **2016**, *22*, 13098 – 13107.

[17] R. Valencia, A. Rodríguez-Fortea, J. M. Poblet, *J. Phys. Chem. A* **2008**, *112*, 4550 – 4555.

[18] A. Rodríguez-Fortea, A. L. Balch, J. M. Poblet, *Chem. Soc. Rev.* **2011**, *40*, 3551 – 3563.

[19] M. Álvarez-Moreno, C. de Graaf, N. López, F. Maseras, J. M. Poblet, C. Bo, *J. Chem. Inf. Model.* **2015**, *55*, 95 – 103.

Manuscript received: May 28, 2018
Accepted manuscript online: June 19, 2018
Version of record online: July 26, 2018

Chapter VI.

Highly Selective Encapsulation and Purification of U-based C$_{78}$-EMFs within a Supramolecular Nanocapsule.

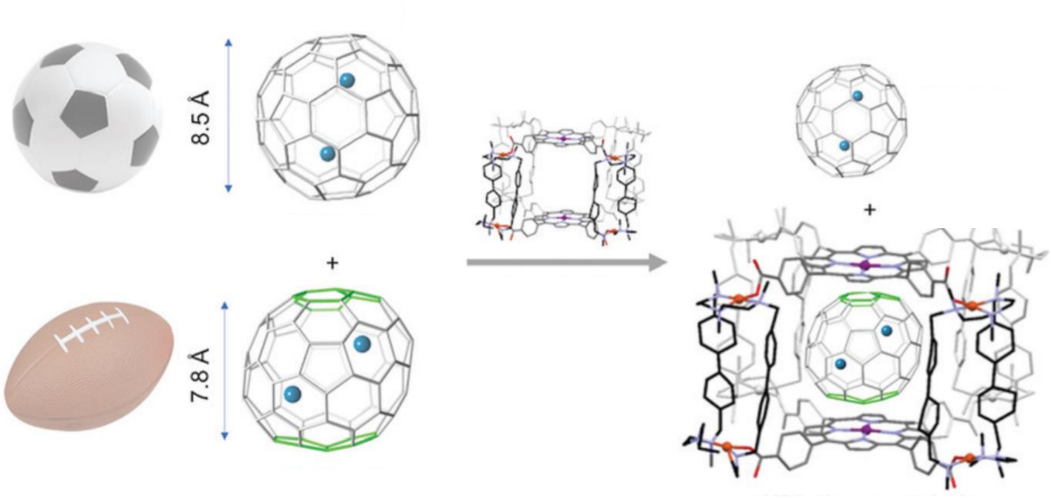

This chapter corresponds to the following publication:

Fuertes-Espinosa, C.; Murillo, J.; Soto, M.; Ceron, M.; MoralesMartínez, R.; Rodríguez-Fortea, A.; Poblet, J.M.; Echegoyen, L. and Ribas, X. *Nanoscale* **2019**, 11, 23035-23041.

Reprinted with permission from Royal society of Chemistry editorial

Nanoscale

PAPER

View Article Online
View Journal | View Issue

Cite this: *Nanoscale*, 2019, **11**, 23035

Highly selective encapsulation and purification of U-based C_{78}-EMFs within a supramolecular nanocapsule†

Carles Fuertes-Espinosa,[a] Jesse Murillo,[b] Marco E. Soto,[b] Maira R. Ceron,[b] Roser Morales-Martínez,[c] Antonio Rodríguez-Fortea,[c] Josep M. Poblet,[c] Luis Echegoyen *[b] and Xavi Ribas *[a]

Received 4th September 2019,
Accepted 5th November 2019

DOI: 10.1039/c9nr07660c

rsc.li/nanoscale

The ability of the tetragonal prismatic nanocapsule **1**·$(BArF)_8$ to selectively encapsulate U-based C_{78} EMFs from a soot mixture is reported, showing enhanced affinity for C_{78}-based EMFs over C_{80}-based EMFs. Molecular recognition driven by the electrostatic interactions between the host and guest is at the basis of the high selectivity observed for ellipsoidal C_{78}-based EMFs compared to spherical C_{80}-based EMFs. In addition, DFT analysis points towards an enhanced breathing adaptability of nanocapsule **1**·$(BArF)_8$ to C_{78}-based EMFs to further explain the selectivity observed when the host is used in the solid phase.

Introduction

Since the discovery of fullerenes in 1985, tremendous interest has been devoted to exploit the cavity of carbon cages for hosting guest atoms or molecules. Specifically, endohedral metallofullerenes (EMFs) typically feature monoatomic or diatomic metal cations of the type $X@C_{2n}$, $X_2@C_{2n}$ (X = metal, and $60 \leq 2n \leq 88$), and also metal clusters such as trimetallic nitrides (M_3N), dimetallic carbides (M_2C and M_2C_2) and metallic oxides and sulphides (M_4O_2, M_2O, M_2S) have been described, among others.[1,2] Interest on these species is due to multiple reasons: (a) the intrinsic nature of the interaction of the naked cation(s) with the carbon cage,[3,4] (b) the unprecedented electronic and magnetic properties of the EMF due to the stabilization of otherwise non-existing clusters,[5] and (c) the cluster-dependent exohedral reactivity of the EMF.[6–11] However, the accumulation of practical amounts of EMFs to study their spectroscopy and their reactivity is hampered by three limiting factors: (1) the synthesis of soot with significant amounts of the desired EMF, (2) the lack of selectivity during their production, and (3) tedious and time-consuming HPLC chromatographic techniques to enrich or purify the selected EMF. Even more challenging is the chromatographic separation of EMFs with the same carbon cage and differing only in the nature of the cluster.[12] Alternative non-chromatographic approaches include the "stir and filter" method (SAFA) that consists of the immobilization of empty cyclopentadienyl- and amino-functionalized silica to enrich the soot with EMFs.[13,14] Also, the addition of Lewis acids such as $FeCl_3$, $AlCl_3$ or $TiCl_4$ allowed the separation of EMFs upon precipitation, while empty fullerenes remained in solution.[15] However, these methods are commonly used as a pre-enrichment of EMFs of a given soot and HPLC chromatography is ultimately necessary. On the other hand, Echegoyen reported the electrochemical purification of Sc_3N-based EMFs.[16]

Over the past years, scarce examples of the encapsulation of EMFs into supramolecular hosts have been reported, *i.e.* $Sc_3N@C_{80}$ or $Gd@C_{82}$.[17–19] Very recently, our group has developed the purification of EMFs by selective encapsulation in supramolecular nanocapsules. Following this strategy, we have recently reported the purification and isolation of $Sc_3N@C_{80}$ (I_h–D_{5h} mixture),[20] $U_2@I_h$-C_{80} and $Sc_2CU@I_h$-C_{80} from different soot.[21] In this work, we expand the ability of the tetragonal prismatic nanocapsule **1**·$(BArF)_8$ to selectively encapsulate novel U-based C_{78} EMFs, showing enhanced affinity for C_{78}-based EMFs compared to C_{80}-based EMFs (Fig. 1). The high selectivity observed is discussed based on the molecular recognition driven by the electrostatic interactions between the host and guest. In addition, the breathing ability of our receptor in the solid phase to better adapt to C_{78}-based EMFs is supported by DFT analysis.

---

[a] *QBIS-CAT group, IQCC and Dept. Química, Universitat de Girona, Campus de Montilivi, E-17003 Girona, Catalonia, Spain. E-mail: xavi.ribas@udg.edu*

[b] *Department of Chemistry, University of Texas at El Paso, 500 West University Avenue, El Paso, Texas 79968, USA. E-mail: echegoyen@utep.edu*

[c] *Departament de Química Física i Inorgánica, Universitat Rovira i Virgili, C/Marcel·lí Domingo 1, 43007 Tarragona, Catalonia, Spain*

† Electronic supplementary information (ESI) available: EMF soot preparation and experimental and computational details. See DOI: 10.1039/c9nr07660c

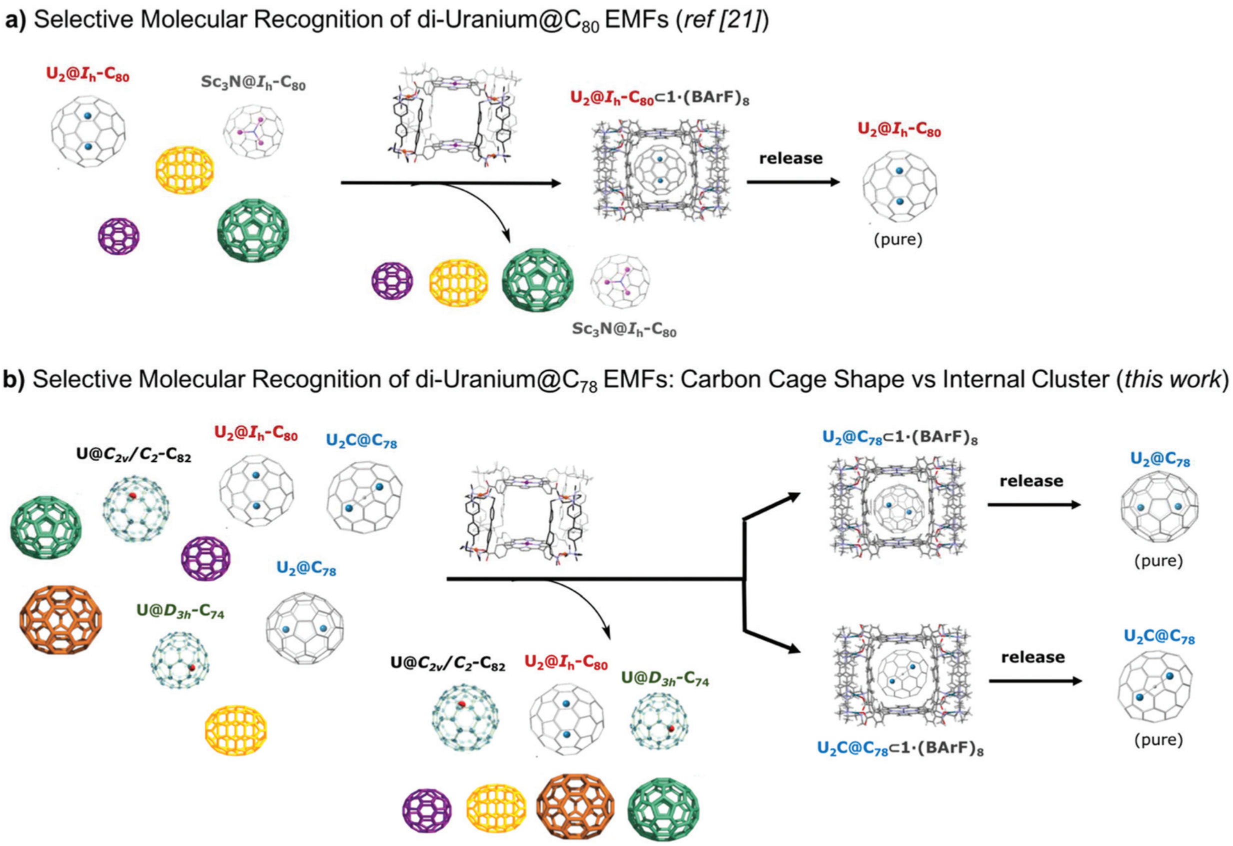

a) Selective Molecular Recognition of di-Uranium@C_{80} EMFs (*ref [21]*)

b) Selective Molecular Recognition of di-Uranium@C_{78} EMFs: Carbon Cage Shape vs Internal Cluster (*this work*)

Fig. 1 (a) Non-chromatographic purification of U-based@C_{80} EMF by selective encapsulation in supramolecular nanocage **1a**·(BArF)$_8$. (b) Highly selective encapsulation and purification of U-based@C_{78} EMFs (this work).

Results and discussion

Previous investigations revealed that supramolecular nanocapsule **1**·(BArF)$_8$ is able to selectively recognize di-uranium-based C_{80} EMFs, in the presence of many other empty fullerenes and EMFs.[21] The production of a new family of uranium-based C_{78} EMFs allowed us to study the electronic and shape complementarity of **1**·(BArF)$_8$ towards these new compounds, in comparison to the previously described selectivity for uranium-based C_{80} EMFs. The low production yield and the complexity of the soot containing di-uranium-based C_{78} EMFs make their chromatographic separation extremely challenging. Aiming at the straightforward isolation of these new EMFs, crystals of **1**·(BArF)$_8$ were soaked in a toluene solution of the crude soot containing di-uranium-based C_{78} EMFs along with many empty fullerenes and mono-uranium EMFs with different size carbon cages. On monitoring the host–guest complexation by LDI-TOF analysis of the species remaining in solution, we clearly observed the selective and quantitative uptake of di-uranium-based C_{78} EMF species ($U_2@C_{78}$ and $U_2C@C_{78}$) after 3 hours, observing a drastic decrease of the peaks belonging to these compounds (Fig. 2), attributed to the inclusion of the EMF within the cavity of solid **1**·(BArF)$_8$. Taking advantage of the encapsulation of the di-uranium@C_{78} EMFs in a crystalline material of the supramolecular nanocapsule, we isolated the solid (di-uranium@C_{78} EMFs)⊂**1**·(BArF)$_8$ complexes simply by filtration. Subsequently, the selectively trapped guests were easily released by washing the crystals with carbon disulfide, in analogy to our previously reported solvent-washing protocol (Fig. 2, bottom).[22] LDI-TOF analysis of the released guests confirms an exceptional selectivity towards $U_2@C_{78}$ and $U_2C@C_{78}$ compared to the rest of the compounds present in the starting soot, including $U_2@C_{80}$, which is known to show very high affinity for **1**·(BArF)$_8$. Remarkably, the target compounds were not kinetically trapped in the cage cavity and could be easily recovered by exploiting the orthogonal solubility between the host and the guest.

To better understand the effect of the size and the shape of the guests on the specific binding observed, we then explored the molecular recognition of $U_2@C_{78}$ in the presence of a variety of U-based EMFs ($U@C_{74}$, $U@C_{82}$ and $U_2@C_{80}$). The addition of crystalline **1**·(BArF)$_8$ to a toluene solution of the soot resulted in a clean and selective binding of $U_2@C_{78}$ over the rest of the EMFs (Fig. 3). The trapped guest was successfully recovered and the LDI-TOF analysis of the released EMF evidenced the unique encapsulation of $U_2@C_{78}$. The presence of the same metal cluster in $U_2@C_{78}$ and $U_2@C_{80}$, which transfers an equal number of electrons to the carbon cages,

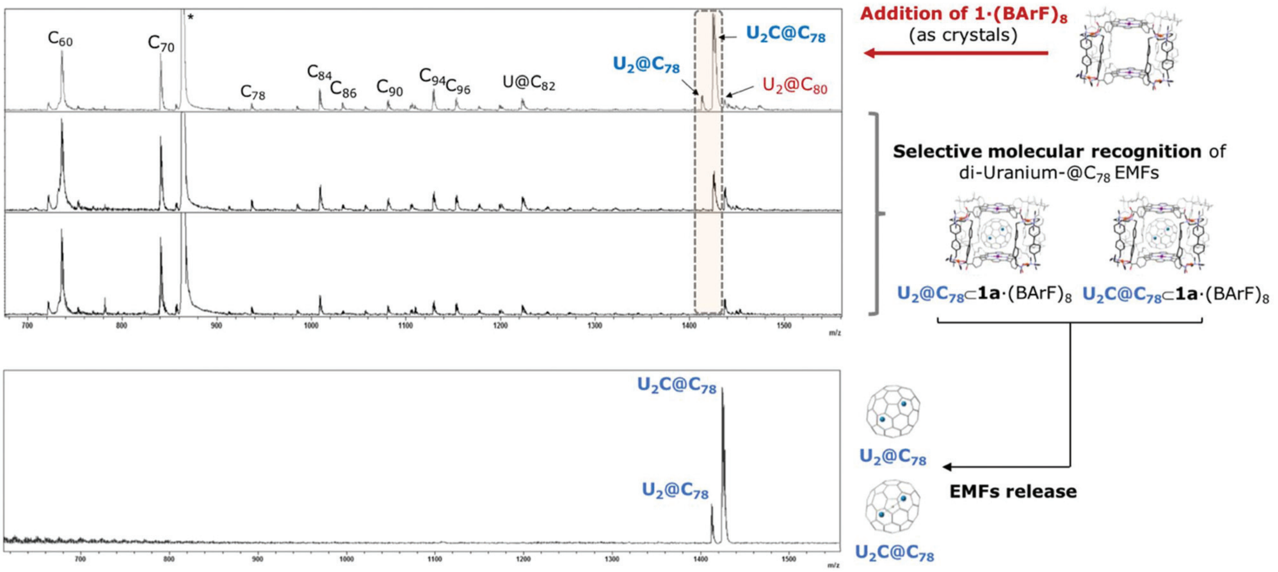

Fig. 2 LDI-TOF monitoring of the remaining supernatant over time during the selective encapsulation of $U_2@C_{78}$ and $U_2C@C_{78}$ within crystals of **1**·(BArF)$_8$ (top). Spectrum of released guests trapped during the molecular recognition (bottom).

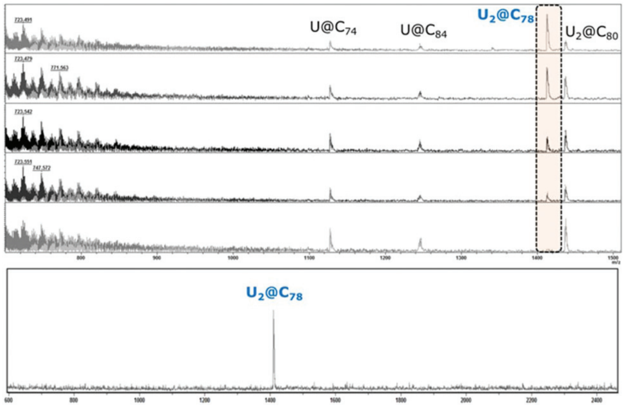

Fig. 3 LDI-TOF monitoring of the remaining supernatant over time during the selective molecular recognition of $U_2@C_{78}$ in a complex soot containing differently sized U-based EMFs (top). Spectrum of pure $U_2@C_{78}$ released from **1**·(BArF)$_8$ (bottom).

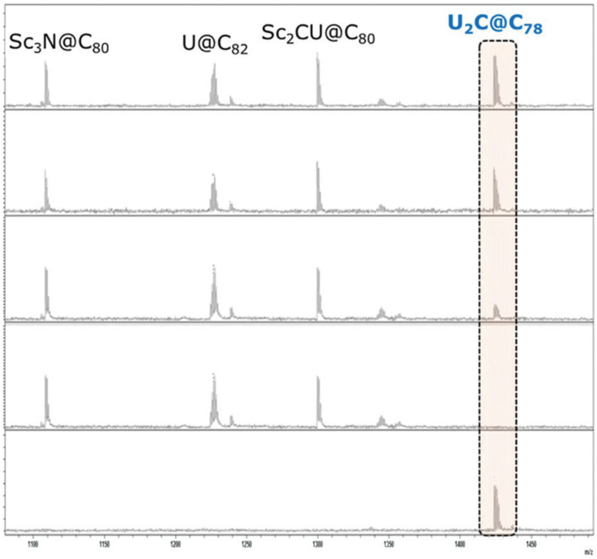

Fig. 4 LDI-TOF monitoring of the remaining supernatant over time during the selective molecular recognition of $U_2C@C_{78}$ in a soot containing C_{80}- and C_{82}-based EMF. Spectrum of pure $U_2C@C_{78}$ released from **1**·(BArF)$_8$ (bottom).

suggested that the selective molecular recognition events are governed by the size/shape relationship between the host and guest. The crystal structures of the previously reported D_{3h}-C_{78} and I_h-C_{80} EMFs showed very similar sizes of the carbon cages,[1] independent of the internal cluster hosted. Thus, the selectivity observed suggested enhanced π-interactions with the flattened regions of the ellipsoidal-shaped D_{3h}-C_{78} in comparison to the spherical I_h-C_{80} carbon cage.

Another soot containing U-based EMFs different from $U_2@C_{78}$ (with a similar proportion of $U_2C@C_{78}$, $Sc_2CU@C_{80}$, U@C_{82} and $Sc_3N@C_{80}$) was studied to evaluate the importance of the carbon cage (size and shape) or the internal cluster (electrostatics) in the observed selectivity (Fig. 4). The selective encapsulation of $U_2C@C_{78}$ was observed upon the addition of crystalline **1**·(BArF)$_8$ to the corresponding soot solution in toluene; LDI-TOF analysis revealed a progressive decrease of the peak of $U_2C@C_{78}$ until its complete disappearance after 4.5 h (Fig. 4). LDI-TOF analysis of the released guest showed a single peak at m/z = 1424.0707, confirming the purification of $U_2C@C_{78}$. Remarkably, the ability of nanocapsule **1**·(BArF)$_8$ to preferentially encapsulate C_{78} over C_{80} EMFs was further evidenced by the encapsulation of $Sc_3N@C_{78}$ over $U_2@C_{80}$ (see Fig. S2†). Therefore, the shape of the carbon cage rules over the nature of the internal cluster, with a higher affinity for C_{78}-based EMFs, irrespective of the nature of the internal cluster.

The presence of EMFs only differing in the nature of the internal clusters is very common in actinide-based EMF soot, making their chromatographic separation very challenging. We previously described the important role of the electron density distribution of EMFs only differing in the internal cluster ($U_2@I_h$-C_{80} *versus* $Sc_2CU@I_h$-C_{80} or $Sc_3N@I_h$-C_{80}) to allow their stepwise separation within nanocapsule **1**·$(BArF)_8$.[21] We hypothesize that the differences in the cluster arrangement of $U_2@C_{78}$ and $U_2C@C_{78}$ could promote different electronic distributions that could impact the electrostatic interaction with **1**·$(BArF)_8$. Therefore, we added precise amounts of crystalline materials of **1**·$(BArF)_8$ to a sample mainly containing $U_2@C_{78}$ and $U_2C@C_{78}$ (see Fig. 5). LDI-TOF monitoring showed the exclusive inclusion of $U_2@C_{78}$. LDI-TOF analysis of the released guest further confirmed the specific molecular recognition of $U_2@C_{78}$ while $U_2C@C_{78}$ remained in the starting sample solution, thus pointing towards the possible separation and purification of C_{78}-based EMF differing only in the internal cluster.

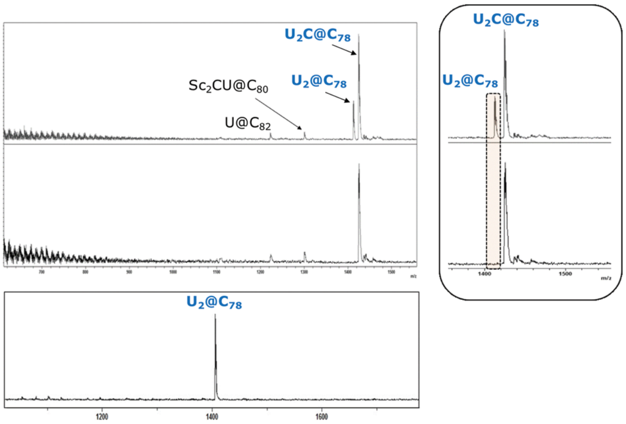

Fig. 5 LDI-TOF monitoring of the remaining supernatant over time during the selective molecular recognition of $U_2@C_{78}$ in front of $U_2C@C_{78}$ (top); spectrum of pure $U_2@C_{78}$ released from **1**·$(BArF)_8$ (bottom).

Finally, we attempted the stepwise encapsulation of $U_2@C_{78}$ and $U_2C@C_{78}$ using a complex soot, which included also $U_2@C_{80}$, mono-U-based EMF, Sc_3N-based EMF and empty fullerene cages. On monitoring the composition of the soot by LDI-TOF (Fig. 6), the peak attributed to $U_2@C_{78}$ completely disappeared (after 2 hours) upon the addition of precise amounts of **1**·$(BArF)_8$. The nanocapsule was filtered and the guest was liberated, obtaining pure $U_2@C_{78}$ as ascertained by LDI-TOF. Subsequently, additional amounts of fresh crystalline **1**·$(BArF)_8$ were added, observing a progressive selective decrease of the $U_2C@C_{78}$ peak. Liberation of the guest allowed the identification of pure $U_2C@C_{78}$.

It is worth noting that the very low concentration of the di-uranium-based C_{78} EMFs present in the soot used makes it very complicated to spectrometrically characterize the host–guest complexes formed during the molecular recognition experiments. Despite these difficulties, the $U_2C@C_{78}{\subset}\mathbf{1}{\cdot}(BArF)_8$ complex was identified by ESI-MS (see Fig. S1†).

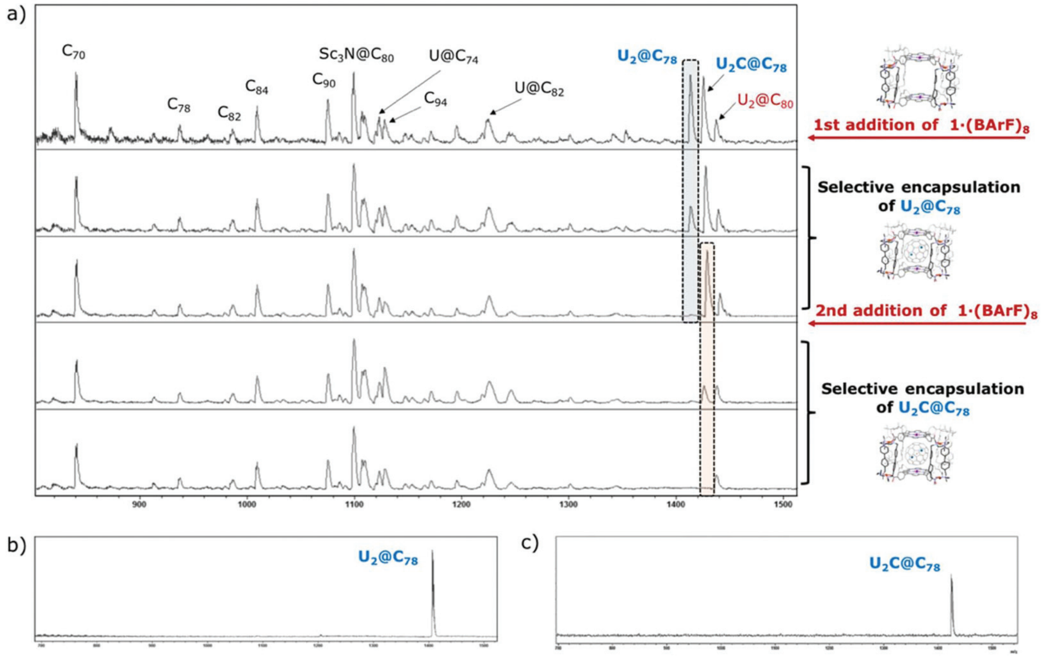

Fig. 6 (a) LDI-TOF monitoring of the remaining supernatant over time during the selective molecular recognition of $U_2@C_{78}$; (b) spectrum of pure $U_2@C_{78}$ and (c) pure $U_2@C_{78}$ released from **1**·$(BArF)_8$.

The encapsulation of $Sc_3N@C_{78}$ into **1**·$(BArF)_8$ in front of $Sc_3N@C_{80}$ is thermodynamically and also kinetically preferred, as demonstrated by competition experiments shown in Fig. S3 and S4.†

To gain a deeper understanding of the reasons behind the selectivity of **1**·$(BArF)_8$ for di-uranium@C_{78} EMFs, DFT calculations were performed to compute the binding energies (BEs) between the two porphyrins of the nanocapsule and the EMFs $U_2@I_h$-C_{80} and $U_2@D_{3h}$-C_{78} in a similar manner as previously reported by us.[21] A systematic study has shown that the interaction energy between the porphyrins and the fullerenes changes significantly with the cage orientation with respect to the porphyrins. The position of the uranium ions inside these cages, however, does not affect so much the interaction energies. In particular, for the highly symmetric I_h-C_{80} the two U atoms have free rotation at room temperature. For D_{3h}-C_{78} the U atoms prefer to occupy the positions along the C_3 axis (Fig. 7 top).

The computed BEs between the EMF and the porphyrins for the structures represented in Fig. 7 are compiled in Table 1. These values from our simplified model would indicate that from a thermodynamic point of view the capture of the $U_2@I_h$-C_{80} EMF would be slightly favored, even though the relative binding energies and the porphyrin–porphyrin separations for the lowest energy orientations of the I_h-C_{80} and D_{3h}-C_{78} cages inside the nanocapsule are not that different. However, a more detailed inspection of the computed structures shows that the optimal dispositions of the EMFs display slightly shorter porphyrin–porphyrin separation for $U_2@C_{78}$. The difference is only about 0.2 Å, but it could be significant if we take into account that the empty nanocapsule **1**·$(BArF)_8$ used in the current experiments has a Zn···Zn separation of about 12 Å in the previously reported crystal structure,[21] considerably shorter than the equilibrium values computed in our models (Table 1).

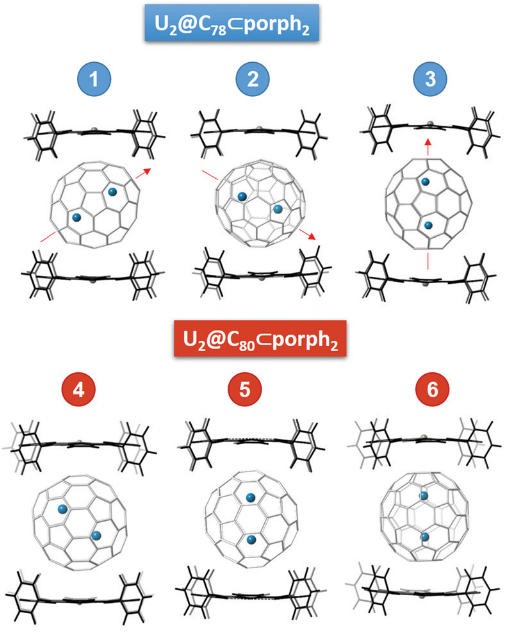

Fig. 7 The lowest energy orientation of $U_2@D_{3h}$-C_{78} (top) and $U_2@I_h$-C_{80} (bottom) in a simplified two tetraphenyl-porphyrin model.

To better evaluate the effect of the breathing of the cage, we have explored how the energy changes when the porphyrin–porphyrin distance shrinks from 14 Å to 13 Å. For the energy scan in Fig. 8, the structures of the porphyrins and EMFs remain frozen and only the porphyrin–porphyrin distance changes. The values in Fig. 8 and Table 2 confirm three main points: (1) the optimal Zn–Zn distances are somewhat longer for I_h-C_{80} EMFs, (2) the binding energy between porphyrin and EMF is slightly larger for I_h-C_{80} and (3) as the porphyrin–porphyrin compression progresses the binding energy increases with a lower slope for D_{3h}-C_{78}. Because of the cylindrical shape of the D_{3h}-C_{78} cage, the energy destabilization of the system is smaller for this fullerene. The difference in BEs between structures **2** and **4** is larger than 8 kcal mol^{-1} at a Zn–Zn distance of 13 Å, with the D_{3h}-C_{78} EMF displaying the largest encapsulation energy. Interestingly, if we allow the fullerene to relax its structure, we observe that C_{80} reorients with respect to the porphyrins at 13 Å, and its BE increases from −33.6 to −38.8 kcal mol^{-1}, whereas the reorganization for the D_{3h}-C_{78} cage is somewhat smaller with an energy change of 3.55 kcal mol^{-1}, from −41.1 to −44.6 kcal mol^{-1}. Thus, the binding energy

Table 1 Binding energies between the endohedral fullerene and two porphyrins

	$U_2@D_{3h}$-C_{78}			$U_2@I_h$-C_{80}		
	1	**2**	**3**	**4**	**5**	**6**
BE[a]	−58.5	−56.9	−48.4	−59.1	−58.9	−52.4
d(Zn···Zn)[b]	13.68	13.65	14.48	13.80	13.95	14.26

[a] Binding energies computed at the BLYP/TZP(D3) level are given in kcal mol^{-1}. [b] Zn···Zn separations are in Å.

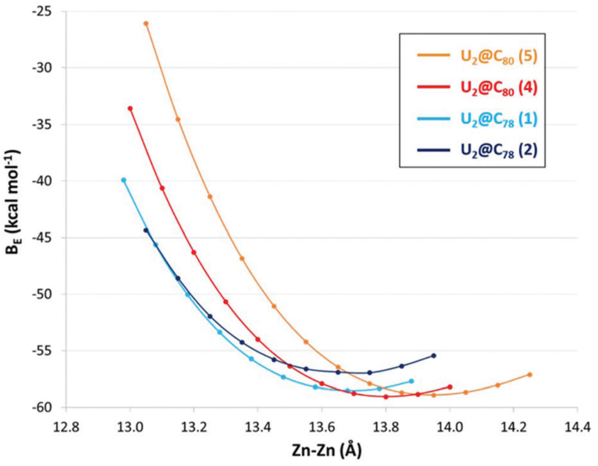

Fig. 8 Energy scan along the Zn···Zn separation maintaining porphyrins and fullerenes fixed. The EMF numeration is identical to that in Fig. 7.

Table 2 Binding energies[a] between the endohedral fullerene and two porphyrin models at different Porph⋯Porph distances

	$U_2@D_{3h}$-C_{78}		$U_2@I_h$-C_{80}	
d(Zn⋯Zn)[b]	**1**	**2**	**4**	**5**
13.0	−41.1	−41.9	−33.7	−21.5
13.2	−50.6	−50.4	−46.3	−38.1
13.4	−56.0	−55.2	−54.1	−49.1
13.6	−58.2	−57.0	−58.0	−55.5
13.8	−58.1	−56.7	−59.1	−58.4
14.0	−56.6	−55.1	−58.3	−58.8

[a] Binding energies computed at the BLYP/TZP(D3) level are given in kcal mol^{-1}. [b] Zn⋯Zn separations are in Å.

difference between the two EMFs is still larger than 6 kcal mol^{-1}. These results suggest that the shape of D_{3h}-C_{78} is more suitable than that of I_h-C_{80} for a relatively small nanocapsule like **1**·(BArF)$_8$, or similarly, that the energy penalty for the breathing of the nanocapsule to catch the EMF is smaller for the flattened D_{3h}-C_{78} than for the spherical I_h-C_{80}. This breathing ability is somewhat reminiscent of the one exhibited by some MOFs.[23]

A similar behavior was observed for $U_2C@D_{3h}$-C_{78}. When an extra C is added into the center of the $U_2@C_{78}$ fullerene, affording a linear U_2C cluster as the most stable conformer, the porphyrin–porphyrin separation and the calculated binding energies are exactly the same as those found for $U_2@D_{3h}$-C_{78} (Fig. S5†). Although very recently DFT calculations for several $U_2C@C_{2n}$ endofullerenes including $U_2C@D_{3h}$-C_{78} suggested that the U=C=U cluster takes a bent form inside the D_{3h}-C_{78} cage,[24] we have verified that the linear arrangement is significantly lower in energy (Fig. S6†). The presence of the central carbon atom and the change in the formal oxidation state of uranium ions from +3 to +5 hardly modifies the electron density on the fullerene surface, as suggested by the molecular electrostatic potential distribution maps represented in Fig. 9. Thus, our very simplified model cannot discriminate the different behaviors observed for $U_2C@D_{3h}$-C_{78} and $U_2@D_{3h}$-C_{78} endohedral metallofullerenes, since the uranium carbide is only captured once $U_2@D_{3h}$-C_{78} has been completely removed from the soot (Fig. 5 and 6). This means that more sophisticated models and, probably, molecular dynamics simulations will be needed to better understand the phenomena of encapsulation of fullerenes by nanocapsules like **1**·(BArF)$_8$ or similar ones.

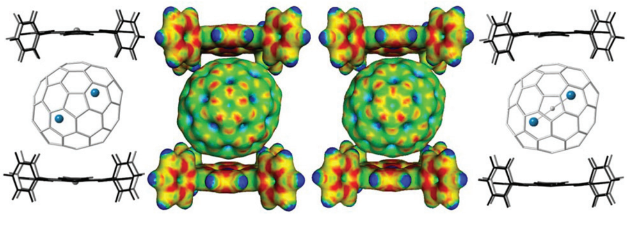

Fig. 9 Comparison of computed structures and molecular electrostatic potential maps for $U_2@D_{3h}$-C_{78}⊂porph$_2$ (left, structure **1** in Fig. 7) and $U_2C@D_{3h}$-C_{78}⊂porph$_2$ in their optimal orientations.

Conclusions

In summary, we report here the ability of supramolecular nanocapsule **1**·(BArF)$_8$ to selectively encapsulate U-based EMFs from highly complex soot containing empty fullerenes and EMFs, ranging from C_{60} to C_{96}. Moreover, the supramolecular host is capable of discriminating C_{78}-based EMFs from C_{80}-based EMFs, thus showing an exquisite ability to discriminate among very similar EMFs. This selectivity stems from the shape differences between a spherical I_h-C_{80} and a flattened D_{3h}-C_{78} carbon cage, and causes an enhanced interaction between the carbon cage and the porphyrin units of the host. Computational analysis also suggests that the breathing ability of the host in the solid state is somewhat limited and that results in a lower breathing energy penalty towards a highly favourable encapsulation of the ellipsoidal D_{3h}-C_{78}-based EMF. Moreover, nanocapsule **1**·(BArF)$_8$ can also sequentially and selectively encapsulate the same D_{3h}-C_{78} carbon cage differing only in the nature of the endohedral cluster, *i.e.* U_2 *vs.* U_2C. This indicates that besides the shape of the carbon cage, the cluster electronics are at interplay in finally determining the affinity for the host. The non-chromatographic supramolecular purification of U-based EMFs reported here has proven to be a viable alternative to HPLC methods, and pure $U_2@D_{3h}$-C_{78} and $U_2C@D_{3h}$-C_{78} EMFs may be accumulated and potentially find utility in several research fields. Moreover, nanocapsule **1**·(BArF)$_8$ and other supramolecular analogues might be designed as platforms to selectively purify targeted EMFs of interest in complex soot.

Conflicts of interest

There are no conflicts to declare.

Acknowledgements

We acknowledge financial support from GenCat (2017 SGR 264 and 2017 SGR 629) and MINECO-Spain (CTQ2016-77989-P and CTQ2017-87269-P). L. E. thanks the US National Science Foundation (NSF) for generous support of this work under the NSF-PREM program (DMR-1205302) and CHE-1408865. The Robert A. Welch Foundation is also gratefully acknowledged for an endowed chair to L. E. (Grant AH-0033). X. R. and J. M. P. are also grateful to ICREA foundation for ICREA-Acadèmia awards.

Notes and references

1 S. Yang, T. Wei and F. Jin, *Chem. Soc. Rev.*, 2017, **46**, 5005–5058.

2 X. Lu, T. Akasaka and S. Nagase, *Chem. Commun.*, 2011, **47**, 5942–5957.

3 X. Zhang, Y. Wang, R. Morales-Martínez, J. Zhong, C. de Graaf, A. Rodríguez-Fortea, J. M. Poblet, L. Echegoyen, L. Feng and N. Chen, *J. Am. Chem. Soc.*, 2018, **140**, 3907–3915.

4 X. Zhang, W. Li, L. Feng, X. Chen, A. Hansen, S. Grimme, S. Fortier, D.-C. Sergentu, T. J. Duignan, J. Autschbach, S. Wang, Y. Wang, G. Velkos, A. A. Popov, N. Aghdassi, S. TDuhm, X. Li, J. Li, L. Echegoyen, W. H. E. Schwarz and N. Chen, *Nat. Commun.*, 2018, **9**, 2753.

5 R. Westerström, J. Dreiser, C. Piamonteze, M. Muntwiler, S. Weyeneth, H. Brune, S. Rusponi, F. Nolting, A. Popov, S. Yang, L. Dunsch and T. Greber, *J. Am. Chem. Soc.*, 2012, **134**, 9840–9843.

6 S. Osuna, M. Swart and M. Solà, *J. Am. Chem. Soc.*, 2009, **131**, 129–139.

7 S. Osuna, M. Swart, J. M. Campanera, J. M. Poblet and M. Solà, *J. Am. Chem. Soc.*, 2008, **130**, 6206–6214.

8 M. Garcia-Borràs, S. Osuna, J. M. Luis, M. Swart and M. Solà, *Chem. – Eur. J.*, 2012, **18**, 7141–7154.

9 N. Martín, *Chem. Commun.*, 2006, 2093–2104, DOI: 10.1039/B601582B.

10 C. M. Cardona, A. Kitaygorodskiy and L. Echegoyen, *J. Am. Chem. Soc.*, 2005, **127**, 10448–10453.

11 Y. Iiduka, O. Ikenaga, A. Sakuraba, T. Wakahara, T. Tsuchiya, Y. Maeda, T. Nakahodo, T. Akasaka, M. Kako, N. Mizorogi and S. Nagase, *J. Am. Chem. Soc.*, 2005, **127**, 9956–9957.

12 H. Shinohara and N. Tagmatarchis, in *Endohedral Metallofullerenes*, Wiley, 2015, pp. 43–68, DOI: 10.1002/9781118698006.ch4.

13 S. Stevenson, K. Harich, H. Yu, R. R. Stephen, D. Heaps, C. Coumbe and J. P. Phillips, *J. Am. Chem. Soc.*, 2006, **128**, 8829–8835.

14 S. Stevenson, M. A. Mackey, J. E. Pickens, M. A. Stuart, B. S. Confait and J. P. Phillips, *Inorg. Chem.*, 2009, **48**, 11685–11690.

15 K. Akiyama, T. Hamano, Y. Nakanishi, E. Takeuchi, S. Noda, Z. Wang, S. Kubuki and H. Shinohara, *J. Am. Chem. Soc.*, 2012, **134**, 9762–9767.

16 M. R. Cerón, F. F. Li and L. Echegoyen, *Chem. – Eur. J.*, 2013, **19**, 7410–7415.

17 L. P. Hernández-Eguía, E. C. Escudero-Adán, J. R. Pinzón, L. Echegoyen and P. Ballester, *J. Org. Chem.*, 2011, **76**, 3258–3265.

18 M.-Y. Ku, S.-J. Huang, S.-L. Huang, Y.-H. Liu, C.-C. Lai, S.-M. Peng and S.-H. Chiu, *Chem. Commun.*, 2014, **50**, 11709–11712.

19 Y. Nakanishi, H. Omachi, S. Matsuura, Y. Miyata, R. Kitaura, Y. Segawa, K. Itami and H. Shinohara, *Angew. Chem., Int. Ed.*, 2014, **53**, 3102–3106.

20 C. Fuertes-Espinosa, C. García-Simón, E. Castro, M. Costas, L. Echegoyen and X. Ribas, *Chem. – Eur. J.*, 2017, **23**, 3553–3557.

21 C. Fuertes-Espinosa, A. Gómez-Torres, R. Morales-Martínez, A. Rodríguez-Fortea, C. García-Simón, F. Gándara, I. Imaz, J. Juanhuix, D. Maspoch, J. M. Poblet, L. Echegoyen and X. Ribas, *Angew. Chem., Int. Ed.*, 2018, **57**, 11294–11299.

22 C. García-Simón, M. Garcia-Borràs, L. Gómez, T. Parella, S. Osuna, J. Juanhuix, I. Imaz, D. Maspoch, M. Costas and X. Ribas, *Nat. Commun.*, 2014, **5**, 5557.

23 A. Schneemann, V. Bon, I. Schwedler, I. Senkovska, S. Kaskel and R. A. Fischer, *Chem. Soc. Rev.*, 2014, **43**, 6062–6096.

24 Y. Li, L. Yang, Z. Li, Q. Hou, L. Li and P. Jin, *Inorg. Chem.*, 2019, **58**, 10648–10655.

Chapter Chapter VII.

Results and Discussion

Coordination-driven self-assembly has opened up new routes for the preparation of highly sophisticated hollow nanocapsules that can be prepared in a straightforward manner. The functionality of these newly designed supramolecular scaffolds provides new opportunities to address efficiently practical problems, such as the design of functional platforms for molecular recognition,[1] separations,[2] stabilization of reactive species[3] and catalysis[4].

From this perspective, QBIS-CAT group has successfully employed subcomponent self-assembly to prepare complex metal-organic 3D nanocapsules from simple building blocks via simultaneous formation of dynamic coordinative bonds. Our group has synthesized and designed a set of hexaaza macrocyclic di-palladium(II) complexes (**Clip 1a**, **Clip 2** and **Clip 3**) with different lengths, which can be considered as molecular pillars (Figure VII.1). The coordination vacancy of the palladium(II) ions, featuring a square-planar geometry, lead to the preparation of heteroleptic 3D coordination nanocapsules through self-assembly reactions with tetracarboxylated metalloporphyrins (M-Porph). The tetragonal prismatic capsules so far reported by the group, i.e. $[(\textbf{Clip 1a})_4(\text{M-Porph})_2]^{8+}$ ($[\textbf{1a}]^{8+}$), $[(\textbf{Clip 2}]_4[\text{M-Porph}]_2]^{8+}$ ($[\textbf{2}]^{8+}$) and $[(\textbf{Clip 3}]_4[\text{M-Porph}]_2]^{8+}$ ($[\textbf{3}]^{8+}$), show inner void cavities with different sizes and geometries (Figure VII.1). The fundamental investigations on the host-guest chemistry of these nano-vessels have led to the development of useful functions and applications in the field of molecular recognition,[5] separation of valuable molecules[6] and catalysis[7].

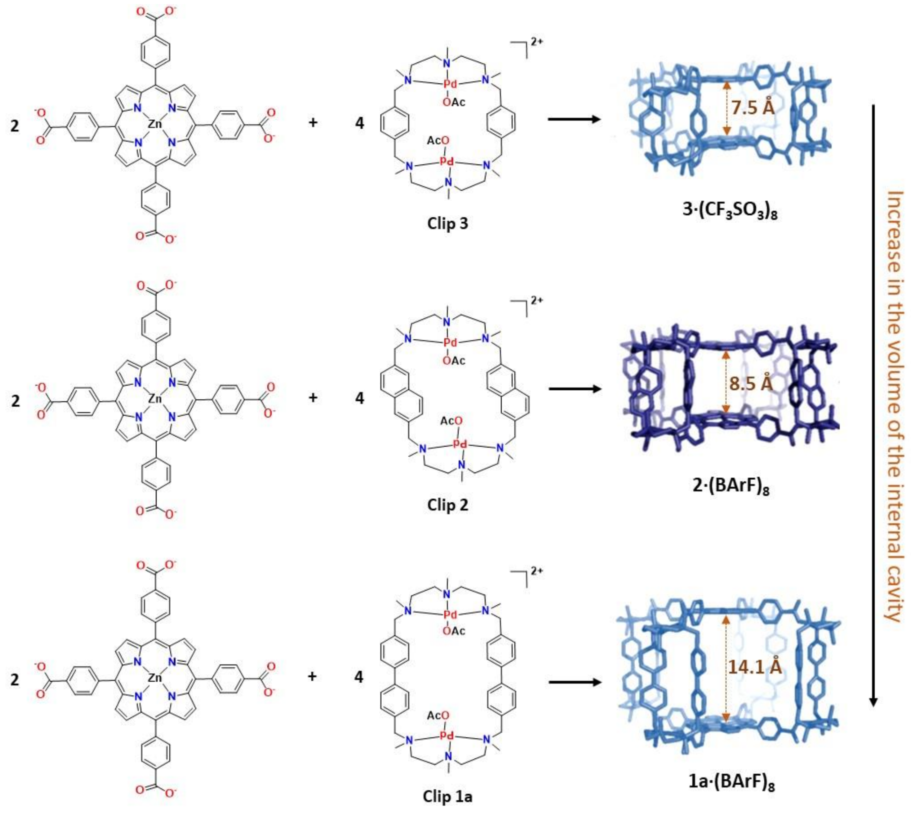

Figure VII.1. Library of the molecular pillars and 3D coordination capsules structures previously reported by QBIS-CAT group.

In 2014, QBIS-CAT group reported **1a**·$(\text{BArF})_8$ supramolecular capsule, bearing the largest cavity among all the supramolecular capsules reported by the group.[6] Such large capsules are attractive because they provide specific platforms to bind large guest selectively, such as fullerenes (Figure VII.2). The functionality of **1a**·(BArF)$_8$ to act as a host for fullerenes was tested with pure C_{60} and C_{70}, yielding in both cases very stable host-guest complexes (association constants are logK_a= 7.44±0.1 and logK_a= 8.6±0.3, respectively). Very interestingly, taking advantage of the orthogonal solubility between the host and the guest, C_{60} can be selectively released by a solvent-washing strategy, which consists in washing a solid sample of the host-guest complex (C_{60}⊂**1a**·(BArF)$_8$) with an appropriate mixture of solvents (Figure VII.2). When the capsule is subjected to a solution of fullerene mixture (containing fullerenes from C_{60} to C_{84}), all the species contained on the sample were encapsulated. However, C_{60} was the only species that can be released by the solvent-washing protocol.

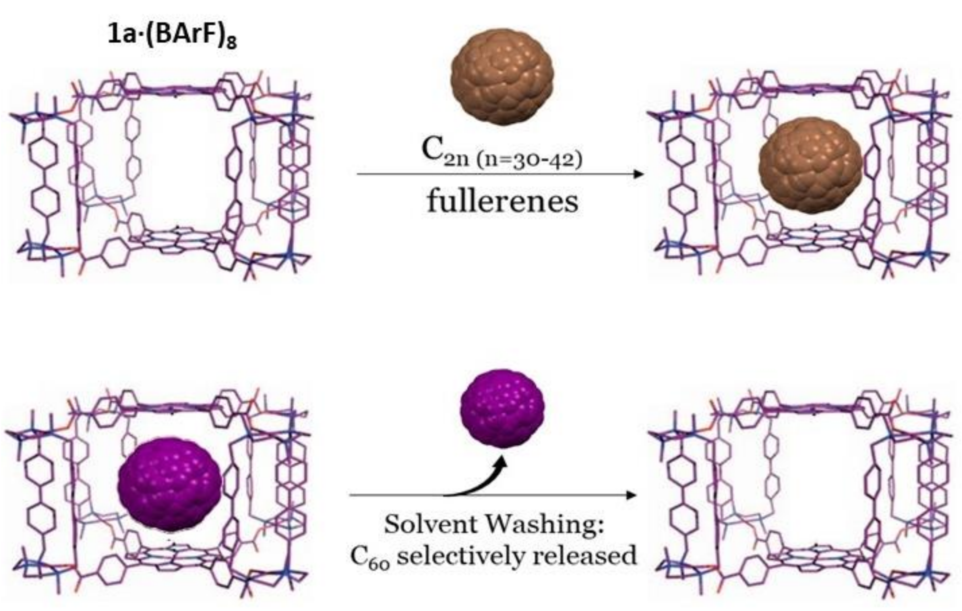

Figure VII.2. Graphical representation of fullerene guest encapsulation within the cavity of 1a·(BArF)$_8$ (top) and C_{60} by using a solvent-washing protocol (bottom)

Furthermore, **1a**·(BArF)$_8$ allowed the use of its internal cavity as an isolated environment to perform catalytic transformations, via the anchoring of active catalysts by axial coordination to the Zn-Porphyrin units.[7] With these considerations in mind, in this thesis is expected to further expand the functionality of **1a**·(BArF)$_8$ as a reactor nano-vessel for the challenging regioselective preparation of fullerene derivatives.

In this thesis we targeted the preparation of a copper(II) based 3D tetragonal prismatic heteroleptic nanocapsule **1b**·(BArF)$_8$, which is the Cu(II) analogue of the Pd(II)-based **1a**·(BArF)$_8$ (Figure VII.2). The Pd(II) metal nodes were replaced by Cu(II), hypothesizing that Cu(II)-carboxylate bonds might be more labile and flexible than Pd(II)-carboxylate bonds, thus facilitating the liberation of larger fullerene or EMFs guests.

VII.1. Supramolecular Fullerene Sponges as Catalytic Masks for Regioselective Functionalization of C_{60}

This section corresponds to the contents of the manuscript by Fuertes-Espinosa et al., *Chem* **2020**, 6, 169-186, which can be found in chapter III of this thesis.

Controlling the chemo- and the regiochemistry of exohedral multiple functionalization of fullerenes is crucial to broaden the applications of these valuable compounds. From a general point of view, multi-adduct mixtures are obtained, and their chromatographic purification is very expensive and time consuming. Regioisomerically pure poly-functionalized fullerene derivatives are highly demanded, however, these valuable compounds are only accessible via stoichiometric and multistep protocols. To accelerate the progress of fullerene chemistry, it is desirable to develop new straightforward methods for the controlled synthesis of fullerene derivatives. With these considerations, our group developed a supramolecular mask strategy, which exert full control on the reactivity and the regioselectiviti of multiple cyclopropanation reactions of confined fullerene C_{60}.

VII.1.1. Synthesis and Characterization of Equatorial Tetrakis-adducts

The supramolecular host **1a**·$(BArF)_8$ and its Cu(II) analog **1b**·$(BArF)_8$ were synthesized following the protocols previously reported by QBIS-CAT group (details for the synthesis of the **1b**·$(BArF)_8$ will be described in the next section VII.2).

In order to gain control during the production of these functional materials, C_{60} was encapsulated within **1a**·$(BArF)_8$ and subjected to standard conditions commonly used for Bingel-Hirsch cyclopropanation reaction (4 equiv. of diethyl bromomalonate and 4 equiv. of NaH). ESI-HRMS monitoring of the reaction revealed a step-wise and quantitative formation of tetrakis-diethylmalonate-C_{60} derivative **2**, after 2 hours (Figure VII.3). Full spectroscopic and spectrometric characterization of the released derivative **2** (via exchange with pristine C_{60} or by capsule disassembly) unequivocally assigned the tetrakis-adduct to a D_{2h}-symmetric *e,e,e,e*-regioisomer (Figure VII.4). Blank experiments further confirmed that the confinement of C_{60} completely modifies not only the reactivity in acetonitrile but also the outcome of the reaction, directing the nucleophilic attack exclusively to the exposed equatorial bonds of the C_{60} and overcoming the over reactivity commonly observed.

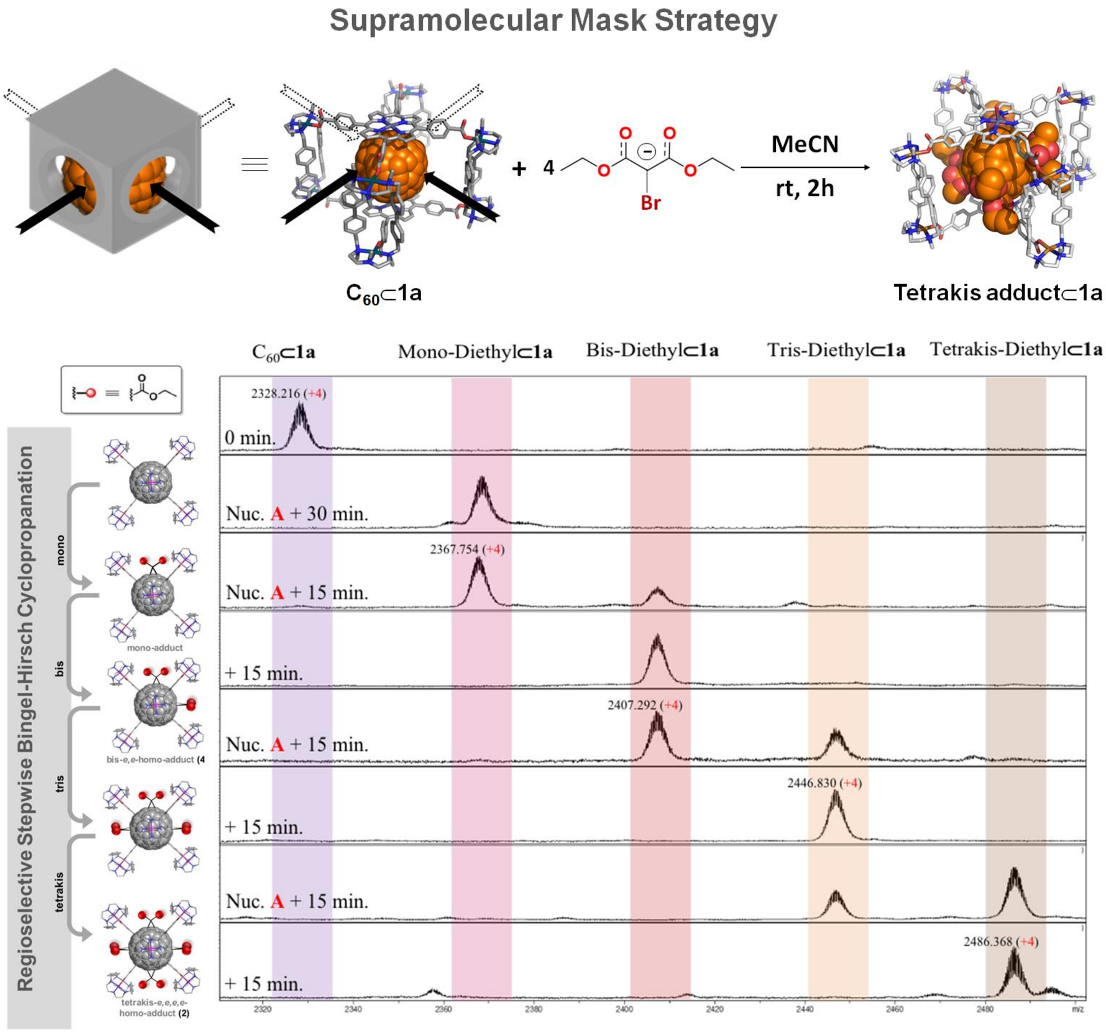

Figure VII.3. ESI-HRMS spectra of stepwise formation of mono-, bis-, tris- and tetrakis-equatorial adducts upon the addition of nucleophile and base to C_{60}⊂**1a**·(BArF)$_8$ (ESI-MS, Positive ion mode, CH_3CN).

Albeit high quality crystals of **2**⊂**1a**·(BArF)$_8$ could not be obtained, we succeed in crystalizing the trapped tetrakis adduct **2** within the analogous Cu(II) based scaffold, i.e. **2**⊂**1b**·(BArF)$_8$, suitable for X-ray analysis under synchrotron radiation. The crystallographic data revealed that the four malonate groups are pointing towards the capsule cross-shaped apertures (Figure VII.4 a). No atom delocalization was onserved in the crystal structure, indicating that the rotation of the guest is impeded or restricted within the nanocapsule. This hypothesis was confirmed by Molecular Dynamic (MD) simulations of the system **2**⊂**1b**·(BArF)$_8$, which showed a totally restricted motion of the malonate addends within a single aperture of the host (Figure VII.5 a and b). Interestingly, the MD simulations revealed persistent CH···π interactions between the alkyl esters of the malonate addends and the aromatic panels present on the **1b**·(BArF)$_8$ cavity, orienting the functional groups towards the molecular pillars instead to stay fixed at the center of the open gates (Figure VII.5 c).

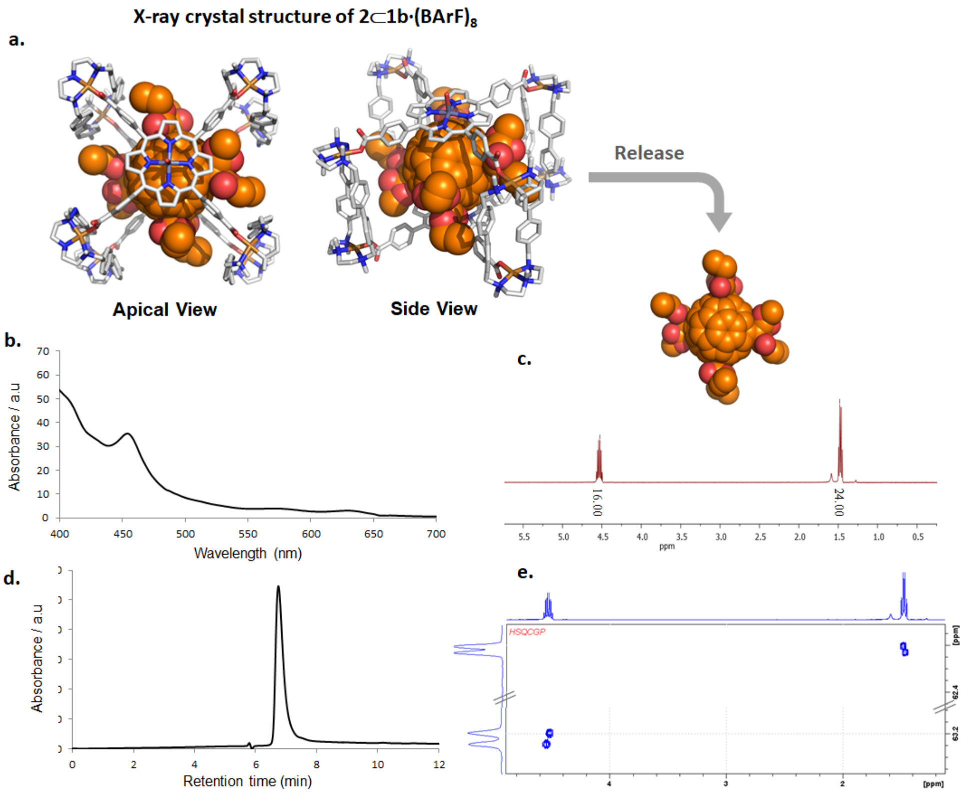

Figure VII.4. a) X-ray crystal structure of **2**⊂**1b**·(BArF)$_8$ (side and apical view), depicting the tetrakis-adduct **2** docked in the nanocapsule **1b**·(BArF)$_8$ (solvent, anions and H atoms are removed for clarity) **b)** UV-vis spectrum (298 K toluene) **c)** 1H-NMR spectrum (500 MHz, 298 K, CDCl$_3$). d) HPLC chromatogram (BuckyPrep M, 0.5 mL/min, 320 nm, toluene) and e) 2D ^{1}H-^{13}C spectral-aliased heteronuclear single quantum correlation (HSQC) spectrum (500 MHz, 298 K, CDCl$_3$) of isolated tetrakis-adduct **2**.

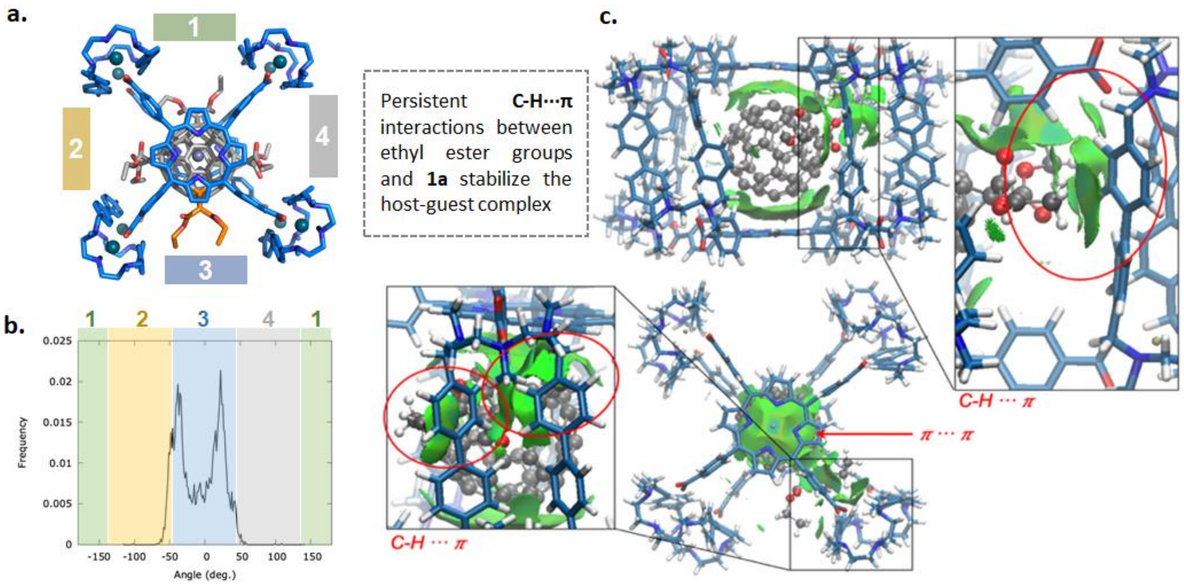

Persistent **C-H···π** interactions between ethyl ester groups and **1a** stabilize the host-guest complex

Figure VII.5. a and b) Analysis of geometric features of **2**⊂**1a**·(Cl)$_8$ complex from 500 ns MD simulations (distances are given in Å and dihedral angles in degrees). **c)** Noncovalent interaction analysis (NCI) revealed the appearance of persistent C–H/p interactions (stabilizing interactions shown as green surfaces) between ester alkyl and the aromatic rings of the nanocapsule.

Following the procedure described above, the substrate scope could be further expanded by using other nucleophiles, such as dimethyl bromomalonate, obtaining a single *e,e,e,e*-regioisomer of tetrakis-dimethylmalonate-C_{60} (Annex. Supp. Info. Chapter III, Supplementary methods, adduct **3**).

VII.1.2. Stepwise Synthesis and Characterization of Equatorial Bis- and Tris-Adducts

From a general point of view, the over-reactivity during the production of fullerene derivatives remains a standing problem, because functionalized C_{60} derivatives are more susceptible towards nucleophilic attacks than pristine C_{60}. However, this persistent over-reactivity problem was completely avoided by performing the reaction into the confined environment of **1a**·(BArF)$_8$. Thanks to the smooth stepwise formation from mono- to tetrakis-adducts by controlling the stoichiometry of the reaction and using a weaker base (NaOAc instead of NaH), a single bis-C_{60} derivative (**4**) could be selectively produced. The full characterization of the released derivative **4** revealed the exclusive formation of C_s-symmetric *e,e*-regioisomer (Annex. Supp. Info. Chapter III, Figure S1), contrasting with seven bis-regioisomers formed in bulk solution (Figure VII.6 c). To get further insights about the regioselectivity induced by the host for the formation of bis-adducts, we performed a conformational analysis of the precursor mono-diethylmalonate-C_{60} within the host cavity (Figure VII.6 a and b). The MD simulations showed that the rotation of the malonate group from one cage aperture to the other is allowed, although partially restricted orientation of the cyclopropane ring were observed, indicating that the orientation of the cyclopropane ring perpendicular to the porphyrin units is favored (as shown in the histogram of Figure VII.6 b). The partially restricted rotation of the mono-diethylmalonate adduct, affected the orientation of the malonate during the second nucleophilic attack, defining the regiochemistry of the bis-adduct formed. However, since both malonate groups in bis-adduct **4** are identical, only one possible equatorial regioisomer can be formed. Conversely to the formation of bis-adduct **4**, the partially restricted rotation of the mono-adduct has a strong effect on the regiochemistry for the formation of hetero-tetrakis-adducts as it will be discussed below.

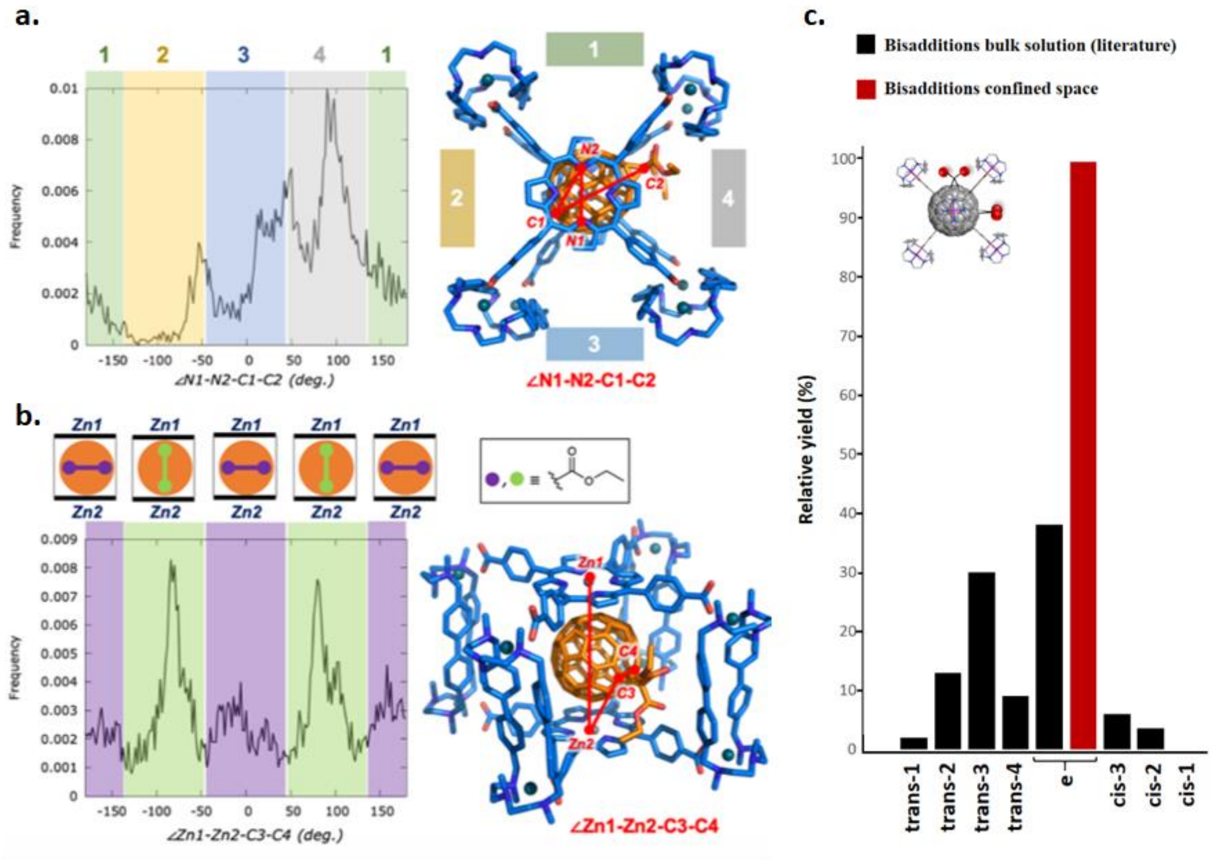

Figure VII.6. a) ∠N1-N2-C1-C2 dihedral angle measured along the MD trajectory of **mono-adduct⊂1a**·(Cl)$_8$. ∠N1-N2-C1-C2 angle describes the relative rotation of the encapsulated fullerene with respect to the capsule, and most visited angle values are shown in the histogram plot (frequency vs. angle value). Different capsule windows (labelled as 1, 2, 3, and 4 in the figure) correspond to different ranges of explored angle values. **b)** ∠Zn1- Zn2-C3-C4 dihedral angle measured along the MD trajectory. ∠Zn1-Zn2-C3-C4 angle describes the relative orientation of the cyclopropane ring with respect to the capsule. ∠Zn1-Zn2-C3-C4 values around 0º and ±180º indicate that the cyclopropane ring stay perpendicular to the porphyrins, while values around ±90º indicate that the cyclopropane ring stays in a parallel conformation with respect to the porphyrins. **c)** Comparison between C$_{60}$ regioisomers obtained in bulk solution and using the supramolecular confinement strategy for bis-adducts.

Analogous to the production of bis-derivatives, the synthesis of equatorial tris-adducts was attained, yielding equimolar amounts of two equatorial and non-chiral isomers **5a** and **5b** (assigned by 1D and 2D NMR) (Figure VII.7 c and Annex. Supp. Info. Chapter III, Figure S2). It is worth to note, that the formation of both **5a** and **5b** isomers are completely unprecedented in bulk solution experiments. The conformational analysis of **4⊂1a**·(Cl)$_8$ host-guest complex by MD simulations revealed that the second nucleophilic attack blocks fullerene gate-to-gate and spin motions completely (Figure VII.7 a and b). Due to the restricted rotation of the confined bis-adduct **4**, the two bonds remaining in the equatorial plain of **4** are exposed to the capsule cross-shaped cavity apertures, being both of them equally susceptible to react. Therefore, these restrictions defined the final statistical mixture of both tris-adducts **5a** and **5b** formed.

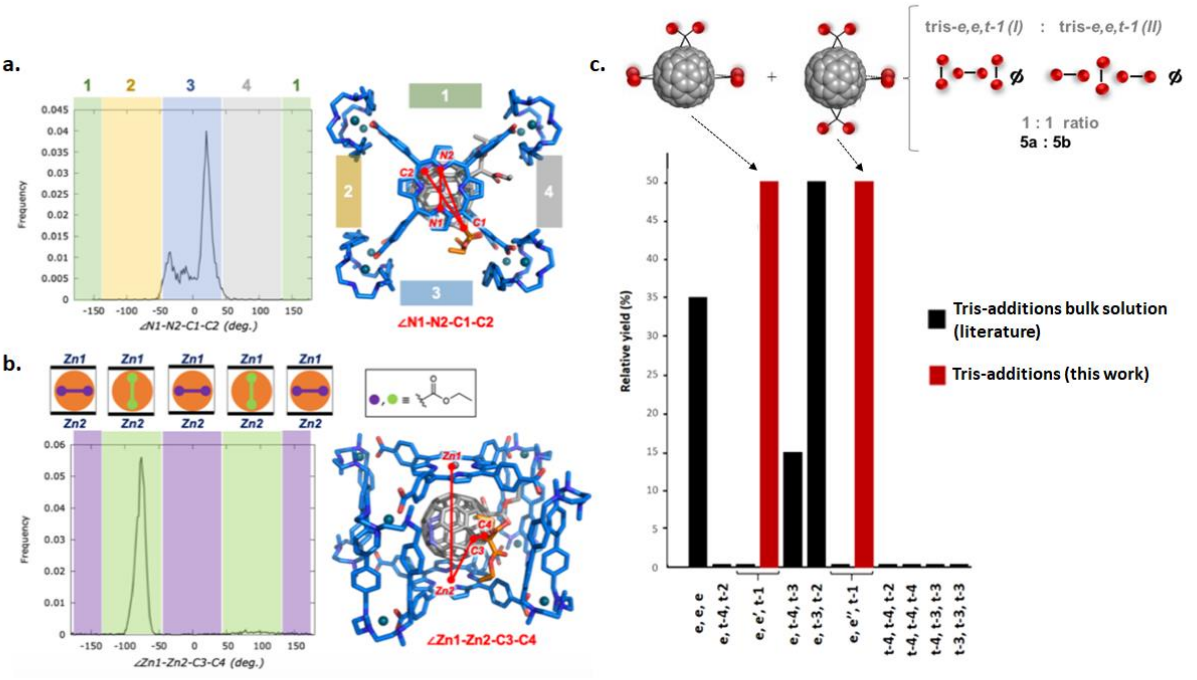

Figure VII.7. a) ∠N1-N2-C1-C2 dihedral angle measured along the MD trajectory of **4⊂1a**·(Cl)$_8$. ∠N1-N2-C1-C2 angle describes the relative rotation of the encapsulated fullerene with respect to the capsule, and most visited angle values are shown in the histogram plot (frequency versus angle value). Different capsule windows (labeled as 1, 2, 3, and 4 in the figure) correspond to different ranges of explored angle values. **b)** ∠Zn1-Zn2-C3-C4 dihedral angle measured along the MD trajectory. ∠Zn1-Zn2-C3-C4 angle describes the relative orientation of the cyclopropane ring with respect to the capsule. ∠Zn1-Zn2-C3-C4 values around 0º and ±180º indicate that the cyclopropane ring stay perpendicular to the porphyrins, while values around ±90º indicate that the cyclopropane ring stays in a parallel conformation with respect to the porphyrins. Distances and angles are given in angstroms (A°) and degree, respectively. **c)** Comparison between C_{60} regioisomers obtained in bulk solution and using the supramolecular confinement strategy for tris-adducts.

VII.1.3. One-Pot Synthesis of Equatorial Hetero-Tetrakis-Adducts

Prompted by the stepwise chemo- and regio-control observed during the production of homo-C_{60} derivatives, we pursued to expand the supramolecular mask strategy for the preparation of more challenging hetero-tetrakis-adducts in a one-pot reaction. Upon the selective formation of *e,e*-dimethyl-bis-adduct (addition of 2 equiv of dimethyl bromomalonate and 2 equiv of NaOAc in a solution of C_{60}⊂**1a**·(BArF)$_8$ in acetonitrile), 2 equiv of diethyl bromomalonate and 2 equiv of NaOAc were added to the reaction mixture, furnishing the fully equatorial hetero-D_{2h}-tetrakis-adduct *e,e*-bis-diethyl-*e,e*-bis-dimethylmalonate-C_{60} (**6**) as a single isomer in very high purity and excellent yield (97% yield) (Figure Annex. Supp. Info. Chapter III, Figure S3). The efficiency and the versatility of the nanocapsule to act as a platform for the one-pot synthesis of hetero-C_{60} derivatives, was further exemplified by the preparation of the fully equatorial *e,e,t-1(I)*-tris-dimethyl-*e*-mono-diethylmalonate-C_{60} (**7a**) (Figure VII.8). Once the mono-diethylmalonate-C_{60} was formed, the addition of 3 equiv of dimethylmalonate and 3 equiv of NaH on the reaction crude, afforded derivative **7a (**Figure VII.8 a). However, thorough 1D and 2D NMR analyses showed the presence of other equatorial isomer **7b** (e,e,t-1(II)-tris-dimethyl-e-mono-diethylmalonate-C_{60}) in minor amount (2.5:1 **7a**:**7b**) (Figure VII.8 b and Annex. Supp. Info. Chapter III, Figure S4).

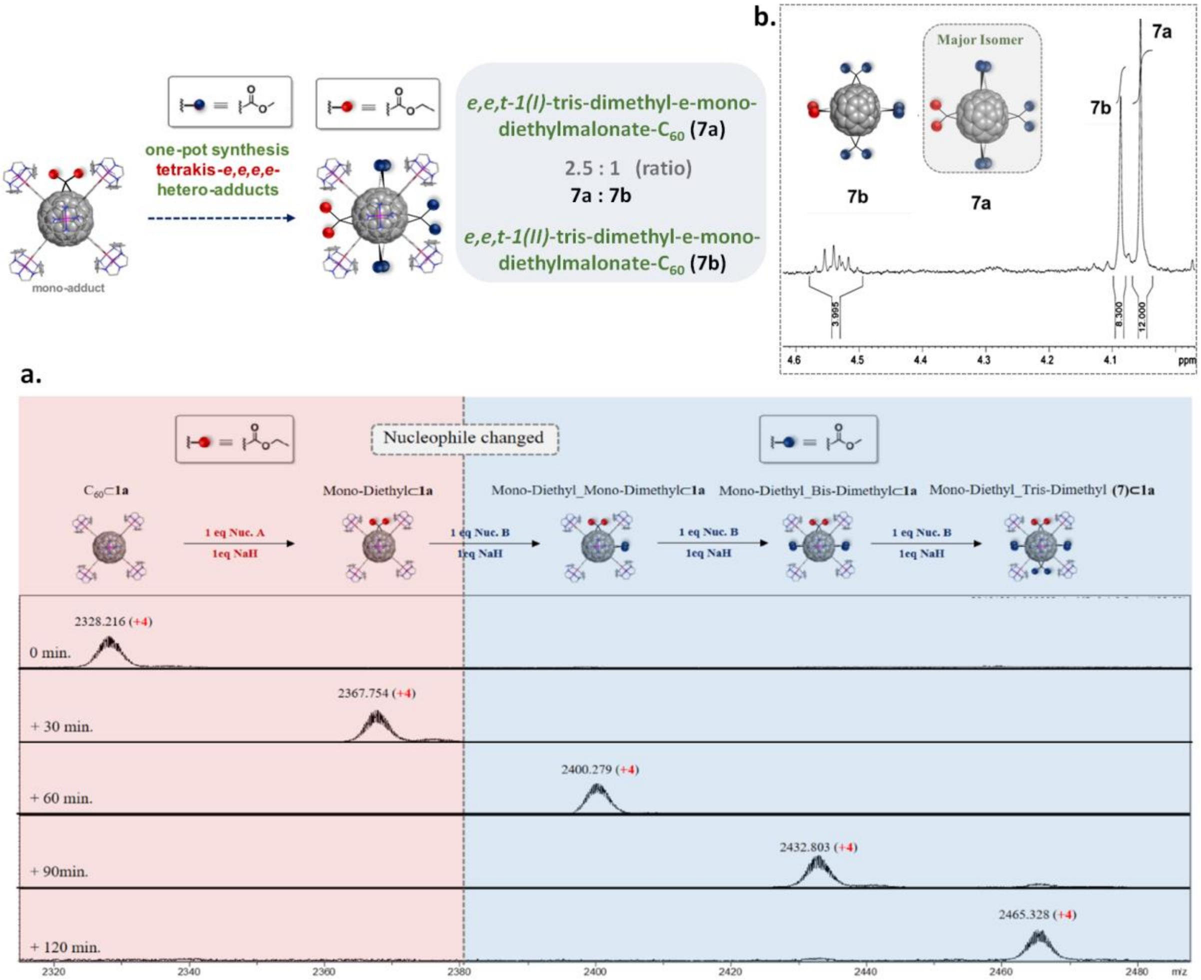

Figure VII.8. a) ESI-HRMS spectra monitoring the formation of (**7a**/**7b**)⊂**1a**·(BArF)$_8$ (Nuc. A: diethyl bromomalonate, Nuc. B: dimethyl bromomalonate) (ESI-MS, Positive ion mode, CH_3CN). **b)** ^{1}H-NMR spectrum of adduct **7a**/**7b** (500 MHz, 298 K, $CDCl_3$), highlighting the multiplet at the methylene region (4.57-4.51 (4H) and the singlets of the methoxide region (4.09 (8H, s), 4.05 (12H, s); the integration area of the methoxide and the methylene signals agrees with a **7a**:**7b** ratio of 2.5:1

To get a better understanding of the parameters dictating the preferential formation of **7a**, the same synthetic protocol was performed using mono-dimethylmalonate-C$_{60}$ adduct as precursor followed by the addition of 3 equivalents of diethyl bromomalonate and base. The products obtained consisted in a mixture of *e,e,t-1(I)*-tris-diethyl-*e*-mono-dimethylmalonate-C$_{60}$ (**8a**) and *e,e,t-1(II)*-tris-diethyl-*e*-mono-dimethylmalonate-C$_{60}$ (**8b**) in ratio 2.8:1 (**8a**:**8b**) (Figure VII.9), which is similar to the ratio observed for the formation of **7a** and **7b**. Aiming at getting further insight in the product distribution observed, the stepwise formation of tris-adducts were studied by MD simulations. The study suggested that the gate-to-gate motion of the malonate groups of the trapped fullerene derivative is completely restricted once the bis-adducts are formed (Figure VII.8 a and b). Conversely, mono-adducts showed higher degree of rotation in the capsule cavity, not only the gate-to-gate motion of the malonate is permitted, but also, it can spin around the cyclopropane axis (Figure VII.6 a and b). Taken together, the simulations indicated that a combination of the preferential orientation of the second malonate attack, and a more favored conformation of the cyclopropane ring of the mono-adduct, fixed the fullerene guest in the capsule cavity yielding **7a** and **8a** in higher ratios. The preferential orientation of the second malonate group during the nucleophilic attack, might be dictated by the non-covalent interactions of the ester groups and the aromatic panels present on the capsule pillars, as observed by MD.

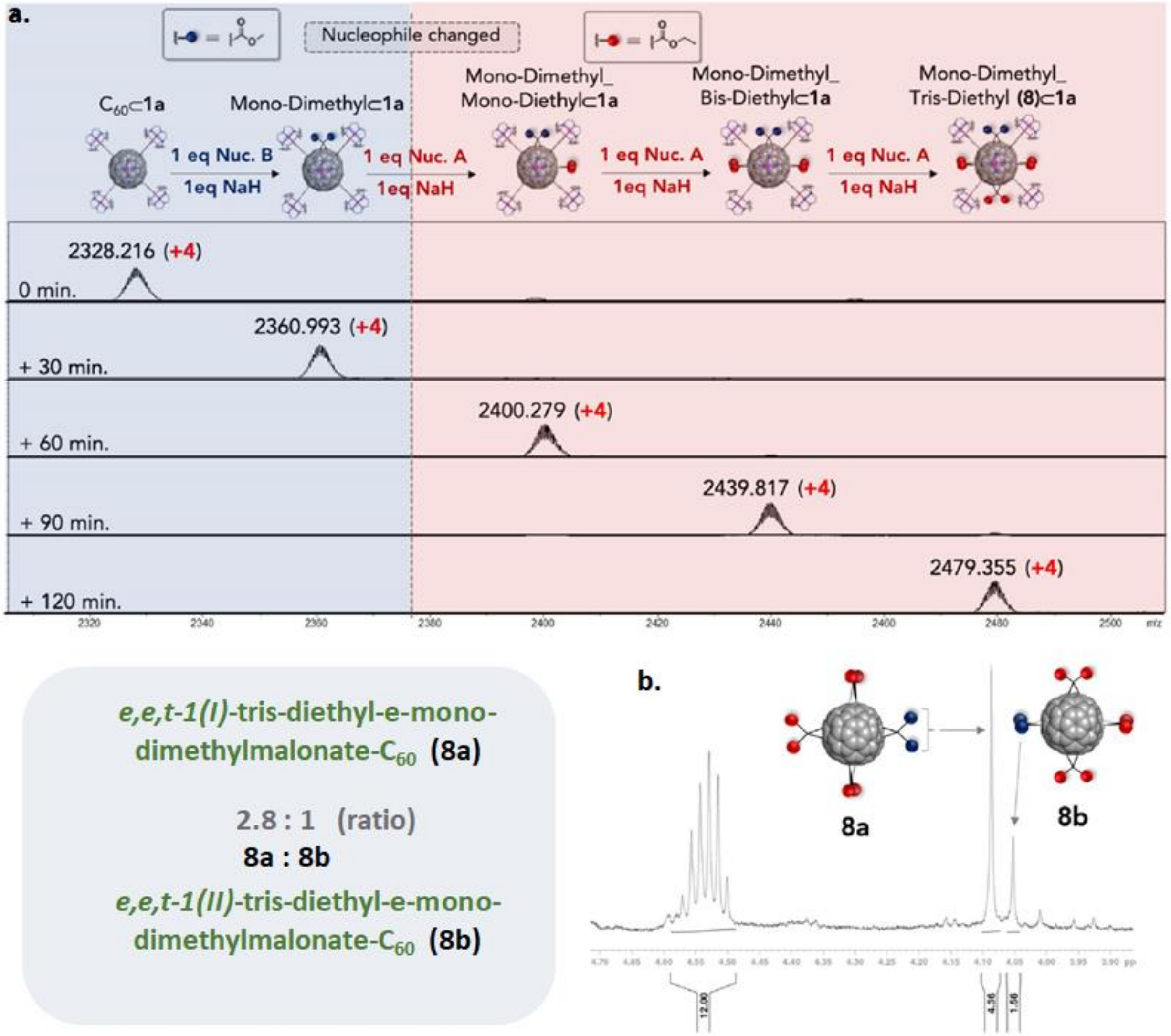

Figure VII.9. a) ESI-HRMS spectra monitoring the formation of (**8a/8b**)⊂**1a**·(BArF)$_8$ (Nuc. A: dimethyl bromomalonate, Nuc. B: diethyl bromomalonate) (ESI-MS, Positive ion mode, CH$_3$CN). **b)** ^{1}H-NMR spectrum of adduct **8a/8b** (500 MHz, 298 K, CDCl$_3$), highlighting the multiplet at the methylene region (4.60-4.50 (4H) and the singlets of the methoxide region (4.09 (4.5H, s), 4.05 (1.5H, s); the integration area of the methoxide and the methylene signals agrees with a **8a**:**8b** ratio of 2.8:1

VII.1.4. One-Pot Synthesis of Equatorial Hetero-Hexakis-Adducts

The versatility of the designed supramolecular mask strategy for the preparation of hetero-poly-adducts, was further exploited by the synthesis of hetero-hexakis-adducts. We observed that by adding an excess of a different nucleophile upon the selective formation of *e,e,e,e*-tetrakis-diethylmalonate-C_{60} within the host, a single isomer of *Th*-hexakis-hetero-adduct (**9**) was produced, as ascertained by UV-Vis, ESI-MS and multidimensional NMR experiments (Figure VII.10 and Supporting X). It is well known that the four equatorial malonate groups of **2**, exert a regiochemical control on the subsequent nucleophilic attacks, directing the additions exclusively to the available axial positions.[8] The presented host can be potentially used as a platform to obtain almost all possible combinations of *Th*-hexakis hetero adducts with octahedral geometry ,using two different addends.[9]

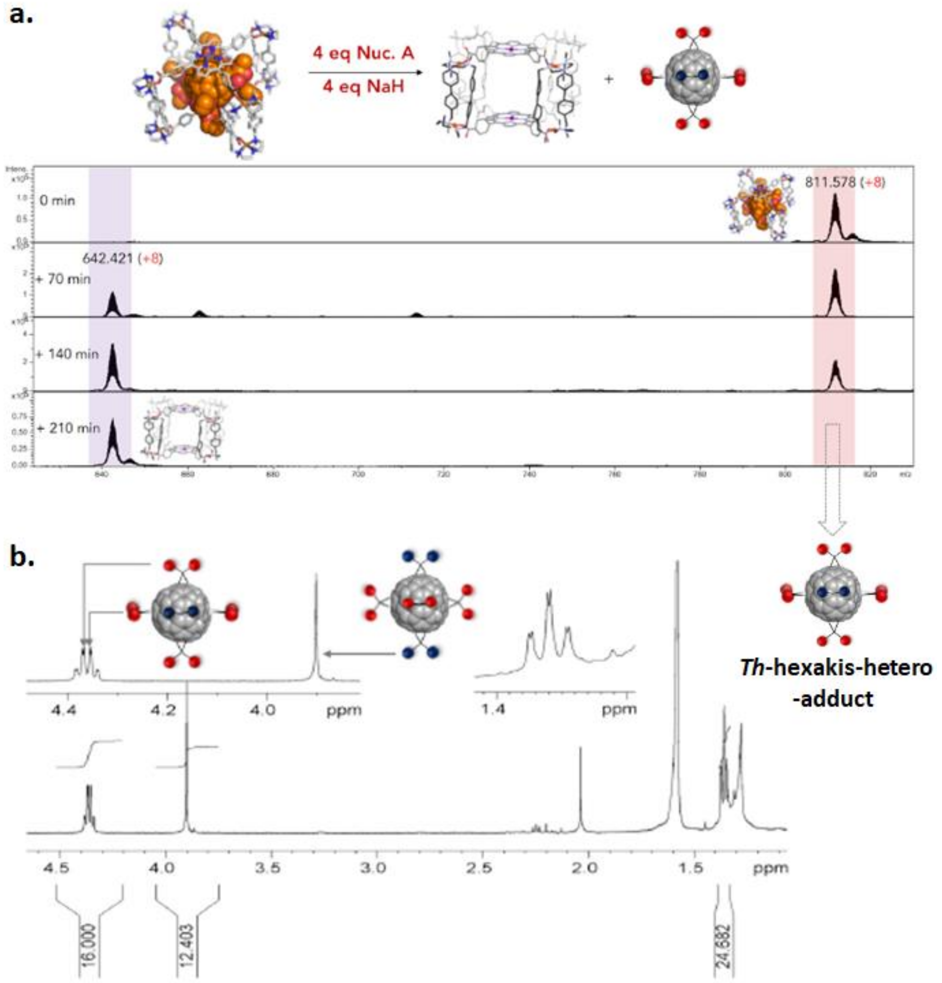

Figure VII.10. a) ESI-HRMS spectra monitoring for the formation of **9** from **2**$\subset$**1a**·(BArF)$_8$. Adduct **2** was released from **2**$\subset$**1a**·(BArF)$_8$ upon the addition of nucleophile B, forming adduct **9** outside the capsule thus observing the formation of empty cage (nucleophile B, dimethyl bromomalonate). **b)** ^{1}H-NMR spectrum of **9** (500 MHz, 298 K, $CDCl_3$), showing two overlapped quadruplets at 4.35 and 4.36 ppm and two overlapped triplets at 1.358 and 1.361 ppm corresponding to the ethyl ester groups oriented vertical or horizontal with respect to the equatorial region, and one singlet at 3.90 ppm corresponding to the methyl esters located at the axial positions of the *Th*-hexakis-adduct.

It is worth to note that the hydrodynamic radii calculated by NMR spectroscopy (DOSY-NMR experiments) for all the fullerene derivatives produced showed good correlation with the expected increasing bulkiness of the molecules (Figure VII.11).

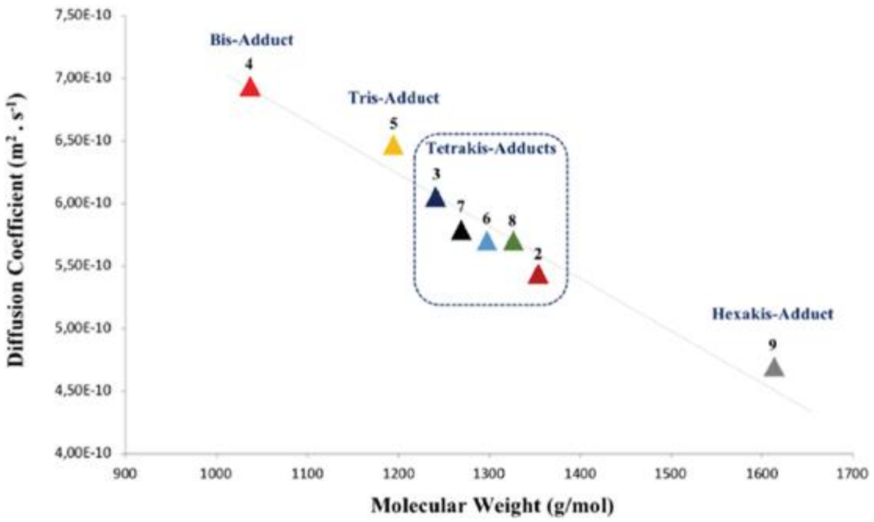

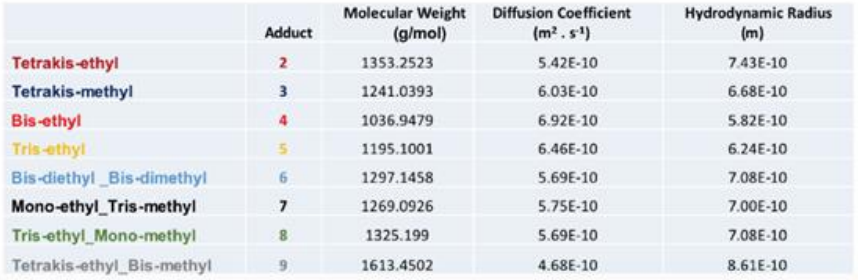

	Adduct	Molecular Weight (g/mol)	Diffusion Coefficient (m^2 . s^{-1})	Hydrodynamic Radius (m)
Tetrakis-ethyl	2	1353.2523	5.42E-10	7.43E-10
Tetrakis-methyl	3	1241.0393	6.03E-10	6.68E-10
Bis-ethyl	4	1036.9479	6.92E-10	5.82E-10
Tris-ethyl	5	1195.1001	6.46E-10	6.24E-10
Bis-diethyl _Bis-dimethyl	6	1297.1458	5.69E-10	7.08E-10
Mono-ethyl_Tris-methyl	7	1269.0926	5.75E-10	7.00E-10
Tris-ethyl_Mono-methyl	8	1325.199	5.69E-10	7.08E-10
Tetrakis-ethyl_Bis-methyl	9	1613.4502	4.68E-10	8.61E-10

Figure VII.11. Correlation between DOSY NMR diffusion coefficients and molecular weight of each adduct (500 MHz, 298 K, $CDCl_3$). Tabulated Diffusion Coefficients (D) and Hydrodynamic radii (rH) for each of adducts produced calculated from Stokes-Einstein equation.

VII.1.5. Biphasic protocol for the Catalytic Synthesis of the Tetrakis-Adduct 2

Finally, we explored the design a biphasic system to perform the regioselective functionalization reaction under cyclic turnover conditions. The feasibility to reversibly transfer **1a**·(BArF)$_8$ (with and without cargo) from the organic (toluene:CH_2Cl_2, 1:1) to the aqueous phase (H_2O:DMSO, 9:1) upon the addition of 5 equivalents of $(nBu_4N)_2SO_4$ was confirmed by ^{1}H-NMR and ESI-HRMS (Annex. Supp. Info. Chapter III, Figure S7). The nanocapsule was transferred back to the organic phase by addition of 10 equivalents of NaBArF (Annex. Supp. Info. Chapter III, Figure S7). The reversible phase transfer catalytic system was implemented by adding 1 equivalent of **1a**·(BArF)$_8$ and 20 equivalents of C_{60} in the organic layer, and 60 equivalents of bromomalonate and 60 equivalents of NaOAc in the aqueous layer (Figure VII.12). After the fast inclusion of C_{60}, the host-guest adduct was transferred to the aqueous layer by adding 5 equivalents of $(nBu_4N)_2SO_4$. The counteranion metathesis simultaneously triggers the phase transfer and the Bingel-Hirch reaction, due to the aqueous phase contains the reactants (the diethyl bromomalonate and NaOAc). After 24 hours the reaction was complete and the addition of 10 equivalents of NaBArF brought the encapsulated tetrakis-adduct **2** into the organic phase, exchanging the reaction product by a new molecule of C_{60}, due to its excess and the higher affinity of the host towards it (25-fold higher affinity than the tetrakis-adduct). Subsequent addition of 5 equivalents more of $(nBu_4N)_2SO_4$ started the next cyclic turnover.

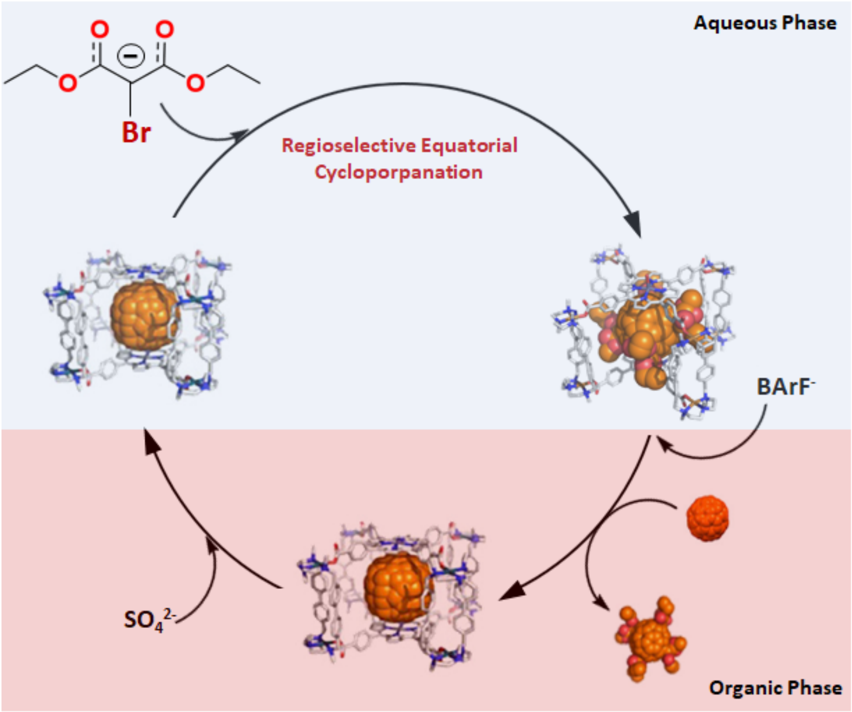

Figure VII.12. Regioselective synthesis of tetrakis-adduct **2** using a reversible phase transfer of $\mathbf{C_{60}\subset 1a}$ from the organic to the aqueous phase and $\mathbf{2\subset 1a}$ from the aqueous phase to the organic. The phase transfer is mediated via counter-anion metathesis reactions.

After 10 cycles, product **2** was quantitatively formed and the HPLC analysis revealed excellent yields (>97% respect to the consumed C_{60}) and high purities. No degradation of the host was observed after 10 cycles. Since the cyclopropanation reaction was confined to the aqueous phase, and the reaction product was maintained in the organic layer, the catalytic protocol designed avoided otherwise common product over-reactivity. All attempts to turn the biphasic catalytic system into heterogeneous catalysis have failed due to the loss of regioselectivity (the reaction is not exclusively confined within the cavity) or loss of reactivity in the cyclopropanation reaction.

To conclude this chapter, based on a rational design approach we developed a supramolecular mask strategy to exert full chemo- and regioselective control towards the preparation of cyclopropanated C_{60} fullerene derivatives. The structural geometry of the host features four cross-shaped apertures, which are the key for the exclusive and stepwise formation of equatorial bis-, tris- and tetrakis-C_{60} adducts, which can be easily released from the host cavity. We further show that these supramolecular scaffold can be used to cleanly produce isomer-pure equatorial hetero-tetrakis-adducts or hetero-*Th*-hexakis-adducts at will in one-pot synthesis for the first time, simply by changing the nucleophile during the reaction. The herein introduced supramolecular mask strategy shows the potential to be upgraded into a catalytic regime (catalytic amounts of host) by designing a biphasic system. In this manner, quantitative formation of equatorial tetrakis-adducts was achieved by an anion metathesis protocol with **1a**·(BArF)$_8$. The transfer of the host and the cargo into the aqueous phase triggers the Bingel-Hirsch reaction which is exclusively confined in this layer, avoiding any sign of overreactivity which is one of the more extended problems in the multiple functionalization of fullerenes.

VII.2. A Copper-based Supramolecular Nanocapsule that Enables Straightforward Purification of Sc_3N-based Endohedral Metallofullerenes Soots.

This section corresponds to the contents of the manuscript by Fuertes-Espinosa et al. *Chem. Eur. J*, **2017**, 23, 3553-3557, which can be found in chapter IV**.**

$Sc_3N@C_{80}$ is the third fullerene produced in largest quantities after C_{60} and C_{70}, however, the availability of this compound is limited by their expensive, inefficient and time consuming purification. On a general basis, the low production of EMFs and the complexity in terms of composition of the crude sample that contains them, limits the chromatographic purification of these materials through HPLC. To overcome these limitations, several alternative purification protocols have been developed,[10] although, still several steps and long reaction times are required. To overcome the limitations described above, our group designed a supramolecular scaffold that allows the straightforward purification of EMFs via reversible host-guest reactions, in one operationally simple step.

VII.2.1. Synthesis and characterization of capsule 5·(OTf)$_8$

The synthesis of the paramagnetic molecular clip [(**Cu-1b**)(OTf)$_2$](OTf)$_2$ was similar to that previously reported for [(**Pd-1a**)(AcO)$_2$](OTf)$_2$.[6] The Cu(II)-based macrocyclic complex was fully characterized by means ESI-MS, UV-vis, FT-IR and combustion analysis (Annex. Supp. Info. Chapter IV, Figure S1-S3). To obtain the corresponding **5**·(OTf)$_8$ capsule,[11] four equivalents of the hexaazamacrocyclic complex [(**Cu-1b**)(OTf)$_2$](OTf)$_2$ were mixed with two equivalents of 5, 10, 15, 20-tetrakis(4-carboxyphenyl)-Zn(II)-porphyrin (porph-Zn) and excess of triethylamine, in DMF at room temperature for 16 hours (Figure VII.13). The subcomponent self-assembly reaction quantitatively produced capsule **5**·(OTf)$_8$, which shows enhanced solubility in acetonitrile than its Pd analogue; thanks to that, counteranion exchange with tetrakis-[3, 5-bis(trifluoromethyl)phenyl]boron anions (BArF$^-$) (to improve capsule solubility in organic solvents) was not required. The structural integrity of **5**·(OTf)$_8$ in solution is further confirmed by ESI-HRMS and UV-vis (Annex. Supp. Info. Chapter IV, Figure S4 and S5).

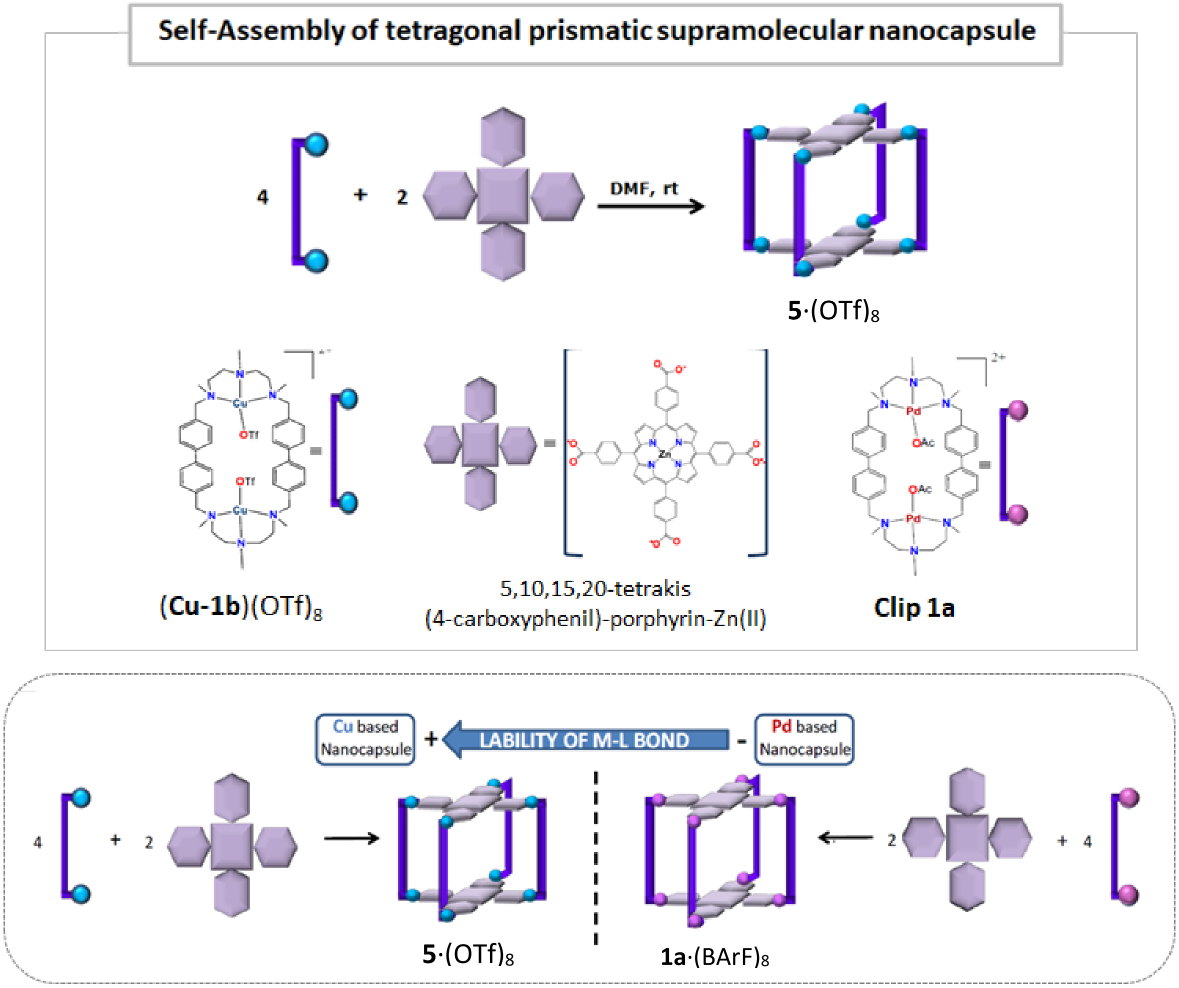

Figure VII.13. Graphical representation of the building blocks (top) used for the self-assembly of supramolecular nanocapsules **5**·(OTf)$_8$ (bottom left) or **1a**·(BArF)$_8$ (bottom right).

VII.2.2. Reversible host-guest complexation of fullerenes

Due to its wide cavity and the known affinity of its Pd(II)-based nanocapsule analogue towards fullerenes,[6] the Cu(II)-based **5·**(OTf)$_8$ was proposed as a potential candidate for the molecular recognition of these spherical carbon allotropes. In addition, an enhanced performance of **5·**(OTf)$_8$ for reversible complexation of higher fullerene guests was predicted, since the lability of the coordinative bonds present on the Cu(II) capsule facilitated their release.

Gratifyingly, rapid inclusion occurred upon mixing a solution of C_{60} or C_{70} in toluene with a solution of **5·**(OTf)$_8$ in acetonitrile (solvent ratio 9:1 (toluene:acetonitrile) and 1:1 molar ratio), at room temperature (Figure VII.14 a and b). UV-vis titration experiments revealed the formation of 1:1 high stable host-guest adducts with both fullerenes ($K_a = 3.53(\pm 0.4) \times 10^6\ M^{-1}$ for C_{60}, and $K_a = 1.76(\pm 0.7) \times 10^7\ M^{-1}$ for C_{70} (Annex. Supp. Info. Chapter IV, Figure S6 and S7) which are 10-fold smaller than for the Pd(II)-based **1a**$^{8+}$.[6] Inclusion of higher fullerenes (up to C_{84}) was also observed using fullerene extract (C_{60} 70%, C_{70} 28% and higher fullerenes 2%) (Annex. Supp. Info. Chapter IV, Figure S8).

The efficiency of capsule **5**·$(OTf)_8$ to liberate trapped fullerene guests was explored. Charging a solid sample of the host-guest adduct in a small column of Celite® and washing it with an appropriate mixture of solvents (exploiting the orthogonal solubility between the host and the guest), the entrapped fullerenes could be released.[6] To our delight, using this solvent-washing protocol, C_{60} and C_{70} were quantitatively released from **5**·$(OTf)_8$ and the empty host recovered, as ascertained by ESI-MS (Annex. Supp. Info. Chapter IV, Figure S9 and Figure VII.14 c, respectively). It is worth to note that the fullerene release from the Pd(II) capsule is limited to C_{60}, thus showcasing the increased lability of the Cu-carboxylate bonds in **5**·$(OTf)_8$. Presumably, the higher lability of the metal-carboxylate bonds (Cu(II)-OOC-R) endows **5**·$(OTf)_8$ with a higher degree of structural flexibility, diminishing the measured K_a and facilitating the release of large fullerene guests.

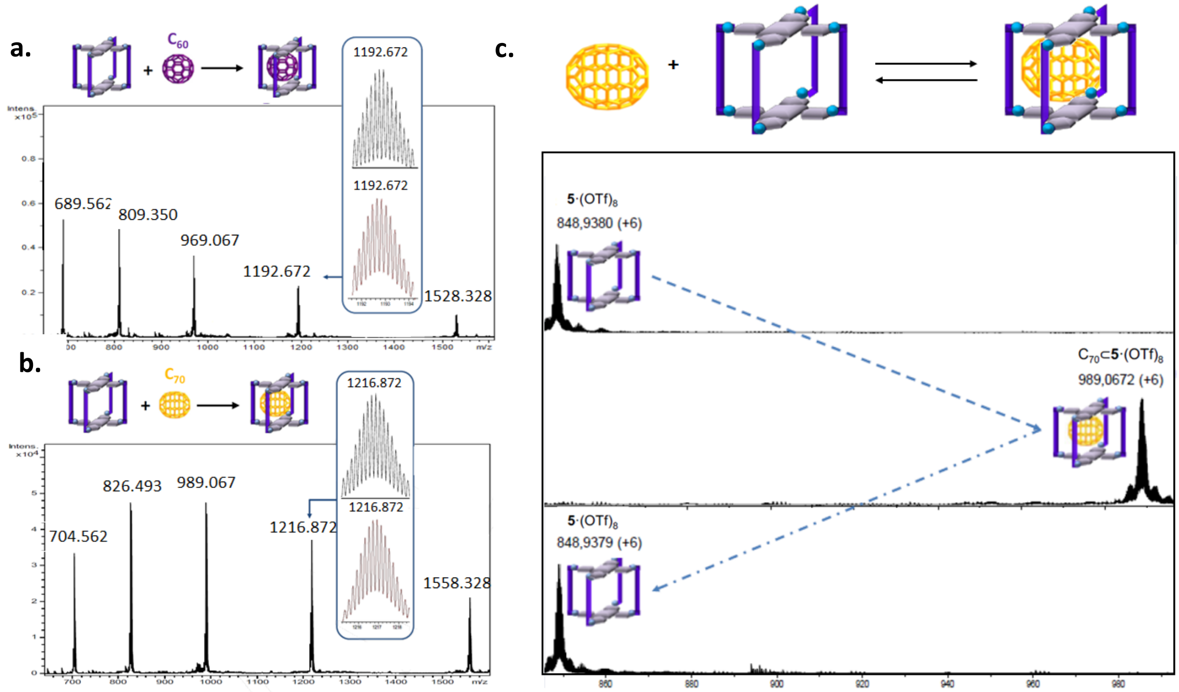

Figure VII.14. HRMS spectrum of C_{60}⊂**5**·$(OTf)_8$ (**a**) and C_{70}⊂**5**·$(OTf)_8$ (**b**) host–guest adduct generated in solution. Simulated spectrum of selected peaks is shown in red. **c)** HRMS monitoring of the C_{70} extraction-washing protocol using pure C_{70} and **5**·$(OTf)_8$ in solid state.

VII.2.3. Reversible host-guest complexation of EMFs

Once the molecular recognition properties of **5**·(OTf)$_8$ towards fullerenes were tested, we explored the reversible inclusion of more challenging endohedral metallofullerenes (EMFs).

The fact that all fullerenes larger than C_{60} remain irreversibly trapped in the Pd(II) capsule cavity, limited its use in the reversible molecular recognition of EMFs (which are commonly larger than C_{60}). Conversely, the enhanced performance of the Cu(II) analogue in terms of guest liberation, endowed **5**·(OTf)$_8$ as a potential candidate for the reversible encapsulation of EMFs. The ability of **5**·(OTf)$_8$ for binding EMFs was tested using a Sc_3N-soot provided by Prof Echegoyen (UTEP). The composition of the Sc_3N-soot was determined by HPLC chromatography (Annex. Supp. Info. Chapter IV, Figure S10)., revealing the presence of C_{60}, C_{70}, $Sc_3N@C_{68}$, $Sc_3N@C_{78}$ and $Sc_3N@C_{80}$ in different concentrations. A solution of **5**·(OTf)$_8$ in acetonitrile was mixed with a solution of the Sc_3N-soot in toluene (1:1 molar ratio, final solvent mixture 9:1 toluene:acetonitrile) for 10 minutes. The ESI-HRMS analysis of the reaction crude revealed the formation of host-guest adducts with all the species present on the Sc_3N-soot (Figure VII.15). Remarkably, all trapped guests (C_{60}, C_{70}, $Sc_3N@C_{68}$, $Sc_3N@C_{78}$ and $Sc_3N@C_{80}$) were easily released by applying the solvent-washing protocol (Figure VII.15). Furthermore, UV-vis titration experiments with pure $Sc_3N@I_h$-C_{80} were performed to quantitatively evaluate the stability of the corresponding host-guest complex. The spectroscopic measurements demonstrate the formation of 1:1 host-guest adduct, with an association constant of $K_a = 2.02(\pm 0.6) \times 10^7\ M^{-1}$ for $Sc_3N@I_h$-C_{80}⊂**5**·(OTf)$_8$ (Annex. Supp. Info. Chapter IV, Figure S12).

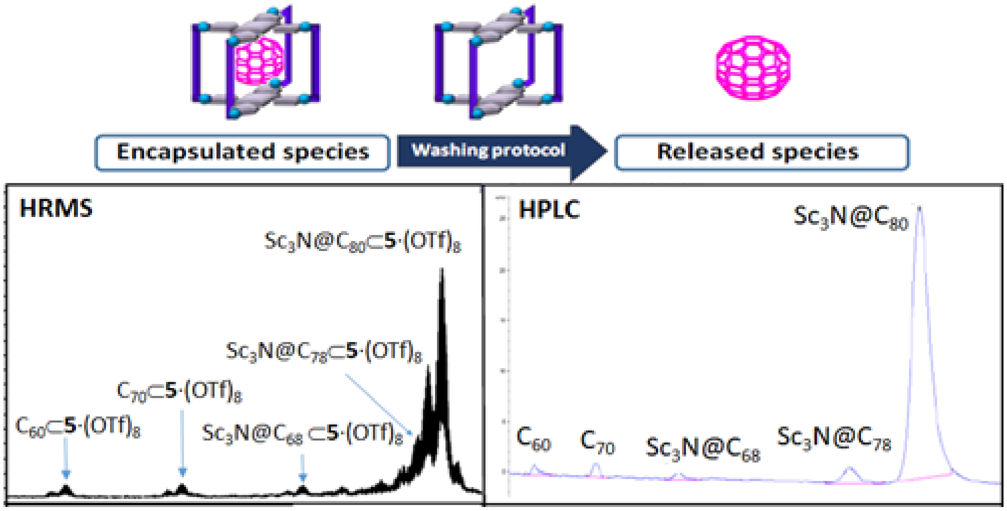

Figure VII.15. HRMS spectrum of Sc-based soot⊂**5**·(OTf)$_8$ host guest complexes formed in solution (left) and HPLC chromatogram of the released guests through the solvent-washing protocol.

VII.2.4. Solid–liquid Host-guest experiments

Analogously to the Pd(II) capsule, the versatility of **5**·(OTf)$_8$ as a supramolecular scaffold for the encapsulation of fullerenes was further exemplified by the capability of trapping guests in heterogeneous systems. Simply by soaking a solid sample of **5**·(OTf)$_8$ in a solution of the corresponding fullerene, the guest was fully encapsulated. To qualitatively evaluate the selectivity shown by **5**·(OTf)$_8$ in solid-liquid interphases in comparison with experiments performed in homogeneous solution, substoichiometric amounts of **5**·(OTf)$_8$ powder were added in a solution of fullerene extract (molar ratio 1:10 capsule/fullerene extract) and stirred at room temperature for 4 hours. In parallel, the same experiment was reproduced using the capsule in solution. Surprisingly, the ESI-HRMS analysis of the host-guest adducts formed in the solid-liquid interphase, revealed the formation of $C_{60}\subset$**5**·(OTf)$_8$ and $C_{70}\subset$**5**·(OTf)$_8$ as the unique reaction products (being $C_{60}\subset$**5**·(OTf)$_8$ the major product, 4:1 ratio) (Annex. Supp. Info. Chapter IV, Figure S8 bottom). Conversely, in the results obtained in the homogeneous experiment (liquid-liquid encapsulation), the $C_{70}\subset$**5**·(OTf)$_8$ was detected as the major product by ESI-HRMS (Annex. Supp. Info. Chapter IV, Figure S8 top). These results indicate that the selectivity towards fullerenes shown by **5**·(OTf)$_8$ could be modified in a controlled manner simply by using the nanocapsule as solid suspended in an appropriate solvent for the molecular recognition experiments. Using a solvent in which exclusively the guests are soluble, the host exhibited preferential encapsulation towards smaller species, in contrast to the results obtained in homogeneous systems. A plausible explanation for the different selectivity exhibited is related to the higher structural rigidity of the host in solid phase, which limits its structural flexibility and adaptability, making its internal cavity more sterically impeded and simultaneously more selective towards fullerenes with smaller occupancy ratios.

VII.2.5. Straightforward purification of $Sc_3N@C_{80}$

Based on the results described above, we hypothesized that our target $Sc_3N@C_{80}$, which is the major component present on the crude mixture, could be purified by designing a heterogeneous host-guest system in which **5**·$(OTf)_8$ as solid selectively encapsulates the smaller species present in the Sc_3N-soot solution, while the $Sc_3N@C_{80}$ remained in solution. To evaluate this hypothesis, two parallel experiments were performed, one as liquid-liquid and the other as solid-liquid, to compare the selectivity of **5**·$(OTf)_8$ towards the species present in the Sc_3N-soot (Figure VII.16). As expected, higher affinity towards the smallest species were observed using a heterogeneous host-guest system when compared with the homogeneous experiment.

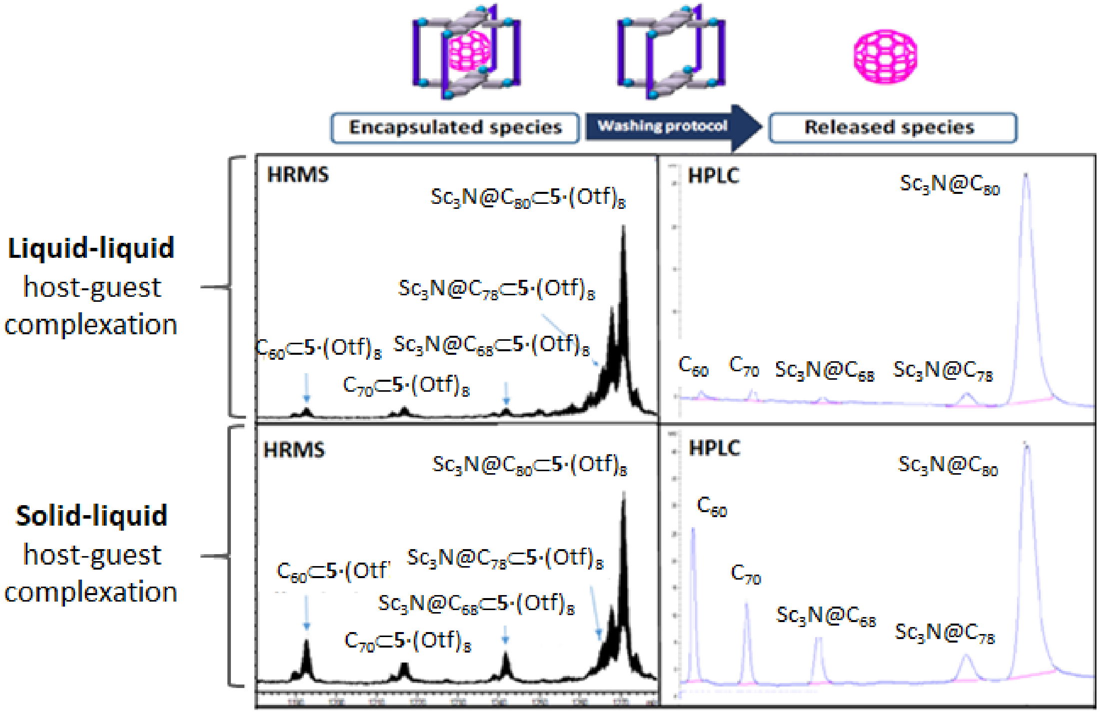

Figure VII.16. HRMS spectrum of Sc-based soot⊂**5**·$(OTf)_8$ formed in solution (top left) and in solid state of **5**·$(OTf)_8$ (bottom left). HPLC chromatograms (top and bottom right) of the released through the solvent-washing protocol

These results were crucial for the development of a purification methodology for the targeted $Sc_3N@C_{80}$, consisting in the addition of an excess of **5**·$(OTf)_8$ as insoluble solid to a toluene solution of the EMFs soot (6:1 capsule:soot molar ratio). The supernatant of the reaction was monitored by HPLC analysis, revealing an increasingly enrichment in $Sc_3N@C_{80}$ over time (Figure VII.17). After 5 hours, the targeted $Sc_3N@C_{80}$ was the unique species remaining in the supernatant (confirmed by HPLC and LDI-TOF analysis, Figure VII.17 and Annex. Supp. Info. Chapter IV, Figure S14 bottom, respectively). At the end of the experiment, from the total $Sc_3N@C_{80}$ contained in the initial soot, 60% was recovered in its pure form (purities up to 99.5% determined by HPLC). On the other hand, the species encapsulated were quantitatively released and the host recovered being ready to be re-used.

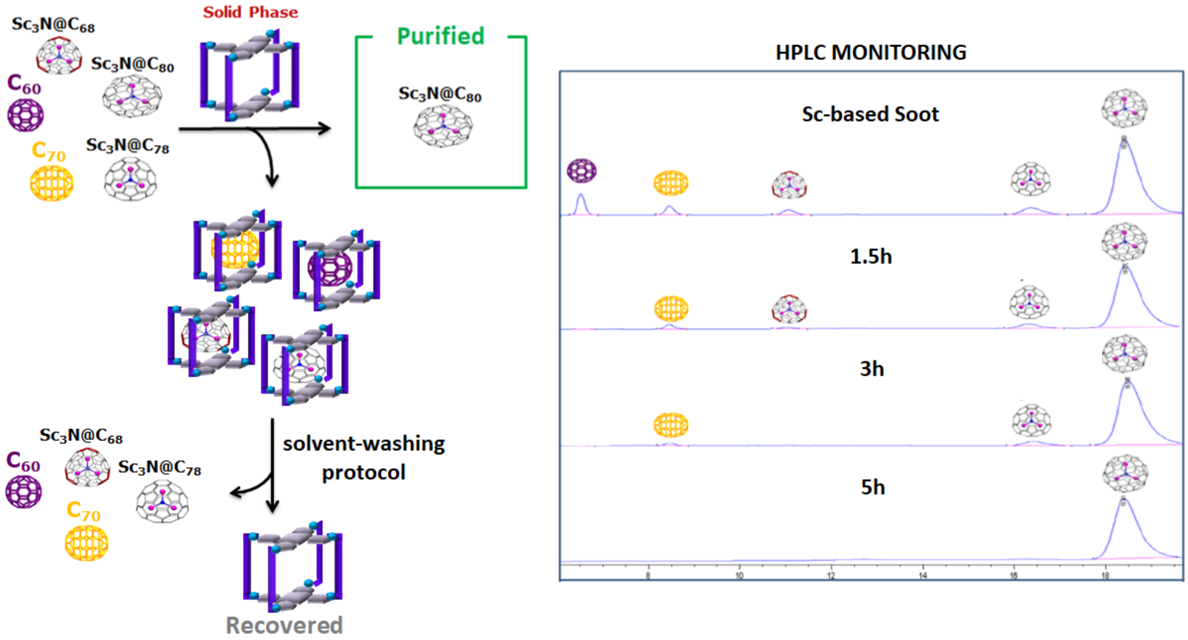

Figure VII.17. Sc_3N-based soot purification protocol using **5**·$(OTf)_8$ in the solid phase, by HPLC monitoring of the remaining supernatant.

Aiming to get further insight about the selectivity observed during the purification experiments, an equimolar mixture of C_{60}, C_{70}, $Sc_3N@C_{80}$ in toluene was subjected to an excess of host as solid (6-fold excess). Analogously, preferential uptake of C_{60} and C_{70} was revealed by the HPLC monitoring of the supernatant (Figure VII.18). Additionally, higher mass recovery of $Sc_3N@C_{80}$ (85% as determined by HPLC quantification) was observed after long reaction times (11 hours). Additional host-guest experiments performed with the purified $Sc_3N@C_{80}$ determined that no selectivity towards the isomeric $Sc_3N@I_h$-C_{80} and $Sc_3N@D_{5h}$-C_{80} carbon cages mixture is present.

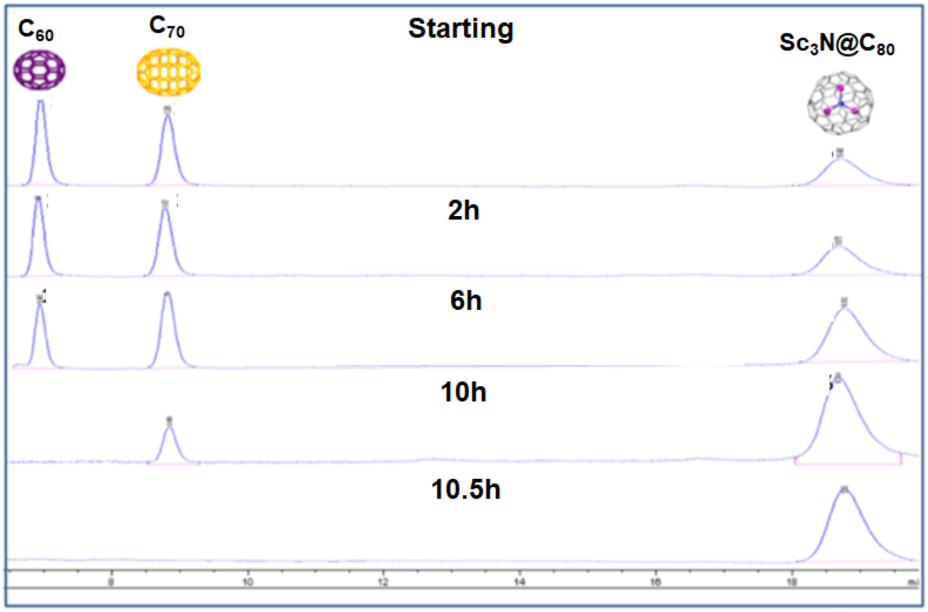

Figure VII.18. Purification of an equimolar mixture of C_{60}, C_{70} and $Sc_3N@C_{80}$ using **5**·(OTf)$_8$ in the solid phase, by HPLC monitoring of the remaining supernatant.

Summarizing this section, a Cu(II)-based tetragonal prismatic nanocapsule was designed to bind fullerenes and EMFs reversibly, providing a new platform for the efficient and simple purification of $Sc_3N@C_{80}$ directly from crude mixtures. The ability of **5**·(OTf)$_8$ to selectively trap several species present on a EMFs soot in a solid-liquid interphase, leaving in solution exclusively the targeted guest in purities up to 99.5%, is unprecedented for a supramolecular entity. Additionally, by using the capsule in homogeneous or heterogeneous phase, the selectivity of encapsulation can be strikingly altered. This study provides a novel method for the purification of Sc_3N-based fullerenes in a single and operationally simple step. Furthermore, the host is recovered at the end of the experiments by solvent-washing release of the trapped guests.

VII.3. Purification of Uranium-based Endohedral Metallofullerenes (EMFs) by Selective Supramolecular Encapsulation and Release.

This section corresponds to the contents of the manuscript by Fuertes-Espinosa et al. *Angew. Chem. Int. Ed*. **2018**, 57, 11294-11299, which can be found in chapter V.

In the early stage of fullerene research, Smalley and co-workers detected spectrometrically for the first time a set of uranium-based EMFs, including mono- and bimetallic species.[12] The discovery of these U-containing carbon structures spurred several investigations, aiming at understanding their physicochemical properties and to enhance their production yield. Despite much efforts, the isolation of uranium-based EMFs remained an elusive goal for more than 20 years. Very recently, in 2018, Echegoyen and Chen reported the isolation by HPLC purification and the structural characterization by X-ray crystallography of the first dimetallic $U_2@I_h$-C_{80}.[13] The soot produced by Echegoyen and Chen also contained several unprecedented mono- and metal-mixed actinide species, but their chromatographic purification was unsuccessful. The low production efficiency of these compounds and the composition of the soot dramatically hinders their purification through HPLC techniques. To accelerate the progress on these field, the development of a non-chromatographic purification strategy to isolate these uranium-based EMFs is highly demanded.

The above considerations, together with the results obtained in the molecular recognition of Sc_3N-based EMFs,[13] prompted us to attempt the purification of these compounds through selective host-guest complexation.

VII.3.1. Synthesis and characterization of capsule 1b·(BArF)$_8$

The carry out this study we decided to use the same nanocapsule as in the previous chapter but bearing BArF- counteranions (nanocapsule **5**·(BArF)$_8$, but for publication reasons we name it as **1b**·(BArF)$_8$ hereafter). The counteranion exchange not only improved the solubility of the host, but also facilitates its crystallization for single-crystal X-ray diffraction (SCXRD) analysis. As expected, the crystal structure revealed a slightly distorted tetragonal prismatic capsule, constituted by two parallel tetracarboxylated Zn(II)-porphyrins connected and four Cu(II)-based macrocycles [(**Cu-1b**)(OTf)$_2$](OTf)$_2$ (Figure VII. 19 and Annex. Supp. Info. Chapter V, Figure S4). Full characterization of the **1b**·(BArF)$_8$ revealed that the capsule maintained its structural integrity in solution (Figure VII.19 and Annex. Supp. Info. Chapter V, Figure S1-S3).

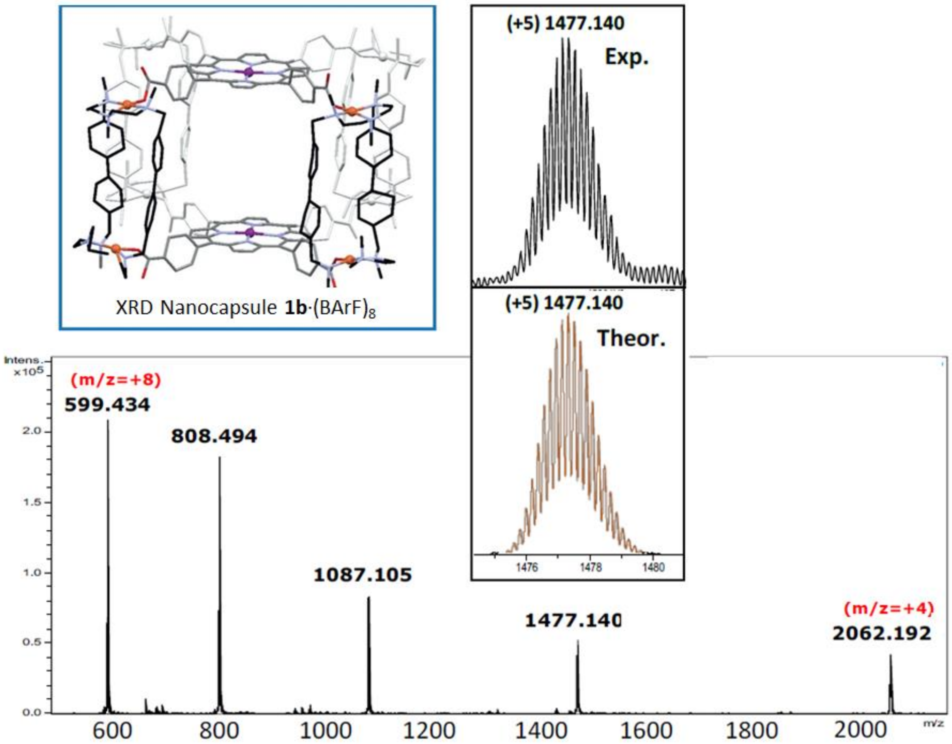

Figure VII.19. HRMS spectrum of **1b**·(BArF)$_8$. Simulated spectra of selected peaks are showed in orange. Inset shows a representation of the crystal structure of the [**1b**]$^{8+}$ cation. Cu orange, Zn purple.

VII.3.2. Production of uranium-based EMFs by arc-discharge methodology

The production of the soot containing the targeted uranium species was carried out by vaporization of graphite-cored rods containing a U_3O_8/Sc_2O_3 oxide mixture in an arc-discharge reactor under a He/H_2 atmosphere. The resulting soot was extracted in a Soxhlet during 6 h with carbon disulfide (CS_2), and after the complete removal of CS_2, the remaining U/Sc-based soot was re-dissolved in toluene. The spectrometric characterization of the soot by LDI-TOF revealed a very complex mixture, which contains empty fullerenes, U-based EMFs, an unknown metal-mixed compound with the molecular formula of Sc_2UC_{81} (spectroscopic and computational studies conducted in this chapter indicated that this compound corresponds to $Sc_2CU@I_h$-C_{80} as discussed below) and a family of Sc-based EMFs.

VII.3.3. One step isolation of $U_2@C_{80}$ directly from crude soots

Taking into account the composition of the produced U/Sc-based soot and the results obtained previously during the isolation of the $Sc_3N@C_{80}$ (described in chapter VII.2), the main objective at the early stage of this work was the selective encapsulation of the smallest species present on the crude by using **1b**·$(BArF)_8$ in solid state, aiming to facilitate the further chromatographic purification of the targeted U and U/Sc-based EMFs.

Substoichiometric amounts of crystals of **1b**·$(BArF)_8$ were added into a toluene solution of the U-based EMF crude soot, and the species remaining in solution (supernatant) were monitored by LDI-TOF. To our delight, the host-guest complexation resulted in the selective uptake of $U_2@C_{80}$, as suggested by an intensity decrease of the peak attributed to the targeted compound over time, while the rest of the species remained in solution (Figure VII.20). Thanks to the host-guest complexation in solid-liquid interphases, the crystals of the **1b**·$(BArF)_8$ containing the targeted EMF absorbed were easily isolated by filtration. The HRMS analysis of the isolated crystals in CH_3CN further confirmed the exclusive encapsulation of $U_2@C_{80}$ (Annex. Supp. Info. Chapter V, Figure S6). In addition, the trapped guest was released by applying our previously described solvent-washing protocol and the LDI-TOF analysis of the released species showed a single peak at m/z 1436.103, attributed to $U_2@C_{80}$ (Figure VII.20 bottom left). Therefore, this experiment demonstrated that our capsule was capable to selectively bind and isolated the targeted $U_2@C_{80}$ in the presence of many other fullerene-like compounds in a single and operationally simple step.

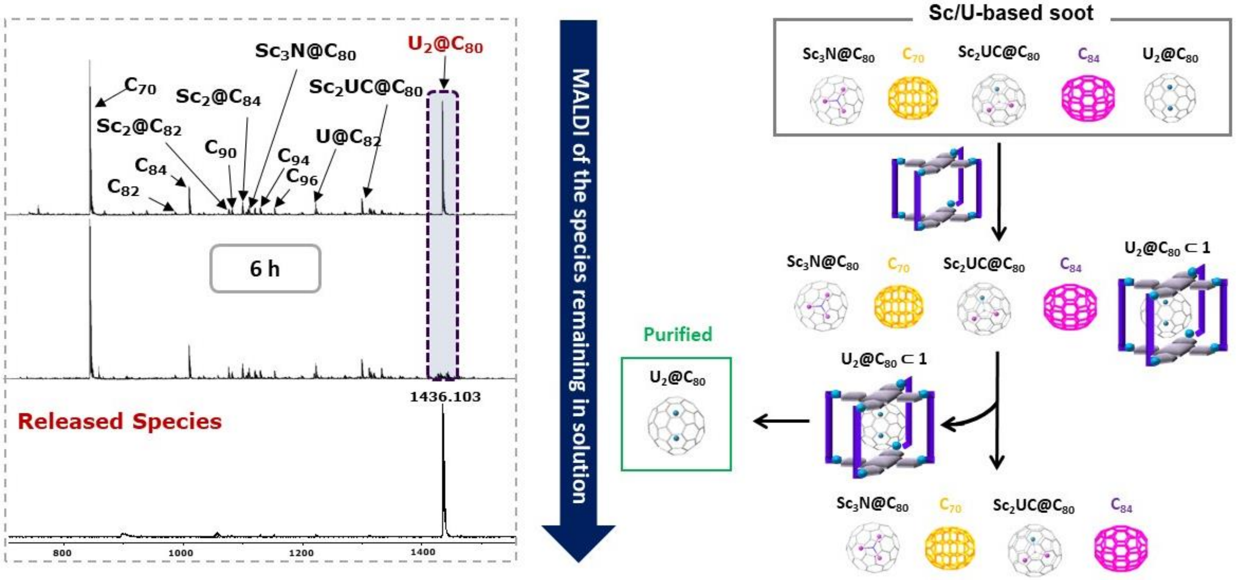

Figure VII.20. LDI-TOF monitoring of the selective complexation of $U_2@C_{80}$ within crystals of **1b**·$(BArF)_8$ soaked in raw Sc/U soot extract solution (left). Spectrum of the starting raw Sc/U soot solution (top left); spectrum of the remaining supernatant solution after soaking crystals of **1b**·$(BArF)_8$ for 6 h (middle left) and spectrum of pure $U_2@C_{80}$ released from **1b**·$(BArF)_8$ (bottom left).

VII.3.4. Selective isolation of the first metal-mixed actinide EMFs $Sc_2CU@C_{80}$

Once the $U_2@C_{80}$ was completely extracted from the crude mixture, the subsequent encapsulation of $Sc_2CU@C_{80}$ was targeted, aiming to explore whether a general trend for the selective encapsulation of U-based C_{80}-EMFs was present. Analogous to the protocol described above, fresh crystals of our host were soaked in the soot solution (which contained the remaining mixture of compounds except $U_2@C_{80}$) and the host-guest complexation was monitored by LDI-TOF analysis of the supernatant along the time. The spectrometric analysis revealed a progressive decay of the peak attributed to our targeted metal-mixed species, until its complete disappearance after 1.5 h (Figure VII.21). The specific molecular recognition of $Sc_2CU@C_{80}$ was confirmed by HRMS of the isolated host-guest adducts generated, showing exclusively the peaks corresponding to $Sc_2CU@C_{80}\subset$**1b**·(BArF)$_8$ (Annex. Supp. Info. Chapter V, Figure S8). After releasing the trapped EMF by using the solvent-washing protocol, it was analysed by LDI-TOF showing a single peak at m/z 1299.963, further confirming the high purity of the isolated product (Figure VII.21 bottom right). It is worth to note that $Sc_2CU@C_{80}$ could not be purified by HPLC due to its low production yield and essentially the same retention time to that $Sc_3N@C_{80}$ (Annex. Supp. Info. Chapter V, Figure S9).

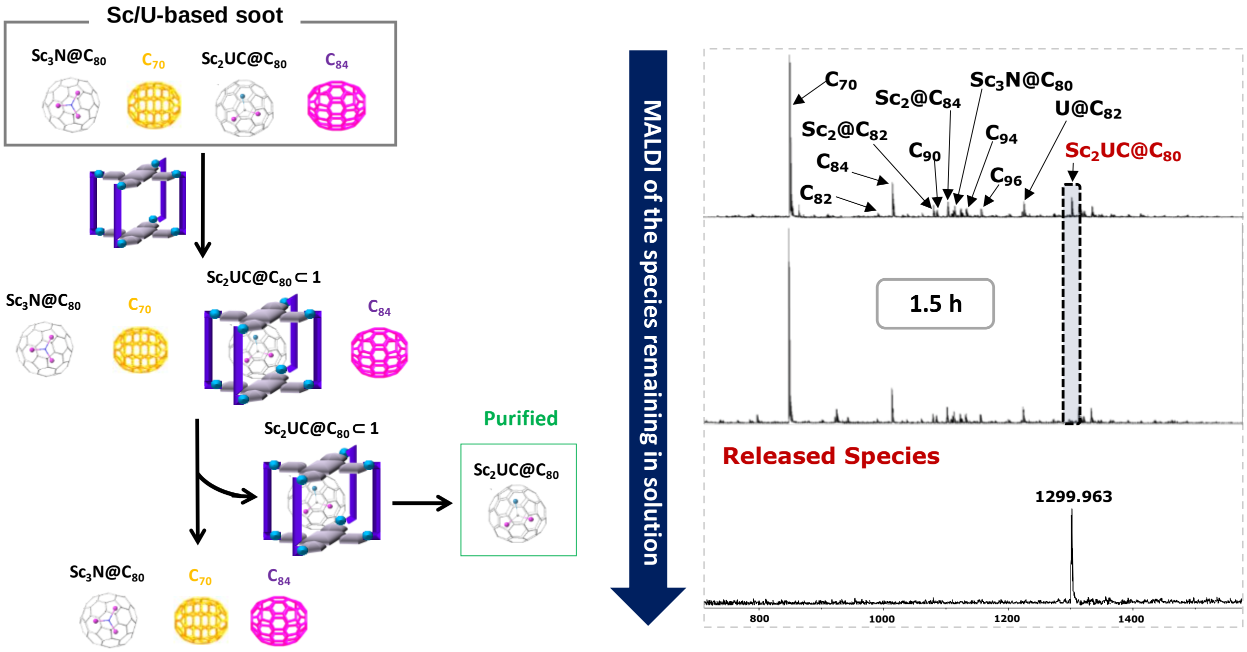

Fig VII.21. LDI-TOF monitoring of the selective complexation of $Sc_2CU@C_{80}$ within crystals of **1b**·(BArF)$_8$ soaked in raw Sc/U soot extract solution after the complete removal of $U_2@C_{80}$ (right). Spectrum of the starting raw Sc/U soot solution (top right); spectrum of the remaining supernatant solution after soaking crystals of **1b**·(BArF)$_8$ for 6 h (middle right) and spectrum of the pure $Sc_2CU@C_{80}$ released from **1b**·(BArF)$_8$ (bottom right).

The UV-Vis spectrum of the isolated $Sc_2CU@C_{80}$ (Annex. Supp. Info. Chapter V, Figure S10) showed absorption features identical to those of $U_2@I_h\text{-}C_{80}$,[13] further suggesting the same cage symmetry and charge transfer from the internal cluster to the carbon cage. These findings confirm that the only distinctive feature between $Sc_2CU@I_h\text{-}C_{80}$ and $U_2@I_h\text{-}C_{80}$ is the internal cluster, subsequently, the selectivity of **1b**·(BArF)$_8$ is in response to the nature of the different internal clusters trapped in the fullerene cages.

VII.3.5. Host-guest competition experiments between EMFs differing only in the internal cluster

Aiming at further understanding the origin of the selectivity observed during the purification protocols, **1b**·(BArF)$_8$ was tested as host for an equimolar mixture of $U_2@I_h\text{-}C_{80}$ and $Sc_3N@I_h\text{-}C_{80}$. The EMFs selected for this experiment possess exactly the same carbon cages and differs one from each other only in the nature of the internal cluster. The LDI-TOF analysis of the species remaining in solution (supernatant) over time, revealed the selective encapsulation of $U_2@I_h\text{-}C_{80}$, leaving $Sc_3N@I_h\text{-}C_{80}$ in solution (Figure VII.22). After 5 hours, $U_2@I_h\text{-}C_{80}$ was solely and quantitatively encapsulated, and the LDI-TOF analysis of the released species further confirmed the very high purity of the dimetallic uranium EMF (Figure VII.22 bottom).

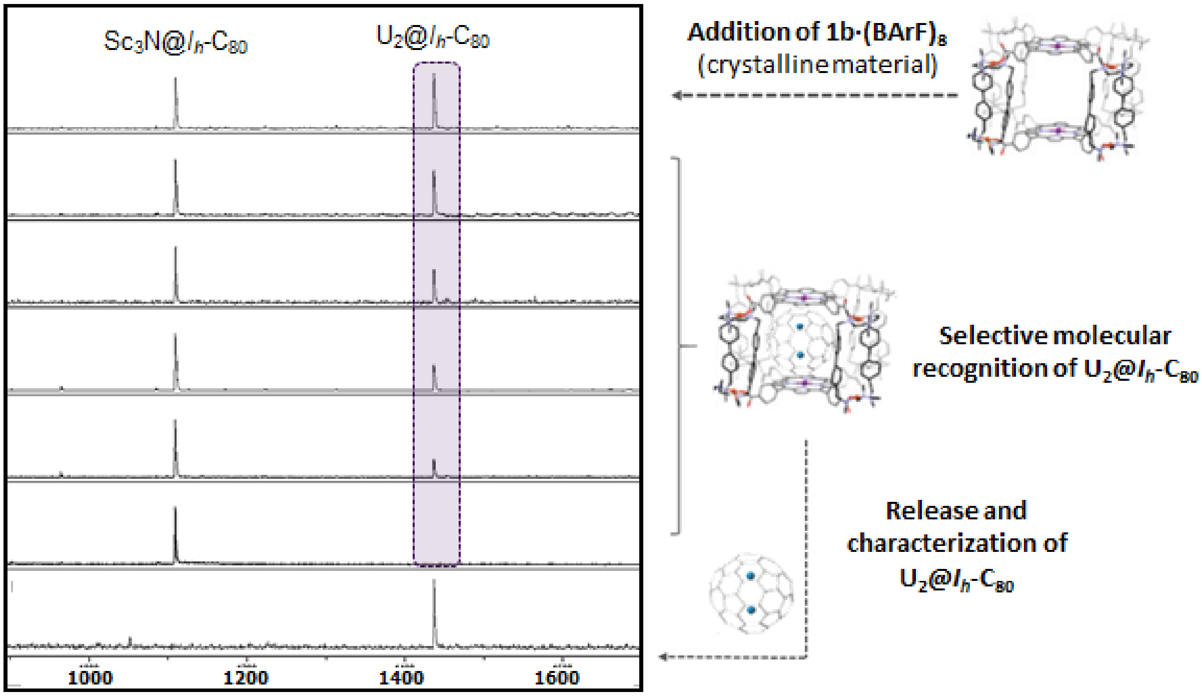

Figure VII.22. LDI-TOF monitoring of the selective complexation of $U_2@I_h\text{-}C_{80}$ within crystals of **1b**·(BArF)$_8$ soaked in an equimolar mixture of $U_2@I_h\text{-}C_{80}$ and $Sc_3N@I_h\text{-}C_{80}$. Top: spectrum of the starting sample. Bottom: spectrum of the pure $U_2@C_{80}$ released from **1b**·(BArF)$_8$.

In addition, the divergent affinity towards $Sc_2CU@\textit{I}_h$-C_{80} and $Sc_3N@\textit{I}_h$-C_{80} was studied by soaking crystals of **1b**·$(BArF)_8$ in a solution of an equimolar mixture of the corresponding EMFs. The host-guest complexation was followed over time by LDI-TOF, as performed in the previous experiments, showing the decay of the peak attributed to $Sc_2CU@\textit{I}_h$-C_{80} (Figure VII.23). After 3 hours the metal-mixed EMF was not detected in the supernatant. These results together with the spectrometric analysis of the released species, unequivocally confirms the selective and exclusive encapsulation of $Sc_2CU@\textit{I}_h$-C_{80} (Figure VII.23 bottom).

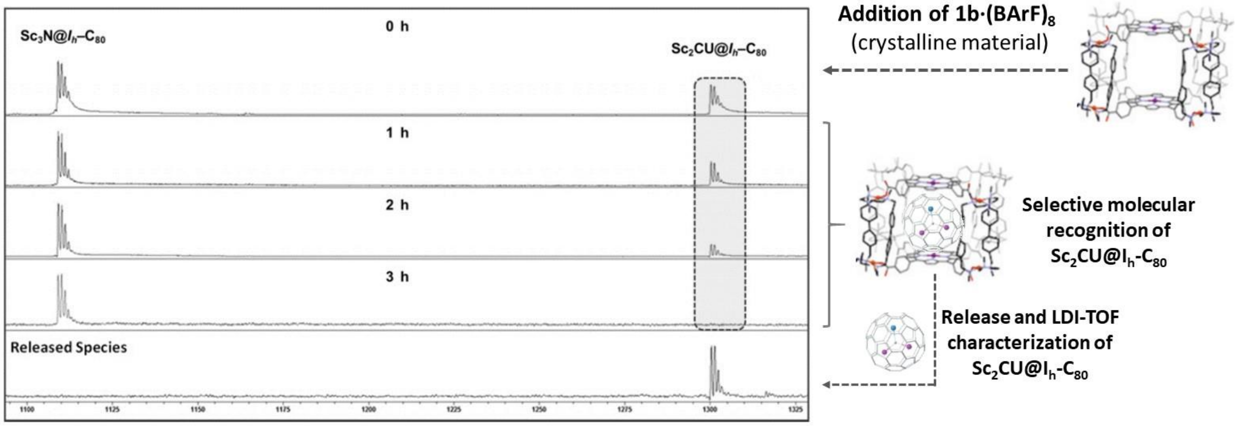

Figure VII.23. LDI-TOF monitoring of the selective complexation of $Sc_2CU@\textit{I}_h$-C_{80} within crystals of **1b**·$(BArF)_8$ soaked in an equimolar mixture of $Sc_2CU@\textit{I}_h$-C_{80} and $Sc_3N@\textit{I}_h$-C_{80}. Top: spectrum of the starting sample. Bottom: spectrum of the pure $Sc_2CU@C_{80}$ released from **1b**·$(BArF)_8$ (bottom).

VII.3.6. Computational studies: unreported $Sc_2CU@\textit{I}_h$-C_{80} and $U_2@\textit{I}_h$-C_{80} and $Sc_3N@\textit{I}_h$-C_{80} host-guest complexes

To gain further insights about the structure and the electronic properties of the unprecedented $Sc_2CU@\textit{I}_h$-C_{80}, this compound was computationally studied at the DFT/BLYP/TZP(D3) level in collaboration with the group of Poblet (URV, Tarragona). Considering that its UV-Vis spectrum presented very similar absorption bands compared to C_{80}-$\textit{I}_h$ carbon cage and by analogy with $Lu_2CTi@\textit{I}_h$-C_{80}, previously reported by Popov and co-workers,[14] we assumed that the Sc_2CU internal cluster beared a planar structure. As anticipated, the oxidation state of uranium in this species is formally 4+ and consequently there is a formal electron transfer of six electrons from the internal metal cluster to the fullerene cage. On the other hand, the U-C bond distance is computed to be 2.070 Å, which is in line to the X-Ray bond length found very recently for a diuranium carbide cluster (U=C=U) stabilized in a C_{80}-$\textit{I}_h$ carbon cage (2.030 Å).[15] Furthermore, the analysis of the highest occupied orbitals for $Sc_2CU@\textit{I}_h$-C_{80} unequivocally corroborated the presence of a double bond between U and C (Annex. Supp. Info. Chapter V, Figure S12).

In an effort to understand the fundamental basis for the binding selectivity observed in this study, DFT calculations were performed using porphyrin-only simplified model systems, focusing only on the role of the Zn-Porphyrin moieties to evaluate the supramolecular interactions between host and guests (Annex. Supp. Info. Chapter V, Figure S11). Subsequently, a screening of different orientations of the $U_2@\textit{I}_h$-C_{80} respect to the Zn(II)-porphyrin units were performed, observing the lowest energy species when the U atoms were oriented almost in perfect alignment with the Zn metal centres (Annex. Supp. Info. Chapter V, Figure S13). In contrast to pristine fullerenes, U_2@*I*$_h$-C_{80} showed a formal transfer of six electrons from the cluster to the fullerene cage,[13] thus the electron density distribution along the fullerene cage could play an important role on the binding affinity. Indeed, the most stable orientation (U atoms aligned with the Zn···Zn axis) seemed to be favoured by the higher negative charge present on the carbon atoms closer to the U^{3+} ions (Figure VII.24). Therefore, the selective binding of C_{80}-I_h when it possesses two encapsulated U ions seems to be related to the linear double-conical symmetry of the electron density, which is induced by the actinide metals (Figure VII.24). On the other hand, in the case of Sc_3N@I_h-C_{80} the electron density is delocalized along an equatorial belt and thus it interacts less efficiently with the porphyrin moieties (Figure VII.24). In line with this, no clear energy differences of the supramolecular system were observed among several orientations of the Sc_3N@I_h-C_{80} with respect the porphyrins of the host (Annex. Supp. Info. Chapter V, Figure S15).

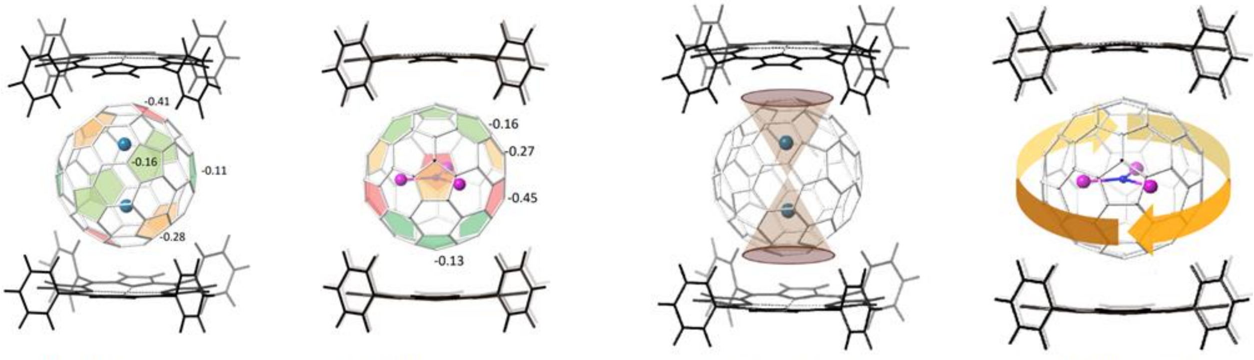

U_2@I_h-C_{80}@C_{80} Sc_3N@I_h-C_{80}@C_{80} U_2@I_h-C_{80}@C_{80} Sc_3N@I_h-C_{80}@C_{80}

Figure VII.24. On the left, The lowest energy orientation of U_2@I_h-C_{80} and Sc_3N@I_h-C_{80} trapped between a simplified two tetraphenyl-Zn(II)-porphyrin model (charge distributions shown on each pentagon). On the right, representation of the electron density distribution, showing a linear double conical interaction for U_2@I_h-C_{80}, whereas a diffuse equatorial belt is found for Sc_3N@I_h-C_{80}.

Thermodynamic insights extracted from DFT calculations were in agreement with the experimental observation, even thought, it is worth to note that kinetic contributions must be strongly relevant in the selective molecular recognition of each EMFs, highlighting those involved in the encapsulation of EMFs in the solid state supramolecular host.

As a conclusion of this section, this work described a straightforward methodology for the isolation of Sc_2CU@I_h-C_{80} and U_2@I_h-C_{80}, directly from crude soots. Our approach consisted in soaking crystals of **1b**·$(BArF)_8$ in a toluene solution of the crude soot, encapsulating selectively and sequentially U_2@I_h-C_{80} and Sc_2CU@I_h-C_{80}. The purification of Sc_2CU@I_h-C_{80} is very remarkable, being the first example of a mixed-metal actinide-based EMFs reported. Computational studies rationalized the binding selectivity observed through the highly directionality and localization of the electron-density distribution transferred from the internal cluster to the carbon cage. The unprecedented ability of our host to distinguish EMFs with the same size and shape, which only differ on the nature of the internal clusters, surpass the limitations of the HPLC techniques.

VII.4. Highly Selective Encapsulation and Purification of U-based C_{78}-EMFs within a Supramolecular Nanocapsule.

This section corresponds to the contents of the manuscript by Fuertes-Espinosa et al. *Nanoscale*. **2019**, 11, 23035-23041, which can be found in chapter VI**.**

In parallel to the discovery of $U_2@I_h$-C_{80},[13] Echegoyen and co-workers detected spectrometrically a new family of di-uranium-based C_{78} EMFs. However, their very low concentration and the complexity of the reaction crudes do not allow their purification through chromatographic techniques. In this context, previous investigations revealed the ability of **1b**·(BArF)$_8$ to purify uranium-based C_{80} EMFs, being able to distinguish compounds that only differs in the nature of the internal cluster and are present in the soot in very low quantities.[16] With these considerations, we thought that the production of a novel family of EMFs open up the opportunity to further explore and expand the applicability of our supramolecular scaffold in the purification of challenging EMFs mixtures.

VII.4.1 Selective molecular recognition of diuranium-based C_{78} EMFs

We aimed at the development of a straightforward purification protocol for the isolation of novel di-uranium-based C_{78} EMFs. Analogous to the purification protocol previously developed by our group,[16] crystals of **1b**·(BArF)$_8$ were added in a toluene solution of the crude soot containing the targeted EMFs (along with many other EMFs and pristine fullerenes) (Figure VII.25 top). To closely follow the host-guest complexation reactions that take place during the purification process, we monitored by LDI-TOF the composition of the supernatant over time. A clear decrease of the peaks belonging to the targeted $U_2@C_{78}$ and $U_2C@C_{78}$ was observed, which was attributed to the selective inclusion of these compounds within the cavity of solid **1b**·(BArF)$_8$ (Figure VII.25). After 3 hours, the selective molecular recognition of $U_2@C_{78}$ and $U_2C@C_{78}$ was quantitative, no presence of these compounds were detected in the LDI-TOF analysis of the supernatant (Figure VII.25). The crystalline host containing the trapped EMFs was easily isolated from the reaction crude by filtration, and the retained guest were released by washing the solid host-guest complex with carbon disulfide. The characterization of the released guests by LDI-TOF confirms an exceptional selectivity of **1b**·(BArF)$_8$ towards di-uranium-based C_{78} compounds (Figure VII.25 bottom).

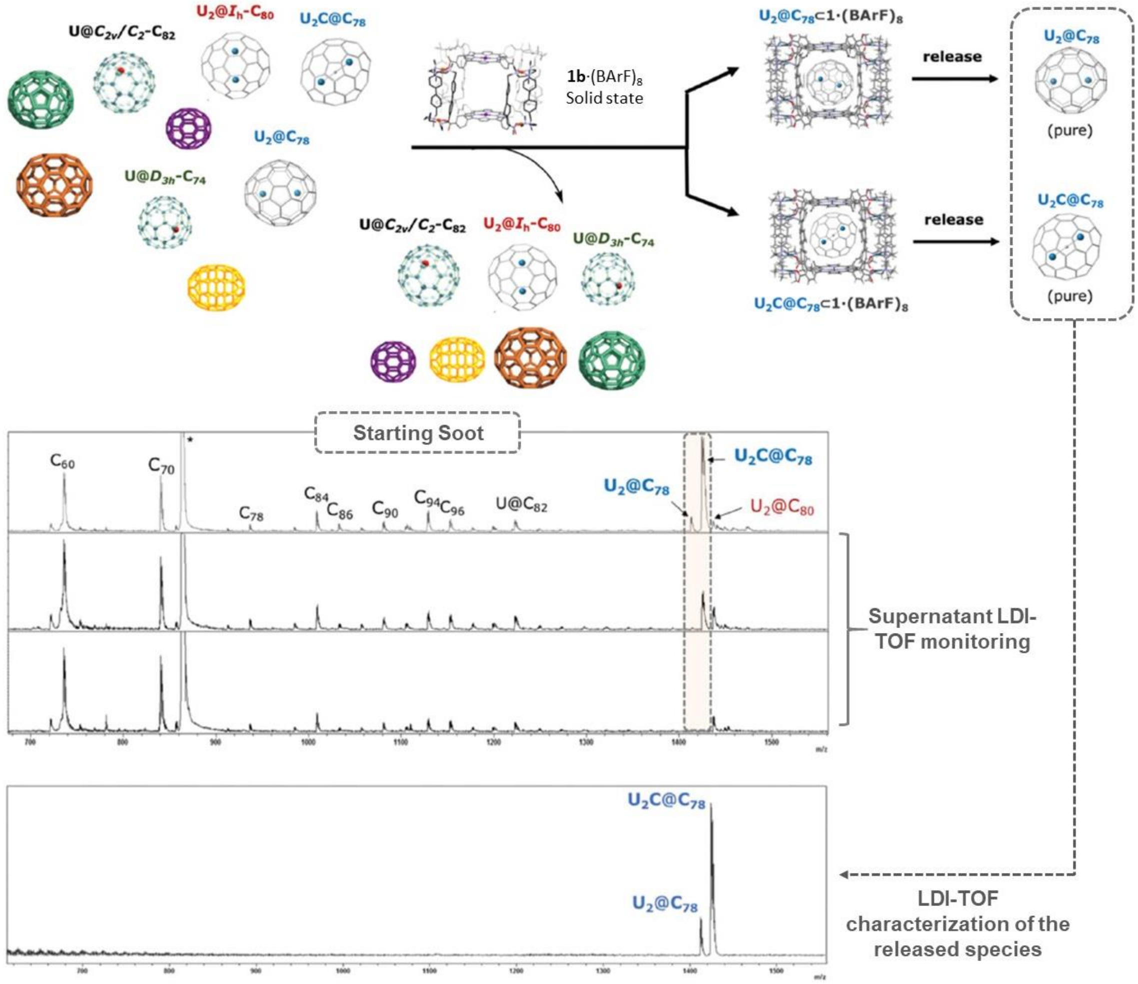

Figure VII.25. LDI-TOF monitoring of the selective complexation of $U_2@C_{78}$ and $U_2C@C_{78}$ within crystals of **1b**·$(BArF)_8$ soaked in a toluene solution of the U-based soot. LDI-TOF spectrum of the soot (top); spectrum of the remaining supernatant solution after soaking crystals of **1b**·$(BArF)_8$ (middle) and spectrum of isolated $U_2@C_{78}$ and $U_2C@C_{78}$ released from **1b**·$(BArF)_8$ (bottom).

VII.4.2 Evaluating the influence of the fullerene cage and the internal clusters on the selective molecular recognition of U-based EMFs

To evaluate the effect of the size and the shape of the fullerene cage on the specific binding observed, we attempted the selective molecular recognition of $U_2@C_{78}$ in a soot containing a variety of different sized U-based EMFs ($U@C_{74}$, $U@C_{84}$ and $U_2@C_{80}$). Scandium free EMFs soots was produced using hollow graphite rods packed with U_3O_8 and graphite powder mixture, which were vaporized in arc plasma under a partial He and NH_3 atmosphere. Using substoichiometric amounts of **1b**·$(BArF)_8$ in solid phase and the soot in solution (as described above), the selective binding of $U_2@C_{78}$ was observed (Figure VII.26), as confirmed by analysing the released guests by LDI-TOF (Figure VII.26 bottom). Remarkably, the presence of the same metal cluster in $U_2@C_{78}$ as in $U_2@C_{80}$, both transferring six electrons to the fullerene cages, suggested that the selectivity observed is dictated by the size/shape complementary between host and guest. The crystallographic characterization of the previously reported D_{3h}-C_{78} and I_h-C_{80} EMFs revealed very similar sizes (in terms of volume of the fullerene cage), but different shapes,[10] irrespective of the nature of the internal cluster. Thus, the selectivity observed was a consequence of the enhanced π-interactions of the porphyrin units with the flattened regions of the ellipsoidal-shaped D_{3h}-C_{78} in comparison to the spherical I_h-C_{80} carbon cage. In previous studies performed by the group, we observed that the **1a**·(BArF)$_8$ (Pd(II)-based analogue of **1b**·(BArF)$_8$) shows higher affinity towards ellipsoidal fullerenes (C_{70}) than the more spherical ones (C_{60}),[6] in line with the observations in this study.

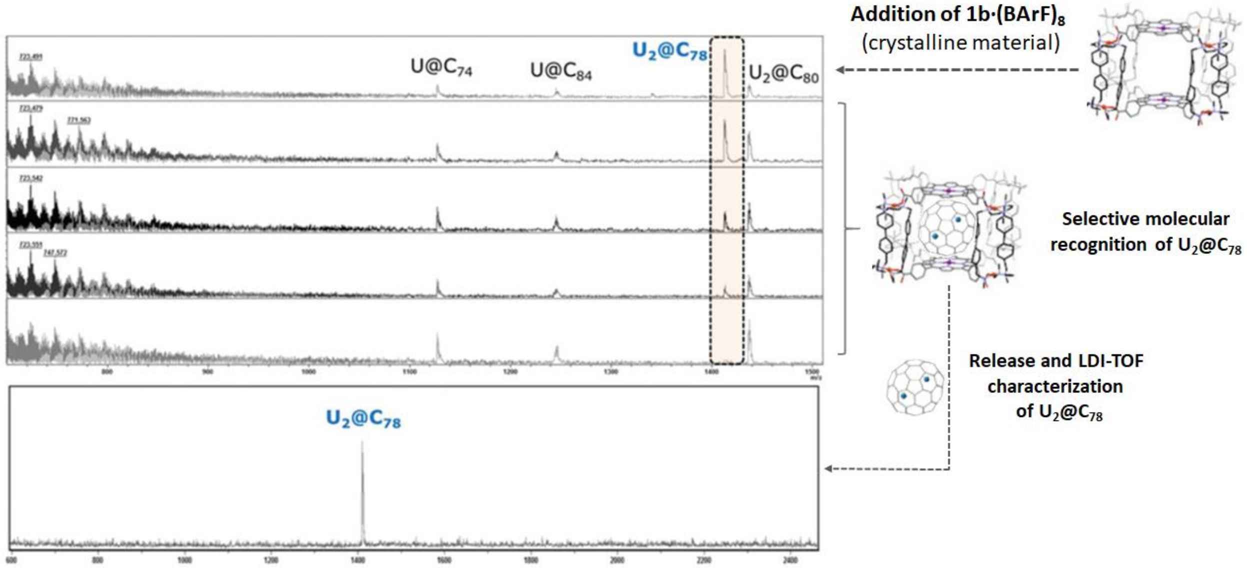

Figure VII.26. LDI-TOF monitoring of the selective complexation of U_2@C_{78} within crystals of **1b**·(BArF)$_8$ soaked in a toluene solution of U-based soot. LDI-TOF spectrum of the starting U soot solution (top); spectra monitoring the remaining supernatant solution after soaking crystals of **1b**·(BArF)$_8$ (middle) and spectrum of pure U_2@C_{78} released from **1b**·(BArF)$_8$ (bottom).

To gain further insight about the effect of the carbon cages (size/shape) and the internal clusters (electrostatics) on the selective binding of EMFs, we attempted the purification of a soot containing similar proportions of U_2C@C_{78}, Sc_2CU@C_{80}, U@C_{82} and Sc_3N@C_{80}. Upon addition of crystals of **1b**·(BArF)$_8$ into the corresponding soot solution, a clear decay of the peak attributed to U_2C@C_{78} was observed in the LDI-TOF monitoring of the supernatant (complete disappearance of the peak attributed to the target U_2C@C_{78} after 4.5 hours) (Figure VII.27). The LDI-TOF analysis of the released guests exclusively show a peak at m/z = 1424.0707 (Figure VII.27 bottom), confirming the purification of U_2C@C_{78}. In addition, it is worth to note that the selectivity shown by **1b**·(BArF)$_8$ (in solid phase) towards D_{3h}-C_{78} carbon cages was further evidenced by the selective encapsulation of Sc_3N@D_{3h}-C_{78} in the presence of Sc_3N@D_{3h}-C_{80} (Annex. Supp. Info. Chapter VI, Figure S3 and S4). These results suggested that the size/shape of the fullerene cage rules over the nature of the internal cluster, showing higher binding affinity for D_{3h}-C_{78} –based EMFs, irrespective of the nature of the trapped metals or metal clusters.

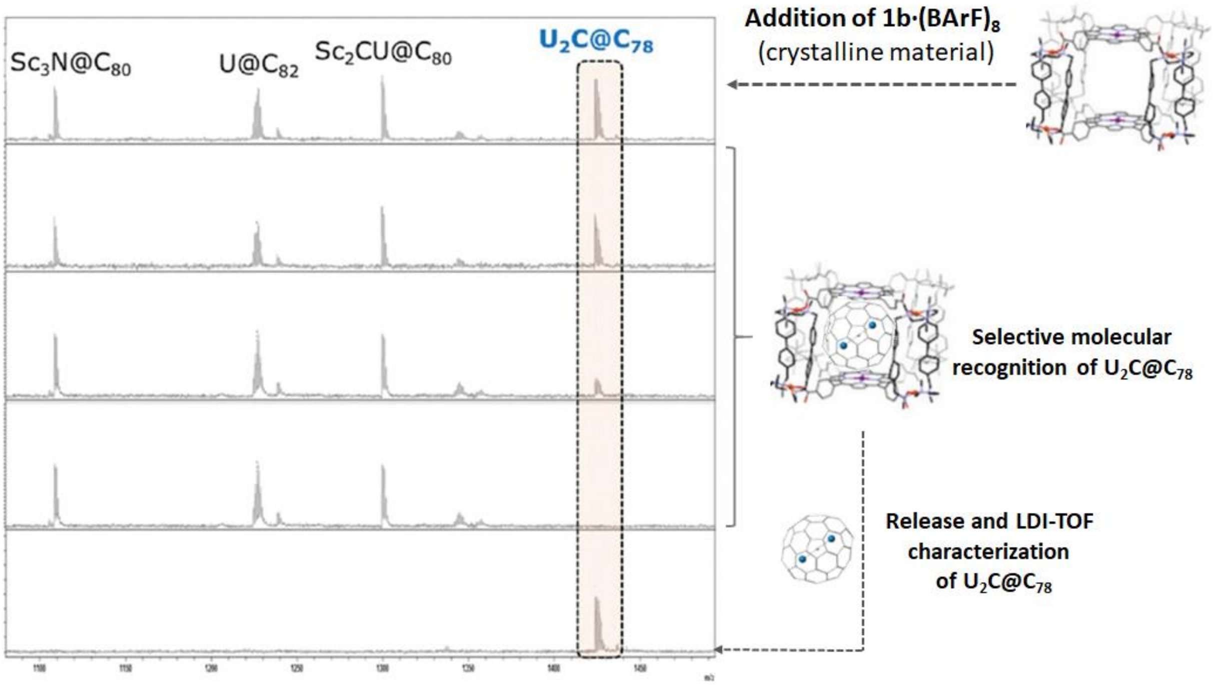

Figure VII.27. LDI-TOF monitoring of the selective complexation of $U_2C@C_{78}$ within crystals of **1b**·(BArF)$_8$ soaked in a Sc/U based soot. Spectrum of the starting U soot solution (top); spectra monitoring the remaining supernatant solution after soaking crystals of **1b**·(BArF)$_8$ (middle) and spectrum of pure $U_2@C_{78}$ released from **1b**·(BArF)$_8$ (bottom).

VII.4.3 Stepwise encapsulation and purification of $U_2@C_{78}$ and $U_2C@C_{78}$ from crude soots

One of the most extended problems for the chromatographic purification of EMFs, is the presence of compounds differing only in the nature of the internal cluster. We previously described the important role of the electron density distribution of EMFs (differing exclusively in the internal cluster) to allow their stepwise and selective host-guest complexation.[16] Given that the different cluster arrangements of $U_2@C_{78}$ and $U_2C@C_{78}$ induce different electronic density distributions, causing an impact on the electrostatic interactions with **1b**·(BArF)$_8$, we attempted the purification of $U_2@C_{78}$ and $U_2C@C_{78}$ EMFs mixture. Therefore, we soaked crystals of **1b**·(BArF)$_8$ to a sample mainly containing $U_2@C_{78}$ and $U_2C@C_{78}$. Gratifyingly, exclusive inclusion of $U_2@C_{78}$ was observed by the LDI-TOF monitoring of the supernatant (Figure VII.28). In addition, the LDI-TOF analysis of the released guest confirmed the specific molecular recognition $U_2@C_{78}$ (Figure VII.28) while its carbide analogue remained in solution. These results pointed towards the possible separation and purification of these novel EMFs directly from crude soots.

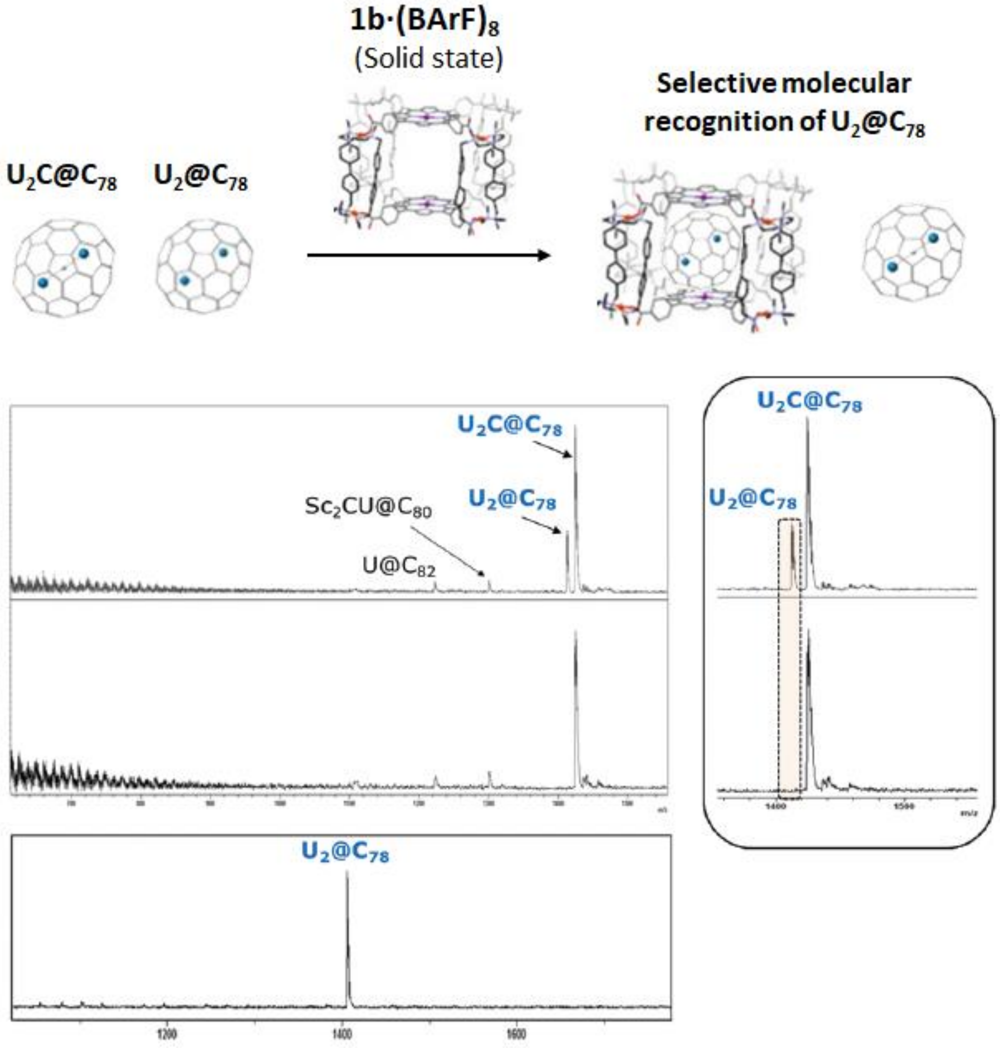

Figure VII.28. LDI-TOF monitoring of the selective complexation of $U_2@C_{78}$ within crystals of **1b**·(BArF)$_8$ soaked in a sample containing mainly $U_2@C_{78}$ and $U_2C@C_{78}$. Spectrum of the starting $U_2@C_{78}$ and $U_2C@C_{78}$ sample solution (top); spectrum of the remaining supernatant solution after soaking crystals of **1b**·(BArF)$_8$ (middle) and spectrum of pure $U_2@C_{78}$ released from **1b**·(BArF)$_8$ (bottom).

With all of these results in hand, we attempted the stepwise host-guest complexation of $U_2@C_{78}$ and $U_2C@C_{78}$ directly from a complex crude soot. The composition of the supernatant was monitored by LDI-TOF along the time upon the addition of the solid **1b**·(BArF)$_8$ in the sample, observing the complete disappearance of the peak attributed to $U_2@C_{78}$ after 2 hours (Figure VII.29). Then, the solid host-guest complexes were isolated and the guest released, obtaining $U_2@C_{78}$ in its pure form (as ascertained by LDI-TOF, Figure VII.29 bottom left). Then, fresh crystals of the host were subsequently added, observing the progressive decay until its complete disappearance of the $U_2C@C_{78}$ signal (Figure VII.29). Liberation of the trapped guest allowed the identification of pure $U_2C@C_{78}$ (Figure VII.29 bottom right). Despite the very low concentration of the targeted EMFs, we succeed in the identification of $U_2C@C_{78}\subset$**1b**·(BArF)$_8$ by ESI-MS (Annex. Supp. Info. Chapter VI, Figure S1).

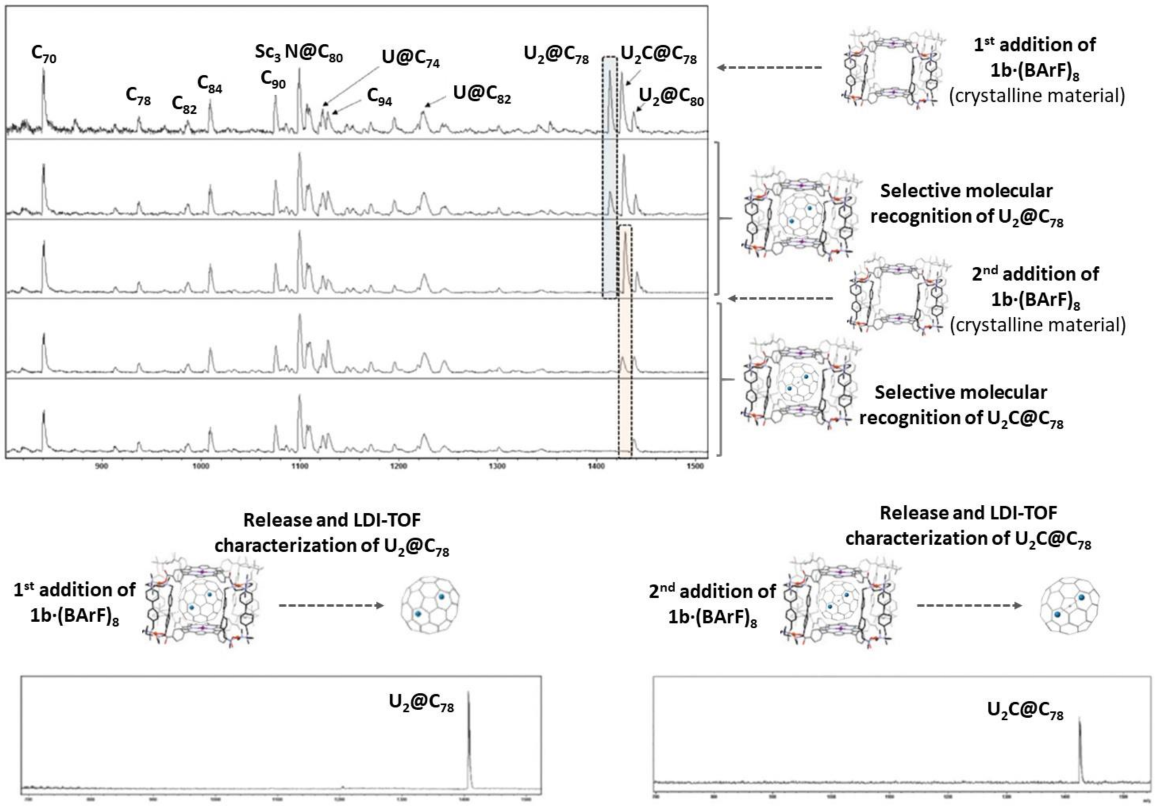

Figure VII.29. LDI-TOF monitoring of the stepwise selective complexation of $U_2@C_{78}$ and $U_2C@C_{78}$ within crystals of **1b**·(BArF)$_8$ soaked in a raw soot solution. Spectrum of the starting soot solution (top); spectra of the remaining supernatant after soaking crystals of **1b**·(BArF)$_8$ along the time (middle) and spectrum of pure $U_2@C_{78}$ and $U_2C@C_{78}$ released from the first sample and the second sample of **1b**·(BArF)$_8$ respectively (bottom).

VII.4.4 Computational studies: evaluation of the parameters directing the selective molecular recognition of di-uranium@C_{78} EMFs

To gain better comprehension of the parameters dictating the host-guest selectivity towards U-based D_{3h}-C_{78} EMFs a porphyrin-only model system was used for a systematic computational analysis of the binding energies (BE) (Annex. Supp. Info. Chapter VI, See Computational Details, Section 3). The study showed that the stabilization energies of the computed host-guest system changed significantly, depending on the relative orientation of the carbon cage of the guests with respect to the porphyrin units (Figure VII.30).

The computed BEs to evaluate the host-guest interactions, do not provide a plausible explanation of the selectivity observed from a thermodynamic point of view (Figure VII.30). However, a more detailed inspection of the computed structures reveals a slightly shorter porphyrin-porphyrin distance when $U_2@D_{3h}$-C_{78} is encapsulated, compared to $U_2@I_h$-C_{80} (Figure VII.30). The difference is about 0.2 Å, which could be significant if we take into account that the porphyrin-porphyrin distance (12 Å) in the crystal structure reported for **1b**·(BArF)$_8$,[16] is considerably shorter than the equilibrium values computed in the model.

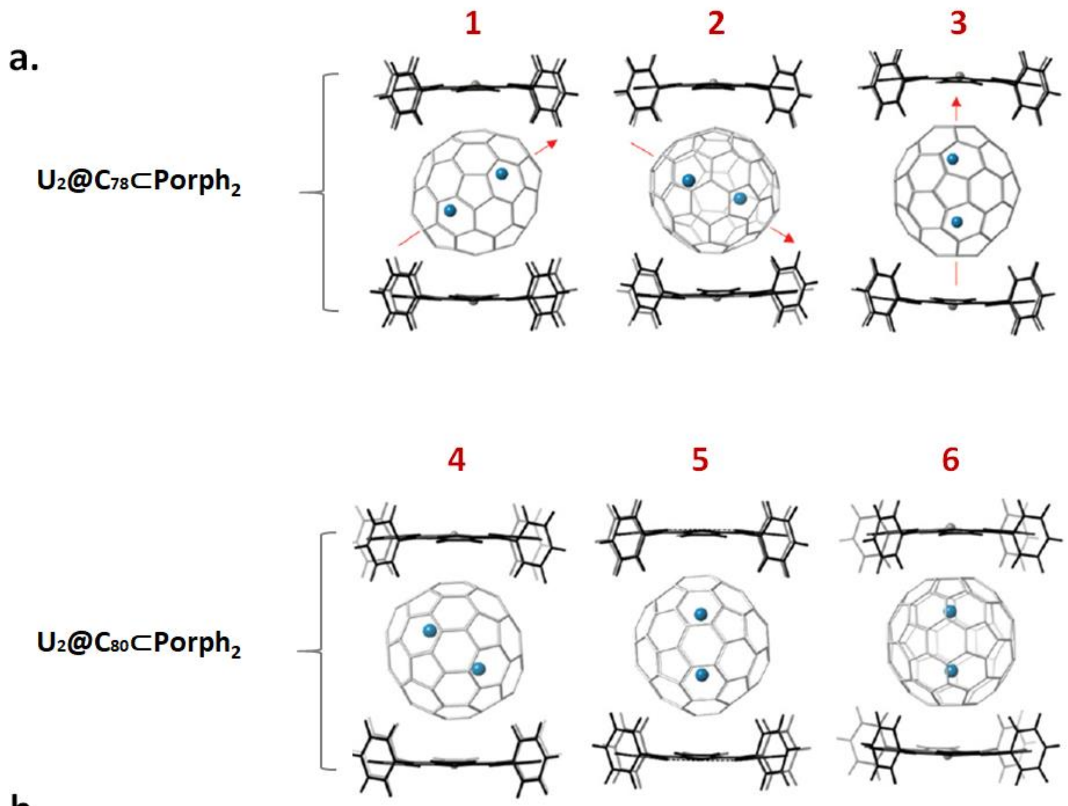

b.

	$U_2@D_{3h}$-C_{78}			$U_2@I_h$-C_{80}		
	1	2	3	4	5	6
BE[a]	−58.5	−56.9	−48.4	−59.1	−58.9	−52.4
d(Zn···Zn)[b]	13.68	13.65	14.48	13.80	13.95	14.26

Figure VII.30. a) The lowest energy orientation of $U_2@D_{3h}$-C_{78} (top) and $U_2@I_h$-C_{80} (bottom) in a simplified two tetraphenyl-porphyrin model. b) Table with BE and D(Zn···Zn) values for the three orientation. [a] Binding energies computed at the BLYP/TZP(D3) level are given in kcal mol^{-1}; [b] Zn···Zn separations are in Å).

To explore the effect of the **1b**·(BArF)$_8$ breathing, we focused our attention towards the energy changes when the porphyrin-porphyrin distances shrinks from 14 Å to 13 Å in the presence a guest ($U_2@D_{3h}$-C_{78} or $U_2@I_h$-C_{80}). The observations during the energy scanning confirmed three main points: (1) for I_h-C_{80} carbon cages the optimal distance between porphyrins is longer, (2) the binding energy between porphyrin and EMF guest is slightly larger for I_h-C_{80} carbon cages and (3) as the porphyrins compression progresses, the binding energy increases with a lower slope for D_{3h}-C_{78}. Due to the cylindrical shape of D_{3h}-C_{78} carbon cage, the energy destabilization of the system upon porphyrin compression is smaller when compared with more spherical I_h-C_{80} carbon cages (Figure VII.31). These results suggested better size/shape complementary between $U_2@D_{3h}$-C_{78} and **1b**·(BArF)$_8$, or in other words, the energy penalty required for the adaptive breathing of **1b**·(BArF)$_8$ to uptake the EMFs is smaller for the flattened *D$_{3h}$*-C$_{78}$ than for the spherical *I$_h$*-C$_{80}$.

a.

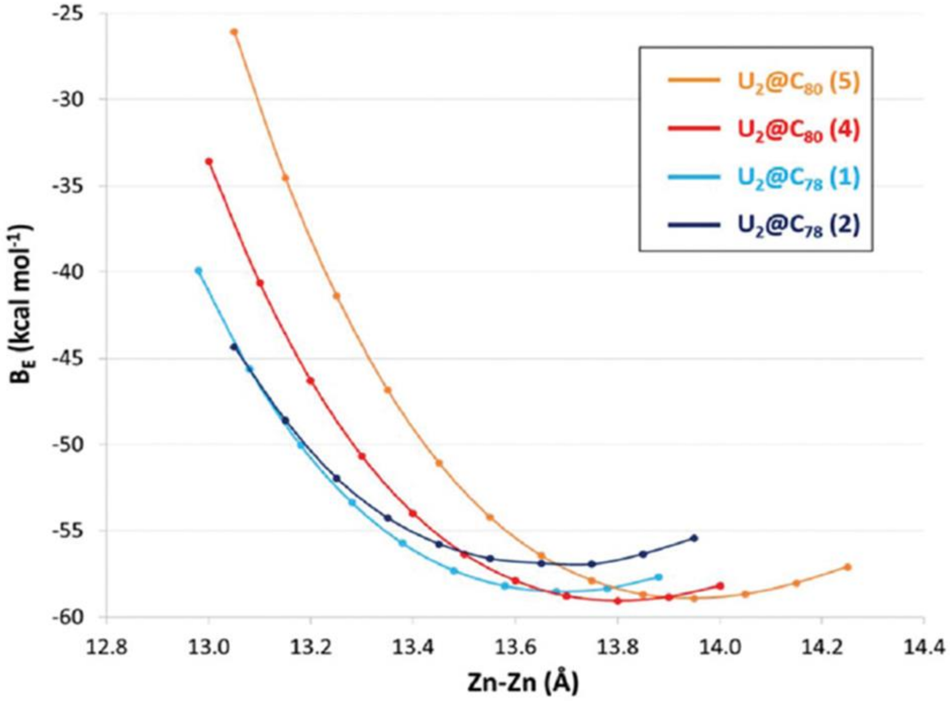

b.

	U$_2$@*D*$_{3h}$-C$_{78}$		U$_2$@*I*$_h$-C$_{80}$	
d(Zn···Zn)^b	**1**	**2**	**4**	**5**
13.0	−41.1	−41.9	−33.7	−21.5
13.2	−50.6	−50.4	−46.3	−38.1
13.4	−56.0	−55.2	−54.1	−49.1
13.6	−58.2	−57.0	−58.0	−55.5
13.8	−58.1	−56.7	−59.1	−58.4
14.0	−56.6	−55.1	−58.3	−58.8

Figure VII.31. a) Energy scan along the Zn···Zn separation maintaining porphyrins and fullerenes fixed. The numbering used is identical as in Figure VII.30. b) Table of BE between the EMFs studied and the two Zn-porphyrin moieties. [a] Binding energies computed at the BLYP/TZP(D3) level are given in kcal mol^{-1}; [b] Zn···Zn separations are in Å).

The computational studies performed with U$_2$C@*D$_{3h}$*-C$_{78}$ revealed exactly the same porphyrin-porphyrin distances and the same calculated BEs as those found for U$_2$@*D$_{3h}$*-C$_{78}$ (Annex. Supp. Info. Chapter VI, Figure S5). The presence of a central carbon atom in the internal cluster and the change in the formal oxidation state of uranium ions from +3 to +5 (equal number of electrons transferred from the cluster to the fullerene cage) hardly modifies the electron density distribution on the fullerene surface. Therefore, more sophisticated host-guest models and molecular dynamic simulations will be needed to get better understanding and representation of the EMFs uptake phenomena within the cavity of **1b**·(BArF)$_8$.

As final remarks of this section, we report the performance of a supramolecular nanocapsule **1b**·(BArF)$_8$ to selectively encapsulate and isolate U-based EMFs from highly complex crude soots. Furthermore, our host is capable to discriminate C_{78}-based EMFs from C_{80}-based EMFs, being compounds differing only in the shape of the carbon cage. This selectivity stems from the slightly shape differences between the spherical I_h-C_{80} and the ellipsoidal D_{3h}-C_{78} (flattened regions on its carbon cage), promoting enhanced π···π interactions between the porphyrins of the host and the EMFs guest. On the other hand, computational studies indicated a limited breathing ability of the host in solid phase and that results in a lower breathing energy penalty towards the encapsulation of an ellipsoidal D_{3h}-C_{78}-based EMF. Moreover, **1b**·(BArF)$_8$ is able to sequentially and selectively uptake D_{3h}-C_{78}-based EMFs species differing only in the nature of the internal cluster (U_2 vs U_2C). This finding indicates that beyond the size/shape host-guest complementary, the electron density induced by the internal cluster finally determines the affinity towards the host. The non-chromatographic supramolecular protocol described here has proven to be a useful alternative to the traditional HPLC methods commonly used for purification of EMFs.

VII.5. References

(1) Ma, L.; Haynes, C. J. E.; Grommet, A. B.; Walczak, A.; Parkins, C. C.; Doherty, C. M.; Longley, L.; Tron, A.; Stefankiewicz, A. R.; Bennett, T. D.; Nitschke, J. R. *Nat. Chem. 2020* **2020**, 1.

(2) Zhang, D.; Ronson, T. K.; Lavendomme, R.; Nitschke, J. R. *J. Am. Chem. Soc.* **2019**, *141* (48), 18949.

(3) Mal, P.; Breiner, B.; Rissanen, K.; Nitschke, J. R. *Science (80-.).* **2009**, *324* (5935), 1697.

(4) Suzuki, K.; Kawano, M.; Sato, S.; Fujita, M. *J. Am. Chem. Soc.* **2007**, *129* (35), 10652.

(5) García-Simón, C.; Garcia-Borràs, M.; Gómez, L.; Garcia-Bosch, I.; Osuna, S.; Swart, M.; Luis, J. M.; Rovira, C.; Almeida, M.; Imaz, I.; Maspoch, D.; Costas, M.; Ribas, X. *Chem. - A Eur. J.* **2013**, *19* (4), 1445.

(6) García-Simón, C.; Garcia-Borràs, M.; Gómez, L.; Parella, T.; Osuna, S.; Juanhuix, J.; Imaz, I.; Maspoch, D.; Costas, M.; Ribas, X. *Nat. Commun.* **2014**, *5* (May), 2.

(7) García-Simón, C.; Gramage-Doria, R.; Raoufmoghaddam, S.; Parella, T.; Costas, M.; Ribas, X.; Reek, J. N. H. *J. Am. Chem. Soc.* **2015**, *137* (7), 2680.

(8) Castro, E.; Azmani, K.; Garcia, A. H.; Aghabali, A.; Liu, S.; Metta-Magana, A. J.; Olmstead, M. M.; Rodríguez-Fortea, A.; Poblet, J. M.; Echegoyen, L. *Chem. - A Eur. J.* **2017**, *23* (63), 15937.

(9) Yan, W.; Seifermann, S. M.; Pierrat, P.; Bräse, S. *Org. Biomol. Chem.* **2015**, *13* (1), 25.

(10) Yang, S.; Wei, T.; Jin, F. *Chem. Soc. Rev.* **2017**, *46* (16), 5005.

(11) Note that 5·(OTf)8 is the same compound as 1b·(OTf)8 (section VII.1); the labelling change is due to publication issues and is kept as tit appears in the published articles to avoid confusion. .

(12) Chai, Y.; Guo, T.; Jin, C.; Haufler, R. E.; Chibante, L. P. F.; Fure, J.; Wang, L.; Alford, J. M.; Smalley, R. E. *J. Phys. Chem.* **1991**, *95* (20), 7564.

(13) Zhang, X.; Wang, Y.; Morales-Martínez, R.; Zhong, J.; De Graaf, C.; Rodríguez-Fortea, A.; Poblet, J. M.; Echegoyen, L.; Feng, L.; Chen, N. *J. Am. Chem. Soc.* **2018**, *140* (11), 3907.

(14) Svitova, A. L.; Ghiassi, K. B.; Schlesier, C.; Junghans, K.; Zhang, Y.; Olmstead, M. M.; Balch, A. L.; Dunsch, L.; Popov, A. A. *Nat. Commun.* **2014**, *5*.

(15) Zhang, X.; Li, W.; Feng, L.; Chen, X.; Hansen, A.; Grimme, S.; Fortier, S.; Sergentu, D. C.; Duignan, T. J.; Autschbach, J.; Wang, S.; Wang, Y.; Velkos, G.; Popov, A. A.; Aghdassi, N.; Duhm, S.; Li, X.; Li, J.; Echegoyen, L.; Schwarz, W. H. E.; Chen, N. *Nat. Commun.* **2018**, *9* (1), 1.

(16) Fuertes-Espinosa, C.; Gómez-Torres, A.; Morales-Martínez, R.; Rodríguez-Fortea, A.; García-Simón, C.; Gándara, F.; Imaz, I.; Juanhuix, J.; Maspoch, D.; Poblet, J. M.; Echegoyen, L.; Ribas, X. *Angew. Chemie - Int. Ed.* **2018**, *57* (35), 11294.

Chapter VIII.

General Conclusions

In this thesis we employed the metal-coordination self-assembly approach to design highly sophisticated 3D tetragonal prismatic nanocapsules. These supramolecular nanocapsules show high and unique affinities for fullerenes and EMFs, providing new opportunities to address the regioselective functionalization of fullerenes and the purification of EMFs.

In **Chapter III**, the Pd(II)-base nanocapsule **1a**·(BArF)$_8$ is used as a supramolecular mask to exert chemo- and regioselective control on cyclopropanation reactions of confined C_{60}. The tetragonal prismatic geometry of **1a**·(BArF)$_8$, featuring four cross-shaped open windows, plays a key role to gain regio-control over the multiple Bingel cyclopropanation reactions on confined C_{60}. Exclusive equatorial regioselectivity and stepwise formation of the bis-, tris- and tetrakis-C_{60} homoadducts have been observed. Furthermore, this equatorial regioselectivity imposed by **1a**·(BArF)$_8$ can be transferred towards the production of tetrakis-C_{60} heteroadducts. On the other hand, a novel synthetic strategy has been developed for the regioselective production of *Th*-hexakis-C_{60} heteroadducts in a one-pot reaction, by the exquisite combination of both, reactivity in confined spaces and in bulk solution. In addition, a biphasic system has been designed to upgrade the supramolecular mask strategy into a catalytic and synthetically useful protocol, achieving quantitative and regioselective formation of a single equatorial tetrakis-C_{60} homoadduct. The reversible phase transfer of **1a**·(BArF)$_8$ (and its cargo) is controlled by anion metathesis with $(TBA)_2(SO_4)$, and the over-reactivity commonly observed in bulk solution is completely avoided. The cyclopropanation reaction is confined at the aqueous layer, whereas the released product is being accumulated into the organic layer, protecting it from further reactions. Indeed, our supramolecular mask strategy opens the door to access a large variety of pure-isomer poly-functionalized C_{60}-based compounds, which are potential candidates for testing on new generation of solar cell devices and biomedical applications.

In **Chapter IV**, the dicopper(II)-based hexaaza-macrocyclic complex [(**Cu-1b**)(OTf)$_2$](OTf)$_2$ has been synthesized and fully characterized. This molecular clip synthon is self-assembled with porph-Zn building blocks for the preparation of a novel 3D tetragonal prismatic nanocapsule, **5**·(OTf)$_8$, which is the Cu(II) analogue of Pd(II)-based **1a**$^{8+}$ and is designed as a more labile coordination nanocapsule. Selective recognition towards fullerenes and EMFs present in Sc_3N-based soot in **5**·(OTf)$_8$ has been found. Simply by soaking a solid sample of **5**·(OTf)$_8$ in a toluene solution of the crude soot, only the targeted $Sc_3N@C_{80}$ is left in solution and therefore is obtained in a single step (I_h–D_{5h} mixture, purity up to 99.5% and up to 85% of recovery). Finally, it has been demonstrated that the rational structural changes performed in **5**·(OTf)$_8$ (respect to its Pd(II)-based analog) strongly modified its host-guest properties, allowing the release of trapped fullerenes and EMFs by a solvent-washing protocol. Thanks to the reversible encapsulation of all the species present in the Sc_3N-based soot, the host can be easily recovered and directly re-used. The distinctive encapsulation of the solid state supramolecular host is thought to offer new opportunities in fullerene-like compounds purification.

In **Chapter V**, we describes a straightforward isolation and purification of challenging actinide based EMFs, $U_2@I_h$-C_{80} and $Sc_2CU@I_h$-C_{80}, directly from crude Sc/U-based soots by using **1b**·(BArF)$_8$ as a host (**1b**·(BArF)$_8$ is identical to **5**·(OTf)$_8$, but possessing different counter-anions).. Thanks to the very precise and selective molecular recognition properties shown by **1b**·(BArF)$_8$, simply by soaking crystals of the host in a toluene solution of the crude soot, $U_2@I_h$-C_{80} and $Sc_2CU@I_h$-C_{80} were sequentially and selectively uptake within the crystals of **1b**·(BArF)$_8$. Furthermore, the guests can be easily released, obtaining both targeted EMFs in their pure forms. It is worth to note that, $Sc_2CU@I_h$-C_{80} represents a new type of actinide-based EMFs, being the first example of a mixed-metal uranium-based EMF. A computational simplified model, consisting in two parallel tetraphenyl-Zn-porphyrins hosting the EMF guest, suggested that a highly directional electron-density distribution (induced from the internal EMF cluster to the carbon cage), is at the basis to explain different electrostatic interactions and selectivity towards very similar EMFs species. The release of the purified EMFs by solvent-washing protocol is further facilitated by the orthogonal solubility between host and guest. Our EMFs purification strategy overcome the limitations of HPLC techniques, distinguishing and separating EMFs species that differ only by the internal cluster, in a single step.

Finally in **Chapter VI**, the ability of **1b**·$(BArF)_8$ to purify challenging EMFs in an easy and simple manner, have been further exemplified by isolating the firsts uranium-based-C_{78} EMFs. The ability to discriminate among very similar EMFs stem from the faintly shape differences between spherical I_h-C_{80} and the more flattened D_{3h}-C_{78} carbon cages, promoting enhanced π···π staking interactions between the fullerene cage and the porphyrin units of the host. On the other hand, DFT calculations indicated that the limited breathing ability of the host in the solid state resulted in a lower breathing energy penalty towards the encapsulation of the ellipsoidal D_{3h}-C_{78} EMFs, when compared with the spherical I_h-C_{80}. Furthermore, we have proven that **1b**·$(BArF)_8$ is capable to distinguish U_2@D_{3h}-C_{78} and U_2C@D_{3h}-C_{78}, which only differ in the nature of the endohedral cluster. These findings suggested that beyond the size/shape complementary between the host and the guest, the electronics of the targeted EMFs are at interplay in defining the affinity towards the host. The non-chromatographic strategy described in this chapter has proven to be a viable alternative to HPLC methodologies. The accumulation of pure U_2@D_{3h}-C_{78} and U_2C@D_{3h}-C_{78} allows the elucidation of their physicochemical properties to potentially find applications in several research fields.

Annex.

Supporting Information

Supporting Information Chapter III

Supramolecular Fullerene Sponges as Catalytic Masks for Regioselective Functionalization of C_{60}

Table of Contents

1. | Supplementary Methods

Reagents and instrumentation: Reagents and solvents used were commercially available reagent quality unless indicated otherwise. Supramolecular nanocapsules **1a**·(BArF)$_8$ and **1b**·(BArF)$_8$ were synthesized according to published procedures.[1-2] ESI-HRMS experiments were collected and analyzed on a Bruker MicroTOF-Q-II, using acetonitrile or dichloromethane:methanol mixture, as the mobile phase. UV-vis spectra were performed with an Agilent 8452 UV-vis spectrophotometer (1 cm quartz cell) in Toluene. HPLC data concerning fullerene adducts purity were collected on Agilent Technologies LC 1200 series instrument equipped with a Cosmosil Buckyprep-M column (10 mm × 250 mm, Nacalai Tesque, Inc.) monitored with a UV detector at 320 nm. Toluene was used as mobile phase (flow: 0.5 mL/min).

NMR experiment details: All NMR experiments were performed at 298 K on a Bruker AVANCE 500 NMR spectrometer operating at 500.13 MHz and equipped with a cryoprobe *z*-gradient inverse probehead capable of producing gradients in the *z* direction with a maximum strength of 53.5 G cm^{-1}. The description of the ^{13}C NMR data is solely focused on the ester groups of the malonate addends. Heteronuclear 2D ^{1}H-^{13}C correlation experiments were acquired using the sensitivity-enhanced HSQC pulse sequence. Conventional and spectral-aliased HSQC experiments were recorded using a ^{13}C spectral width (SW(^{13}C)) of 160 and 5 or 2 ppm, respectively. The high-resolution achieved in the ^{13}C dimension of spectral-aliased HSQC (SA-HSQC) spectra were used to discern between cross-peaks displaying very similar ^{1}H and ^{13}C chemical shifts. ^{13}C chemical shifts in SA-HSQC are calculated according to $\delta^{real}=\delta^{aliased}+\kappa$*SW(^{13}C), where κ is the aliasing factor which can be determined from the conventional reference HSQC spectrum. For instance, a methyl signal appearing at δ(^{13}C)=54.08 ppm in the SA-HSQC spectrum acquired with SW(^{13}C)=5 ppm means that its δ(^{13}C)^{real} is 14.08 ppm and κ=8.

DOSY experiments were recorded using the double stimulated echo sequence incorporating bipolar gradient pulses and a longitudinal eddy current delay (dstegp3s in the BRUKER library). The gradient strength was linearly incremented in 16 steps from 2% up to 95% of the maximum gradient strength. Diffusion times and gradient pulse durations were optimized for each experiment to achieve a 95% decrease in the resonance intensity at the largest gradient amplitude; typically, diffusion times between 150 ms and bipolar rectangular gradient pulses between 1.5 ms were employed. After Fourier transformation followed by the same phase and baseline correction of each 1D dataset, the diffusion dimension of the 2D DOSY spectra was obtained by using the dosy protocol included into the of the Bruker TOPSPIN software package. The diffusion coefficients obtained from the DOSY experiments were used to evaluate the hydrodynamic radius of the fullerene systems for all samples according to the Stokes-Einstein equation.

X-Ray diffraction details (synchrotron radiation): Single crystals of **2⊂1b**·(BArF)$_8$ were obtained by slow diffusion of Et$_2$O into a solution of in CH$_2$Cl$_2$ containing 5% of CH$_3$CN. Crystallographic data for **2⊂1b**·(BArF)$_8$ (CCDC code 1913118) were collected at the XALOC beamline of the ALBA synchrotron at 100 K using a MD2M single-axis diffractometer (Maatel, France) and a Pilatus 6 M detector (Dectris, Switzerland).[3] Due to their sensitivity to solvent loss, a crystal of **2⊂1b**·(BArF)$_8$ was mounted in a thin glass capillary and cryopreserved at 100 K. This single crystal was introduced into the capillary suspended in a small volume of ether/DMF (solution used to grow the crystal saturated with ether). The data set was collected on omega single-axis scans with 1-s per frame exposures at λ = 0.82653 Å. The crystal was diffracting at a moderate resolution (1.6 Å) and showed degradation due to radiation damage. This poor density and fast degradation is attributed to the high symmetry, solvent loss and severe motions of the solvents (volatile ether) and counteranion molecules (BArF) in the large cavities of the crystal lattice. The data were integrated and scaled using XDS.[4] The structure was solved using SHELXT[5] refined by the full matrix least-squares based of F^2 using SHELXL97.[6] Although the limited quality of the data, we have been able to locate the functionalized fullerene inside the cage as well as the BArF counteranions. However, terminal CF$_3$ groups of the BArF counteranions showed high disorder and strong agitations that could not be refined adequately. For these reasons, we refined them imposing restraints (DELU, ISOR). Attempts to identify and model the disordered solvent molecules were unsatisfactory; therefore, the PLATON/SQUEEZE routine was applied to mask out the disordered electron density (6703 electrons per unit cell).[7]

Molecular Dynamics (MD) simulations: Molecular Dynamics simulations were performed using the GPU code (*pmemd*)[8] of the AMBER 16 package.[9] Parameters for fullerenes and acetonitrile (solvent) were generated within the *antechamber* module using the general AMBER force field (*gaff*),[10] with partial charges set to fit the electrostatic potential generated at the HF/6-31G(d) level by the RESP model.[11] The charges were calculated according to the Merz–Singh–Kollman scheme[12-13] using the Gaussian 09 package.[14] Parameters for supramolecular metallo-cages were generated using the MCPB.py[15] module included in AmberTools16.[9] Each host-guest system was immersed in a pre-equilibrated truncated octahedron box with a 12 Å buffer of acetonitrile molecules using the *leap* module, resulting in the addition of around 750 solvent molecules. The systems were neutralized by addition of explicit counter ions (Cl^-). All subsequent calculations were done using the Stony Brook modification of the Amber14 force field (*ff14sb*).[16] A two-stage geometry optimization approach was performed. The first stage minimizes the positions of solvent molecules and ions imposing positional restraints on the solute by a harmonic potential with a force constant of 500 $kcal\cdot mol^{-1}\cdot Å^{-2}$ and the second stage minimizes all the atoms in the simulation cell except those involved in the harmonic distance restraint. The systems were gently heated using six 50 ps steps, incrementing the temperature by 50 K for each step (0–300 K) under constant-volume and periodic-boundary conditions. Long-range electrostatic effects were modelled using the particle-mesh-Ewald method.[17] An 8 Å cutoff was applied to Lennard–Jones and electrostatic interactions. Bonds involving hydrogen were constrained with the SHAKE algorithm. Harmonic restraints of 30 $kcal\cdot mol^{-1}$ were applied to the solute and the Andersen equilibration scheme was used to control and equalize the temperature. The time step was kept at 1 fs during the heating stages, allowing potential inhomogeneities to self-adjust. Each system was then equilibrated for 2 ns with a 2 fs time step in the NPT ensemble. Production trajectories were then run for an additional 500 ns under the NVT ensemble and periodic-boundary conditions.

Non-Covalent Interaction (NCI) analysis: Non-Covalent Interaction (NCI) analyses were performed with the NCIPLOT program[18-19] on selected snapshots from MD simulations. Promolecular densities, defined as the sum of atomic contributions, were used. Although promolecular density does not consider the relaxation due to the SCF procedure, it has been shown that results provided by relaxed density and promolecular density are qualitatively equivalent. The NCI analysis is based on considering the reduced density gradient, s, and the electron density, ρ (eq. 1):[19]

$$s = \frac{1}{2(3\pi^2)^{1/3}}\frac{|\nabla\rho|}{\rho^{4/3}} \qquad \text{(Equation 1)}$$

A change in the reduced density gradient between interacting atoms occurs when a weak inter- or intramolecular interaction is present, appearing density critical points between interacting fragments.[19] The density and reduced density gradient are computed at a number of grid points around the atoms. Dispersion interactions appear at very low density values ($\rho > 0.01$ a.u.), while stronger interactions such hydrogen bonding appear at higher density values ($0.01 < \rho < 0.05$ a.u.). The sign of the second eigenvalue (λ_2) of the electron density Hessian matrix is used as a tool for distinguishing between bonded (attractive interaction $\lambda_2 < 0$) or nonbonded (repulsive interaction, $\lambda_2 > 0$) interactions. Consequently, the gradient is plotted against the product of the sign (λ_2) and the electron density function. For the isosurface representation (isosurface value 0.3 a.u.), a RGB (red-blue-green) scale was used: red represents repulsive interactions, blue represents attractive interactions, and green shows weak van der Waals interactions. For further details on NCI and NCIPLOT.[18-20]

2. | Supplementary Synthetic Protocols

Synthesis of tetrakis-diethylmalonate-C$_{60}$ adduct (2)

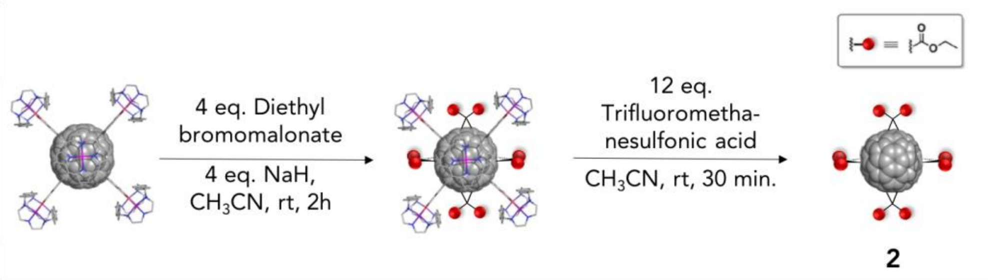

Diethyl bromomalonate (2.4 mg, 10 µmol) and sodium hydride (0.24 mg, 10 µmol) were added to a solution of **C$_{60}$$\subset$1a**·(BArF)$_8$ (32 mg, 2.5 µmol) in dry CH$_3$CN and the reaction was stirred for 2h at room temperature under N$_2$. The crude was filtered through a PTFE filter (0.45 µm pore size), trifluoromethanesulfonic acid (4.5 mg, 30 µmol) was added, after which the solution turned dark green. The resulting mixture was stirred for 30 minutes. The solvent was removed under vacuum, the reaction crude was washed with diethyl ether (10 ml x 3) and then evaporated to dryness under a stream of nitrogen gas. 10 ml of toluene were added on the remaining solid, filtered through a PTFE filter (0.45 µm pore size) and the solvent was removed under vacuum to furnish adduct **2** (3.1 mg, 2.47 µmol, 99% yield).

^{1}H NMR (500 MHz, CDCl$_3$) δ ppm: 4.54 (8H, q, J = 7.1 Hz), 4.51 (8H, q, J = 7.1 Hz), 1.48 (12H, t, J = 7.1 Hz), 1.46 (12H, t, J = 7.1 Hz).

^{13}C NMR (125 MHz, CD$_3$CN) δ ppm: 63.24, 63.19, 14.23, 14.20.

HRMS of 2$\subset$1a (CH$_3$CN), m/z: calc. for [**2**$\subset$**1a**]$^{8+}$ 811.5671, observed 811.5675; calc. for [**2**$\subset$**1a**·(BArF)$_1$]$^{7+}$ 1050.8340, observed 1050.8347; calc. for [**2**$\subset$**1a**·(BArF)$_2$]$^{6+}$ 1369.8417, observed 1369.8433; calc. for [**2**$\subset$**1a**·(BArF)$_3$]$^{5+}$ 1816.4524, observed 1816.4530; calc. for [**2**$\subset$**1a**·(BArF)$_4$]$^{4+}$ 2486.3680, observed 2486.3687.

HRMS (CH$_2$Cl$_2$:MeOH), m/z: calc. for [**2**+Na]$^+$ 1375.2209, observed 1375.2202.

Synthesis of tetrakis-dimethylmalonate-C$_{60}$ adduct (3)

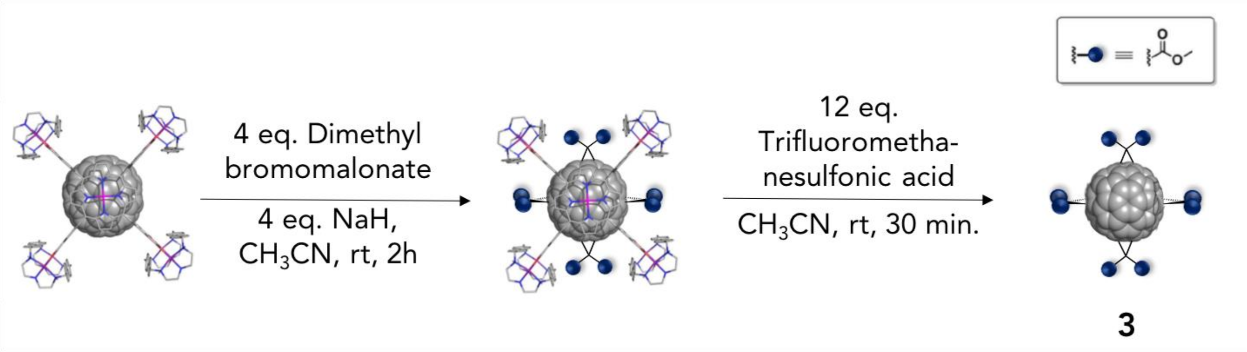

Dimethyl bromomalonate (2.1 mg, 10 µmol) and sodium hydride (0.86 mg, 10 µmol) were added to a solution of **$C_{60}$$\subset$1a**·(BArF)$_8$ (32 mg, 2.5 µmol) in dry CH3CN and the reaction was stirred for 2h at room temperature under N_2 The crude was filtered, trifluoromethanesulfonic acid (4.5 mg, 30 µmol) was added (disassembling **1a**·(BArF)$_8$ and release of adduct **3**) and the mixture was stirred for 30 min. The solvent was removed under vacuum and adduct **3** was recovered washing the remaining solid with toluene (2.57 mg, 2.07 µmol, 83% purity, 89% yield).

^{1}H NMR (500 MHz, $CDCl_3$) δ ppm: 4.09 (12H, s), 4.06 (12H, s).

^{13}C NMR (125 MHz, CD_3CN) δ ppm: 54.1, 54.0.

HRMS of 3$\subset$1a (CH_3CN), m/z: calc. for [**3$\subset$1a**]$^{8+}$ 797.5509, observed 797.5516: calc. for [**3$\subset$1a**·(BArF)$_1$]$^{7+}$ 1034.8036, observed 1034.8042; calc. for [**3$\subset$1a**·(BArF)$_2$]$^{6+}$ 1351.1395, observed 1351.1403; calc. for [**2$\subset$1a**·(BArF)$_3$]$^{5+}$ 1794.0099, observed 1794.0104; calc. for [**3$\subset$1a**·(BArF)$_4$]$^{4+}$ 2458.1531, observed 2458.1540.

HRMS (CH_2Cl_2:MeOH), m/z: calc. for [**3**+Na]$^+$ 1281.1062, observed 1281.1054.

Synthesis of bis-diethylmalonate-C_{60} adduct (4)

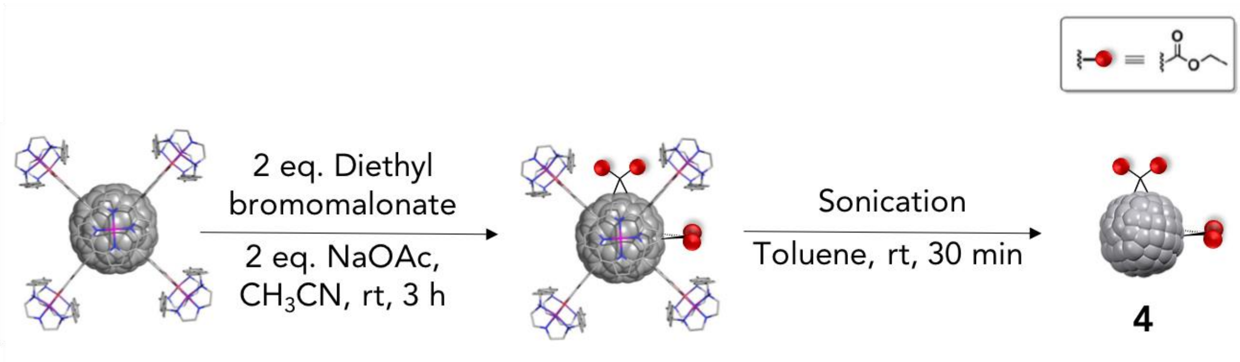

Diethyl bromomalonate (1.2 mg, 5 µmol) and sodium acetate (0.43 mg, 5 µmol) were added to a solution of **$C_{60}$$\subset$1a**·(BArF)$_8$ (32 mg, 2.5 µmol) in dry CH_3CN and the reaction was stirred for 3h at room temperature. The crude was filtered, the solvent was removed under vacuum and the remaining solid was washed with diethyl ether (10 ml x 3). The host-guest complex **4$\subset$1a**·(BArF)$_8$ was suspended in 10 ml of toluene and after 30 min of sonication the adduct **4** (2.51 mg, 2.42 µmol, 97% yield) was quantitatively released from **1a**·(BArF)$_8$.

^{1}H NMR (500 MHz, $CDCl_3$) δ ppm: 4.54-4.44 (8H, m), 1.47-1.42 (12H, m)

^{13}C NMR (125 MHz, CD_3CN) δ ppm: 63.2, 14.18.

HRMS of 4$\subset$1a (CH_3CN), m/z: calc. for [**4$\subset$1a**]$^{8+}$ 772.0525, observed 772.0520; calc. for [**4$\subset$1a**·(BArF)$_1$]$^{7+}$ 1005.6477, observed 1005.6469; calc. for [**4$\subset$1a**·(BArF)$_2$]$^{6+}$ 1317.1243, observed 1317.1235; calc. for [**4$\subset$1a**·(BArF)$_3$]$^{5+}$ 1753.1916, observed 1753.1911; calc. for [**4$\subset$1a**·(BArF)$_4$]$^{4+}$ 2407.2929, observed 2407.2924.

HRMS (CH_2Cl_2:MeOH), m/z: calc. for [**4**+Na]$^+$ 1059.1050, observed 1059.1046.

Synthesis of tris-diethylmalonate-C$_{60}$ adducts (5a and 5b)

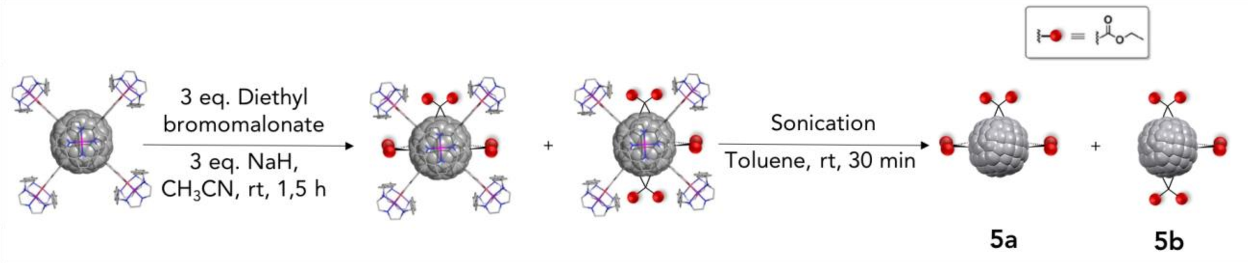

Diethyl bromomalonate (1.8 mg, 7.5 µmol) and sodium hydride (0.18 mg, 7.5 µmol) were added to a solution of **C$_{60}$$\subset$1a**·(BArF)$_8$ (32 mg, 2.5 µmol) in dry CH$_3$CN and the reaction was stirred for 1.5 h at room temperature under N$_2$. The crude was filtered, the solvent was removed under vacuum and the remaining solid was washed with diethyl ether (10 ml x 3). The host-guest complex **5$\subset$1a**·(BArF)$_8$ was suspended in 10 ml of toluene and after 30 min of sonication, adduct **5** (equimolar mixture of two isomers: *e,e,t1(I)* (**5a**) : *e,e,t1(II)* (**5b**), 1:1). 2.9 mg, 2.42 µmol, 97% yield) were quantitatively recovered.

^{1}H NMR (500 MHz, CDCl$_3$) δ ppm: 4.63 (2H, q, J = 7.1 Hz), 4.58-4.56 (4H, m), 4.50 (2H, q, J = 7.1 Hz), 4.47 (2H, q, J = 7.1 Hz), 4.44 (2H, q, J = 7.1 Hz), 1.55 (3H, t, J = 7.1 Hz), 1.51 (3H, t, J = 7.1 Hz), 1.50 (3H, t, J = 7.1 Hz), 1.45 (3H, t, J = 7.1 Hz), 1.42 (3H, t, J = 7.1 Hz), 1.40 (3H, t, J = 7.1 Hz).

^{13}C NMR (125 MHz, CD$_3$CN) δ ppm: 63.43, 63.34, 63.33, 63.22, 63.18, 63.16, 14.31, 14.26, 14.22, 14.21, 14.18, 14.16.

HRMS of 5$\subset$1a (CH$_3$CN), m/z: calc. for [**5$\subset$1a**]$^{8+}$ 791.8095, observed 791.8098; calc. for [**5$\subset$1a**·(BArF)$_1$]$^{7+}$ 1028.2408, observed 1028.2413; calc. for [**5$\subset$1a**·(BArF)$_2$]$^{6+}$ 1343.4830, observed 1343.4832; calc. for [**5$\subset$1a**·(BArF)$_8$]$^{5+}$ 1784.8220, observed 1784.8225; calc. for [**5$\subset$1a**·(BArF)$_4$]$^{4+}$ 2446.8305, observed 2446.8310.

HRMS (CH$_2$Cl$_2$:MeOH), m/z: calc. for [**5**+Na]$^+$ 1217.1535, observed 1217.1541.

Synthesis of *e,e*-bis-dimethyl-*e,e*-bis-diethylmalonate-C$_{60}$ hetero adduct (6)

Dimethyl bromomalonate (1.05 mg, 5 µmol) and sodium acetate (0.43 mg, 5 µmol) were added to a solution of **C$_{60}$$\subset$1a**·(BArF)$_8$ (32 mg, 2.5 µmol) in dry CH$_3$CN and the reaction was stirred for 3 h at room temperature. Then, diethyl bromomalonate (1.2 mg, 5 µmol) and sodium acetate (0.43 mg, 5 µmol) were added in the resulting mixture and stirred for 3 h at room temperature. The crude was filtered, trifluoromethanesulfonic acid (4.5 mg, 30 µmol) was added (disassembling **1a**·(BArF)$_8$ and release of adduct **6**) and the mixture was stirred for 30 min. The solvent was removed under vacuum and adduct **6** was recovered by washing the remaining solid with toluene (3.2 mg, 2.47 µmol, 99% yield).

^{1}H NMR (500 MHz, $CDCl_3$) δ ppm: 4.55 (2H, q, J = 7.1 Hz), 4.54 (2H, q, J = 7.1 Hz), 4.52 (4H, q, J = 7.1 Hz), 4.090 (3H, s), 4.087 (3H, s), 4.05 (6H, s), 1.48-1.47 (12H, m).

^{13}C NMR (125 MHz, CD_3CN) δ ppm: 63.26, 63.24, 54.10, 53.96, 14.22, 14.23.

HRMS of 6$\subset$1a (CH_3CN), m/z: calc. for [**6**$\subset$**1a**]$^{8+}$ 804.5592, observed 804.5589; calc. for [**6**$\subset$**1a**·(BArF)$_1$]$^{7+}$ 1042.8188, observed 1042.8187; calc. for [**6**$\subset$**1a**·(BArF)$_2$]$^{6+}$ 1360.4906, observed 1360.4900; calc. for [**6**$\subset$**1a**·(BArF)$_3$]$^{5+}$ 1805.2311, observed 1805.2306; calc. for [**6**$\subset$**1a**·(BArF)$_4$]$^{4+}$ 2472.3420, observed 2472.3416.

HRMS (CH_2Cl_2:MeOH), m/z: calc. for [**6**+Na]$^+$ 1319.1583, observed 1319.1982.

Synthesis of tris-dimethyl-*e*-mono-diethylmalonate-C$_{60}$ hetero adducts (7a and 7b)

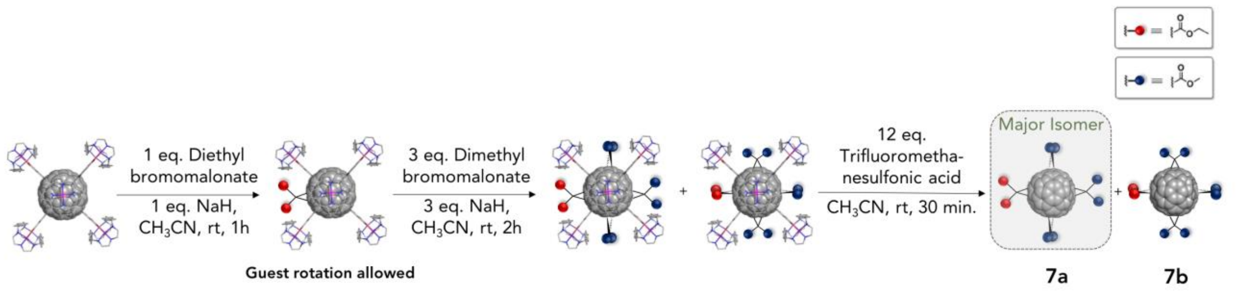

Diethyl bromomalonate (0.6 mg, 2.5 µmol) and sodium hydride (0.06 mg, 7.5 µmol) were added to a solution of **C$_{60}$$\subset$1a**·(BArF)$_8$ (32 mg, 2.5 µmol) in dry CH_3CN and the reaction was stirred for 1 h at room temperature under N_2. Then, dimethyl bromomalonate (1.6 mg, 7.5 µmol) and sodium hydride (0.18 mg, 7.5 µmol) were added in the resulting mixture and stirred for 2 h at room temperature. The crude was filtered, trifluoromethanesulfonic acid (4.5 mg, 30 µmol) was added (disassembling **1a**·(BArF)$_8$ and release of adduct **7**) and the mixture was stirred for 30 minuts. The solvent was removed under vacuum and the adduct **7** (mixture of **7a** and **7b**) was recovered by washing the remaining solid with toluene (3.05 mg, 2.4 µmol, 96% yield).

^{1}H NMR (500 MHz, $CDCl_3$) δ ppm: 4.57-4.51 (4H, m), 4.09 (8H, s), 4.05 (12H, s), 1.50-1.44 (6H, m). The integration area of the methoxy and the methylene signals agrees with a **7a**:**7b** ratio of 2.5:1.

^{13}C NMR (125 MHz, CD_3CN) δ ppm: 63.29, 54.12, 53.97, 14.21.

HRMS of 7$\subset$1a (CH_3CN), m/z: calc. for [**7**$\subset$**1a**]$^{8+}$ 801.0553, observed 801.0549; calc. for [**7**$\subset$**1a**·(BArF)$_1$]$^{7+}$ 1038.8112, observed 1038.8110; calc. for [**7**$\subset$**1a**·(BArF)$_2$]$^{6+}$ 1355.8151, observed 1355.8148; calc. for [**7**$\subset$**1a**·(BArF)$_3$]$^{5+}$ 1799.6205, observed 1799.6208; calc. for [**7**$\subset$**1a**·(BArF)$_4$]$^{4+}$ 2465.3287, observed 2465.3281.

HRMS (CH_2Cl_2:MeOH), m/z: calc. for [**7**+Na]$^+$ 1291.1175, observed 1291.1167.

Synthesis of tris-diethyl-*e*-mono-dimethylmalonate-C_{60} hetero adduct (8a and 8b)

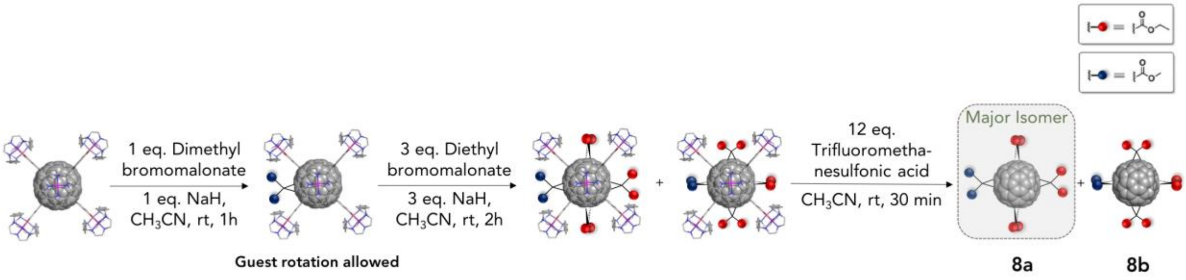

Dimethyl bromomalonate (0.53 mg, 2.5 µmol) and sodium hydride (0.06 mg, 2.5 µmol) were added to a solution of **$C_{60}\subset$1a**·(BArF)$_8$ (32 mg, 2.5 µmol) in dry CH_3CN and the reaction was stirred for 30 min at room temperature under N_2. The crude was filtered and diethyl bromomalonate (1.8 mg, 7.5 µmol) and sodium hydride (0.18 mg, 7.5 µmol) were added in the resulting mixture and stirred for 1.5 h at room temperature. The crude was filtered, trifluoromethanesulfonic acid (4.5 mg, 30 µmol) was added (disassembling **1a**·(BArF)$_8$ and release of adduct **8**) and the mixture was stirred for 30 minuts. The solvent was removed under vacuum and adduct **8** was recovered by washing the remaining solid with toluene (3.25 mg, 2.45 µmol, 98% yield).

^{1}H NMR (500 MHz, $CDCl_3$) δ ppm: 4.55-4.52 (12H, m), 4.08 (4.4H, s), 4.06 (1.6H, s), 1.48-1.47 (18H, m). The integration area of the methoxy signals from ethyl esters is in agreement with a **8a**:**8b** ratio of 2.8:1.

^{13}C NMR (125 MHz, CD_3CN) δ ppm: 63.25, 63.22, 54.09, 14.22, 14.21.

HRMS of 8$\subset$1a (CH_3CN), m/z: calc. for [**8$\subset$1a**]$^{8+}$ 808.0631, observed 808.0627; calc. for [**8$\subset$1a**·(BArF)$_1$]$^{7+}$ 1046.8264, observed 1046.8258; calc. for [**8$\subset$1a**·(BArF)$_2$]$^{6+}$ 1365.1661, observed 1365.1656; calc. for [**8$\subset$1a**·(BArF)$_3$]$^{5+}$ 1810.8418, observed 1810.8412; calc. for [**8$\subset$1a**·(BArF)$_4$]$^{4+}$ 2479.3553, observed 2479.3549.

HRMS (CH_2Cl_2:MeOH), m/z: calc. for [**8**+Na]$^{1+}$ 1347.1896, observed 1347.1884.

Synthesis of *e,e,e,e*-tetrakis-diethylmalonate-*t-1,t-1*-bis-dimethylmalonate-C_{60} hetero-hexakis adduct (9)

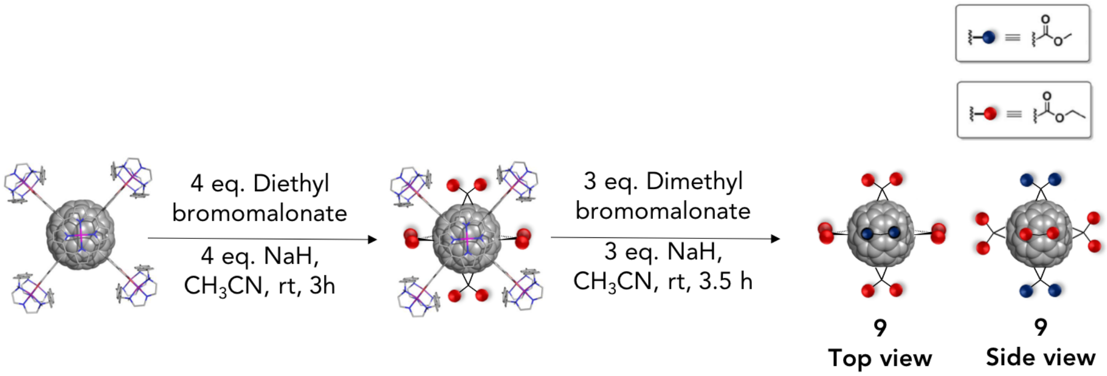

Diethyl bromomalonate (2.4 mg, 10 µmol) and sodium hydride (0.24 mg, 10 µmol) were added to a solution of **$C_{60}\subset$1a**·(BArF)$_8$ (32 mg, 2.5 µmol) in a mixture of CH_2Cl_2:CH_3CN (1:1) and the reaction was stirred for 2h at room temperature under N_2. Dimethyl bromomalonate (1.58 mg, 7.5 µmol) and sodium hydride (0.18 mg, 7.5 µmol) were added in the resulting mixture and stirred for 3.5 h at room temperature. The crude was filtered, the solvent was removed under vacuum and adduct **9** was recovered by washing the remaining solid with toluene (3.98 mg, 2.47 µmol, 99% yield).

^{1}H NMR (500 MHz, $CDCl_3$) δ ppm: 4.36 (8H, q, J = 7.1 Hz), 4.35 (8H, q, J = 7.1), 3.90 (12H, s), 1.361 (12H, t, J = 7.1 Hz), 1.358 (12H, t, J = 7.1 Hz).

^{13}C NMR (125 MHz, CD_3CN) δ ppm: 62.92, 53.75, 1.36.

HRMS (CH_2Cl_2:MeOH), m/z: calc. for [**9**+Na]$^+$ 1635.2738, observed 1635.2741.

Synthesis of C_{60} Bingel-Hirsch adducts in bulk solution

Diethyl bromomalonate (2.4 mg, 10 µmol) and sodium hydride (0.24 mg, 10 µmol) were added to a solution of **C_{60}** (1.8 mg, 2.5 µmol) in a 1,2-dichlorobenzene and the reaction was stirred for 30 minutes at room temperature under N_2. Then, the crude was filtered and analyzed by HPLC (Fig. S6).

Reversible phase transfer monitored by UV-Vis

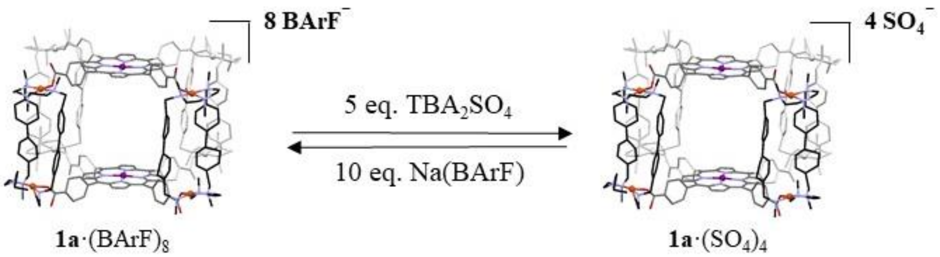

The reversible phase transfer experiments were monitored by UV-Vis according to a modified reported procedure.[21] Tetrabutylammonium sulfate (TBA_2SO_4) solution in H_2O (3.55 µL, 0.058 M, 5 eq.) was added to a biphasic system of cage **1a**·(BArF)$_8$ in CH_2Cl_2:Toluene (1:1, 0.5ml, 83µM, 1 eq.) and H_2O:DMSO (9:1, 0.5 ml), after which the aqueous layer (top) turned purple and the organic layer (bottom) turned colorless. Aliquots (50 µL) from each layer were added to quartz cuvettes with a 1 cm path length, and the volumes were adjusted at 2 ml with the same solvent mixture, respectively. The UV-Vis spectrum collected from the organic layer showed no Soret band, indicating a quantitative phase transfer of cage **1a**·(BArF)$_8$ from organic to aqueous layer. To further confirm the quantitative formation of cage **1a**·(SO_4)$_4$, a stock solution of **1a**·(SO_4)$_4$ (83µM) in H_2O:DMSO (9:1) was prepared (see footnote †). Aliquot (50 µL) of the stock solution of **1a**·(SO_4)$_4$ was added to a quartz cuvette with a 1 cm path length, and the volume was adjusted at 2 ml. The UV-Vis spectrum collected showed a Soret band (432 nm) with an intensity of 0.75 a.u., which was matched by the experimental spectrum of the aqueous layer upon the addition of 5 eq. of TBA_2SO_4, confirming a quantitative phase transfer. Then, to analyze the complete reversibility of the phase transfer, tetrakis(3,5-bis(trifuoromethyl)phenyl)borate (BArF) solution (6.2 µL, 0.067 M, 10 eq.) in CH_2Cl_2 was added to the biphasic system of cage **1a**·(SO_4)$_4$ in H_2O:DMSO (9:1, 0.5 ml, 83µM, 1 eq.) and CH_2Cl_2:Toluene (1:1, 0.5ml), after which the aqueous layer (top) turned colorless and the organic layer (bottom) turned reddish. The UV-Vis collected from the aqueous layer showed no trace of Soret band and the spectrum collected from the organic layer shows a Soret band (418 nm) with the same intensity than the stock solution of **1a**·(BArF)$_8$ (83µM) in CH_2Cl_2:Toluene (1:1).

Analogous phase transfer experiment were performed with $C_{60}\subset$**1a**·(BArF)$_8$, and no alterations of the phase transfer process were observed upon addition of cargo guests.

Footnote †: TBA_2SO_4 solution in H_2O (17.3 µL, 0.058 M, 10 eq.) was added to a solution of **1a**·(BArF)$_8$ (1.08 µM, 1 eq.) in CH3CN (1 ml) leading to complete precipitation of dark purple solid after 10 minutes stirring (the addition of twice the number of anions required forced to reach the quantitative formation of **1a**·$(SO_4)_4$). The solid was washed with CH_3CN:H_2O (9:1, 1ml), the resulting mixture was centrifuged and the supernatant was decanted; this process was repeated 3 times. Cage **1**·$(SO_4)_4$ was recovered as a dark purple solid (5.48 mg, 0.99 µmol, 92% yield).

Synthesis of tetrakis-diethylmalonate-C_{60} adduct 2 in aqueous phase

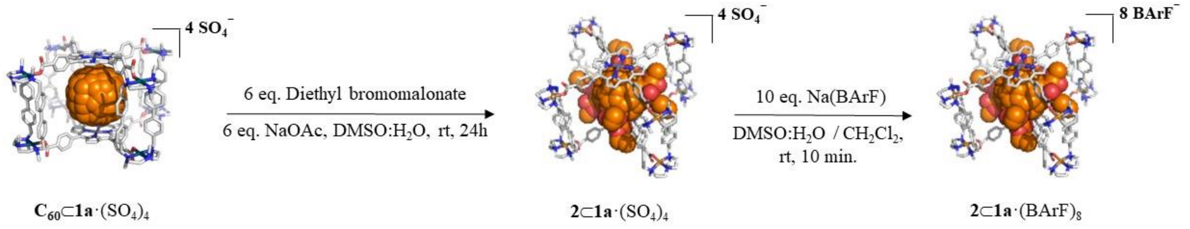

$C_{60}\subset$1a·$(SO_4)_4$ (8.6 mg, 1.6 µmol, 1 eq.), diethyl bromomalonate (6.7 mg, 9.6 µmol, 6 eq.) and sodium acetate (2.28 mg, 9.6 µmol, 6 eq.) were dissolved in H_2O:DMSO (9:1, 3 ml), and the reaction was stirred at room temperature for 24 hours. Addition of CH_2Cl_2 (2 ml) formed a biphasic system. Then, BArF solution (58. µL, 0.27 M, 10 eq.) in CH_2Cl_2 was added, after which the aqueous layer (top) turned colorless and the organic layer (bottom) turned brownish. The CH_2Cl_2 layer was then removed into a 10 ml round bottom flask, magnesium sulfate was added and filtered through Celite. The solvent was removed under vacuum, the remaining solid was dissolved in CH_3CN and analyzed by ESI-MS. The ESI-MS spectrum showed peaks exclusively corresponding to **2**$\subset$**1a**·(BArF)$_8$ host-guest adduct (residual peaks of empty **1a**·(BArF)$_8$ were also detected).

Catalytic biphasic system for the selective production of tetrakis-C_{60} adduct 2

As detailed in Fig. 10 in the main text, a biphasic system of diethyl bromomalonate (11.2 mg, 47 µmol, 60 eq.) and sodium acetate (3.8 mg, 47 µmol, 60 eq.) in H_2O:DMSO (9:1, 3.5 ml) and **$C_{60}\subset$1a**·(BArF)$_8$ (10 mg, 0.78 µmol, 1 eq.) and C_{60} (16.67 mg, 14.8 µmol, 19 eq.) in CH_2Cl_2:Toluene (1:1, 3.5 ml) was prepared. The addition of TBA_2SO_4 solution in H_2O (37.8 µL, 0.116 M, 5 eq.) under stirring caused a color change in the aqueous layer (top) from colorless to brownish, while the organic layer (bottom) turned light purple (excess of C_{60} in organic solvent solution). After 24h stirring at room temperature, BArF (65.5 µL, 0.134 M, 10 eq.) in CH_2Cl_2 was added, transferring the encapsulated product, to the organic layer, i.e. **2**$\subset$**1a**·(BArF)$_8$,. The biphasic system was stirred during additional 30 minutes, to ensure the quantitative guest exchange of **2** by C_{60} due to higher affinity for **1a·**(BArF)$_8$. The protocol described above was repeated over 9 cycles more. After 3, 6 and 10 cycles, aliquots (30 µL) of the organic layer was evaporated to dryness under a stream of nitrogen gas and washed with CH_3CN (0.5 ml). The remaining solid was dissolved in toluene and analyzed by HPLC. The chromatograms showed an increment over every cycle of the area from the peak attributed to adduct **2,** in comparison with the peak attributed to C_{60}. After 10 cycles, the organic layer containing adduct **2** and C_{60} was removed into a 10 ml round bottom flask and filtered through Celite. The solvent was removed under vacuum and the remaining solid was washed with CH_3CN (0.5 ml). Purification by flash column chromatography (CH_2Cl_2) furnished fullerene adduct **2** as a brown solid (11.5 mg, 8.5 µmol, 97%), along with the recovery of C_{60} in excess.

Heterogeneous catalysis in organic solvent

An heterogeneous catalytic system of diethyl bromomalonate (7.46 mg, 29 µmol, 80 eq., previously deprotonated with NaH), **C_{60}⊂1a**·(BArF)$_8$ (5 mg, 0.39 µmol, 1 eq.) and C_{60} (8.34 mg, 7.25 µmol, 19 eq.) was prepared in CH_3CN (0.2 ml). After 96 h stirring at room temperature, an aliquot (30 µL) of the suspension was evaporated to dryness under a stream of nitrogen gas and washed with CH_3CN (0.5 ml). The remaining solid was dissolved in toluene and analyzed by HPLC (BuckyPrep M). The chromatograms showed two different peaks of similar intensity, one attributed to a mixture of hexakis- adducts (retention time 6.06 min, 0.5ml/min, Toluene, 298K) and the other attributed to unreacted C_{60}. Then, the solvent of the system was removed under vacuum and the remaining solid was washed with CH_3CN (1.5 ml). Purification by preparative chromatography (CH_2Cl_2) furnished fullerene hexakis- adducts (mixture of isomers) as a red solid (characterization in Figure S14), along with the recovery of C_{60} in excess.

The same heterogeneous catalysis was attempted in pure nitromethane as solvent. Albeit the solubility of the cage was good, after 3 days of reaction only traces of tetrakis-adduct **2** were observed. Heating to 55 ºC for 3 more days didn't improve the result. The catalysis performing the reaction in nitromethane:CH_3CN 9:1 afforded the same results, observing traces of **2** after 4 days of reaction.

General procedures for UV–vis titrations.

Host–guest interactions in solution were studied by UV–vis spectroscopy. The UV–vis titration experiments between **1a**·(BArF)$_8$ (4.32×10^{-7} M) and C_{60} or adduct **2** (1.39×10^{-5} M) were performed by using toluene/acetonitrile (9/1) or toluene/dichloromethane (1/1) as solvent. The host concentration was kept constant.

A magnetic stir bar and 2 ml of nanocapsule solution were added to the cuvette, then it was inserted into the spectrometer and the stirrer activated and the substrate added. The stoichiometry of the complexes was studied using the method of continuous variations. Solutions of nanocapsule **1a**·(BArF)$_8$ and guests (4.32×10^{7} M) in toluene/acetonitrile (9/1) or toluene/dichloromethane (1/1) were mixed at different ratios. All the experiments were carried out at 25ºC. The data obtained from the UV–vis were analyzed using the online software BindFit vo.5 (*Supramolecular.org*). Final values are:

- K_a (**2**) = 1.4 (±0.3)·10^6 M^{-1}; K_a (C_{60}) = 3.6 (±0.2)·10^7 M^{-1} in CH_2Cl_2:toluene 1:1)
- K_a (**2**) = 1.0 (±0.4)·10^6 M^{-1}; K_a (C_{60}) = 2.8 (±0.6)·10^7 M^{-1} in CH_3CN:toluene 1:9)

3. | Supplementary Text

Dynamic behavior of host-guest complexes analyzed from MD simulations

Molecular dynamics (MD) simulations carried out describe some degree of adaptability of the nanocapsule **1a** depending on the encapsulated fullerene adduct. The largest Zn···Zn distance is observed when tetrakis-*e,e,e,e*-adduct (**2**) is encapsulated (mean value = 13.1 Å, Fig. 3, S8-S10), and slightly shorter distances around 12.9-13.0 Å are observed for bis-*e,e*-adduct (**4**) (Fig. 8) and mono-adduct host-guest systems (Fig. S11-S13). In both mono- and bis-adducts a distortion of the nanocapsule that becomes slightly twisted along the Zn···Zn axis (distortion described by the dihedral angle ∠N1-N2-N3-N4) is also observed. Usually, the shorter the Zn···Zn distances are found to be correlated with the degree of the nanocapsule twisting (∠N1-N2-N3-N4 angle values deviated from zero, Fig. 3, 8 and S11).

MD simulations on tetrakis-*e,e,e,e*-adduct (**2**) (Fig. 3, S8-S10) and bis-*e,e*-adduct (**4**) (Fig. 8) encapsulated in nanocapsule **1a** revealed that gate-to-gate motions of the malonate groups through fullerene rotations inside the nanocapsule are completely restricted in these two systems. ∠N1-N2-C1-C2 angle describes the relative orientation of the encapsulated fullerene with respect to the nanocapsule, and values for this angle explored in tetra- and bis-adduct MD simulations indicate that malonate groups stay in a single nanocapsule gate during all the simulation time (see Fig. 8, and Supporting Movies **VS1** and **VS3**). Fullerene rotations along Zn···Zn axis are restricted to a range of 90º, which correspond to rotations that bring the malonate groups from one nanocapsule clip to the other one in the same nanocapsule gate. Indeed, most visited angle values correspond to those where the malonate groups are close to the molecular clips, directly interacting with their aromatic rings, and establishing persistent C–H···π interactions as revealed by Non-covalent interaction (NCI) analysis (Fig. 3 and S10).

On the other hand, MD simulations on the encapsulated Bingel-Hirsch-Hirsch **mono-diethylmalonate-C_{60}** adduct show that in this case the gate-to-gate rotation of the single malonate addend is taking place (Fig. S11-S13), although this rotation is not fast (about 50-100 ns time gap between gate-to-gate rotations (see Supporting Movie **VS2**). MD simulations also show that the malonate group of the monoadduct can interact with the aromatic rings of the molecular clips (see NCI analysis in Fig. S12), and that it can mainly explore two different relative conformations with respect to the nanocapsule. This is described by the ∠Zn1-Zn2-C3-C4 dihedral angle measured along the MD trajectory (Fig. S11). ∠Zn1-Zn2-C3-C4 angle describes the relative orientation of the cyclopropane ring with respect to the capsule, where angle values around 0º and ±180º indicate that the cyclopropane ring stay perpendicular to the porphyrins (conformer 1), while values around ±90º indicate that the cyclopropane ring stays in a parallel conformation with respect to the porphyrins (conformer 2) (see Fig. S11). Due to these two main conformations explored by the malonate group of the mono-adduct, two main interacting modes between the ester groups of the malonate and the aromatic rings of the nanocapsule molecular clips are observed (Fig. S12) that maximize the stabilizing non-covalent interactions between them.

The interactions observed between the malonate groups and the capsule aromatic rings in the mono-adduct (Fig. S11) and bis-adduct (Fig. 8) host-guest complexes control the relative orientation of the fullerene inside the capsule, and thus which bonds suitable to be functionalized in subsequent cyclopropanations are exposed to the solvent from the other nanocapsule gates, and also how they are exposed. Consequently, those interactions are proposed to play a role on the observed regioselectivity in hetero-tetrakis-adduct formation experiments (Fig. 1c in the main text), together with the preferential second nucleophilic attack (as described below).

The interconversion between the two mono-adduct conformations (conformers 1 and 2) takes place fast (only few ns), and when the second nucleophilic addition takes place and the bis-adduct gets formed, this rotation becomes totally suppressed (see bis-adduct measured angle in Fig. 8). The latter observation is important because it means that it is the second cyclopropanation the responsible of determining the selectivity of the tris- and tetra-adduct subsequent functionalizations, by fixing the relative regiochemistry of the two first malonate addends with respect to the capsule once the bis-adduct is formed.

We know from hetero-tetrakis-adduct formation experiments (Fig. 1c in the main text) that there exists a preference for the *e,e,t*-1(I)-tris-dimethy-*e*-mono-diethylmalonate-C_{60} formation (**7a**) when starting from ethyl malonate mono-adduct (2.5:1 ratio for **7a**:**7b** formation). This implies that the second functionalization at the adjacent position of the mono-ethyl-malonate-C_{60} preferentially occurs when the ester groups of the former ethyl-malonate-C_{60} are in the parallel plane to the two nanocapsule porphyrins; and that the malonate performing the second nucleophilic attack to the fullerene approaches with the ester groups pointing perpendicular to each porphyrin.

The source of this regiochemical control can be qualitatively rationalized when examining the conformations explored by the mono-adduct when encapsulated in **1a**. For instance, see Fig. S11 and S12, (**mono-diethylmalonate-C_{60})⊂1a**·$(Cl)_8$ snapshots at 324 ns and 354 ns, where second functionalization should take place at nanocapsule gates labelled as "*1*" and "*3*" to form the C_s-symmetric *e,e*-bis-adduct regioisomer experimentally observed. In 354 ns snapshot, reactive bonds exposed in gates *1* and *3* would form the second adduct with the ester groups pointing perpendicular to the porphyrins, leading to the major isomer **7a** after tris- and tetrakis- subsequent derivatization. However, in 324 ns snapshot, reactive bonds in gates *1* and *3* would require an approach of the second malonate with the ester groups directly pointing to the molecular clips, which is sterically less favorable, to form the bis-adduct intermediate that leads to the minor tetrakis-isomer **7b**.

Since interconversion between mono-adduct relative conformations observed in 324 ns and 354 ns snapshots is fast (as discussed earlier), the more favored (sterically less hindered) nucleophilic attack to generate the bis-adduct (and fix the relative regiochemistry with respect to the capsule) would be the responsible of the final observed hetero-tetrakis selective formation. Taking all these together, we hypothesize that malonates with more bulkier ester groups may result into higher regioselectivities due to enhanced steric interactions with the nanocapsule due to encapsulation

4. | Supplementary Figures

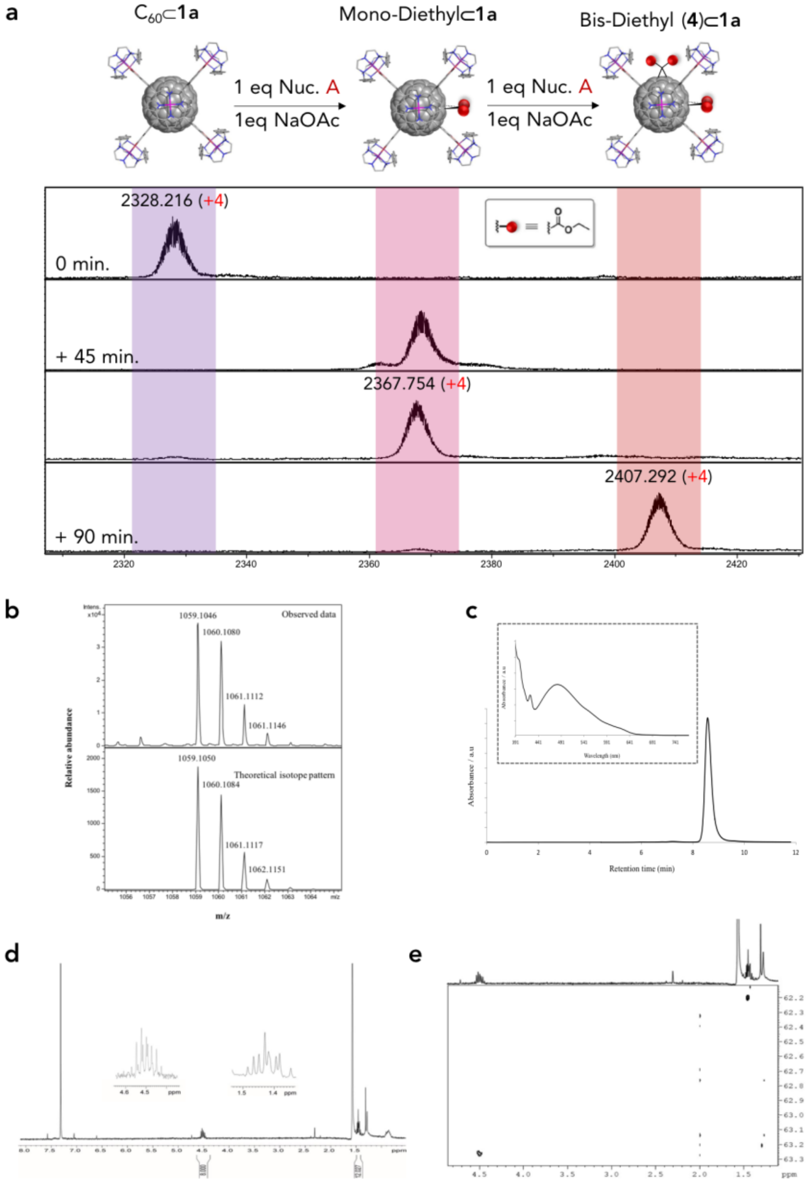

Fig. S1 | Synthesis of *bis*-adduct-*e*,*e*-diethylmalonate-C_{60} (4) (related to Figure 1 and 5). a, HRMS monitoring for the formation of **4** from $C_{60}\subset$**1a**·(BArF)$_8$. (Nuc. A: Diethyl bromomalonate) (ESI-MS, Positive ion mode, CH_3CN, 298 K). **b**, Theoretical isotope pattern and high resolution ESI-MS of adduct **4** (M+Na) (ESI-MS, Positive ion mode, CH_2Cl_2:MeOH). **c**, HPLC chromatogram of **4** (0.5 ml/min, 320 nm, Toluene) (inset: UV-vis absorption spectrum of **4** (298 K, Toluene). **d**, ^{1}H-NMR spectrum of **4** (500 MHz, 298 K, $CDCl_3$), showing multiplets at 1.44 and 4.50 ppm in agrrement with an e,e-bis-adduct isomer. **e**, 2D ^{1}H-^{13}C spectral aliased HSQC spectrum of **4** (500 MHz, 298 K, $CDCl_3$).

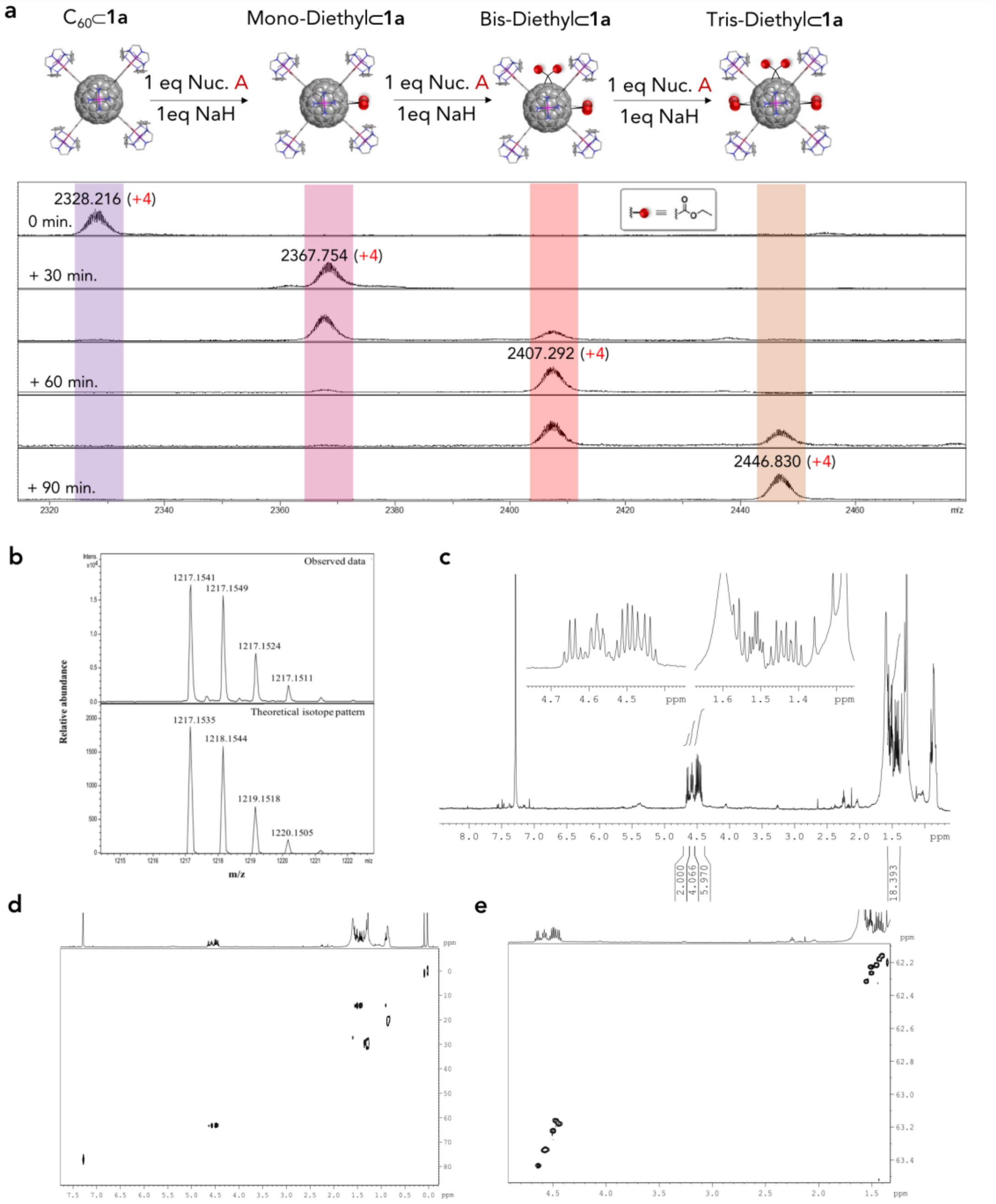

Fig. S2 | Synthesis of equatorial e,e,e-tris-diethylmalonate-C_{60} (equimolar amounts of 5a and 5b) (related to Figure 1). **a**, Mass spectrum monitoring the formation of (**5a**/**5b**)$\subset$**1a**•(BArF)$_8$ (ESI-MS, Positive ion mode, CH_3CN). **b**, Experimental and theoretical isotope pattern of high resolution ESI-MS of **5a/5b** (M+Na) (ESI-MS, Positive ion mode, CH_2Cl_2:MeOH). **c**, ^1H-NMR spectrum of adduct **5a/5b** (500 MHz, 298 K, $CDCl_3$). **d**, 2D ^1H-^{13}C HSQC spectrum of adduct **5a/5b** (500 MHz, 298 K, $CDCl_3$). **e**, 2D ^1H-^{13}C spectral-aliased HSQC spectrum of adduct **5a/5b** (500 MHz, 298 K, $CDCl_3$), showing five different CH_2-type carbons, corresponding to 4:2 signals (**5a**) and 2:2:2 signals (**5b**), where the two isomers are present in equimolar amounts.

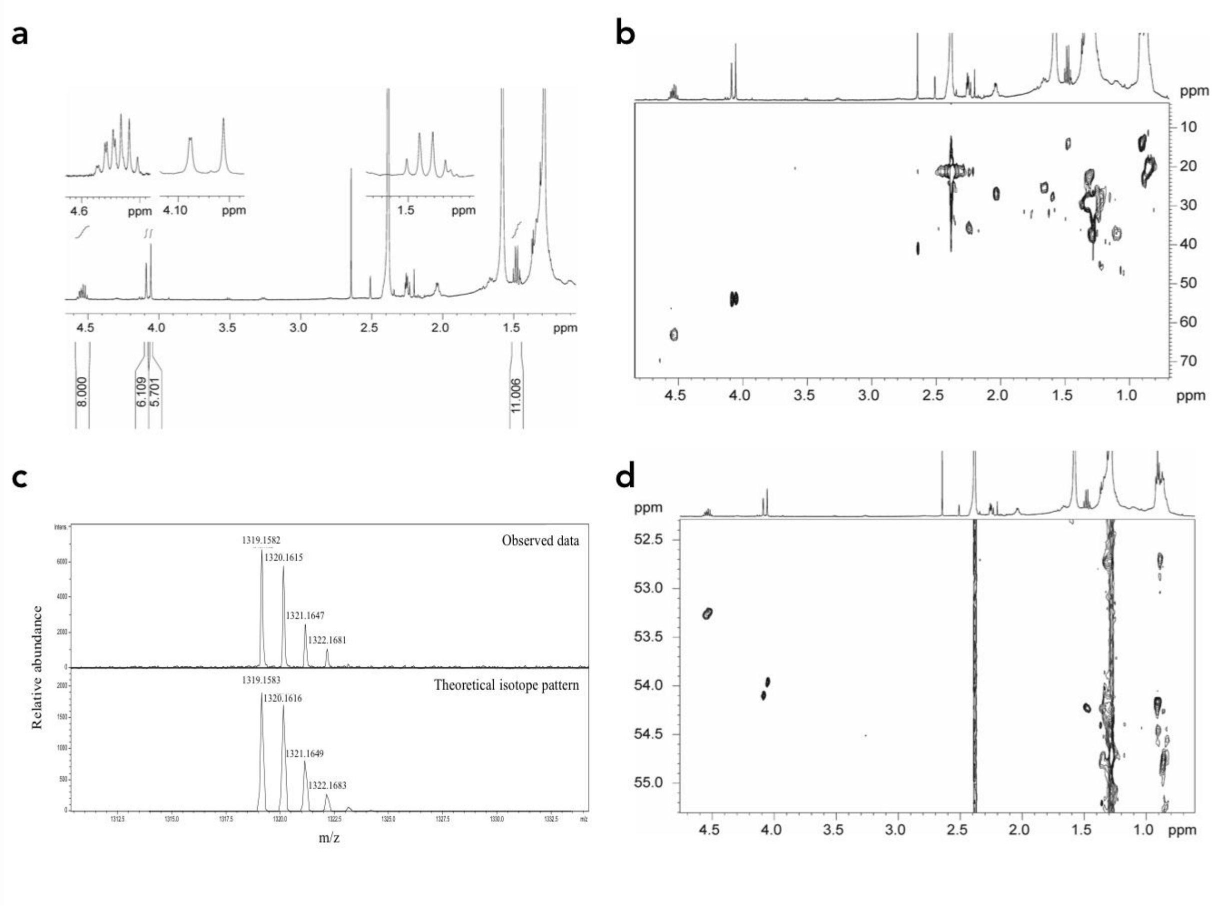

Fig. S3 | Characterization of hetero-tetrakis-adduct *e,e*-bis-diethyl-*e,e*-bis-dimethylmalonate-C_{60} 6 (Nuc. B = dimethyl bromomalonate) (related to Figure 6). **a,** ^1H-NMR spectrum of adduct **6**, highlighting the expected 1:1:2 intensity pattern for the methylene region (4.55 (2H), 4.54 (2H), 4.52 (4H) ppm), and the 1:1:2 intensity pattern for the methyl region (4.090 (3H), 4.087 (3H), 4.05 (6H) ppm) (500 MHz, 298 K, $CDCl_3$). **b**, 2D ^1H-^{13}C HSQC spectrum of adduct **6** (500 MHz, 298 K, $CDCl_3$) **c**, Theoretical isotope pattern and high resolution ESI-MS of adduct **6** (M+Na) (ESI-MS, Positive ion mode, CH_2Cl_2:MeOH). **d**, 2D ^1H-^{13}C spectral-aliased HSQC spectrum of adduct **6** (500 MHz, 298 K, $CDCl_3$).

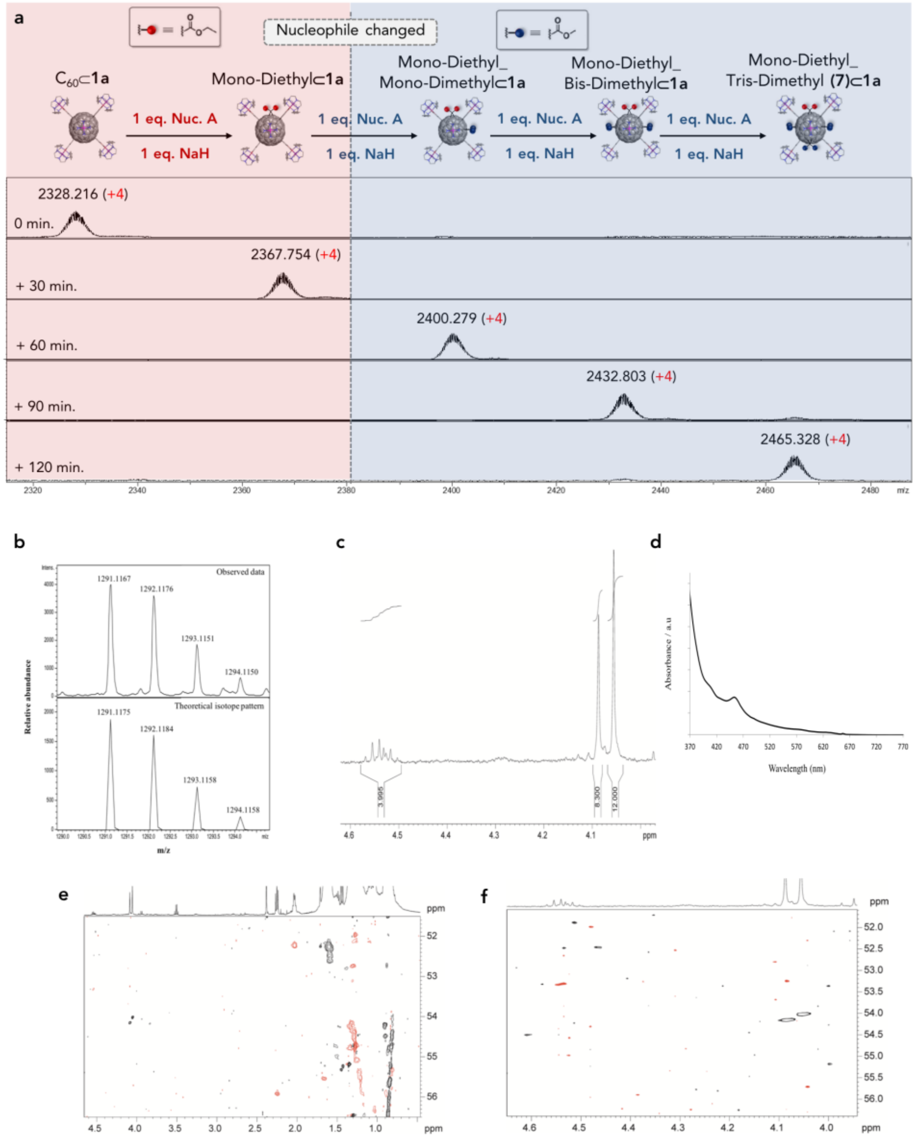

Fig. S4 | Synthesis of equatorial hetero-tetrakis-adduct *e,e,t-1(I)*-tris-dimethyl-*e*-mono-diethylmalonate-C_{60} (7a) and *e,e,t-1(II)*-tris-dimethyl-*e*-mono-diethylmalonate-C_{60} (7b) (7a:7b ratio 2.5:1) (related to Fig. 1 and 7). a, Mass spectrum monitoring the formation of (**7a/7b**)⊂**1a**·(BArF)$_8$ (Nuc. A: Diethyl bromomalonate, Nuc. B: Dimethyl bromomalonate) (ESI-MS, Positive ion mode, CH_3CN) . **b**, Experimental and theoretical isotope pattern of high resolution ESI-MS of **7a/7b** (M+Na) (ESI-MS, Positive ion mode, CH_2Cl_2:MeOH)**. c**, ^{1}H-NMR spectrum of adduct **7a/7b** (500 MHz, 298 K, $CDCl_3$), highlighting the multiplet at the methylene region (4.57-4.51 (4H) and the singlets of the methoxy region (4.09 (8H, s), 4.05 (12H, s); the integration area of the methoxy and the methylene signals agrees with a **7a**:**7b** ratio of 2.5:1. **d**, UV-vis absorption spectrum of adduct **7a/7b** (298 K, Toluene). **e**, 2D ^{1}H-^{13}C HSQC spectrum of adduct **7a/7b** (500 MHz, 298 K, $CDCl_3$). **f**, 2D ^{1}H-^{13}C spectral-aliased HSQC spectrum of adduct **7a/7b** (500 MHz, 298 K, $CDCl_3$).

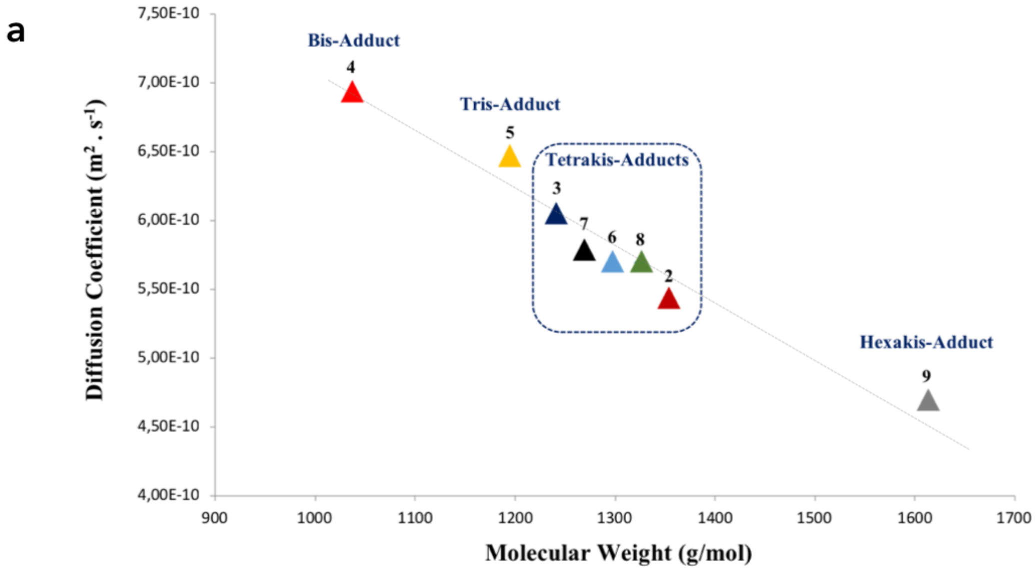

b

	Adduct	Molecular Weight (g/mol)	Diffusion Coefficient ($m^2 . s^{-1}$)	Hydrodynamic Radius (m)
Tetrakis-ethyl	2	1353.2523	5.42E-10	7.43E-10
Tetrakis-methyl	3	1241.0393	6.03E-10	6.68E-10
Bis-ethyl	4	1036.9479	6.92E-10	5.82E-10
Tris-ethyl	5	1195.1001	6.46E-10	6.24E-10
Bis-diethyl _Bis-dimethyl	6	1297.1458	5.69E-10	7.08E-10
Mono-ethyl_Tris-methyl	7	1269.0926	5.75E-10	7.00E-10
Tris-ethyl_Mono-methyl	8	1325.199	5.69E-10	7.08E-10
Tetrakis-ethyl_Bis-methyl	9	1613.4502	4.68E-10	8.61E-10

Fig. S5 | Diffusion coefficients of fullerene adducts 2, 3, 4, 5, 6, 7, 8 and 9 (related to Figure 1). **a**, Correlation between DOSY NMR Diffusion Coefficients and Molecular Weight of each adduct (500 MHz, 298 K, $CDCl_3$). **b**, Tabulated Diffusion Coefficients (D) and Hydrodynamic radii (r_H) for each of the adducts calculated from Stokes-Einstein equation.

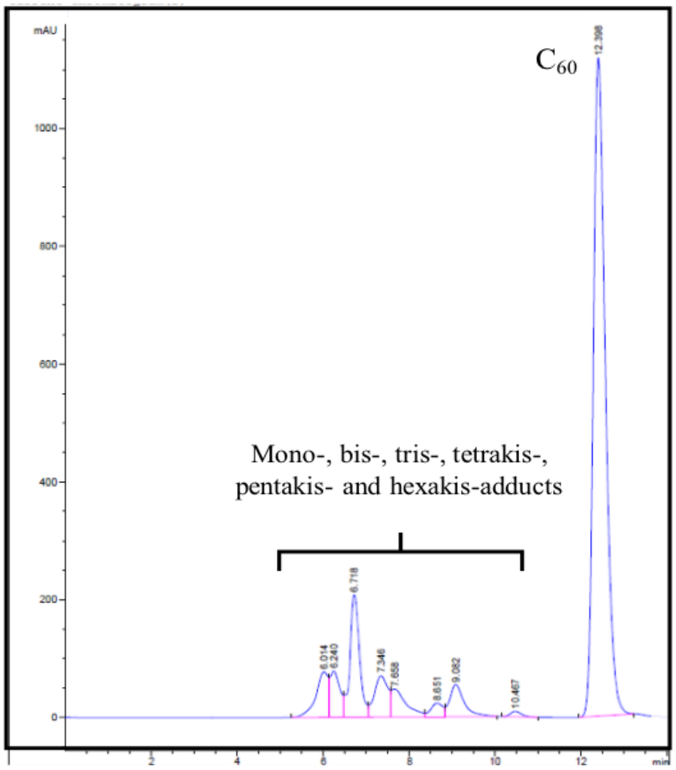

Retentio time (min.)	Area %
6,01392746	4,84
6,239563465	3,837
6,718294144	10,23
7,346037388	4,755
7,657731533	3,583
8,651453972	1,378
9,081720352	3,99
10,46740818	0,514
12,39805698	66,872

Fig. S6 | HPLC chromatogram of the crude obtained from the synthesis of C$_{60}$ adducts in bulk solution (related to Figure 5). Reaction after 30 min of reaction (0.5 ml/min, 320 nm, Toluene)

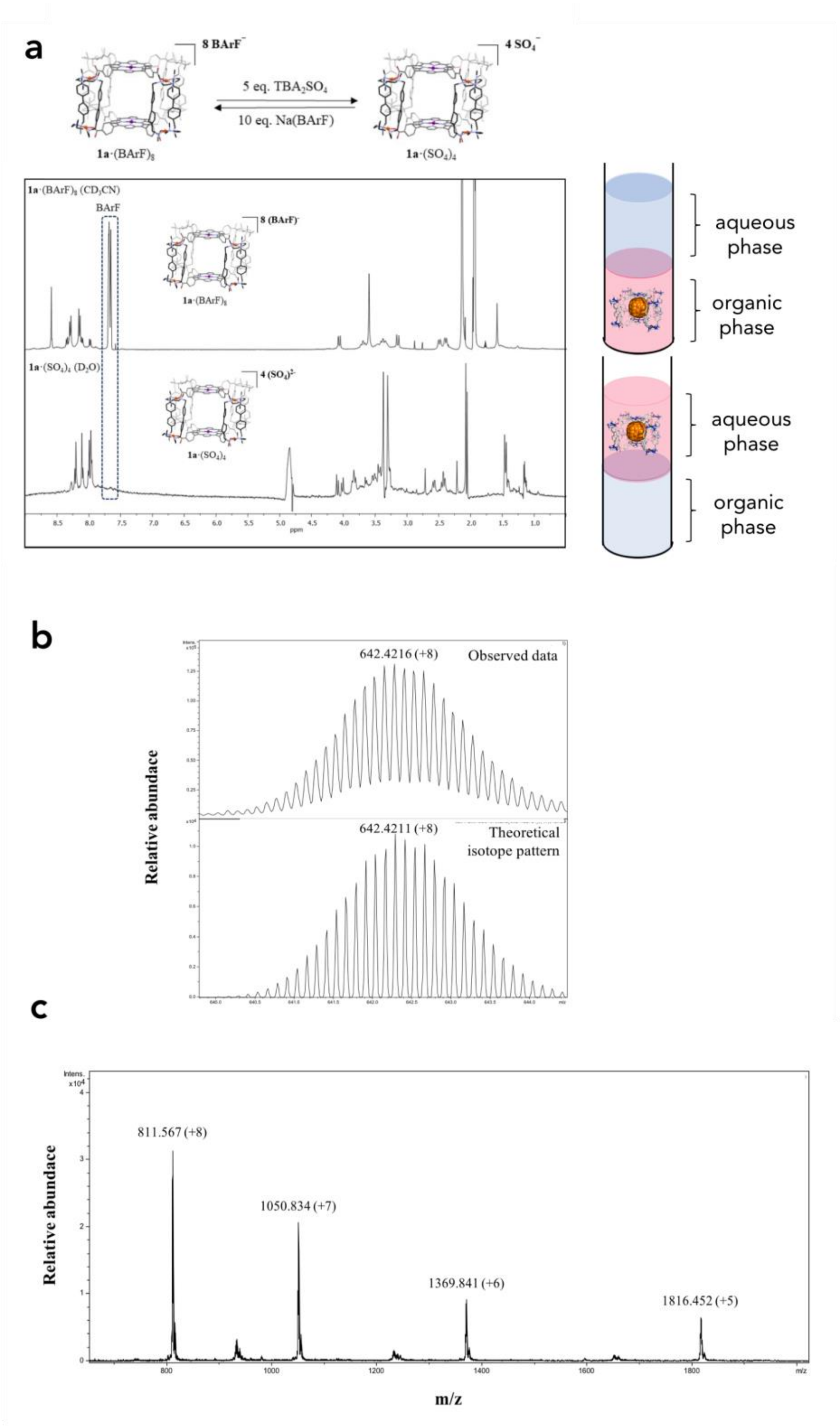

Fig S7 | Characterization of cage 1a·(SO_4)$_4$ in D_2O (related to Figure 10). **a,** ^{1}H-NMR spectrum of cage **1a·(BArF)$_8$** in CD_3CN (top) and ^{1}H-NMR spectrum of cage **1a·(SO_4)$_4$** in D_2O (bottom, no remaining peak corresponding to BArF anions) (400 MHz, 298 K, D_2O). **b**, Theoretical isotope pattern and high resolution ESI-MS of **1a**·(SO_4)$_4$ (ESI-MS, Positive ion mode, CH_3CN:H_2O 9:1). **c**, High resolution ESI-MS of **2**$\subset$**1a**·(BArF)$_8$ transferred from aqueous phase (ESI-MS, Positive ion mode, CH_3CN).

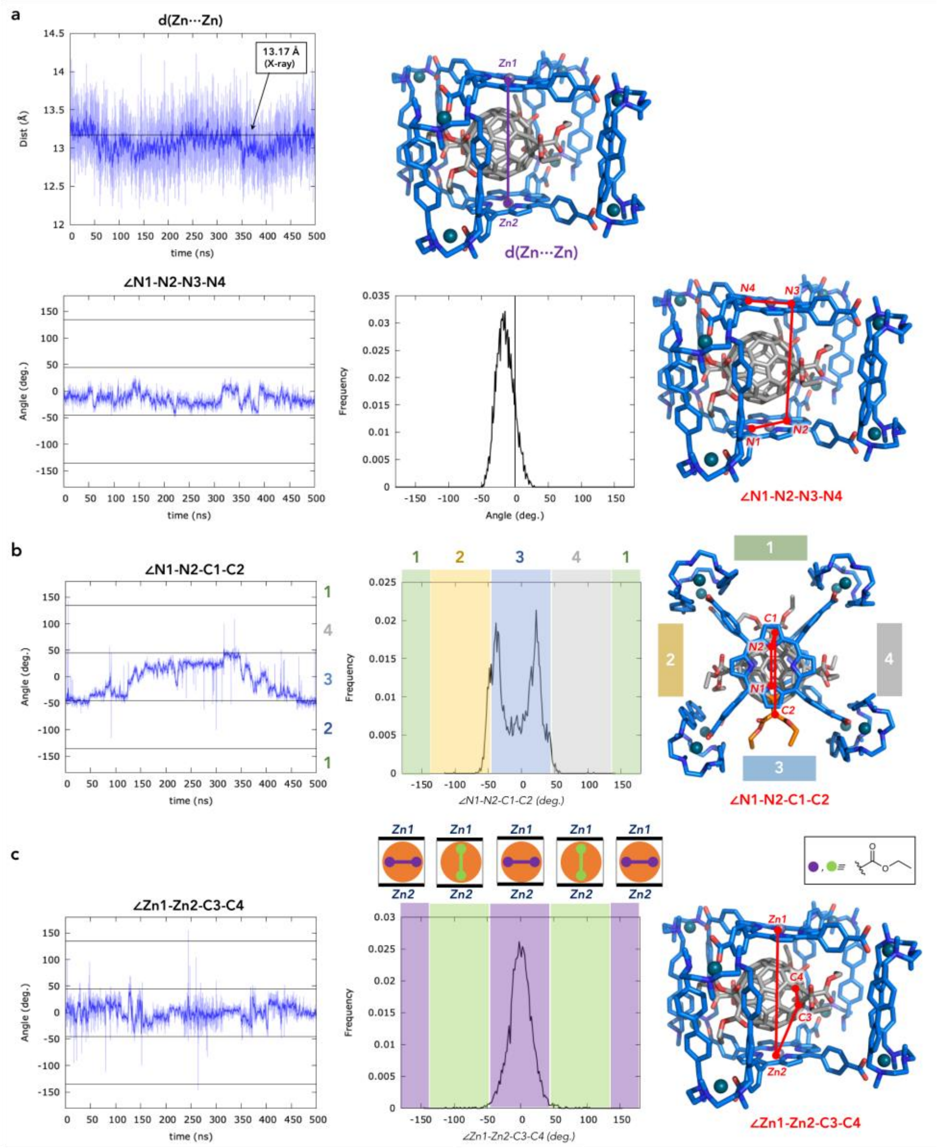

Fig. S8 | Conformational analysis of $2\subset1a\cdot(Cl)_8$ (tetrakis-*e,e,e,e*-adduct) host-guest complex from 500 ns of Molecular Dynamics (MD) trajectories in explicit CH_3CN solvent. Distances and angles are given in Angstroms (Å) and degrees (º), respectively. **a**. Zn···Zn distance and ∠N1-N2-N3-N4 dihedral angle measured along the MD trajectory. ∠N1-N2-N3-N4 dihedral angle describes the torsion of the nanocapsule: the larger deviation from ∠N1-N2-N3-N4 = 0 angle, the more twisted the capsule. Most visited angle values are shown in the histogram plot (frequency vs. angle value). **b**. ∠N1-N2-C1-C2 dihedral angle measured along the MD trajectory. ∠N1-N2-C1-C2 angle describes the relative rotation of the encapsulated fullerene with respect to the capsule, and most visited angle values are shown in the histogram plot (frequency vs. angle value). Different capsule windows (labelled as 1, 2, 3, and 4 in the figure) correspond to different ranges of explored angle values. **c**. ∠Zn1-Zn2-C3-C4 dihedral angle measured along the MD trajectory. ∠Zn1-Zn2-C3-C4 angle describes the relative orientation of the cyclopropane ring with respect to the capsule. ∠Zn1-Zn2-C3-C4 values around 0º and ±180º indicate that the cyclopropane ring stay perpendicular to the porphyrins, while values around ±90º indicate that the cyclopropane ring stays in a parallel conformation with respect to the porphyrins.

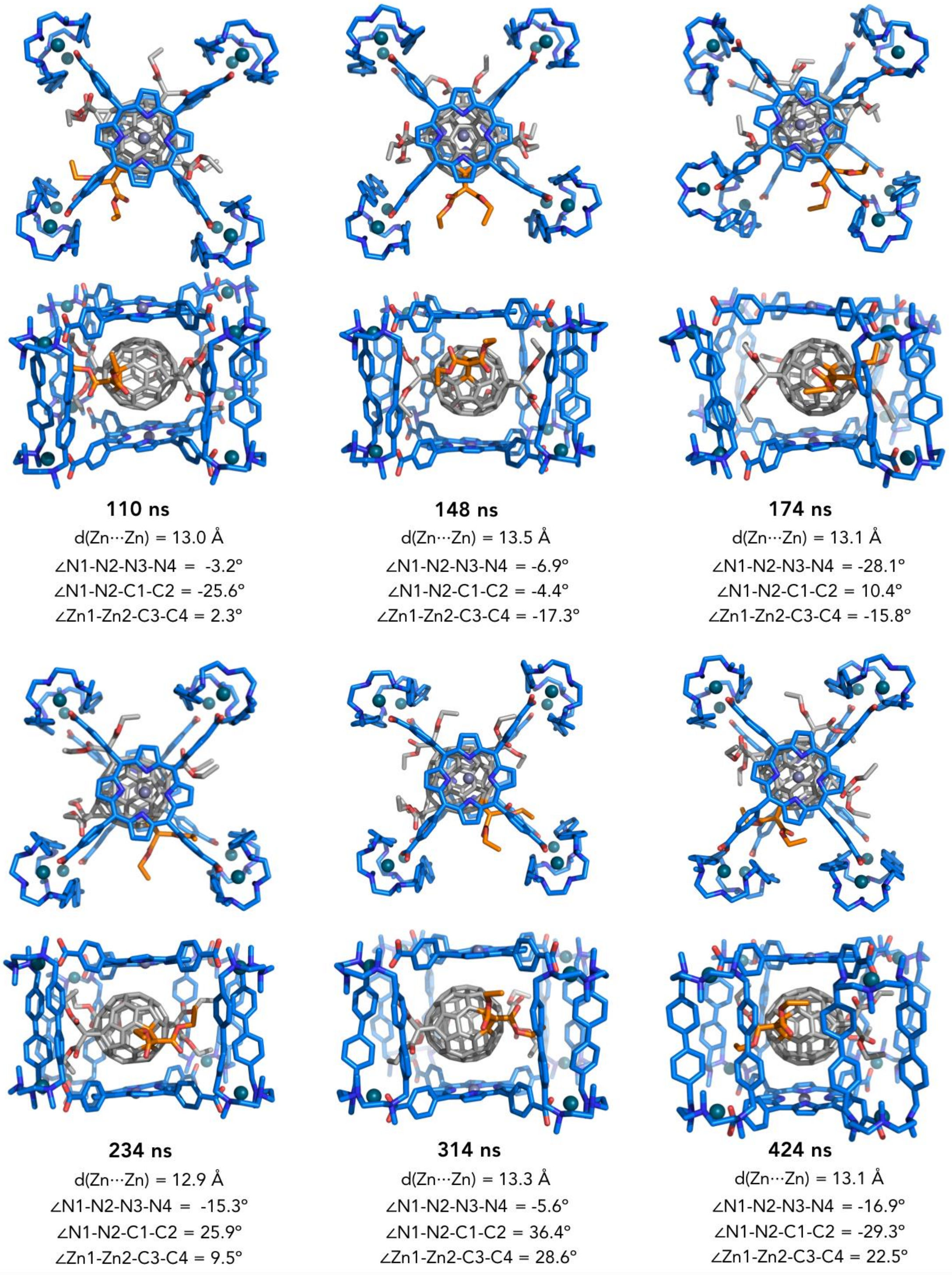

110 ns
d(Zn···Zn) = 13.0 Å
∠N1-N2-N3-N4 = -3.2°
∠N1-N2-C1-C2 = -25.6°
∠Zn1-Zn2-C3-C4 = 2.3°

148 ns
d(Zn···Zn) = 13.5 Å
∠N1-N2-N3-N4 = -6.9°
∠N1-N2-C1-C2 = -4.4°
∠Zn1-Zn2-C3-C4 = -17.3°

174 ns
d(Zn···Zn) = 13.1 Å
∠N1-N2-N3-N4 = -28.1°
∠N1-N2-C1-C2 = 10.4°
∠Zn1-Zn2-C3-C4 = -15.8°

234 ns
d(Zn···Zn) = 12.9 Å
∠N1-N2-N3-N4 = -15.3°
∠N1-N2-C1-C2 = 25.9°
∠Zn1-Zn2-C3-C4 = 9.5°

314 ns
d(Zn···Zn) = 13.3 Å
∠N1-N2-N3-N4 = -5.6°
∠N1-N2-C1-C2 = 36.4°
∠Zn1-Zn2-C3-C4 = 28.6°

424 ns
d(Zn···Zn) = 13.1 Å
∠N1-N2-N3-N4 = -16.9°
∠N1-N2-C1-C2 = -29.3°
∠Zn1-Zn2-C3-C4 = 22.5°

Fig. S9 | Representative snapshots of $2\subset 1a\cdot(Cl)_8$ (tetrakis-*e,e,e,e*-adduct) host-guest complex taken from 500 ns of Molecular Dynamics (MD) trajectory in explicit CH_3CN solvent. Distances and angles are given in Angstroms (Å) and degrees (º), respectively. Solvent molecules, Cl$^-$ ions and hydrogen atoms are omitted for clarity.

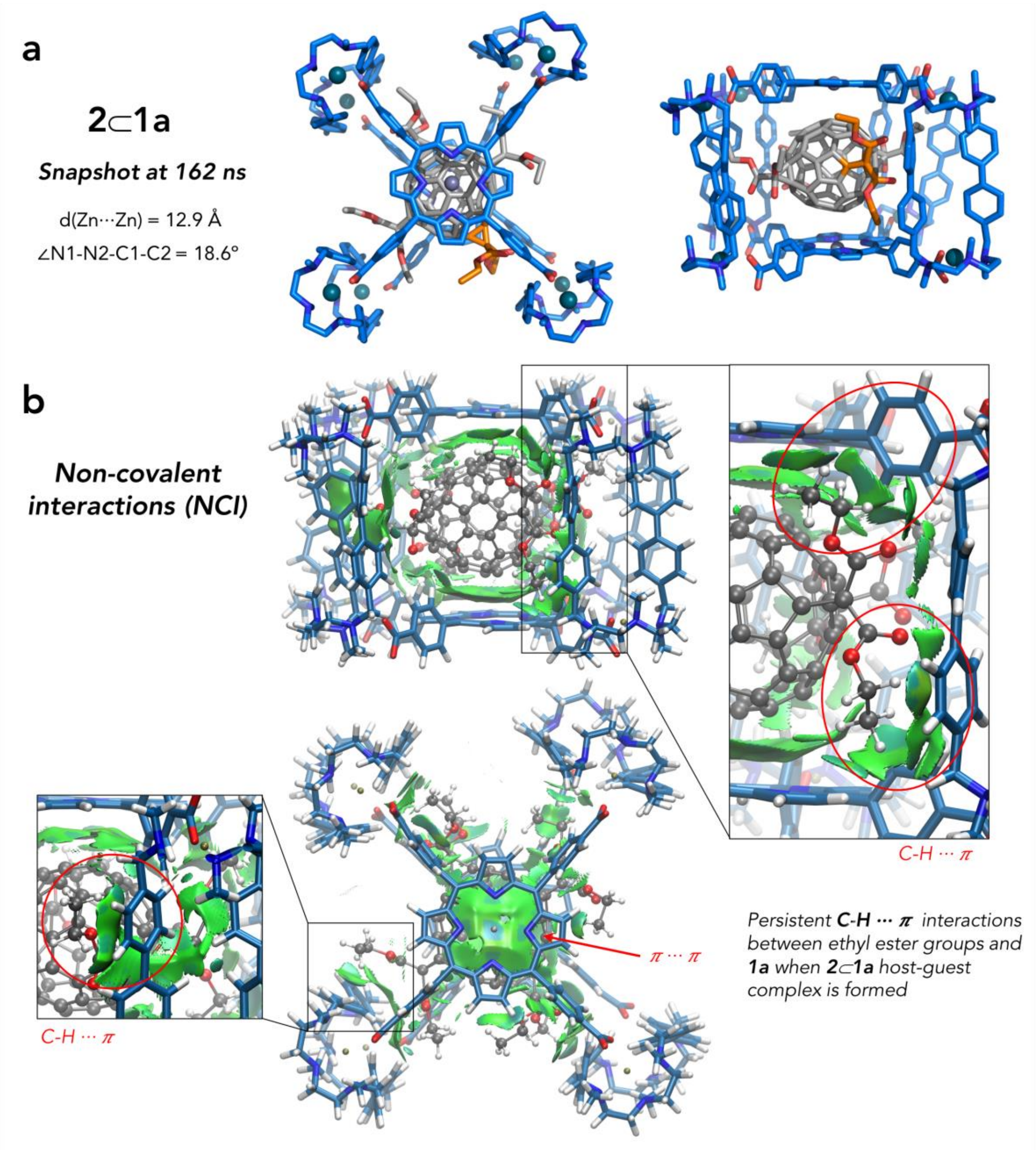

*Persistent **C-H ··· π** interactions between ethyl ester groups and **1a** when **2⊂1a** host-guest complex is formed*

Fig. S10 | Non-covalent interaction (NCI) analysis of $2\subset1a\cdot(Cl)_8$ (tetrakis-*e,e,e,e*-adduct) host-guest complex from a representative snapshot taken from 500 ns of Molecular Dynamics (MD) trajectory in explicit CH$_3$CN solvent. Solvent molecules and Cl$^-$ ions are omitted for clarity. Gradient isosurface with s = 0.5 a.u., and RGB scale according to the sign(λ_2)ρ over the range [-0.04:0.04] a.u. .

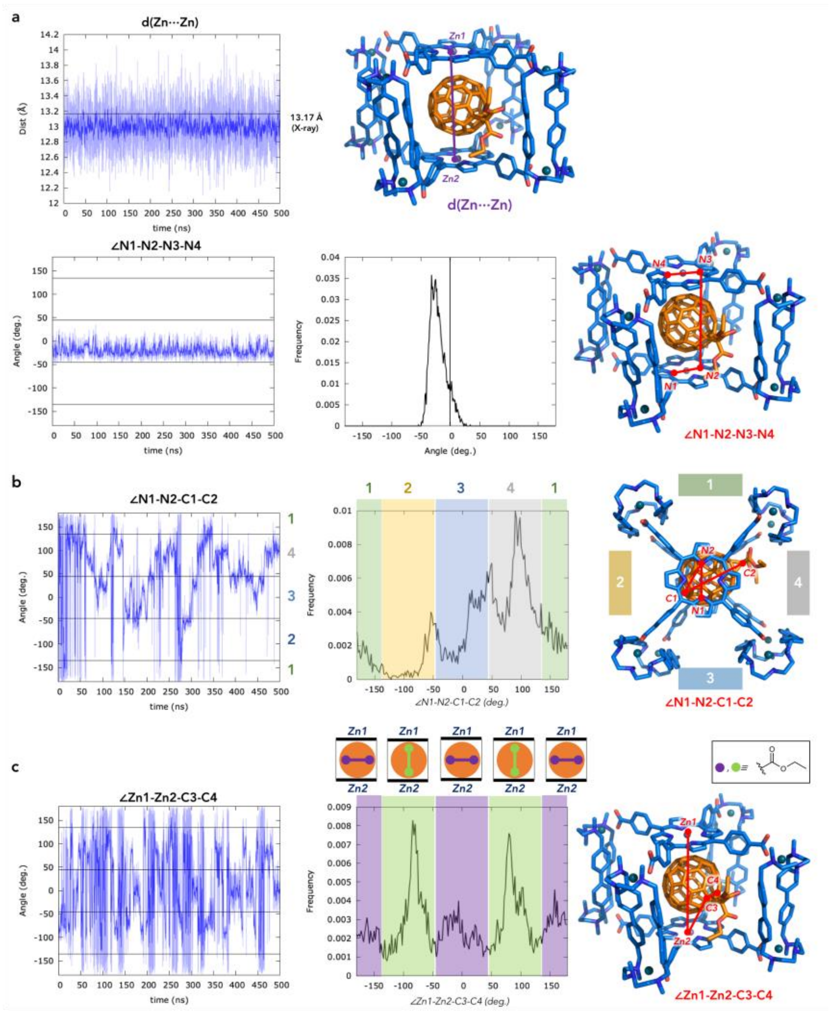

Fig. S11 | Conformational analysis of (mono-diethylmalonate-C_{60})⊂1a·$(Cl)_8$ (mono-adduct) host-guest complex from 500 ns of Molecular Dynamics (MD) trajectories in explicit CH_3CN solvent (related to Figure 8). Distances and angles are given in Angstroms (Å) and degrees (º), respectively. **a.** Zn···Zn distance and ∠N1-N2-N3-N4 dihedral angle measured along the MD trajectory. ∠N1-N2-N3-N4 dihedral angle describes the torsion of the nanocapsule: the larger deviation from ∠N1-N2-N3-N4 = 0 angle, the more twisted the capsule. Most visited angle values are shown in the histogram plot (frequency vs. angle value). **b.** ∠N1-N2-C1-C2 dihedral angle measured along the MD trajectory. ∠N1-N2-C1-C2 angle describes the relative rotation of the encapsulated fullerene with respect to the capsule, and most visited angle values are shown in the histogram plot (frequency vs. angle value). Different capsule windows (labelled as 1, 2, 3, and 4 in the figure) correspond to different ranges of explored angle values. **c**. ∠Zn1-Zn2-C3-C4 dihedral angle measured along the MD trajectory. ∠Zn1-Zn2-C3-C4 angle describes the relative orientation of the cyclopropane ring with respect to the capsule. ∠Zn1-Zn2-C3-C4 values around 0º and ±180º indicate that the cyclopropane ring stay perpendicular to the porphyrins, while values around ±90º indicate that the cyclopropane ring stays in a parallel conformation with respect to the porphyrins.

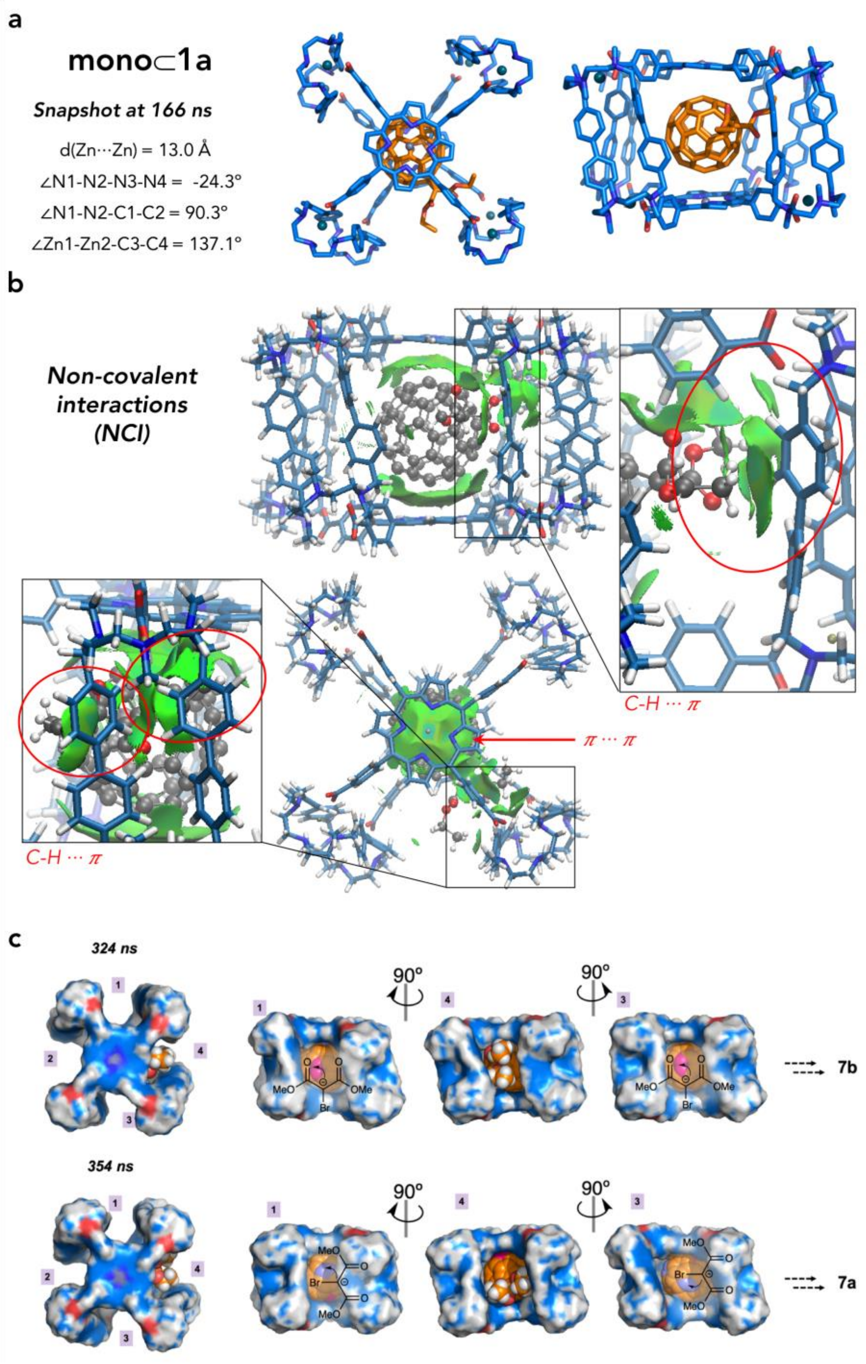

Fig. S12 | Non-covalent interaction (NCI) analysis and schematic representation of the two possible orientational attacks on (mono-diethylmalonate-C_{60})⊂1a·(Cl)$_8$ (mono-adduct) host-guest complex (related to Figure 8). **a**, NCI analysis from two representative snapshots taken from 500 ns of Molecular Dynamics (MD) trajectory in explicit CH_3CN solvent. Solvent molecules and Cl^- ions are omitted for clarity. **b**, Gradient isosurface with s = 0.5 a.u., and RGB scale according to the sign(λ_2)ρ over the range [-0.04:0.04] a.u.. **c**, Schematic representation of the two possible orientational nucleophilic attack of the second malonate on the **(mono-diethylmalonate-C_{60})⊂1a**·(Cl)$_8$ (selected snapshots from MD simulations). The second nucleophilic attack blocks fullerene gate-to-gate and spin motions, and defines the final hetero-tetrakis-isomer that is formed (**7a** vs. **7b**).

Fig. S13 | Representative snapshots of (mono-diethylmalonate-C_{60})⊂1a·$(Cl)_8$ (mono-adduct) host-guest complex taken from 500 ns of Molecular Dynamics (MD) trajectory in explicit CH_3CN solvent. a. Top view and 4 additional perspectives (for each nanocapsule window) of the host-guest complex. Nanocapsule **1a** is shown in surface mode and **mono-diethylmalonate-C_{60}** adduct is show in space filling format. Solvent molecules, Cl^- ions and hydrogen atoms are omitted for clarity. **b**. Bonds suitable to be functionalized during the second cyclopropanation reaction to form the bis-adduct are highlighted in purple and pink.

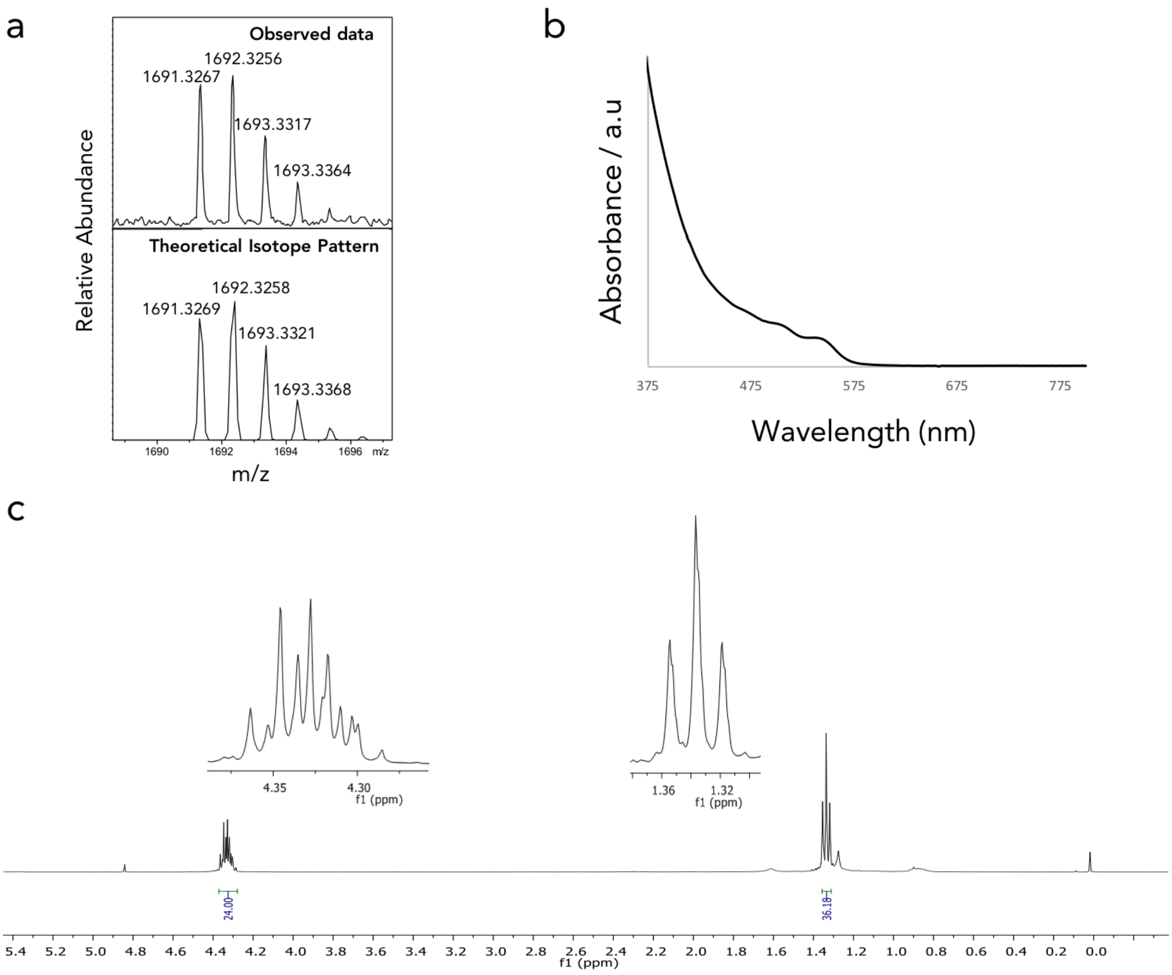

Fig. S14 | Hexakis-adducts mixture obtained via heterogeneous catalysis in CH_3CN. a, Experimental and theoretical isotope pattern of high resolution ESI-MS of hexakis-adduct mixture (M+Na) (ESI-MS, Positive ion mode, CH_2Cl_2:MeOH). **b**, UV-vis absorption spectrum of the hexakis adduct mixture (298 K, Toluene), differing from the pure *Th*-isomer obtained with the biphasic protocol (see Figure 9, main text). **c**, ^{1}H-NMR spectrum of the mixture of hexakis-adducts, specially distinct from pure *Th*-isomer in the multiplet obtained at the methylene region (4.30-4.36 ppm) (500 MHz, 298 K, $CDCl_3$).

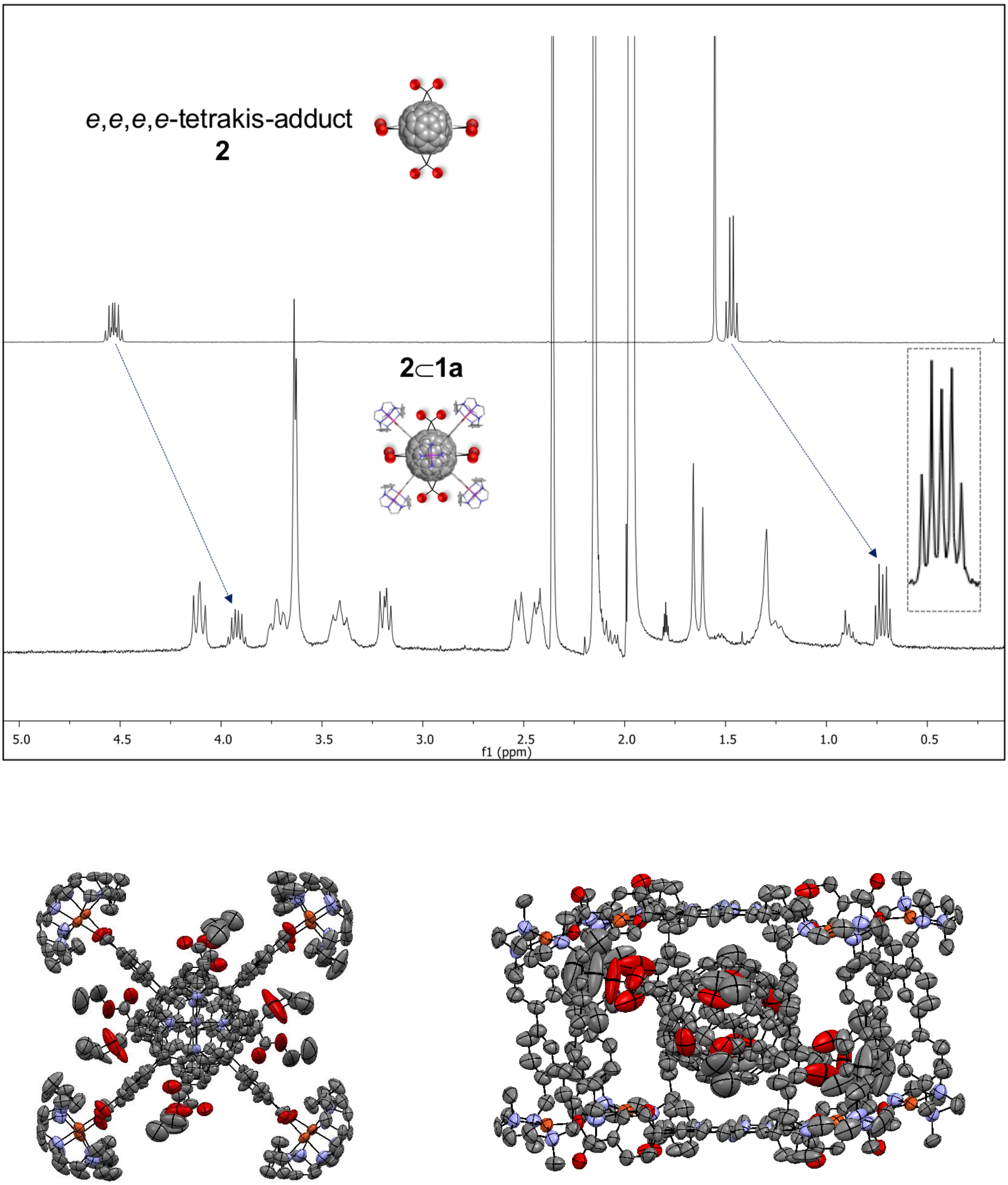

Fig. S15 | Comparison of ^{1}H NMR peaks of free tetrakis-adduct 2 and encapsulated in 1a. Top, ^{1}H NMR of **2** (500 MHz, 298 K, $CDCl_3$). Middle, ^{1}H NMR of **2**$\subset$**1a** ((400 MHz, 298 K, CD_3CN). Bottom, Ortep view of the crystallographic characterization of **2**$^{8+}$

5. | Supplementary Tables

Table S1 | Crystal data and structure refinement for **2⊂1b**·(BArF)$_8$ (CCDC code 1913118) (related to Figure 2).

Empirical Formula	$C_{608}H_{420}B_8Cu_8F_{192}N_{32}O_{34}Zn_2$
Formula Weight/g.mol^{-1}	13091.28
Temperature/K	100(2)
Crystal system	Monoclinic
Space Group	$P2_1/n$
a/Å	31.550(5)
b/Å	33.120(5)
c/Å	35.300(5)
β/º	94.75(5)
Volume/ Å^3	367560(10)
Z	2
ρ_{calc}/g.cm^{-3}	1.183
μ/mm^{-1}	0.587
F(000)	13248
X-Ray Wavelenght/Å	0.82653
Crystal size/mm	0.6×0.6×0.6
2θ range for data collection /º	2.370 to 24.410
Index ranges	$-31\leq h\leq 31$, $-33\leq h\leq 33$, $-34\leq h\leq 34$
Reflections Collected	126610
Independent Reflections	36692
Data/restraints/parameters	21440/3950/3983
Goodness-of-fit on F^2	1.387
Final R indexes [I>=2σ(I)]	R_1=0.1266, wR_2=0.3381
Final R indexes [all data]	R_1=0.1753, wR_2=0.3973

6. | Supplementary references

[1] C. García-Simón, M. Garcia-Borràs, L. Gómez, T. Parella, S. Osuna, J. Juanhuix, I. Imaz, D. Maspoch, M. Costas and X. Ribas, (2014), Sponge-like molecular cage for purification of fullerenes, Nat. Commun. *5*, 5557.

[2] C. Fuertes-Espinosa, A. Gómez-Torres, R. Morales-Martínez, A. Rodríguez-Fortea, C. García-Simón, F. Gándara, I. Imaz, J. Juanhuix, D. Maspoch, J. M. Poblet, L. Echegoyen and X. Ribas, (2018), Purification of Uranium-based Endohedral Metallofullerenes (EMFs) by Selective Supramolecular Encapsulation and Release, Angew. Chem. Int. Ed. *57*, 11294-11299.

[3] J. Juanhuix, F. Gil-Ortiz, G. Cuni, C. Colldelram, J. Nicolas, J. Lidon, E. Boter, C. Ruget, S. Ferrer and J. Benach, (2014), Developments in optics and performance at BL13-XALOC, the macromolecular crystallography beamline at the Alba Synchrotron, J. Synchrotron Rad. *21*, 679-689.

[4] W. Kabsch, (2010), XDS, Acta Crystal. D *66*, 125-132.

[5] G. Sheldrick, (2015), SHELXT - Integrated space-group and crystal-structure determination, Acta Cryst. A *71*, 3-8.

[6] G. Sheldrick, (2015), Crystal structure refinement with SHELXL, Acta Cryst. C *71*, 3-8.

[7] A. Spek, (2009), Structure validation in chemical crystallography, Acta Cryst. D *65*, 148-155.

[8] R. Salomon-Ferrer, A. W. Götz, D. Poole, S. Le Grand and R. C. Walker, (2013), Routine Microsecond Molecular Dynamics Simulations with AMBER on GPUs. 2. Explicit Solvent Particle Mesh Ewald, J. Chem. Theory Comput. *9*, 3878-3888.

[9] D. S. C. D.A. Case, T.E. Cheatham, III, T.A. Darden, R.E. Duke, T.J. Giese, H. Gohlke, A.W. Goetz, D. Greene, N. Homeyer, S. Izadi, A. Kovalenko, T.S. Lee, S. LeGrand, P. Li, C. Lin, J. Liu, T. Luchko, R. Luo, D. Mermelstein, K.M. Merz, G. Monard, H. Nguyen, I. Omelyan, A. Onufriev, F. Pan, R. Qi, D.R. Roe, A. Roitberg, C. Sagui, C.L. Simmerling, W.M. Botello-Smith, J. Swails, R.C. Walker, J. Wang, R.M. Wolf, X. Wu, L. Xiao, D.M. York and P.A. Kollman in *AMBER 2017*, *Vol.* University of California, San Francisco, **2017**.

[10] J. Wang, R. M. Wolf, J. W. Caldwell, P. A. Kollman and D. A. Case, (2004), Development and testing of a general amber force field, J. Comput. Chem. *25*, 1157-1174.

[11] C. I. Bayly, P. Cieplak, W. Cornell and P. A. Kollman, (1993), A well-behaved electrostatic potential based method using charge restraints for deriving atomic charges: the RESP model, J. Chem. Phys. *97*, 10269-10280.

[12] B. H. Besler, K. M. Merz and P. A. Kollman, (1990), Atomic charges derived from semiempirical methods, J. Comput. Chem. *11*, 431-439.

[13] U. C. Singh and P. A. Kollman, (1984), An approach to computing electrostatic charges for molecules, J. Comput. Chem. *5*, 129-145.

[14] G. W. T. M. J. Frisch, H. B. Schlegel, G. E. Scuseria, M. A. Robb, J. R. Cheeseman, G. Scalmani, V. Barone, G. A. Petersson, H. Nakatsuji, X. Li, M. Caricato, A. Marenich, J. Bloino, B. G. Janesko, R. Gomperts, B. Mennucci, H. P. Hratchian, J. V. Ortiz, A. F. Izmaylov, J. L. Sonnenberg, D. Williams-Young, F. Ding, F. Lipparini, F. Egidi, J. Goings, B. Peng, A. Petrone, T. Henderson, D. Ranasinghe, V. G. Zakrzewski, J. Gao, N. Rega, G. Zheng, W. Liang, M. Hada, M. Ehara, K. Toyota, R. Fukuda, J. Hasegawa, M. Ishida, T. Nakajima, Y. Honda, O. Kitao, H. Nakai, T. Vreven, K. Throssell, J. A. Montgomery, Jr., J. E. Peralta, F. Ogliaro, M. Bearpark, J. J. Heyd, E. Brothers, K. N. Kudin, V. N. Staroverov, T. Keith, R. Kobayashi, J. Normand, K. Raghavachari, A. Rendell, J. C. Burant, S. S. Iyengar, J. Tomasi, M. Cossi, J. M. Millam, M. Klene, C. Adamo, R. Cammi, J. W. Ochterski, R. L. Martin, K. Morokuma, O. Farkas, J. B. Foresman, and D. J. Fox, (2009), Gaussian 09, Revision A. 02. Gaussian, Inc.: Wallingford, CT.

[15] P. Li and K. M. Merz, (2016), MCPB.py: A Python Based Metal Center Parameter Builder, J. Chem. Inf. Model. *56*, 599-604.

[16] J. A. Maier, C. Martinez, K. Kasavajhala, L. Wickstrom, K. E. Hauser and C. Simmerling, (2015), ff14SB: Improving the Accuracy of Protein Side Chain and Backbone Parameters from ff99SB, J. Chem. Theory Comput. *11*, 3696-3713.

[17] T. Darden, D. York and L. Pedersen, (1993), Particle mesh Ewald: An N·log(N) method for Ewald sums in large systems, J. Chem. Phys. *98*, 10089-10092.

[18] J. Contreras-García, E. R. Johnson, S. Keinan, R. Chaudret, J.-P. Piquemal, D. N. Beratan and W. Yang, (2011), NCIPLOT: A Program for Plotting Noncovalent Interaction Regions, J. Chem. Theory Comput. *7*, 625-632.

[19] E. R. Johnson, S. Keinan, P. Mori-Sánchez, J. Contreras-García, A. J. Cohen and W. Yang, (2010), Revealing Noncovalent Interactions, J. Am. Chem. Soc. *132*, 6498-6506.

[20] R. Chaudret, B. de Courcy, J. Contreras-García, E. Gloaguen, A. Zehnacker-Rentien, M. Mons and J. P. Piquemal, (2014), Unraveling non-covalent interactions within flexible biomolecules: from electron density topology to gas phase spectroscopy, Phys. Chem. Chem. Phys. *16*, 9876-9891.

[21] A. B. Grommet, J. B. Hoffman, E. G. Percástegui, J. Mosquera, D. J. Howe, J. L. Bolliger and J. R. Nitschke, (2018), Anion Exchange Drives Reversible Phase Transfer of Coordination Cages and Their Cargoes, J. Am. Chem. Soc. *140*, 14770-14776.

Supporting Information Chapter IV

A Copper-based Supramolecular Nanocapsule that Enables Straightforward Purification of Sc_3N-based Endohedral Metallofullerene Soots

Table of Contents

1. Material and instrumentation.

Reagents and solvents used were commercially available reagent quality unless indicated otherwise. Ligand **1b** was synthesized according to published procedures.[1] The Sc_3N-based soot was prepared following a published procedure.[2] ESI-MS experiments were collected and analyzed on a Bruker MicroTOF-Q-II, using acetonitrile as the mobile phase. UV–vis spectroscopy was performed on an Agilent 8452 UV–vis spectrophotometer with 1 cm quartz cell, equipped with a temperature control cryostat from Unisoku Scientific Instruments (Japan), using a toluene/acetonitrile 9/1 (v/v) mixture as solvent. HPLC data concerning fullerene and endofullerene identity were collected on Agilent series 1200 chromatograph equipped with Cromasil Buckyprep-M column, or **LC-9130 NEXT apparatus (Japan Analytical Industry Co. Ltd.) monitored using a UV detector at 320 nm**. Toluene as eluent (1 mL/min flow). MALDI-MS spectrum concerning to endofullerenes identity were collected on Bruker Ultraflex MALDI-TOF (no matrix was used). FT-IR-ATR experiments were collected and analyzed on a **Bruker Alpha FT-IR spectrometer (FT-IR)**. **The liberation of entrapped fullerenes and endohedral metallofullerenes from 5·(OTf)$_8$ was achieved following a reported procedure,[1] consisting in charging the filled nanocapsule in a column and applying consecutive washings with 1,2-dichlorobenzene/CS_2 (1/1 v/v mixture).**

2. Compound synthesis

Synthesis and characterization of [Cu-1b](CF_3SO_3)$_4$ molecular clip. In a round-bottom flask, 0.04 g of **1b** ligand (0.063 mmols), 0.045 g of [Cu(CF_3SO_3)$_2$] (0.124 mmols) and 2.5 mL of anhydrous acetonitrile were mixed. The mixture is stirred at room temperature for 45 min. After this time, the reaction mixture is filtered through an Olimpeak disc and recrystallized under slow diethyl ether diffusion. Bright blue crystalline solid is obtained (Yield: 93.2%).
HRMS (m/z): calculated 1221.116 and found 1221.115 ([(**Cu-1b**)·(CF_3SO_3)$_3$]$^{+1}$); calculated 536.116 and found 536.115 ([(**Cu-1b**)·(CF_3SO_3)$_2$]$^{+2}$).
FT-IR-ATR (ν, cm^{-1})**:** characteristic bands at 1222, 1025 and 634 cm^{-1}. The high-energy band is assigned to S-O$^-$ stretching mode (634 cm^{-1}), the lower energy components correspond to the corresponding S=O stretching mode (ν_{sym} 1025 cm^{-1} and ν_{as} 1222 cm^{-1}).
UV-vis characterization: λ_{max} = 265 nm (ε=42800 l·mol^{-1}·cm^{-1})
Combustion-Analysis: % N calc. 6.13, found 6.05; **% C** calc. 40.32, found 40.06; **% H** calc. 4.27, found 4.45.
Synthesis and characterization of 5·(OTf)$_8$ nanocapsule. 6.23 mg of 5,10,15,20-tetrakis (4-carboxyphenyl) porphyrin-Zn^{II} (0.00729 mmols) are weighted in a 10 mL flask, then 1 mL of DMF is added. Subsequently, 6.1µL of triethylamine (0.043 mmols) dissolved in 0.5 ml of DMF are added to the porphyrin solution. Finally 20 mg of [(**Cu-1b**)·(CF_3SO_3)$_4$] complex (0.014 mmols) dissolved in 2.5 ml of DMF are added to the mixture. The solution obtained is stirred at room temperature for 16h. After the reaction time, the mixture is filtered through an Olimeak disc and recrystallized by slow diethyl ether diffusion. The product is obtained as a purple crystalline powder (Yield: 89%).
HRMS m/z: [{**5**·(OTf)$_5$}$^{+3}$]: calculated 1348.191 and found 1348.189
[{**5**·(OTf)$_4$}$^{+4}$]: calculated 1048.505 and found 1048.503
[{**5**·(OTf)$_3$}$^{+5}$]: calculated 848.938 and found 848.936
[{**5**·(OTf)$_2$}$^{+6}$]: calculated 706.530 and found 706.528
[{**5**·(OTf)}$^{+7}$]: calculated 599.415 and found 599.413[{**5**·(OTf)}$^{+8}$].
The nanocapsule was spectroscopically characterized by **FT-IR-ATR** and **UV-vis** spectroscopy. The most distinctive features of the respective **IR spectra** are four strong bands at 1603, 1249, 1028 and 637 cm^{-1}. The high-energy band is assigned to S-O$^-$ stretching mode (637 cm^{-1}), the lower energy components correspond to the corresponding S=O stretching mode (ν_{sym} 1028 cm^{-1} and ν_{as} 1249 cm^{-1}) and the ν_{as} C=O stretching mode (1603 cm^{-1}) of the carboxylates. In the **IR spectra** corresponding to free 1,5,10,15,20-tetrakis (4-carboxyphenyl)-porphyrin-Zn(II), the most distinctive bands are assigned to O-H stretching mode (2986 cm^{-1}) and C=O stretching mode (1684 cm^{-1}) of the carboxylates.
UV-vis: Soret band: 425 nm (ε= 634500 l·mol^{-1}·cm^{-1}); Q bands: 564 nm (ε=20000 l·mol^{-1}·cm^{-1}) and 605 nm (ε=10850 l·mol^{-1}·cm^{-1})
^{1}H NMR: very broad spectrum (the paramagnetic nature of the Cu(II) centers precluded the NMR characterization).

3. Preparation and characterization of fullerene and EMFs adducts.

Preparation of $C_{60}\subset\mathbf{5}\cdot(OTf)_8$: 2.8 mg of nanocapsule $\mathbf{5}\cdot(OTf)_8$ (0.46 µmols, 1 equivalent) are dissolved in 0.5 mL of acetonitrile. Then one equivalent of C_{60} dissolved in 4.5 mL of toluene is added to the cage solution. The mixture is stirred at room temperature for 5 min. The reaction crude is filtered and the solvent is removed under vacuum.

HRMS m/z: $[\{C_{60}\subset\mathbf{5}\cdot(OTf)_4\}^{+4}]$: calculated 1528.328 and found 1528.328
$[\{C_{60}\subset\mathbf{5}\cdot(OTf)_3\}^{+5}]$: calculated 1192.672 and found 1192.672
$[\{C_{60}\subset\mathbf{5}\cdot(OTf)_2\}^{+6}]$: calculated 969.067 and found 969.067
$[\{C_{60}\subset\mathbf{5}\cdot(OTf)\}^{+7}]$: calculated 809.351 and found 809.350
$[\{C_{60}\subset\mathbf{5}\}^{+8}]$: calculated 689.562 and found 689.562

Preparation of $C_{70}\subset\mathbf{5}\cdot(OTf)_8$: 2.8 mg of nanocapsule $\mathbf{5}\cdot(OTf)_8$ (0.46 µmols, 1 equivalent) are dissolved in 0.5 mL of acetonitrile. Then one equivalent of C_{70} dissolved in 4.5 mL of toluene is added to the cage solution. The mixture is stirred at room temperature for 5 min. The reaction crude is filtered and the solvent is removed under vacuum.

HRMS m/z: calculated 1558.328 and found 1558.328 $[\{C_{70}\subset\mathbf{5}\cdot(OTf)_4\}^{+4}]$; calculated 1216.872 and found 1216.872 $[\{C_{70}\subset\mathbf{5}\cdot(OTf)_3\}^{+5}]$; calculated 989.067 and found 989.067 $[\{C_{70}\subset\mathbf{5}\cdot(OTf)_2\}^{+6}]$; calculated 826.494 and found 826.493 $[\{C_{70}\subset\mathbf{5}\cdot(OTf)\}^{+7}]$; calculated 704.562 and found 704.752$[\{C_{70}\subset\mathbf{5}\}^{+8}]$.

Preparation of fullerene extract$\subset\mathbf{5}\cdot(OTf)_8$: The preparation of the adducts between nanocapsule $\mathbf{5}\cdot(OTf)_8$ and fullerene extract was carried out following procedures analogous to the preparation of C_{60} and C_{70} fullerenes (assuming that all the fullerenes from fullerene extract were C_{60}).

HRMS m/z:

($C_{60}\subset\mathbf{5}\cdot(OTf)_8$): calculated 1528.328 and found 1528.328 $[\{C_{60}\subset\mathbf{5}\cdot(OTf)_4\}^{+4}]$; calculated 1192.672 and found 1192.672 $[\{C_{60}\subset\mathbf{5}\cdot(OTf)_3\}^{+5}]$; calculated 969.067 and found 969.067 $[\{C_{60}\subset\mathbf{5}\cdot(OTf)_2\}^{+6}]$; calculated 809.351 and found 809.351 $[\{C_{60}\subset\mathbf{5}\cdot(OTf)\}^{+7}]$;calculated 689.562 and found 689.562 $[\{C_{60}\subset\mathbf{5}\}^{+8}]$.

($C_{70}\subset\mathbf{5}\cdot(OTf)_8$): calculated 1558.328 and found 1558.328 $[\{C_{70}\subset\mathbf{5}\cdot(OTf)_4\}^{+4}]$; calculated 1216.872 and found 1216.872 $[\{C_{70}\subset\mathbf{5}\cdot(OTf)_3\}^{+5}]$; calculated 989.067 and found 989.067 $[\{C_{70}\subset\mathbf{5}\cdot(OTf)_2\}^{+6}]$; calculated 826.494 and found 826.493 $[\{C_{70}\subset\mathbf{5}\cdot(OTf)\}^{+7}]$; calculated 704.562 and found 704.752 $[\{C_{70}\subset\mathbf{5}\}^{+8}]$.

($C_{76}\subset\mathbf{5}\cdot(OTf)_8$): calculated 1576.328 and found 1576.328 $[\{C_{76}\subset\mathbf{5}\cdot(OTf)_4\}^{+4}]$; calculated 1231.272 and found 1231.272$[\{C_{76}\subset\mathbf{5}\cdot(OTf)_3\}^{+5}]$; calculated 1001.234 and found 1001.233$[\{C_{76}\subset\mathbf{5}\cdot(OTf)_2\}^{+6}]$; calculated 836.779 and found 836.779$[\{C_{76}\subset\mathbf{5}\cdot(OTf)\}^{+7}]$; calculated 713.562 and found 713.562$[\{C_{76}\subset\mathbf{5}\}^{+8}]$.

($C_{84}\subset\mathbf{5}\cdot(OTf)_8$): calculated 1600.328 and found 1600.328 $[\{C_{84}\subset\mathbf{5}\cdot(OTf)_4\}^{+4}]$; calculated 1250.472 and found 1250.472$[\{C_{84}\subset\mathbf{5}\cdot(OTf)_3\}^{+5}]$; calculated 1017.234 and found 1017.234$[\{C_{84}\subset\mathbf{5}\cdot(OTf)_2\}^{+6}]$; calculated 850.493 and found 850.493 $[\{C_{84}\subset\mathbf{5}\cdot(OTf)\}^{+7}]$; calculated 744.181 and found 744.182$[\{C_{84}\subset\mathbf{5}\}^{+8}]$.

($C_{90}\subset\mathbf{5}\cdot(OTf)_8$): calculated 1618.328 and found 1618.328 $[\{C_{90}\subset\mathbf{5}\cdot(OTf)_4\}^{+4}]$; calculated 1264.872 and found 1264.872 $[\{C_{90}\subset\mathbf{5}\cdot(OTf)_3\}^{+5}]$; calculated 1029.234 and found 1029.234$[\{C_{90}\subset\mathbf{5}\cdot(OTf)_2\}^{+6}]$; calculated 860.922 and found 860.922$[\{C_{90}\subset\mathbf{5}\cdot(OTf)\}^{+7}]$; calculated 734.562 and found 734.562$[\{C_{90}\subset\mathbf{5}\}^{+8}]$.

Preparation of Sc_3N-based soot$\subset\mathbf{5}\cdot(OTf)_8$: 2.8 mg of nanocapsule $\mathbf{5}\cdot(OTf)_8$ (0.46 µmols, 1 equivalent) are dissolved in 0.5 mL of acetonitrile. Then one equivalent of Sc-based soot (assuming that all fullerenes and endofullerenes were $Sc_3N@C_{80}$) dissolved in 4.5 mL of toluene is added to the cage solution. The mixture is stirred at room temperature for 5 min. The reaction crude is filtered and the solvent is removed under vacuum.

HRMS (m/z). **($Sc_3N@C_{80}\subset\mathbf{5}\cdot(OTf)_8$):** calculated 1625.545 and found 1625.545 $[\{Sc_3N@C_{80}\subset\mathbf{5}\cdot(OTf)_4\}^{+4}]$; calculated 1270.646 and found 1270.646 $[\{Sc_3N@C_{80}\subset\mathbf{5}\cdot(OTf)_3\}^{+5}]$; calculated 1034.046 and found 1034.046 $[\{Sc_3N@C_{80}\subset\mathbf{5}\cdot(OTf)_2\}^{+6}]$; calculated 864.903 and found 864.904 $[\{Sc_3N@C_{80}\subset\mathbf{5}\cdot(OTf)\}^{+7}]$; calculated 738.171 and found 738.171 $[\{Sc_3N@C_{80}\subset\mathbf{5}\}^{+8}]$.

($Sc_3N@C_{78}\subset\mathbf{5}\cdot(OTf)_8$): calculated 1619.545 and found 1619.544 $[\{Sc_3N@C_{78}\subset\mathbf{5}\cdot(OTf)_4\}^{+4}]$; calculated 1265.846 and found 1265.846 $[\{Sc_3N@C_{78}\subset\mathbf{5}\cdot(OTf)_3\}^{+5}]$; calculated 1030.046 and found 1030.046 $[\{Sc_3N@C_{78}\subset\mathbf{5}\cdot(OTf)_2\}^{+6}]$; calculated 861.475 and found 861.476 $[\{Sc_3N@C_{78}\subset\mathbf{5}\cdot(OTf)\}^{+7}]$; calculated 735.171 and found 738.172 $[\{Sc_3N@C_{78}\subset\mathbf{5}\}^{+8}]$.

($Sc_3N@C_{68}\subset\mathbf{5}\cdot(OTf)_8$): calculated 1589.545 and found 1589.545 $[\{Sc_3N@C_{68}\subset\mathbf{5}\cdot(OTf)_4\}^{+4}]$; calculated 1241.846 and found 1241.846 $[\{Sc_3N@C_{68}\subset\mathbf{5}\cdot(OTf)_3\}^{+5}]$; calculated 1009.879 and found 1009.880 $[\{Sc_3N@C_{68}\subset\mathbf{5}\cdot(OTf)_2\}^{+6}]$; calculated 844.332 and found 844.332 $[\{Sc_3N@C_{68}\subset\mathbf{5}\cdot(OTf)\}^{+7}]$; calculated 720.171 and found 720.171 $[\{Sc_3N@C_{68}\subset\mathbf{5}\}^{+8}]$.

($C_{60}\subset\mathbf{5}\cdot(OTf)_8$): calculated 1528.328 and found 1528.328 $[\{C_{60}\subset\mathbf{5}\cdot(OTf)_4\}^{+4}]$; calculated 1192.672 and found 1192.672 $[\{C_{60}\subset\mathbf{5}\cdot(OTf)_3\}^{+5}]$; calculated 969.067 and found 969.067 $[\{C_{60}\subset\mathbf{5}\cdot(OTf)_2\}^{+6}]$; calculated 809.351 and found 809.351 $[\{C_{60}\subset\mathbf{5}\cdot(OTf)\}^{+7}]$;calculated 689.562 and found 689.562 $[\{C_{60}\subset\mathbf{5}\}^{+8}]$.
($C_{70}\subset\mathbf{5}\cdot(OTf)_8$): calculated 1558.328 and found 1558.328 $[\{C_{70}\subset\mathbf{5}\cdot(OTf)_4\}^{+4}]$; calculated 1216.872 and found 1216.872 $[\{C_{70}\subset\mathbf{5}\cdot(OTf)_3\}^{+5}]$; calculated 989.067 and found 989.067 $[\{C_{70}\subset\mathbf{5}\cdot(OTf)_2\}^{+6}]$; calculated 826.494 and found 826.493 $[\{C_{70}\subset\mathbf{5}\cdot(OTf)\}^{+7}]$; calculated 704.562 and found 704.752 $[\{C_{70}\subset\mathbf{5}\}^{+8}]$.

Purification of an equimolar mixture of C_{60}:C_{70}:$Sc_3N@C_{80}$ (1:1:1) using $\mathbf{5}\cdot(OTf)_8$ in the solid phase: 0.34 mg of pure C_{60}(0.46 µmols, 1 equivalent), 0.39 mg of pure C_{70}(0.46 µmols, 1 equivalent) and 0.52 mg of pure $Sc_3N@C_{80}$(0.46 µmols, 1 equivalent) are dissolved in 10 mL of toluene. Then 16.8 mg of nanocapsule $\mathbf{5}\cdot(OTf)_8$ (2.76 µmols, 6 equivalents) in the solid phase are added to the equimolar mixture of C_{60}:C_{70}:$Sc_3N@C_{80}$ in toluene. The suspension is stirred at room temperature for 11 hours. Aliquots of the supernatant are filtered, and analysed by HPLC at different times (Figure 4, main text).

4. General procedure for UV-vis titrations.

Host-guest interactions in solution were studied by UV-vis spectroscopy. The UV-vis titration experiments between $\mathbf{5}\cdot(OTf)_8$ (6.75 x 10^{-7} M) and the different fullerenes tested (2.11 x 10^{-5} M) were performed by using toluene/acetonitrile (9/1) as solvent. The concentration of the nanocapsule was kept constant. A magnetic stir bar and 2 mL of nanocapsule solution were added to the cuvette, then it was inserted into the spectrometer and the stirrer activated and the substrate added. The stoichiometry of the complexes was studied using the method of continuous variations. Solutions of nanocapsule $\mathbf{5}\cdot(OTf)_8$ and fullerenes in toluene/acetonitrile (9/1) were mixed at different ratios. All the experiments were carried out at 22 °C. The data obtained from the UV-vis spectrophotometric titrations were analyzed using the software Origin Pro 8.

5. Supplementary figures

Figure S1. HRMS spectrum of clip complex [Cu-1b](CF_3SO_3)$_4$ complex. Simulated spectra of selected peaks are showed in red. Experimental conditions: 100µM in acetonitrile, registered with a Bruker Micro TOF-Q-II exact mass spectrometer.

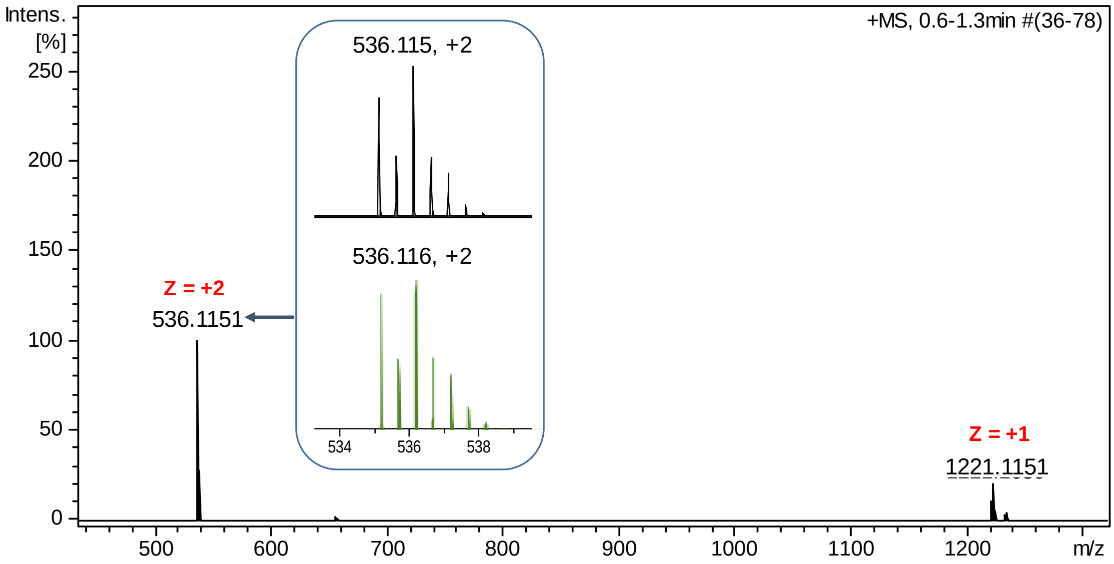

Figure S2. UV-Vis spectrum of clip complex [Cu-1b](CF_3SO_3)$_4$ complex ($3.37 \cdot 10^{-6}$ M solution in acetonitrile).

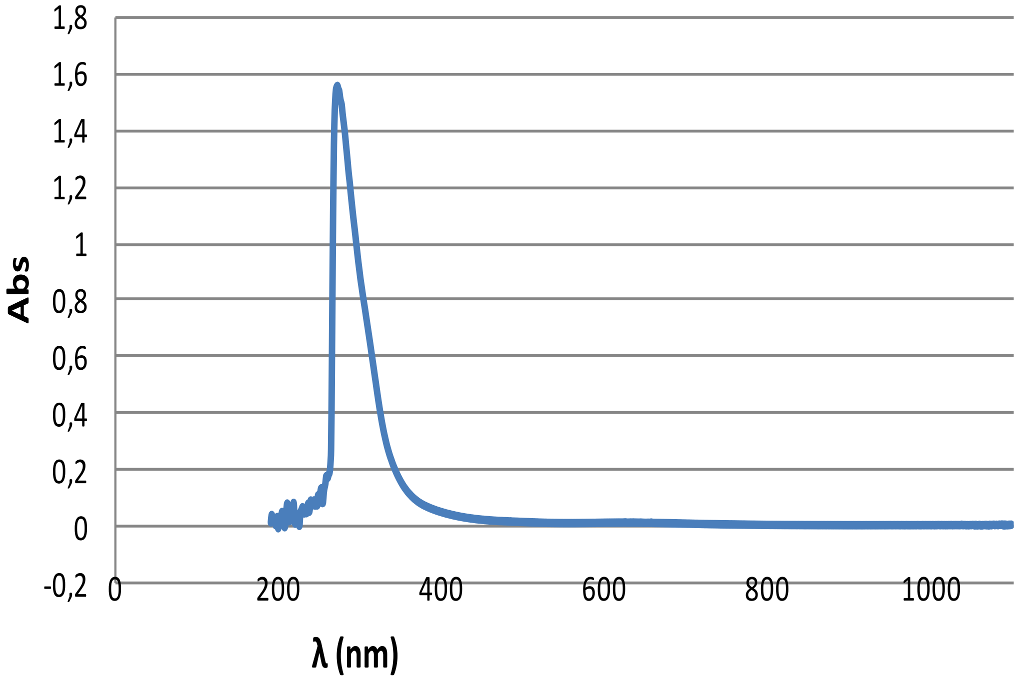

Figure S3. FT-IR-ATR of clip complex [Cu-1b](CF_3SO_3)$_4$ complex.

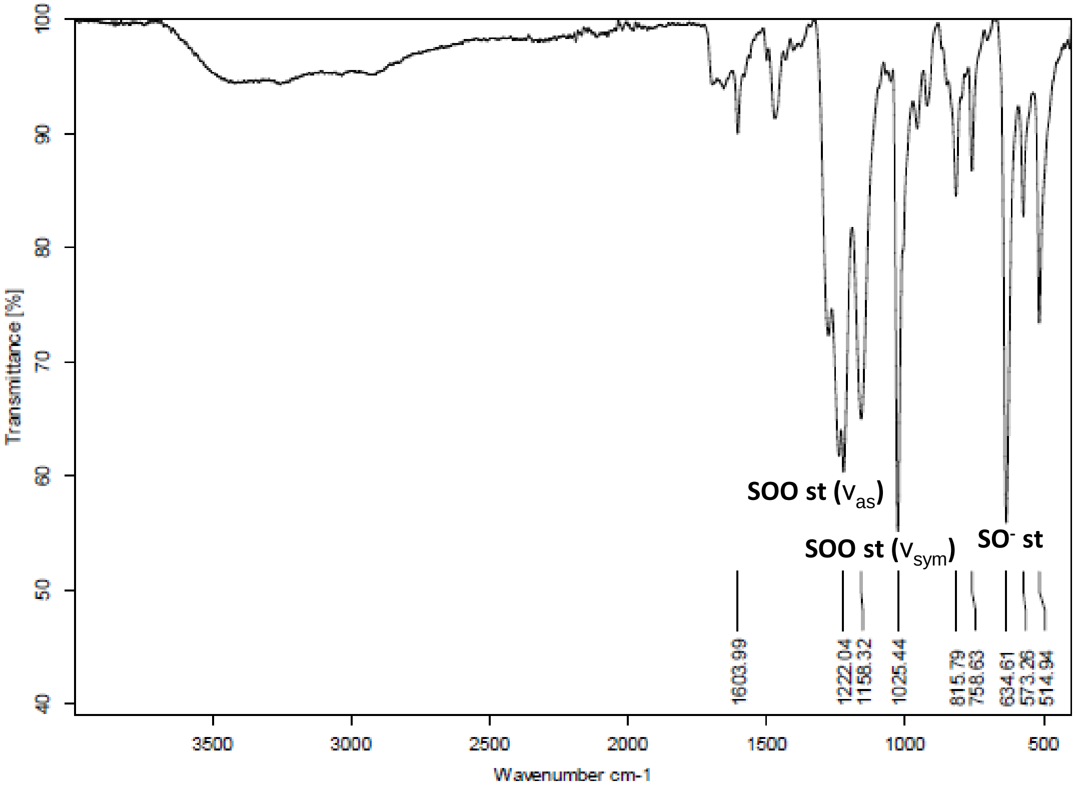

Figure S4. UV-Vis spectrum of nanocapsule 5·(OTf)$_8$ (3.37·10^{-6} M solution in acetonitrile).

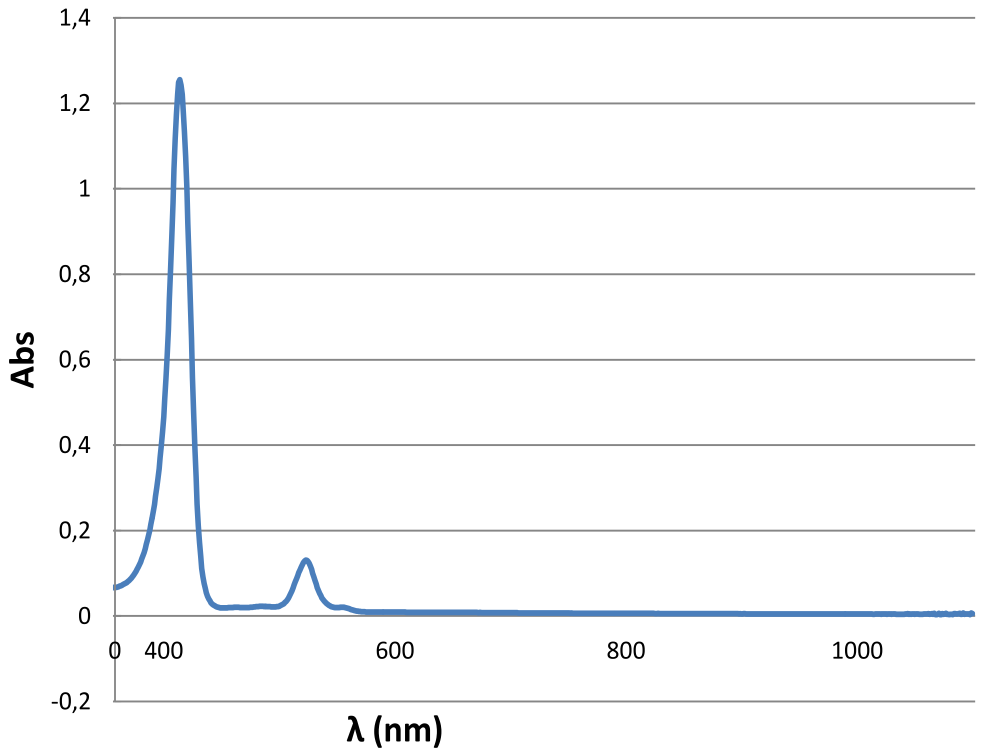

Figure S5. FT-IR-ATR of nanocapsule 5·(OTf)$_8$.

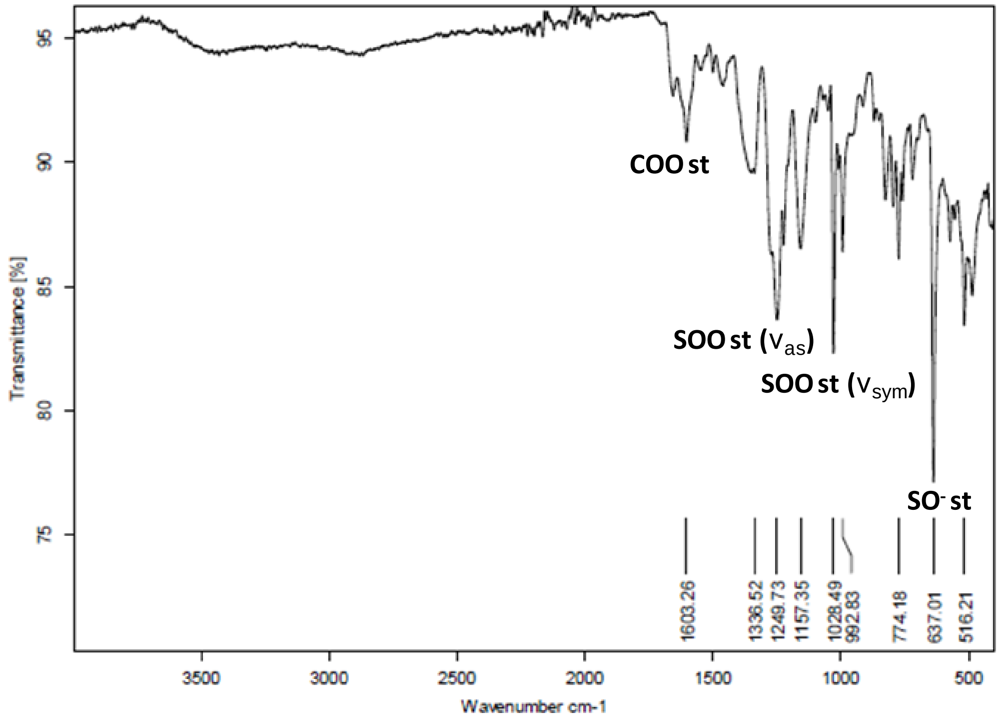

Figure S6. UV-Vis monitoring of the titration of nanocapsule 5·(OTf)$_8$ with fullerene C$_{60}$. Fixed total concentration (6.75·10^{-7} M) of nanocapsule in toluene/acetonitrile (9:1). Inset: Absorbance variation at 425 nm Soret band vs. different equivalents of added substrate.

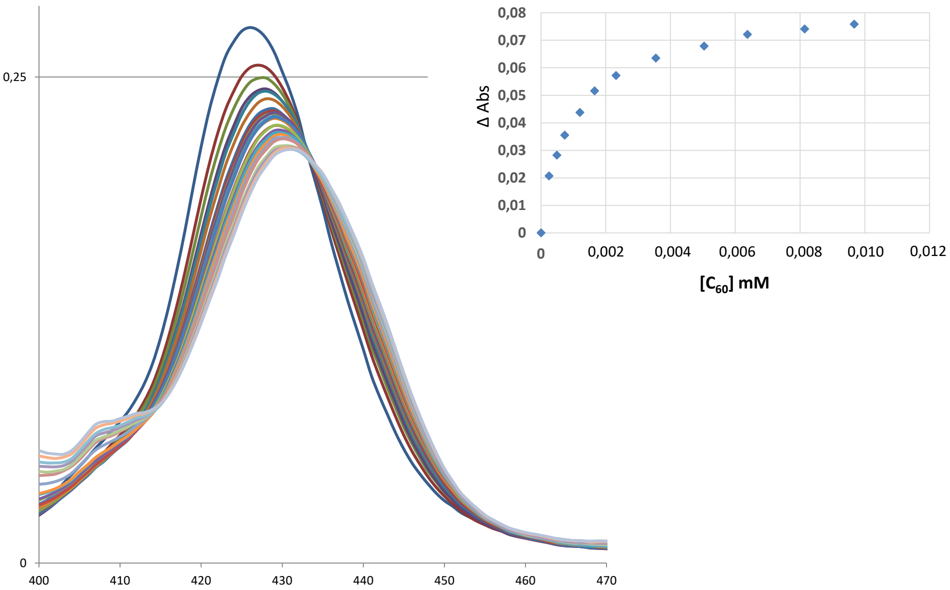

Figure S7. UV-Vis monitoring of the titration of nanocapsule 5·(OTf)$_8$ with fullerene C$_{70}$. Fixed 6.75·10^{-7} M concentration of nanocapsule in toluene/acetonitrile (9:1). Inset: Absorbance variation at 425 nm Soret band vs. different equivalents of added substrate.

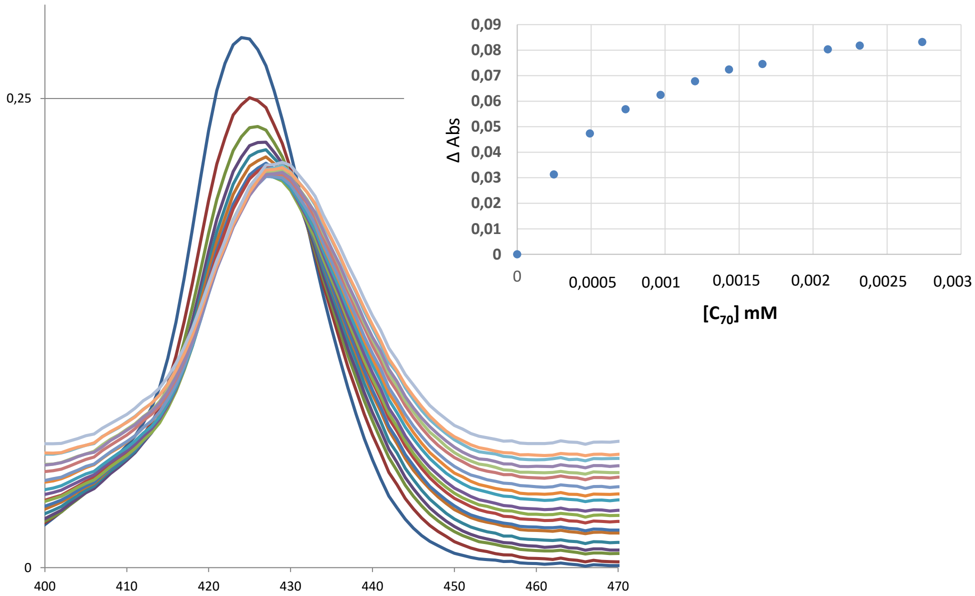

Figure S8. HRMS spectrum of fullerene extract⊂5·(OTf)$_8$ host-guest adducts formed a) using the nanocapsule in solution (toluene:acetonitrile 9:1) and b) using the nanocapsule in solid phase (toluene as solvent phase). Simulated spectra of selected peaks are showed in red. Experimental conditions: 10:1 fullerene extract:**5**·(OTf)$_8$ molar ratio, assuming that all the species are C_{60}. Registered with a Bruker Micro TOF-Q-II exact mass spectrometer.

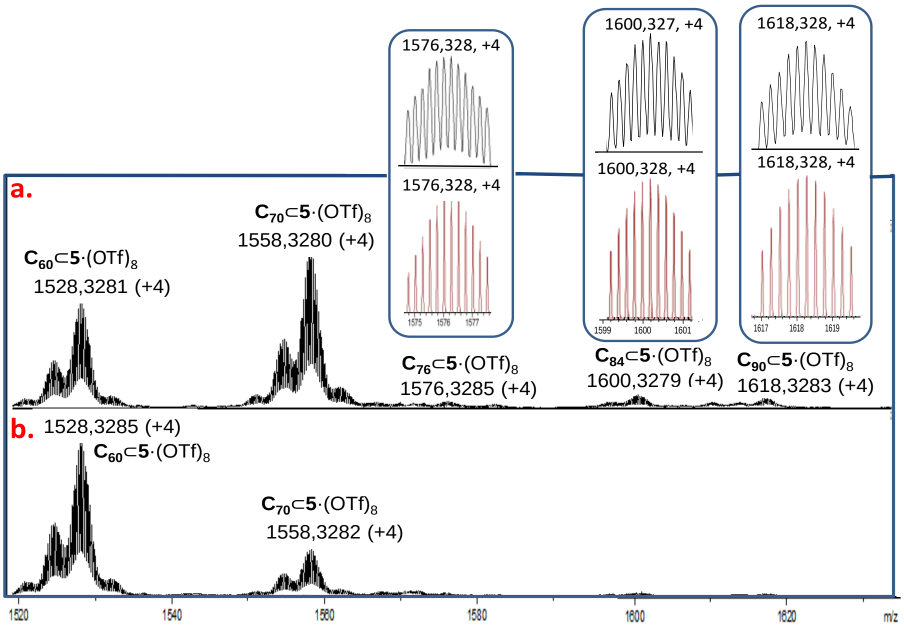

Figure S9. Solid state extraction of fullerene C_{60} from 5·(OTf)$_8$. HRMS monitoring of the C_{60} extraction washing-protocol using pure C_{60} encapsulated in **5**·(OTf)$_8$ in the solid phase.

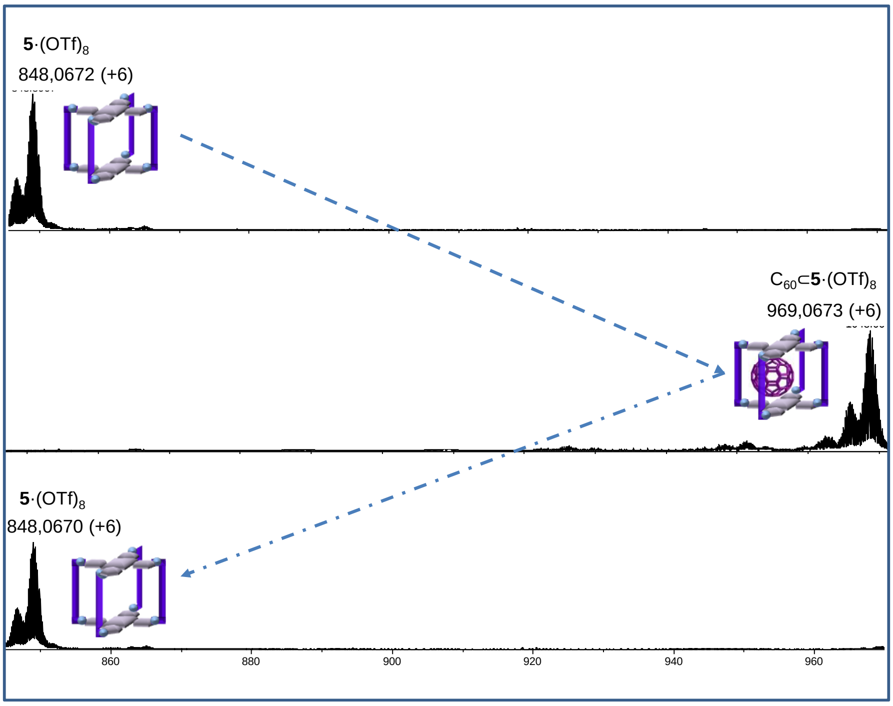

Figure S10. HPLC chromatogram of Sc_3N-based crude soot. Experimental conditions: $1.8 \cdot 10^{-4}$ M in toluene, approximate concentration assuming that all the species are $Sc_3N@C_{80}$ (HPLC separation mediated by a Cosmosil Buckyprep-M column, Flow: 1ml/min).

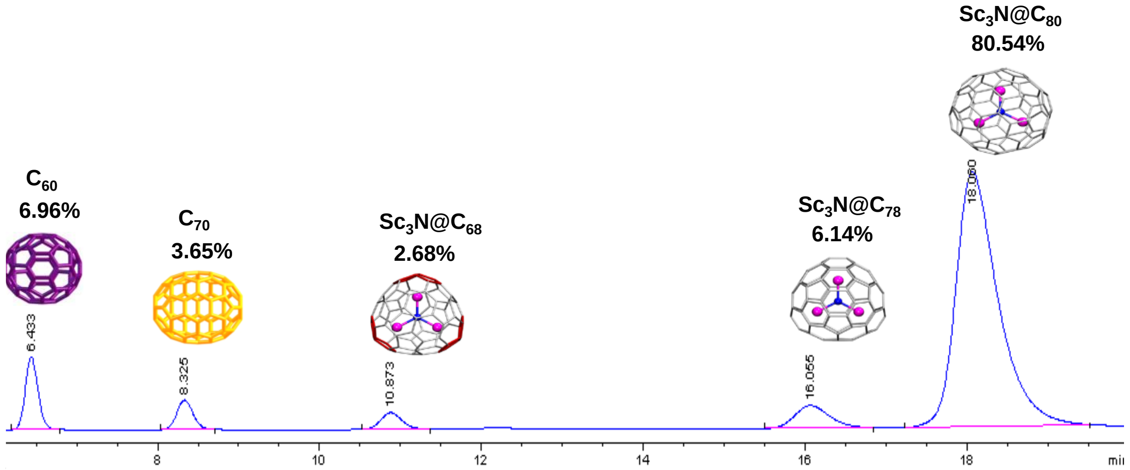

Figure S11. HRMS spectrum of Sc-based soot⊂5·$(OTf)_8$ host-guest adducts. Simulated spectra of selected peaks are showed in red. Experimental conditions: 100 µM in toluene:acetonitrile (9:1), registered with a Bruker Micro TOF-Q-II exact mass spectrometer.

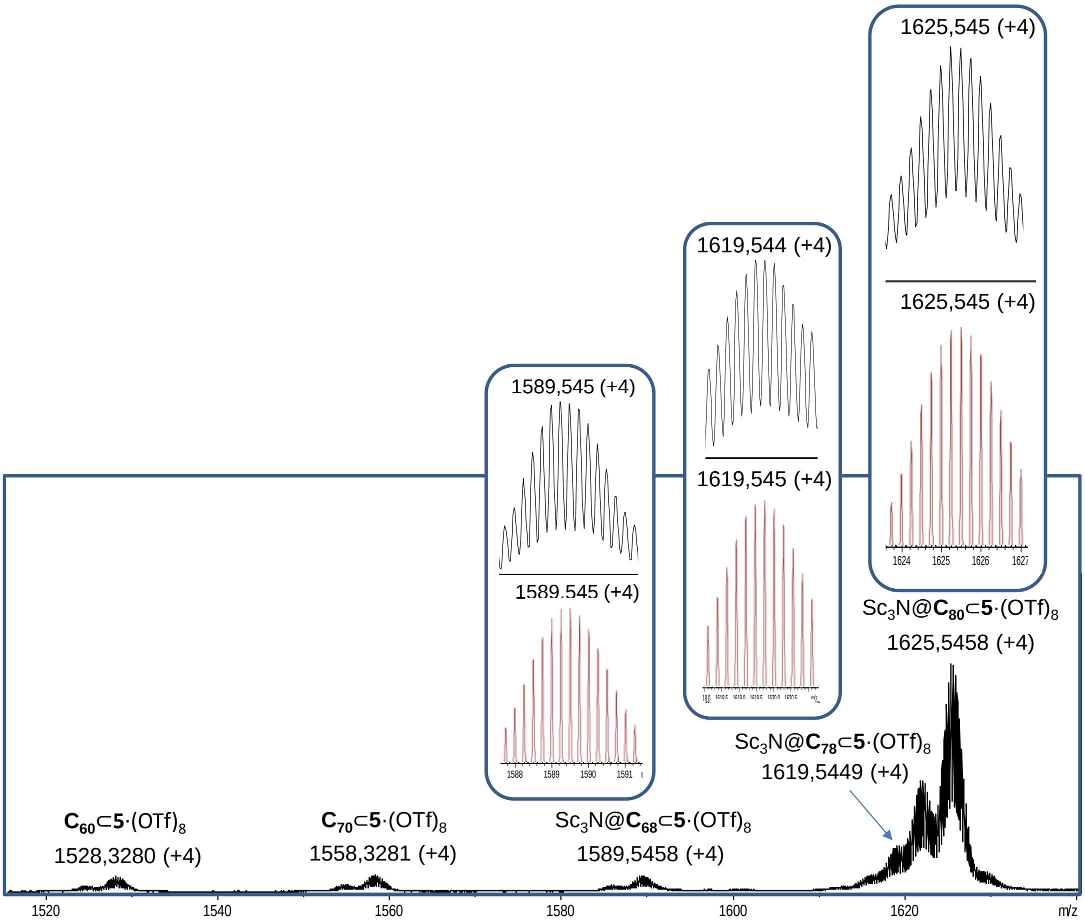

Figure S12. UV-Vis monitoring of the titration of 5·(OTf)$_8$ nanocapsule with pure Sc$_3$N@C$_{80}$. Fixed total concentration (6.75·10^{-7} M) of nanocapsule in toluene/acetonitrile (9:1). Inset: Absorbance variation at 425 nm Soret band vs. different equivalents of added substrate.

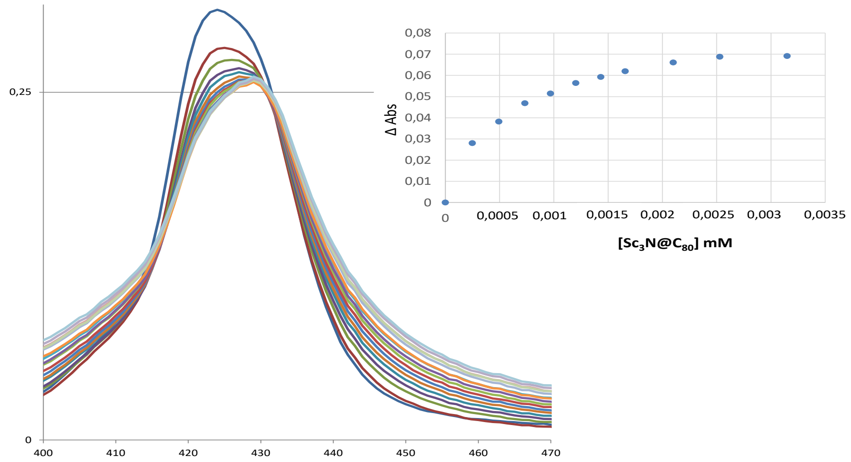

Figure S13. Solid state extraction of EMFs and fullerenes (Sc$_3$N-based soot) from 5·(OTf)$_8$. HRMS monitoring of the species contained on the Sc$_3$N-based soot extraction washing-protocol using Sc$_3$N-based soot encapsulated in **5**·(OTf)$_8$ in the solid phase.

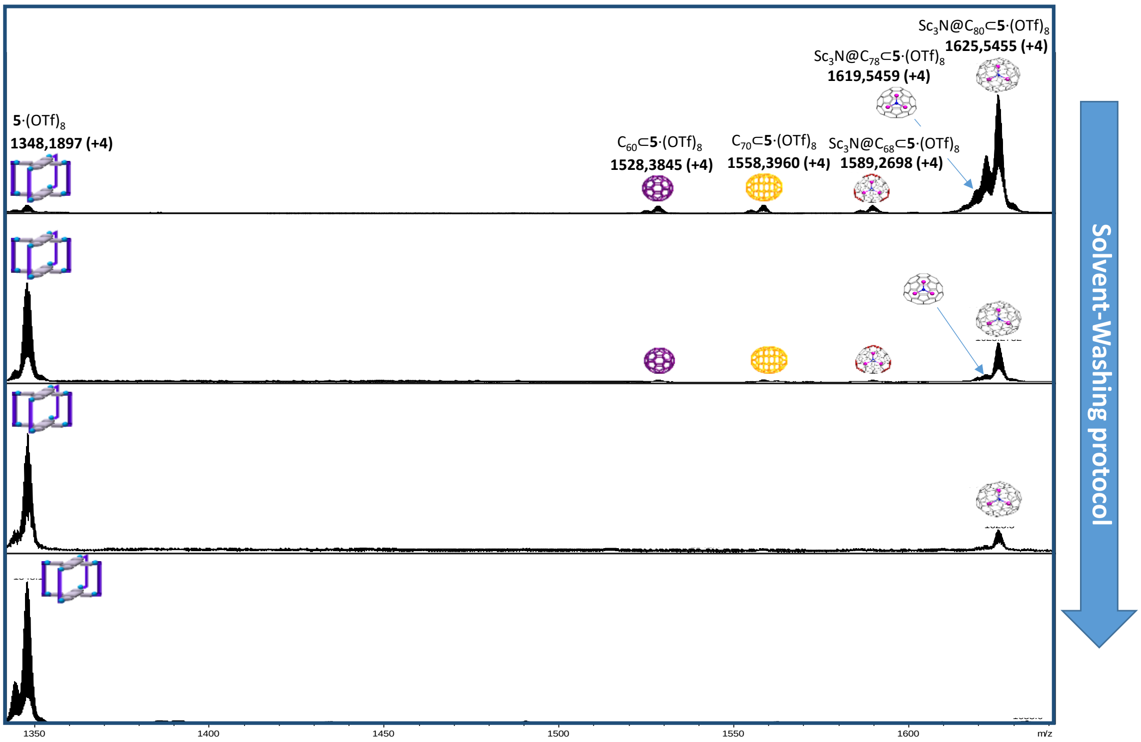

Figure S14. Positive ion mode MALDI spectra of a) Sc-based crude soot and b) purified fraction of $Sc_3N@C_{80}$.

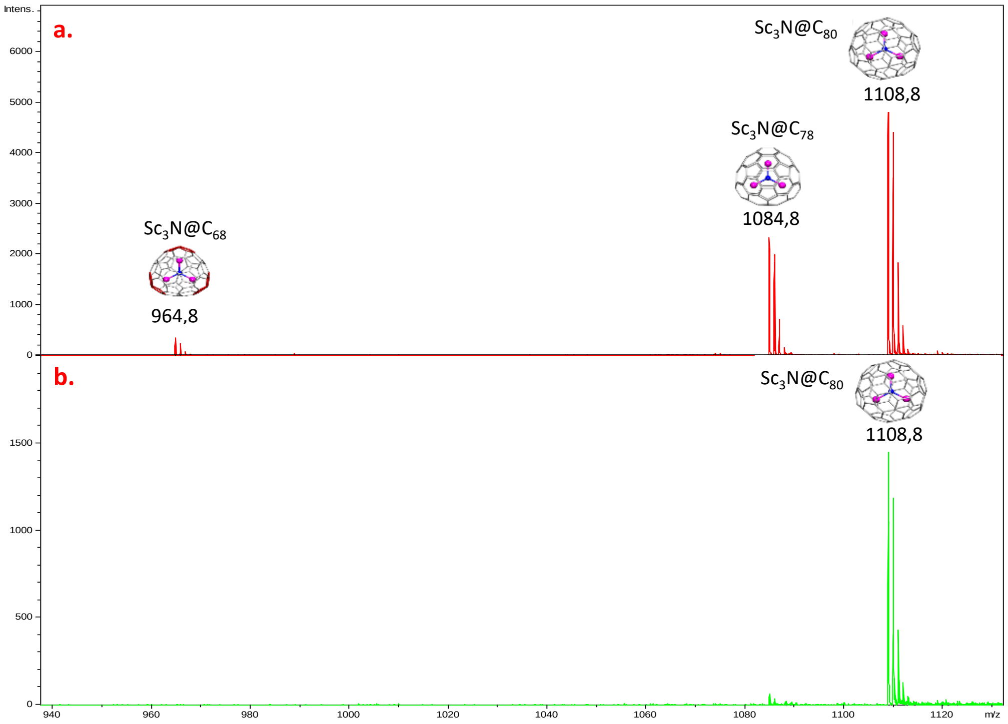

Figure S15. HRMS spectrum of recovered 5·(OTf)$_8$ nanocapsule after applying the washing protocol for the liberation of the species entrapped during the purification protocol. Experimental conditions: 100µM in acetonitrile, registered with a Bruker Micro TOF-Q-II exact mass spectrometer.

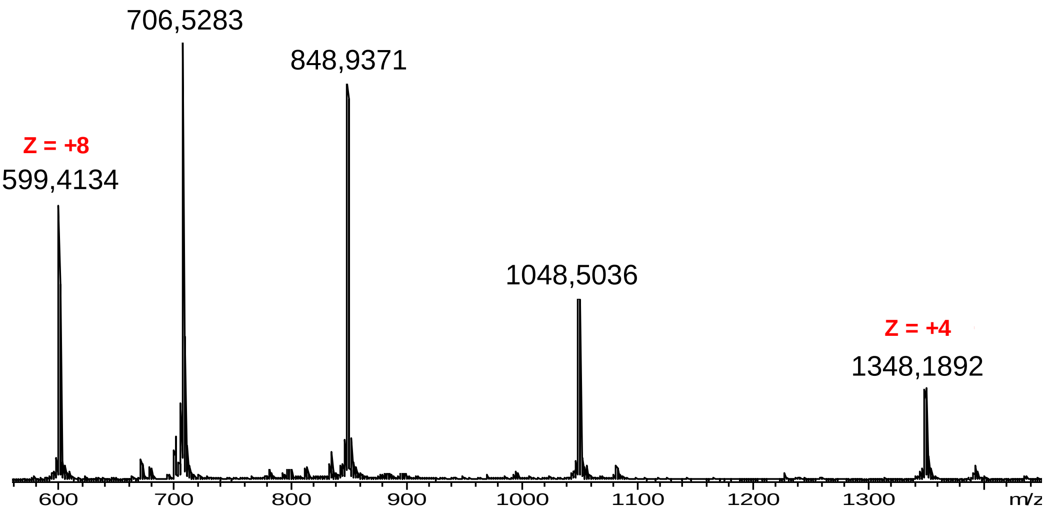

Figure S16. HPLC analysis of the remaining supernatant during the purification of the Sc_3N-based crude soot at long reaction time. Experimental conditions: $1.8 \cdot 10^{-4}$ M in toluene; concentration assuming that all the species are $Sc_3N@C_{80}$.

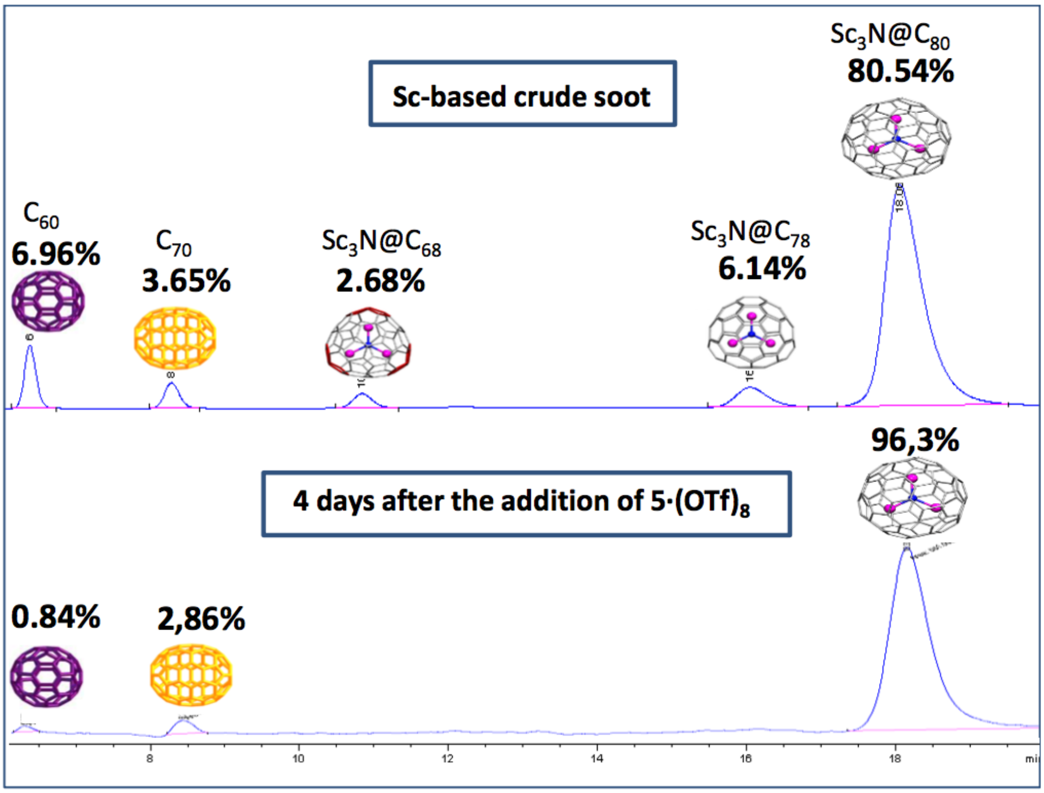

6. Supplementary references

1. García-Simón, C.; Garcia-Borràs, M.; Gómez, L.; Parella, T.; Osuna, S.; Juanhuix, J.; Imaz, I.; Maspoch, D.; Costas, M.; Ribas, X., *Nat. Commun.* **2014,** *5*, 5557.

2. Stevenson, S.; Rice, G.; Glass, T.; Harich, K.; Cromer, F.; Jordan, M. R.; Craft, J.; Hadju, E.; Bible, R.; Olmstead, M. M.; Maitra, K.; Fisher, A. J.; Balch, A. L.; Dorn, H. C., *Nature* **1999,** *401* (6748), 55-57.

Supporting Information Chapter V

Purification of Uranium-based Endohedral Metallofullerenes (EMFs) by Selective Supramolecular Encapsulation and Release

Table of Contents

1. Material and instrumentation.

Reagents and solvents used were commercially available reagent quality unless indicated otherwise. Dinuclear Cu^{II}-based macrocyclic synthon (**[Cu-1b](CF_3SO_3)$_4$**) and nanocapsule **1·(OTf)$_8$** were synthesized according to published procedures.[1] The carbon soot containing uranium EMFs were synthesized by the direct-current arc discharge method. The graphite rods, packed with U_3O_8/Sc_2O_3 powders and graphite powders (0.0103:0.0079:1 molar ratio), were vaporized in the arcing chamber under 20 Torr Hydrogen and 200 Torr Helium atmosphere. The resulting soot was refluxed in CS_2 for 6h. Laser desorption/ionization time-of-flight (LDI-TOF) mass spectrometry was conducted on a Bruker Microflex LRF mass spectrometer. ESI-MS experiments were collected and analyzed on a Bruker MicroTOF-Q-II, using acetonitrile as the mobile phase. Vis-NIR spectra were obtained with a Cary 5000 UV-Vis-NIR spectrophotometer in CS_2. HPLC data concerning EMFs purity were collected on Varian Prostar instrument equipped with Buckyprep column (10 mm × 250 mm, Cosmosil Nacalai Tesque) monitored using a UV detector at 320nm. Toluene as mobile phase (1 mL/min flow). The liberation of entrapped fullerenes and endohedral metallofullerenes from **1·(BArF)$_8$** was achieved following a reported procedure,[1-2] consisting in charging the filled nanocapsule in a column and applying consecutive washings with 1,2-dichlorobenzene/CS_2 (1/1 v/v mixture).

2. Compound synthesis and characterization

Synthesis and characterization of 1·(BArF)$_8$ nanocapsule. 20 mg of previously reported nanocapsule **1·(OTf)$_8$** (3.28 µmols)[1] were suspended in 12 ml of dichloromethane in the presence of 10 equivalents of NaBArF. The reaction mixture was stirred at room temperature for 16h. After the reaction time, the solution obtained was filtered through an Olimpeak disc and recrystallized by slow diethyl ether diffusion. **1·(BArF)$_8$** nanocapsule was obtained as dark purple crystals (Yield: 78%). The high resolution mass spectrometry (HRMS) spectrum of **1·(BArF)$_8$** showed exclusively ions corresponding to the cage with consecutive loss of counteranions, demonstrating its integrity in solution (**Fig. S1**).

HRMS m/z:

[{1·(BArF)$_4$}$^{+4}$]: calculated 2062.192 and found 2062.192

[{1·(BArF)$_3$}$^{+5}$]: calculated 1477.140 and found 1477.140

[{1·(BArF)$_2$}$^{+6}$]: calculated 1087.105 and found 1087.105

[{1·(BArF)$_1$}$^{+7}$]: calculated 808.494 and found 808.495

[{1·(BArF)$_0$}$^{+8}$]: calculated 599.434 and found 599.434

Nanocapsule **1·(BArF)$_8$** was spectroscopically characterized by **FT-IR-ATR** (Fig. S2) and **UV-vis** (Fig. S3) spectroscopy. The most distinctive features of the respective IR spectra are four bands at 1608, 1352, 1272 and 1114 cm^{-1}. The 1352, 1272 and 1114 cm^{-1} bands are assigned to BArF$^-$ counteranion and the band at 1603 cm^{-1} is assigned to ν_{as} C=O stretching mode of the carboxylates groups of the porphyrin units of **1·(BArF)$_8$**.

UV-vis characterization (Agilent UV-vis 8453): Soret band: 422 nm (ε= 1445200 M^{-1}·cm^{-1}); Q bands: 562 nm (ε=62800 M^{-1}·cm^{-1}) and 606 nm (ε=39726 M^{-1}·cm^{-1})

3. Purification of EMFs and characterization of Host-Guest adducts

Purification of $U_2@C_{80}$ using 1·(BArF)$_8$ in the solid phase and characterization of $U_2@C_{80}\subset$1·(BArF)$_8$: 0.25 mg of nanocapsule **1·(BArF)$_8$** (0.021 µmols) in the solid phase are added to a toluene solution of the soot extract. The suspension is stirred at room temperature for 6h. Aliquots of the supernatant are filtered, and analyzed by LDI-TOF at different times (Fig. S4). The HRMS spectrum of the host-guest adducts formed show ions corresponding to the **$U_2@C_{80}\subset$1·(BArF)$_8$** complex with consecutive loss of counteranions (Fig. S5).

HRMS m/z:

[{$U_2@C_{80}\subset$1·(BArF)$_4$}$^{+4}$]: calculated 2421.217 and found 2421.217

[{$U_2@C_{80}\subset$1·(BArF)$_3$}$^{+5}$]: calculated 1764.360 and found 1764.360

[{$U_2@C_{80}\subset$1·(BArF)$_2$}$^{+6}$]: calculated 1326.455 and found 1326.455

[{$U_2@C_{80}\subset$1·(BArF)$_1$}$^{+7}$]: calculated 1013.651 and found 1013.651

[{$U_2@C_{80}\subset$1·(BArF)$_0$}$^{+8}$]: calculated 778.946 and found 778.946

Purification of $Sc_2CU@C_{80}$ using 1·(BArF)$_8$ in the solid phase and characterization of $Sc_2CU@C_{80}\subset$1·(BArF)$_8$: 0.10 mg of nanocapsule **1·(BArF)$_8$** (0.008 µmols) in the solid phase are added to a toluene solution of the remaining soot extract (after the complete removal of $U_2@C_{80}$). The suspension is stirred at room temperature during 1.5h. Aliquots of the supernatant are filtered, and analyzed by LDITOF at different times (Fig. S6). The HRMS spectrum of the host-guest adducts formed show ions corresponding to the $Sc_2CU@C_{80}$ $\subset$**1·(BArF)$_8$** complex with consecutive loss of counteranions (Fig. S7).

HRMS m/z:

[{$Sc_2CU@C_{80}\subset$**1**·(BArF)$_4$}$^{+4}$]: calculated 2387.182 and found 2387.182

[{$Sc_2CU@C_{80}\subset$**1**·(BArF)$_3$}$^{+5}$]: calculated 1737.132 and found 1737.132

[{$Sc_2CU@C_{80}\subset$**1**·(BArF)$_2$}$^{+6}$]: calculated 1303.765 and found 1303.765

[{$Sc_2CU@C_{80}\subset$**1**·(BArF)$_1$}$^{+7}$]: calculated 994.203 and found 994.203

[{$Sc_2CU@C_{80}\subset$**1**·(BArF)$_0$}$^{+8}$]: calculated 761.929 and found 761.930

Purification of an equimolar mixture of $Sc_3N@C_{80}$ and $U_2@C_{80}$ using 1·(BArF)$_8$ in the solid phase: 0.2 mg of pure $Sc_3N@C_{80}$ (0.18 µmols, 1 equivalent) and 0.26 mg of pure $U_2@C_{80}$ (0.18 µmols, 1 equivalent) are dissolved in 5 ml of toluene. Then 2.1 mg of **1·(BArF)$_8$** (0.18 µmols, 1 equivalent) in the solid phase are added to an equimolar mixture of $Sc_3N@C_{80}$:$U_2@C_{80}$ in toluene. The suspension is stirred at room temperature for 5h. Aliquots of the supernatant are filtered, and analyzed by LDI-TOF at different times (Figure 4, main text).

Purification of an equimolar mixture of $Sc_3N@C_{80}$ and $Sc_2CU@C_{80}$ using 1·(BArF)$_8$ in the solid phase: 0.1 mg of pure $Sc_3N@C_{80}$ (0.09 µmols, 1 equivalent) and 0.12 mg of pure $Sc_2CU@C_{80}$ (0.09 µmols, 1 equivalent) are dissolved in 5 ml of toluene. Then 1.1 mg of **1·(BArF)$_8$** (0.09 µmols, 1 equivalent) in the solid phase are added to an equimolar mixture of $Sc_3N@C_{80}$: $Sc_2CU@C_{80}$ in toluene. The suspension is stirred at room temperature for 3h. Aliquots of the supernatant are filtered, and analyzed by LDI-TOF at different times (Figure 5, main text).

4. Computational details

All optimizations were carried out with the ADF 2017 package[3] using BLYP exchange-correlation functional.[4] To describe valence electron we employed Slater triple-zeta polarization (TZP) basis sets whereas frozen cores were described by means of single Slater functions, consisting of the 1s shell for C and N, the 1s to 5d shells for U. Scalar relativistic corrections were included by means of the ZORA formalism. Dispersion corrections by Grimme were also included.[5]

Optimization of the whole system, endohedral metallofullerene + nanocapsule, is computationally expensive and very challenging because of the large size and flexibility of the system. Therefore, we used in the calculations a simplified model of the nanocapsule made by two 5,10,15,20-tetrakis(4-carboxyphenil)-porphyrin-Zn(II) (ZnTPP) molecules, as shown in green in Figure S11. Constraints on the phenyls were incorporated during the optimization to keep them at 90º with respect to the porphyrins.

Full set of xyz data for all compounds studied is deposited in the ioChem-BD repository[6] and can be accessed via https://doi.org/10.19061/iochem-bd-2-26.

5. X-ray Diffraction Spectroscopy details

Crystallographic data was collected at the XALOC beamline of the ALBA synchrotron at 100 K using a MD2M single axis diffractometer (Maatel, France) and a Pilatus 6M detector (Dectris, Switzerland).[7] Due to their sensitivity to solvent loss, crystals were mounted in thin glass capillaries and cryopreserved at 100 K. Single crystals were introduced into the capillary suspended in a small volume of the solution in which the crystals were grown (diethyl ether/DCM). The data sets were collected at $\lambda = 0.82656$ Å. The quality of the collected data was severely limited by the stability of the obtained single crystals, and the intrinsic disorder inherent to this class of porous compounds.

For the best dataset, reflections were observed up to a maximum resolution of 1.15 Å, and any data beyond this value was discarded after integration due to the low $I/\sigma(I)$ values (<2). Integration and scale were performed with the Mosflm program included in the CCP4 software package.[8] An initial structure solution was found with the use of the charge flipping method by using *superflip* program.[9] The generated electron density maps were visualized with the Chimera software.[10] According to superflip, the generated electron density maps were found to have symmetry corresponding to the $P2_1/c$ space group, which was consistent with the observed reflection conditions. The position of the metal atoms and part of the atoms of the organic linkers were clearly identified in the initial solution. The crystal structure was refined with the use of XL and OLEX2 program,[11] following a full matrix least square refinement. The rest of the atoms belonging to the organic ligands were located in the difference Fourier maps. The metal and the porphyrin ligand atoms were anisotropically refined with the use of soft restrains, while the atoms for the Cu(II) macrocycle were maintained isotropic, since anisotropic refinement was proved to be impractical due to the large displacement parameters of these atoms arising from structural disorder. Upon location of the atoms belonging to the molecular cages, a solvent mask was subsequently applied to complete the refinement. The results of the solvent masking procedure indicate presence of a large amount of residual electron density occupying the accessible void space in the fraction of unit cell left by the packing of the cages (75.9% accessible volume), which are attributed to the sixteen tetrakis[3,5-bis(trifluoromethyl)phenyl]borate counter-anions, and crystallization solvent molecules that could not be located from the electron density maps.

6. Supplementary Figures:

Figure S1. HRMS spectrum of **1·(BArF)$_8$**. Simulated spectra of selected peaks are showed in orange. Experimental conditions: 100 µM in acetonitrile, registered with a Bruker Micro TOF-Q-II exact mass spectrometer.

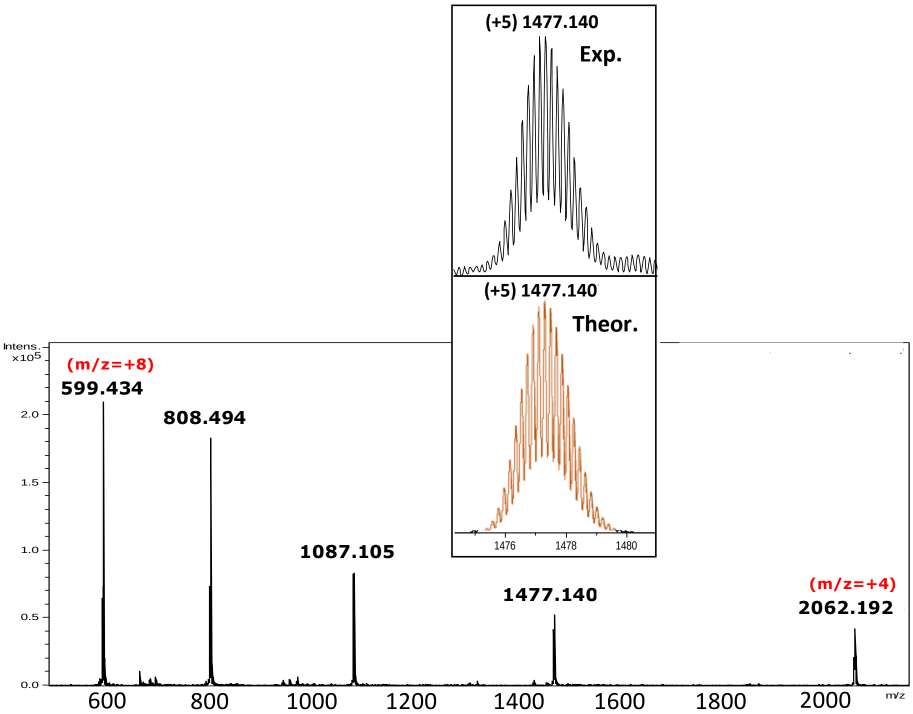

Figure S2. FT-IR-ATR of nanocapsule **1·(BArF)$_8$**

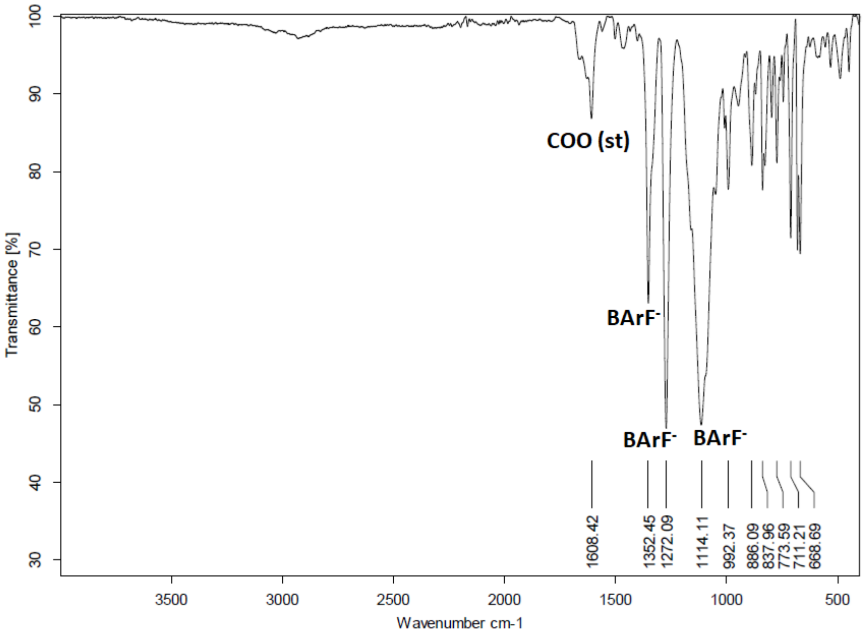

Figure S3. UV-Vis spectrum of nanocapsule **1·(BArF)$_8$** (6.55·10^{-7} M solution in acetonitrile).

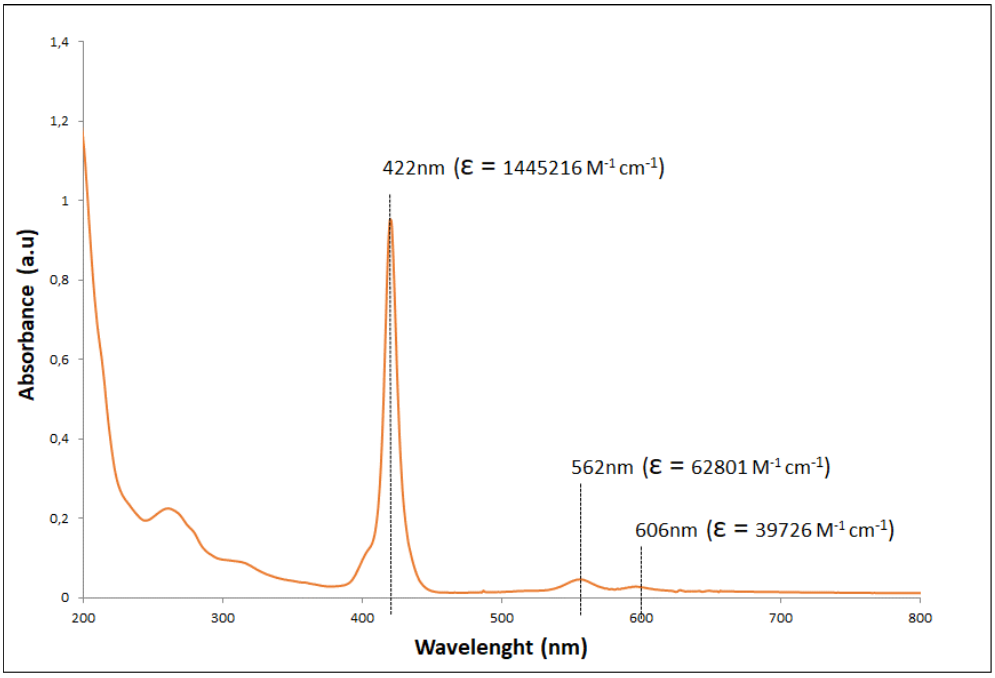

Figure S4. Ortep view of the crystallographic characterization of $\mathbf{1}^{8+}$ (CCDC 1845202)

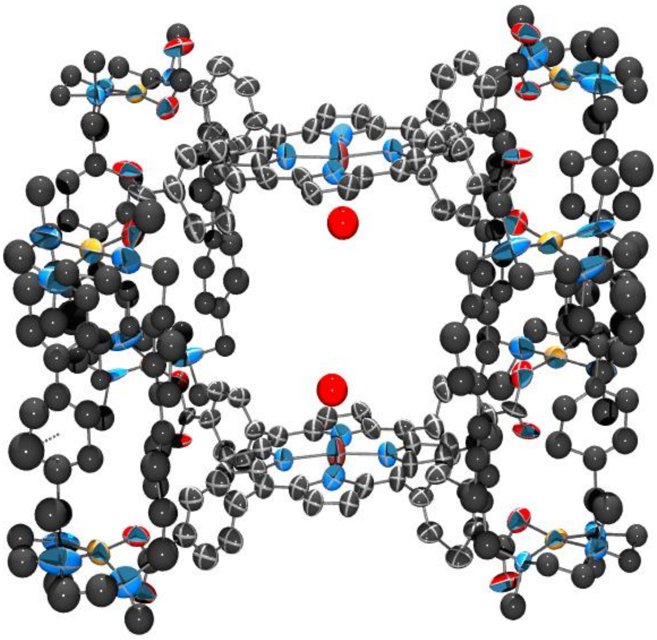

Figure S5. Positive-ion mode LDI-TOF mass spectrum monitorization of the remaining Sc/U soot extract solution in toluene, during the selective complexation of $U_2@C_{80}$ within crystals of **1·(BArF)$_8$**. Registered with a Bruker Microflex LRF mass spectrometer.

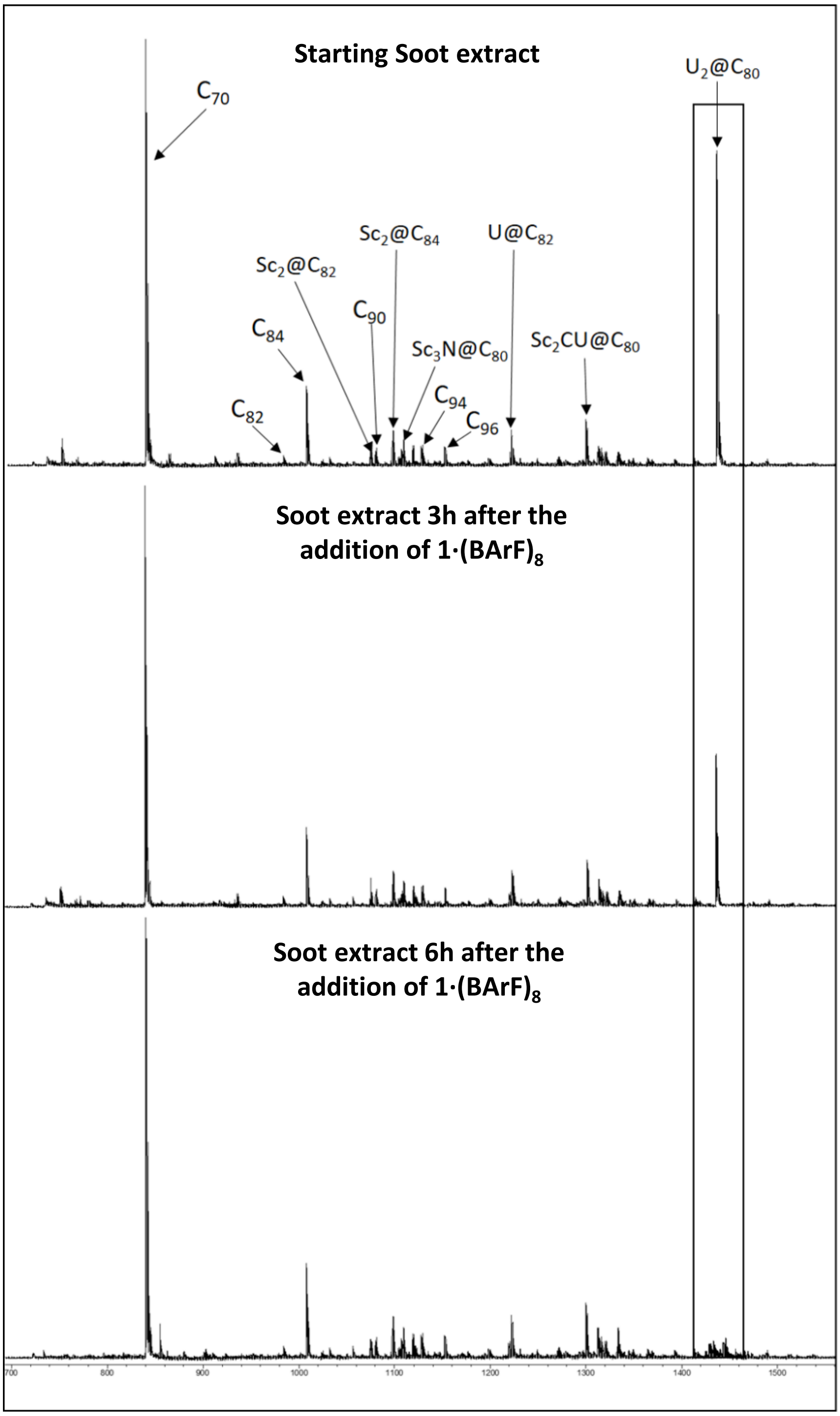

Starting Soot extract

Soot extract 3h after the addition of 1·(BArF)$_8$

Soot extract 6h after the addition of 1·(BArF)$_8$

Figure S6. HRMS spectrum of $U_2@C_{80}\subset$**1·(BArF)$_8$** selectively formed soaking crystals of **1·(BArF)$_8$** in Sc/U soot extract solution in toluene**.** Simulated spectra of selected peaks are showed in orange. Experimental conditions: 100µM in acetonitrile, registered with a Bruker Micro TOF-Q-II exact mass spectrometer.

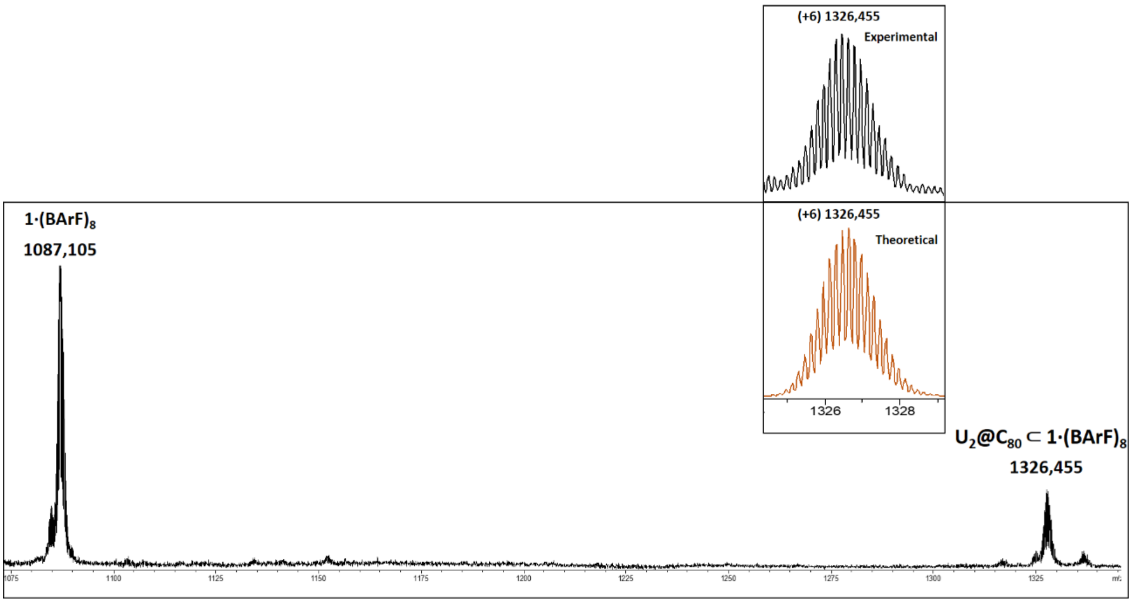

Figure S7. Positive-ion mode LDI-TOF mass spectrum monitorization of the remaining Sc/U soot extract solution in toluene, during the selective complexation of $Sc_2CU@C_{80}$ within crystals of **1·(BArF)$_8$** . Registered with a Bruker Microflex LRF mass spectrometer.

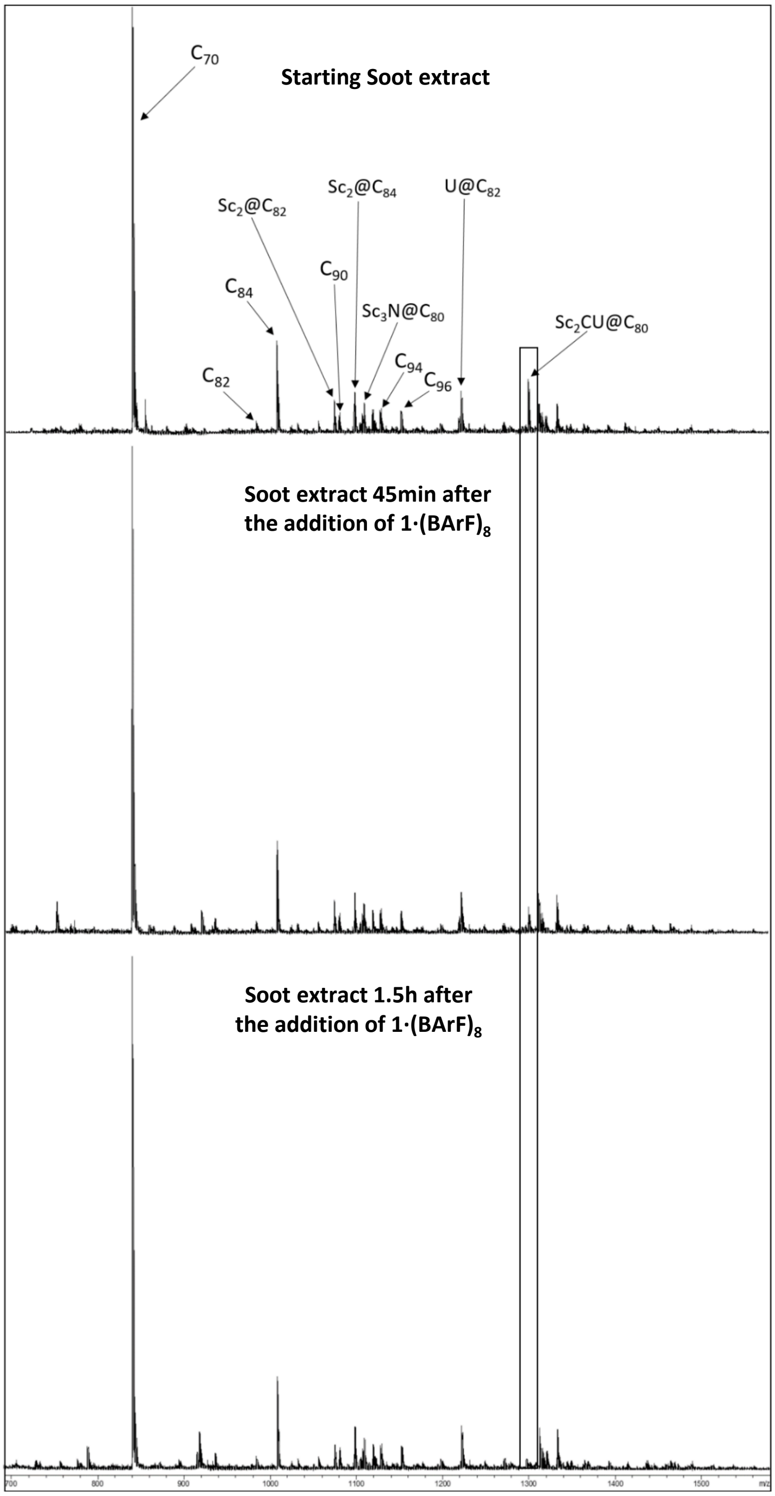

Figure S8. HRMS spectrum of $Sc_2CU@C_{80} \subset$ **1·(BArF)$_8$** selectively formed soaking crystals of **1·(BArF)$_8$** in Sc/U soot extract solution in toluene (after the complete removal of $U_2@C_{80}$). Simulated spectra of selected peaks are showed in red. Experimental conditions: 100µM in acetonitrile, registered with a Bruker Micro TOF-Q-II exact mass spectrometer.

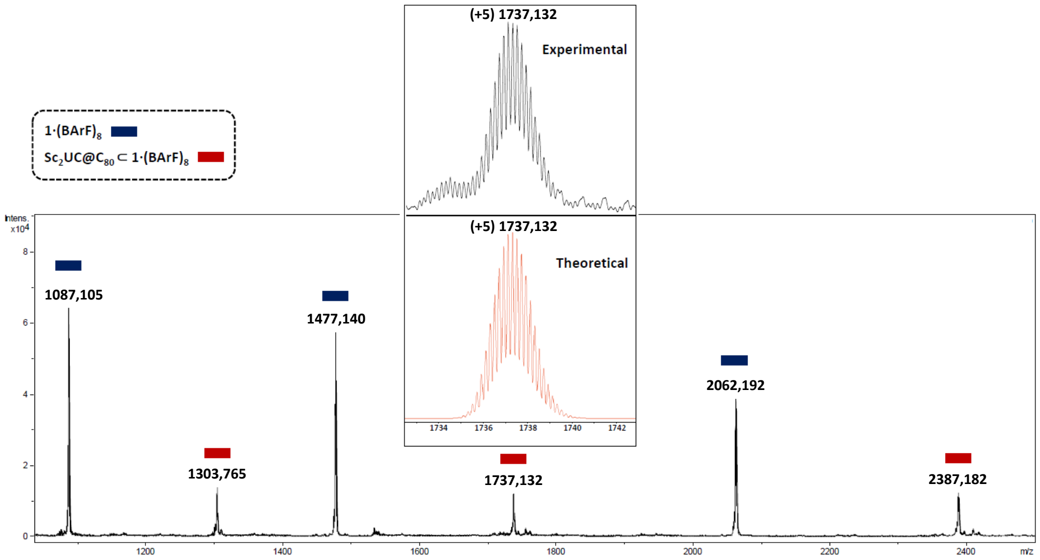

Figure S9. Positive-ion mode LDI-TOF mass spectrum and HPLC chromatogram of a) $Sc_2CU@C_{80}$ purified using **1·(BArF)$_8$** and b) enriched fraction of $Sc_2CU@C_{80}$ obtained after 3 HPLC steps (bottom). LDI-TOF registered with a Bruker Microflex LRF mass spectrometer and HPLC chromatogram using Cosmosil Buckyprep column; Flow rate: 1ml/min; toluene as a mobile phase. (*) Solvent peak

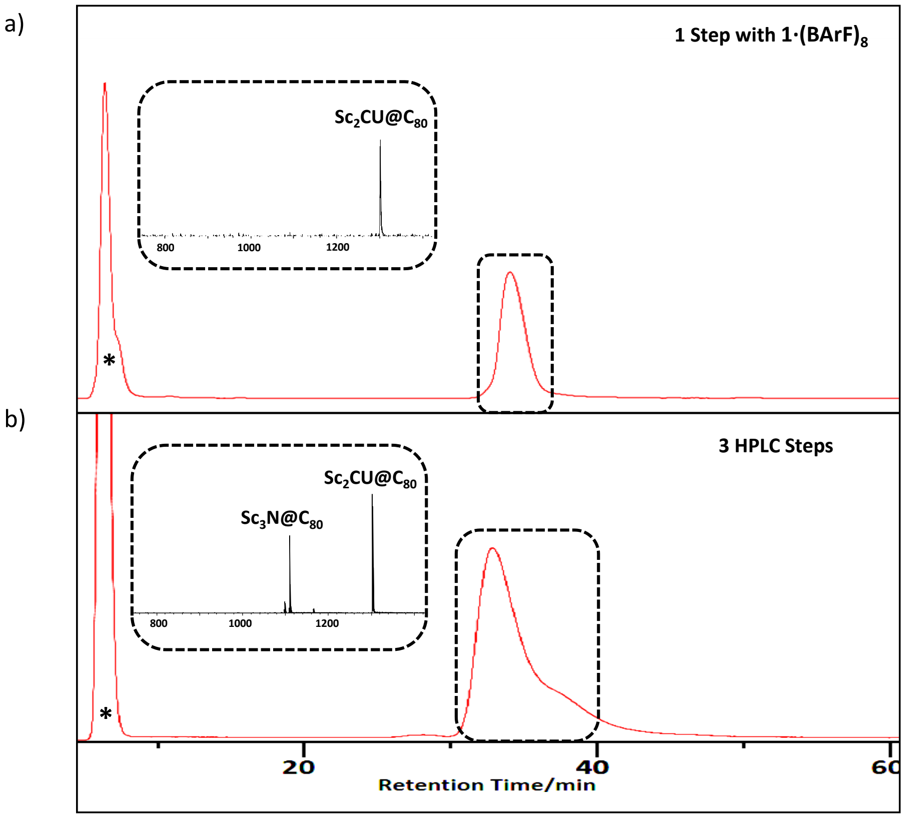

Figure S10. UV-vis-NIR absorption spectrum of $Sc_2CU@C_{80}$ in CS_2. Registered with a Cary 5000 UV-Vis-NIR spectrophotometer at 320 nm.

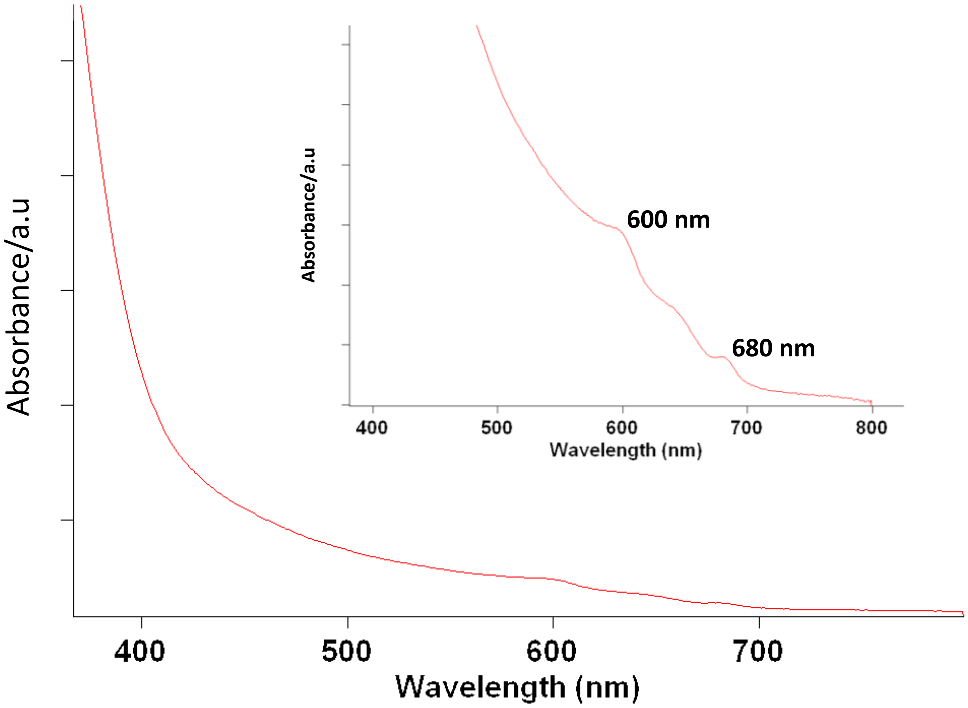

Figure S11. a) 3D representation of nanocapsule without BArF$^-$ ions. The two porphyrin fragments used in DFT calculations are highlighted in green; b) molecular scheme of zinc tetraphenylporphyrin (ZnTPP) molecule used in the DFT calculations.

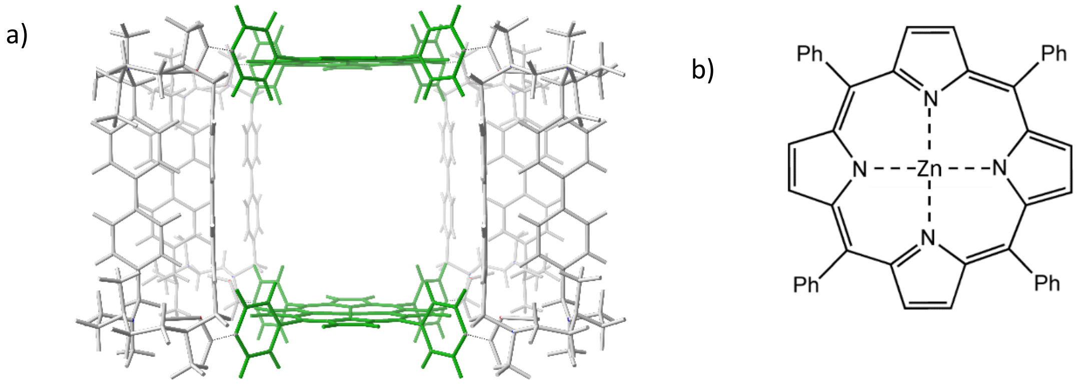

Figure S12. Molecular orbitals that describe the unpaired electrons in U (SOMO and SOMO-1) and the bonding in the internal Sc_2CU cluster in $Sc_2CU@C_{80}$.

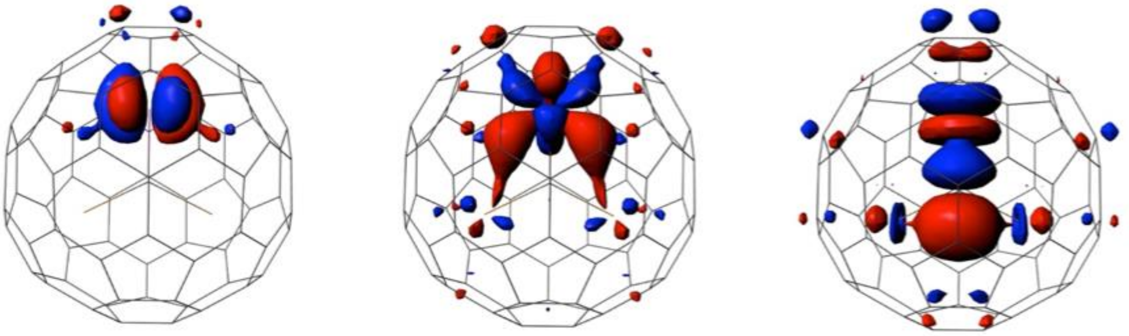

SOMO SOMO-1 σ U-C bond

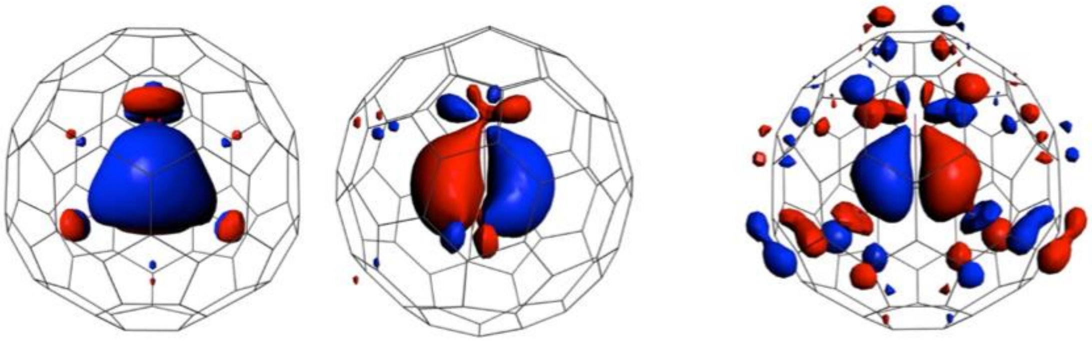

π U-C bond (two views) σ Sc-C bond

Figure S13. Two views of four optimized structures for $U_2@C_{80}$ interacting with two porphyrins.

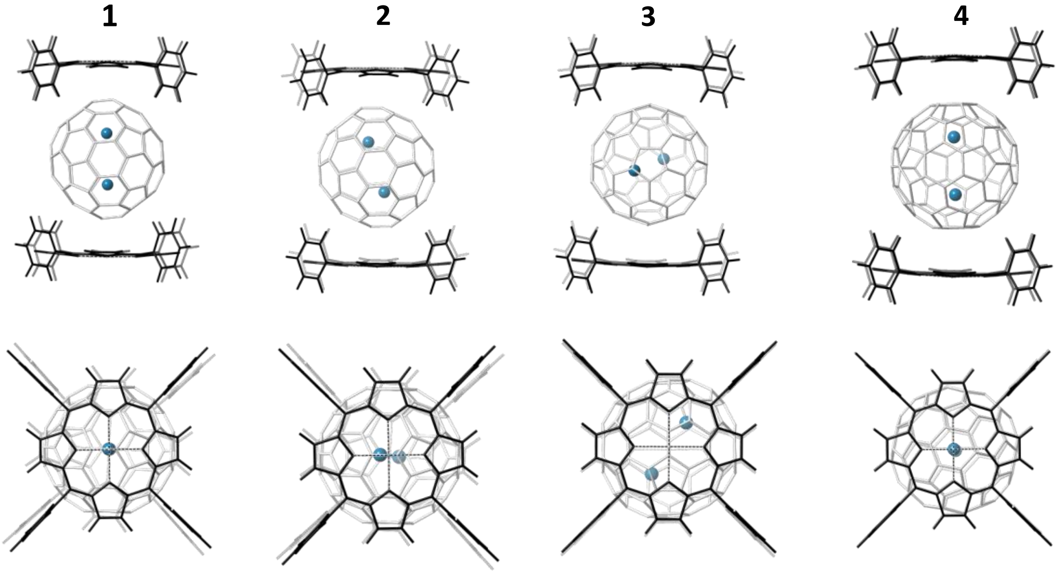

Zn-Zn (Å)	13.95	13.92	13.82	14.26
BE (kcal mol^{-1})	-58.9	-58.3	-57.6	-52.4

Figure S14. Representation of the a) Bader atomic charges computed for U_2@C_{80} (left) and Sc_3N@C_{80} (right); b) Electron density distribution for U_2@C_{80} (left) and Sc_3N@C_{80} (right) among pentagons, which are colored according to their charge (red more charged and green less charged). Bader charges for colored pentagons are also given.

a)

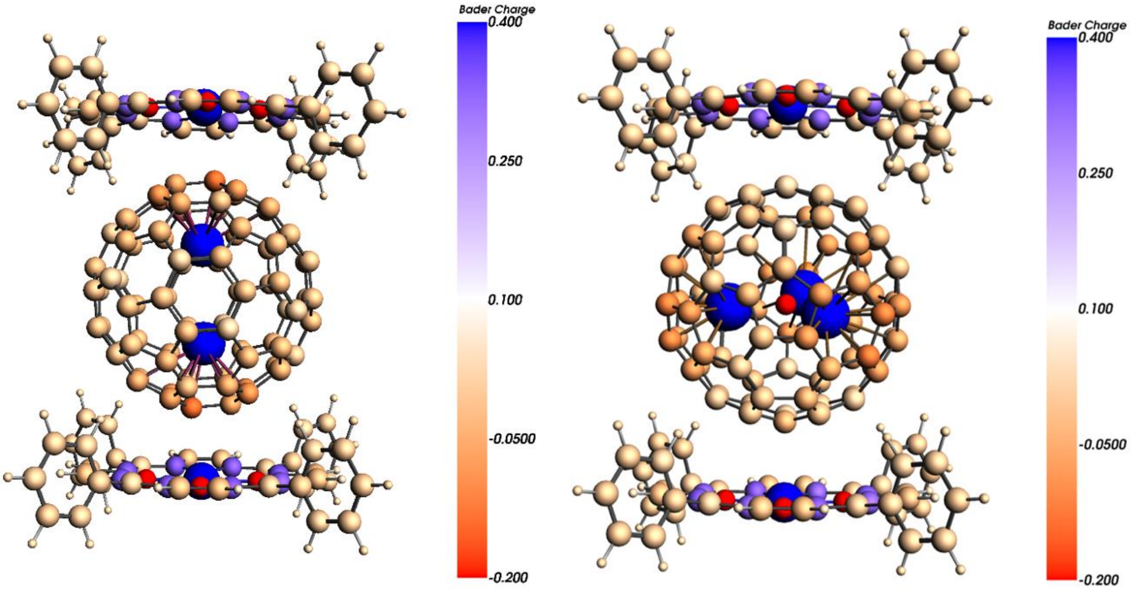

b)

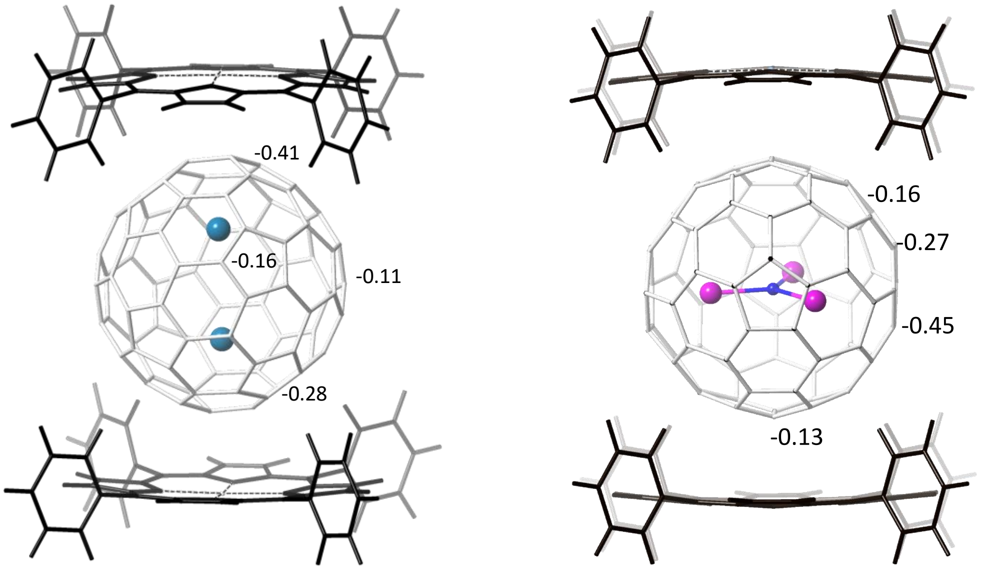

Figure S15. Two views of three optimized structures for $Sc_3N@C_{80}$ interacting with two porphyrins

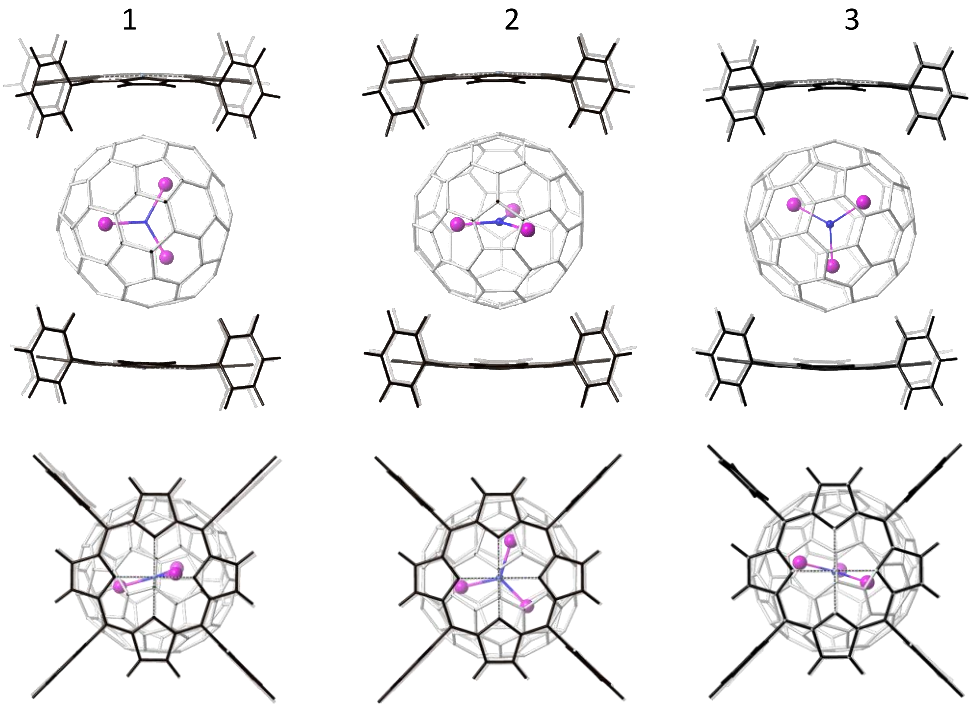

Zn-Zn (Å)	13.86	13.85	13.88
B_E kcal mol^{-1}	-56.9	-57.2	-56.4

Figure S16. Three optimized structures for C_{70} interacting with two porphyrins.

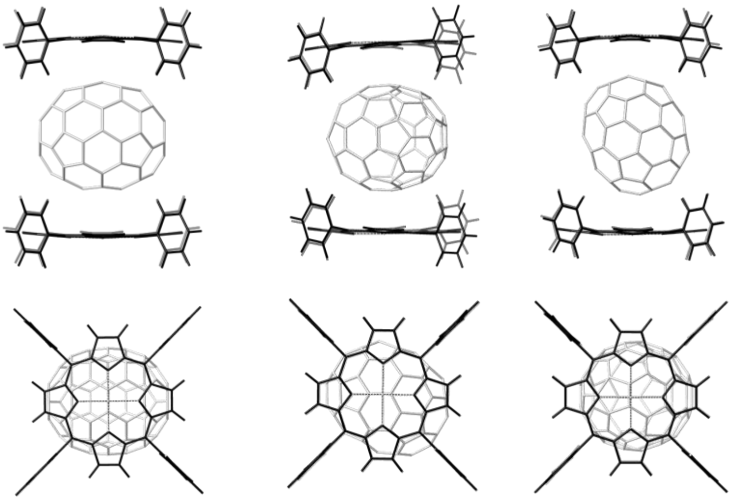

Zn-Zn (Å)	13.02	12.88	13.88
BE (kcal mol^{-1})	-48.0	-48.7	-43.1

Figure S17. Optimal structures computed for four fullerenes interacting with two porphyrins.

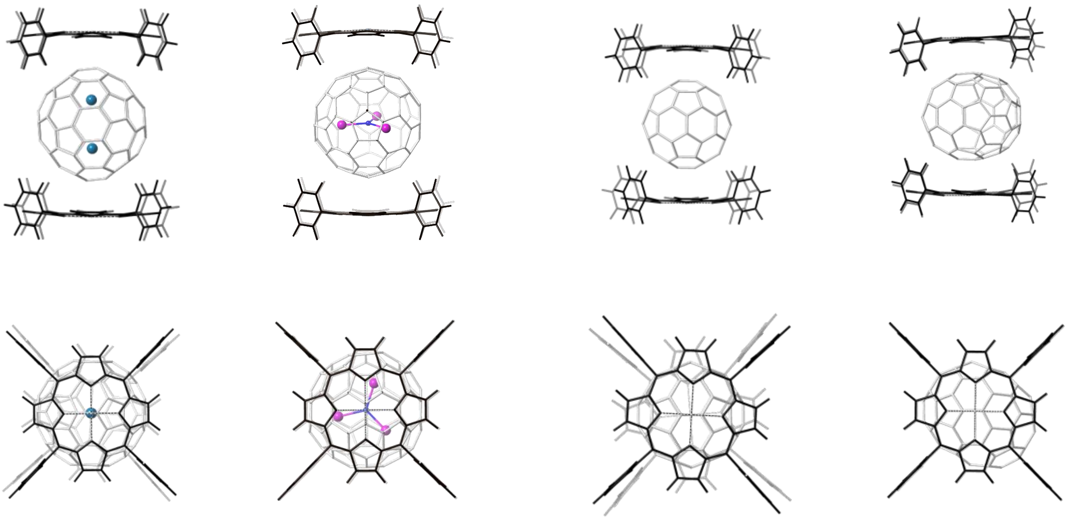

	$U_2@C_{80}$ porph$_2$	$Sc_3N@C_{80}$ porph$_2$	C_{60} porph$_2$	C_{70} porph$_2$
Zn-Zn (Å)	13.95	13.85	12.62	12.88
BE (kcal mol^{-1})	-58.9	-57.2	-51.5	-48.7

7. Supplementary Tables:

Table S1. Crystal data and structure refinement for **1**$^{8+}$ (CCDC 1845202).

Empirical formula	$C_{526}Cu_{16}N_{64}O_{40}Zn_4$
Formula weight	9132.02
Temperature/K	100.(2)
Crystal system	monoclinic
Space group	$P2_1/c$
a/Å	45.200(7)
b/Å	45.530(9)
c/Å	34.840(9)
α/°	90
β/°	92.22(3)
γ/°	90
Volume/Å^3	71645(26)
Z	2
ρ_{calc}/ g/cm^3	0.423
μ/mm^{-1}	0.482
F(000)	9016.0
Crystal size/mm^3	0.4 × 0.4 × 0.3
X-ray wavelength/ Å	λ = 0.8265(6)
2Θ range for data collection/°	1.712 to 43.998
Index ranges	$0 \le h \le 40$, $-41 \le k \le 41$, $-31 \le l \le 31$
Reflections collected	53931
Independent reflections	53931 [R_{int} = 0.170, R_{sigma} = 0.1268]
Data/restraints/parameters	53931/622/2046
Goodness-of-fit on F^2	1.357
Final R indexes [I>=2σ (I)]	R_1 = 0.1580, wR_2 = 0.4157
Final R indexes [all data]	R_1 = 0.1871, wR_2 = 0.4385

Table S2. Computed U-C distances (in Å) for endohedral metallofullerene $Sc_2CU@C_{80}$, uranium methylidene $H_2C=UHF$ and uranium methylidyne $HC\equiv UF_3$ at BLYP/TZP(D3) level. Ball and stick representations are also included (U in pink, Sc in orange, C in dark grey, F in green and H in white).

	$Sc_2CU@C_{80}$ 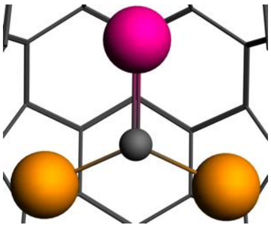	$H_2C=UHF$ 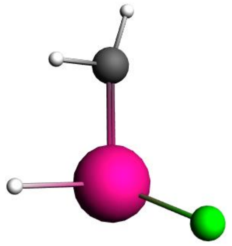	$HC\equiv UF_3$ 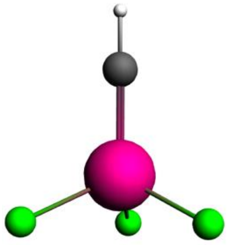
U-C (Å)	2.070	2.113	1.952

Table S3. Binding energies between fullerene and two porphyrins.

	C_{60}	C_{70}	$Sc_3N@I_h$-C_{80}	$U_2@I_h$-C_{80}
BE [a)]	-51.5	-48.7	-57.2	-58.9
d(Zn···Zn)[b)]	12.6	12.9	13.8	13.9

[a)] Binding energies computed at the BLYP/TZP(D3) level are given in kcal·mol^{-1}; Zn···Zn separations are in Å. For the optimal orientation of the fullerenes see Figures 7 and S17. Computed structures are given in the SI and a data set collection of computational results is available in the ioChem-BD repository[6] and can be accessed via https://doi.org/10.19061/iochem-bd-2-26.

8. Supplementary References

[1] C. Fuertes-Espinosa, C. García-Simón, E. Castro, M. Costas, L. Echegoyen and X. Ribas, *Chem. Eur. J.* **2017**, *23*, 3553-3557.

[2] C. García-Simón, M. Garcia-Borràs, L. Gómez, T. Parella, S. Osuna, J. Juanhuix, I. Imaz, D. Maspoch, M. Costas and X. Ribas, *Nat. Commun.* **2014**, *5*, 5557.

[3] G. te Velde, F. M. Bickelhaupt, E. J. Baerends, C. Fonseca Guerra, S. J. A. Van Gisbergen, J. G. Snijders and T. Ziegler, *J. Comput. Chem.* **2001**, *22*, 931-967.

[4] a) A. *D.* Becke, *Phys. Rev. A* **1988**, *38*, 3098-3100; b) C. Lee, W. Yang and R. G. Parr, *Phys. Rev. B* **1988**, *37*, 785-789.

[5] S. Grimme, S. Ehrlich and L. Goerigk, *J. Comput. Chem.* **2011**, *32*, 1456-1465.

[6] M. Álvarez-Moreno, C. de Graaf, N. López, F. Maseras, J. M. Poblet and C. Bo, *J. Chem. Inf. Model.* **2015**, *55*, 95-103.

[7] J. Juanhuix, F. Gil-Ortiz, G. Cuni, C. Colldelram, J. Nicolas, J. Lidon, E. Boter, C. Ruget, S. Ferrer and J. Benach, *J. Synchrotron Rad.* **2014**, *21*, 679-689.

[8] M. D. Winn, C. C. Ballard, K. D. Cowtan, E. J. Dodson, P. Emsley, P. R. Evans, R. M. Keegan, E. B. Krissinel, A. G. W. Leslie, A. McCoy, S. J. McNicholas, G. N. Murshudov, N. S. Pannu, E. A. Potterton, H. R. Powell, R. J. Read, A. Vagin and K. S. Wilson, *Acta Cryst. D* **2011**, *67*, 235-242.

[9] L. Palatinus and G. Chapuis, *J. Appl. Cryst.* **2007**, *40*, 786-790.

[10] E. F. Pettersen, T. D. Goddard, C. C. Huang, G. S. Couch, D. M. Greenblatt, E. C. Meng and T. E. Ferrin, *J. Comput. Chem.* **2004**, *25*, 1605-1612.

[11] O. V. Dolomanov, L. J. Bourhis, R. J. Gildea, J. A. K. Howard and H. Puschmann, *J. Appl. Cryst.* **2009**, *42*, 339-341.

Supporting Information Chapter VI

Highly selective encapsulation and purification of U-based C_{78}-EMFs within a supramolecular nanocapsule

Table of Contents

1. Material and instrumentation.

Reagents and solvents used were commercially available reagent quality unless indicated otherwise. Tetragonal prismatic nanocapsule **1·(BArF)$_8$** was synthesized according to published procedures.[1] All soot containing uranium EMFs were synthesized in an electrical arc discharge reactor using a Krätschmer–Huffman type apparatus. For soot containing Sc species of endohedrals, hollow graphite rods were packed with a 0.0103:0.0079:1 molar ratio of uranium oxide (U_3O_8) / scandium oxide (Sc_2O_3) and graphite powder mixture. Packed graphite rods were vaporized in an arc plasma under a partial He and H_2 atmosphere (200 torr and 20 torr respectively). Scandium free endohedral soot was produced using hollow graphite rods packed with a 0.0095:1 molar ratio of uranium oxide (U_3O_8) / graphite powder mixture vaporized in arc plasma under a partial He and NH_3 atmosphere (200 torr and 30 torr respectively). Endohedral species were extracted from the resulting carbon soot using CS_2 in a Soxhlet extractor under reflux for 4-6hrs. Laser desorption/ionization time-of-flight (LDI-TOF) mass spectrometry was conducted on a Bruker Microflex LRF mass spectrometer. ESI-MS experiments were collected and analyzed on a Bruker MicroTOF-Q-II, using acetonitrile as the mobile phase.

The liberation of entrapped fullerenes and endohedral metallofullerenes from **1·(BArF)$_8$** was achieved following a reported procedure,[1] consisting in charging the filled nanocapsule in a column and applying consecutive washings with 1,2-dichlorobenzene/CS2 (1/1 v/v mixture).

2. Selective molecular recognition of U-based EMFs and Host-Guest adduct characterization:

The amount of a given EMF present in a soot sample cannot be precisely quantified, because they are produced as a mixture of compounds. In order to have an approximate idea of the amount of nanocapsule needed for the quantitative encapsulation of the desired EMF, we took an aliquot from the soot and we add 50 µL of a suspension of **1·(BArF)$_8$** (1 mg) in toluene (1 ml) (corresponding to 0.05 mg of **1·(BArF)$_8$**). Monitoring by MALDI the EMFs left in the supernatant of the sample, we can infer the amount of the target EMF encapsulated and thus the total amount of it present in the initial mixture. Then, these results are used as a guideline for the purification of the Soot sample, adding stoichiometric amounts of capsule with respect to the target EMF.

Selective encapsulation of U2@C78 and U2C@C78 from soot sample-1 using 1·(BArF)8 in the solid phase: 0.40 mg of nanocapsule **1·(BArF)8** (0.0336 µmols) in the solid phase are added to a toluene solution of sample-1. The suspension is stirred at room temperature for 3h. Aliquots of the supernatant are filtered, and analyzed by LDI-TOF every 60 minutes (Fig 2).

Selective encapsulation of U2@C78 from soot sample-2 using 1·(BArF)8 in the solid phase: 0.12 mg of nanocapsule **1·(BArF)8** (0.01 µmols) in the solid phase are added to a toluene solution of sample-2. The suspension is stirred at room temperature for 1h. Aliquots of the supernatant are filtered, and analyzed by LDI-TOF every 15 minutes (Fig 3).

Selective encapsulation of U2C@C78 from soot sample-3 using 1·(BArF)8 in the solid phase: 0.12 mg of nanocapsule **1·(BArF)8** (0.01 µmols) in the solid phase are added to a toluene solution of sample-3. The suspension is stirred at room temperature for 45 minuts. Aliquots of the supernatant are filtered, and analyzed by LDI-TOF every 15 minutes (Fig 4).

Selective encapsulation of U2@C78 from soot sample-4 using 1·(BArF)8 in the solid phase: 0.10 mg of nanocapsule **1·(BArF)8** (0.0083 µmols) in the solid phase are added to a toluene solution of sample-4. The suspension is stirred at room temperature for 20 minuts. Aliquot of the supernatant is filtered, and analyzed by LDI-TOF (Fig 5).

Sequential molecular recognition of U2@C78 and U2C@C78 from soot sample-5 using 1·(BArF)8 in the solid phase: For the purification of U2@C78, 0.25 mg of nanocapsule **1·(BArF)8** (0.017 µmols) in the solid phase are added to a toluene solution of the sample-5. The suspension is stirred at room temperature for 45 minutes. Aliquots of the supernatant are filtered, and analyzed by LDI-TOF at different times (Fig. 6). The Host-Guest adducts are isolated by filtration. Subsequently, for the purification of U2C@C78, 0.25 mg of nanocapsule **1·(BArF)8** (0.017 µmols) in the solid phase are added to a toluene solution of the remaining sample-5 (after complete removal of U2@C78). Then, the suspension is stirred at room temperature for 2h, analyzing aliquots of the supernatant by LDI-TOF every 30 minutes (Fig. 6).

Competition experiment between U2C@C78 and Sc3N@C78 using 1·(BArF)8 in the solid phase: 0.25 mg of nanocapsule **1·(BArF)8** (0.017 µmols) in the solid phase are added to a toluene solution of U2C@C78 and Sc3N@C78 equimolar mixture.[2] The suspension is stirred at room temperature for 3 h. The Host-Guest adducts are isolated by filtration and analyzed by HRMS.

Spectrometric characterization of U2C@C78⊂1·(BArF)8 host-guest adducts formed during the purification of soot sample-5: The HRMS spectrum of the host-guest adducts formed show ions corresponding to the **U2C@C78⊂1·(BArF)8** complex with consecutive loss of counteranions (Fig. S1).

HRMS m/z:

[{U2C@C78⊂**1**·(BArF)4}$^{+4}$]: calculated 2418.468 and found 2418.468
[{U2C@C78⊂**1**·(BArF)3}$^{+5}$]: calculated 1762.161 and found 1762.163
[{U2C@C78⊂**1**·(BArF)2}$^{+6}$]: calculated 1324.611 and found 1324.611
[{U2C@C78⊂**1**·(BArF)1}$^{+7}$]: calculated 1011.953 and found 1011.953
[{U2C@C78⊂**1**·(BArF)0}$^{+8}$]: calculated 777.575 and found 777.577

Spectrometric characterization of Sc3N@C78⊂1·(BArF)8 host-guest adducts formed during the competition experiment between U2C@C78 and Sc3N@C78: The HRMS spectrum of the host-guest adducts formed show ions corresponding to the **Sc3N@C78⊂1·(BArF)8** complex with consecutive loss of counteranions (Fig. S2).

HRMS m/z:

[{U2C@C78⊂**1**·(BArF)4}$^{+4}$]: calculated 2333.744 and found 2333.748
[{U2C@C78⊂**1**·(BArF)3}$^{+5}$]: calculated 1694.352 and found 1694.354
[{U2C@C78⊂**1**·(BArF)2}$^{+6}$]: calculated 1268.091 and found 1268.095
[{U2C@C78⊂**1**·(BArF)1}$^{+7}$]: calculated 963.619 and found 963.621
[{U2C@C78⊂**1**·(BArF)0}$^{+8}$]: calculated 735.265 and found 735.266

Competition experiment, $Sc_3N@C_{80}\subset$1·(BArF)$_8$ exposed to $Sc_3N@C_{78}$. A encapsulated sample of $Sc_3N@C_{80}$ in **1**·(BArF)$_8$ was prepared following previously reported protocols (Chem. Eur. J. 2017, 23, 3553 – 3557),[3] and its full encapsulation checked by HRMS. The $Sc_3N@C_{80}\subset$**1**·(BArF)$_8$ adduct in the solid state (0.043 mmols) was exposed to a toluene solution of $Sc_3N@C_{78}$ (0.043 equiv, 5 mL) for 48 hours, followed by filtration and analysis by HRMS of the solid adduct (Figure S3).

Competition experiment, 1 equiv. of $Sc_3N@C_{80}$ and 1 equiv. of $Sc_3N@C_{78}$ with 2 equiv. of nanocapsule 1·(BArF)$_8$ monitored by HRMS at 2.5 hours. A toluene solution (7 mL) of 1 equiv. of $Sc_3N@C_{80}$ (0.043 mmol) and 1 equiv. of $Sc_3N@C_{78}$ (0.043 mmol) was stirred with 2 equivalent of **1**·(BArF)$_8$ (0.086 mmol) in the solid state for 2.5 hours. The suspension was then filtered and analysed by HRMS (in CH_3CN). The spectra showed the sole uptake of $Sc_3N@C_{78}$ despite empty nanocapsule was still remaining (only traces of [$Sc_3N@C_{80}\subset$**1**·(BArF)$_4$]$^{4+}$). The latter experiment and HRMS spectrum is depicted in Figure S4.

3. Computational details

All geometry optimizations and single point calculations were carried out with the ADF 2017 package[4] using BLYP exchange-correlation functional.[5, 6] To describe valence electron we employed Slater triple-zeta polarization (TZP) basis sets whereas frozen cores were described by means of single Slater functions, consisting of the 1s shell for C and N, the 1s to 2p shells for Zn and the 1s to 4f shells for U. Scalar relativistic corrections were included by means of the ZORA formalism. Dispersion corrections by Grimme were also included.[7] A data set collection of computational results is available in the ioChem-BD repository[8] and can be accessed via https://doi.org/10.19061/iochem-bd-2-XX.

4. Supplementary figures

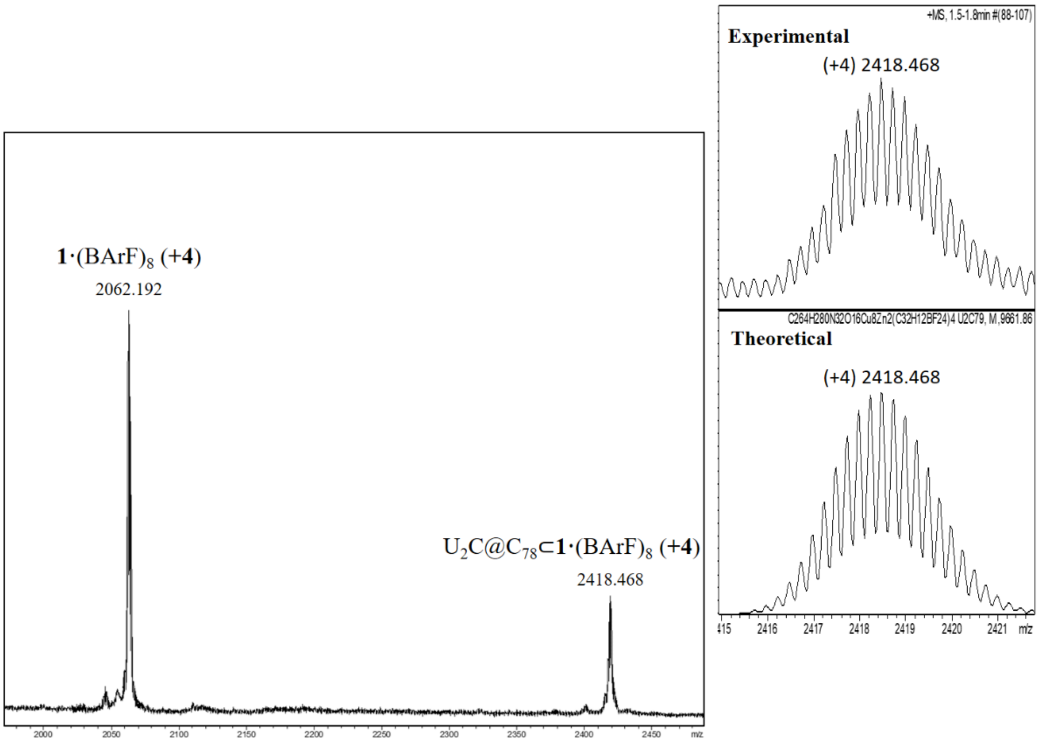

Figure S1. ESI-MS characterization of $U_2C@C_{78}\subset$**1**·(BArF)$_8$.

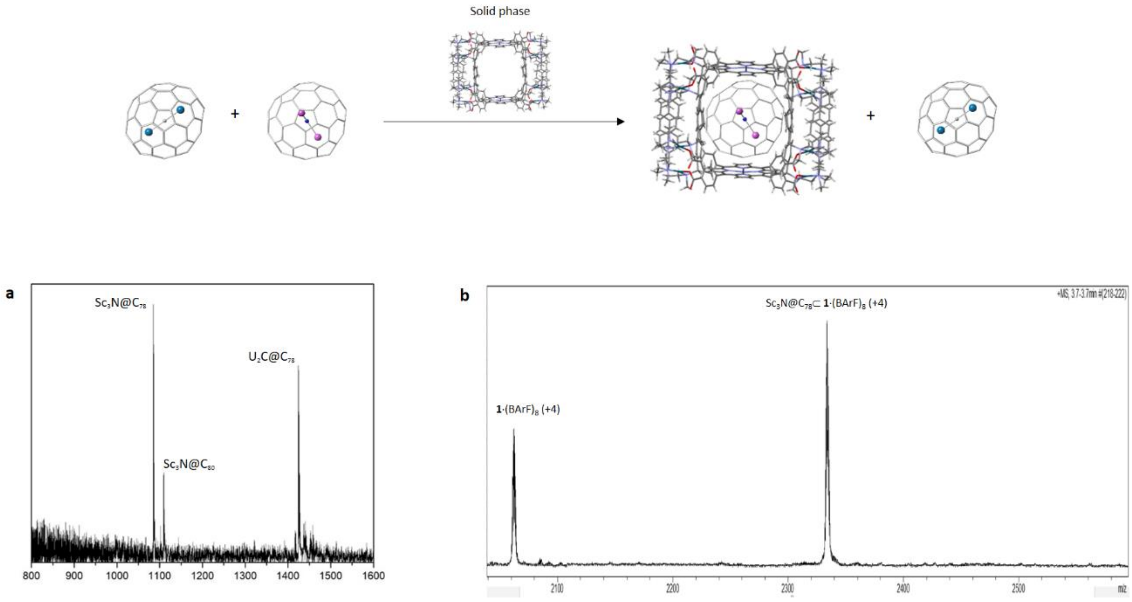

Figure S2.A) MALDI-MS showing the composition of the starting mixture of $U_2C@C_{78}$ and $Sc_3N@C_{78}$ (sample contains traces of $Sc_3N@C_{80}$ as an impurity). B) ESI-MS characterization of the host guest complex produced during the competition experiment between $U_2C@C_{78}$ and $Sc_3N@C_{78}$.

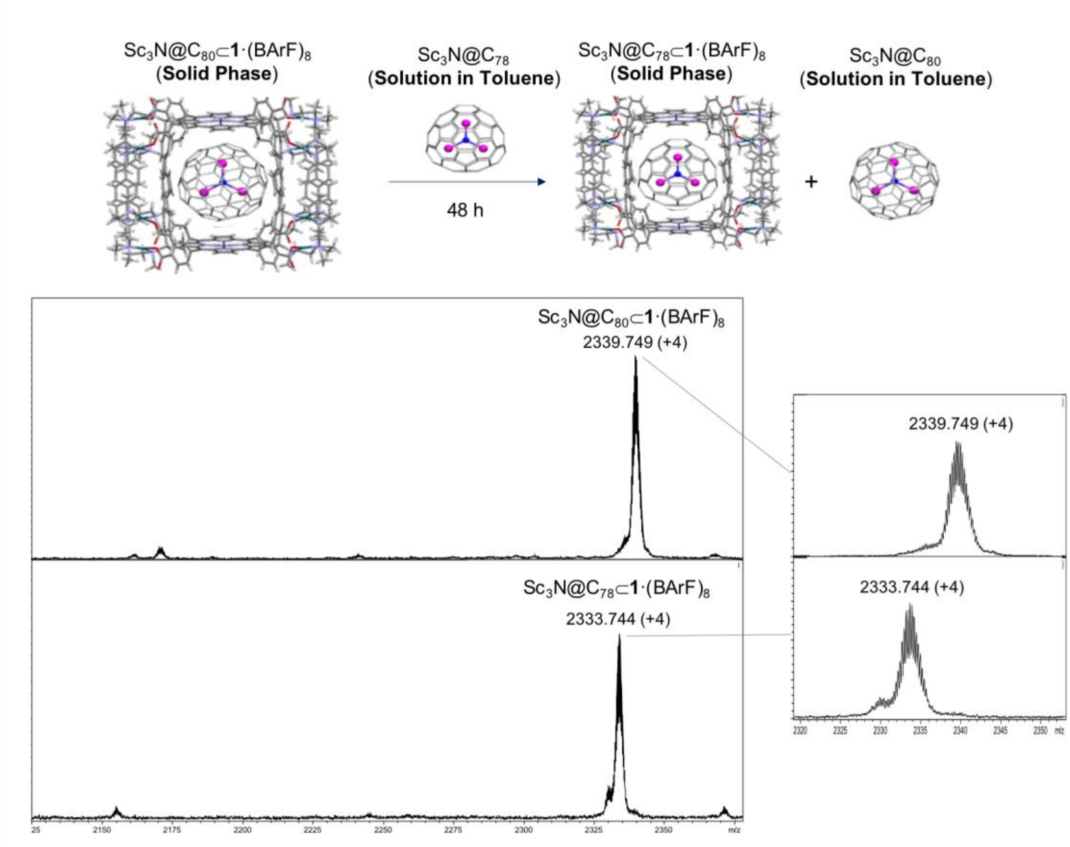

Figure S3. HRMS showing the starting encapsulated $Sc_3N@C_{80}\subset$**1**·(BArF)$_8$ and the complete exchange with $Sc_3N@C_{78}$ to form exclusively the corresponding adduct $Sc_3N@C_{78}\subset$**1**·(BArF)$_8$ (reaction time 48 h).

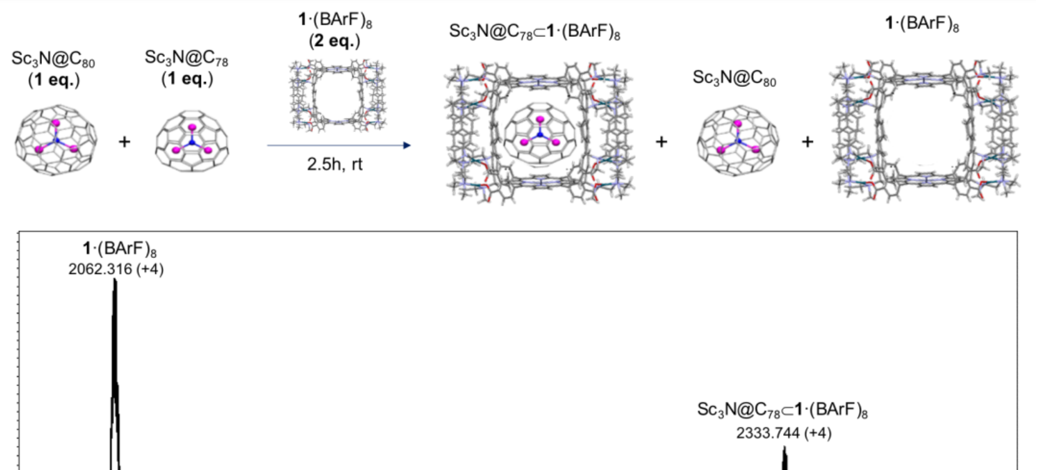

Figure S4. HRMS showing the sole encapsulation of $Sc_3N@C_{78}$ upon mixing (2.5 hours) 1 equiv. of $Sc_3N@C_{80}$ and 1 equiv. of $Sc_3N@C_{78}$ with 2 equiv. of nanocapsule **1**·(BArF)$_8$.

d(Zn···Zn)[b)]	$U_2@C_{78}$	$U_2C@C_{78}$
13.0	-41.1	-41.9
13.2	-50.6	-50.4
13.4	-56.0	-55.2
13.6	-58.2	-57.0
13.8	-58.1	-56.7
14.0	-56.6	-55.1

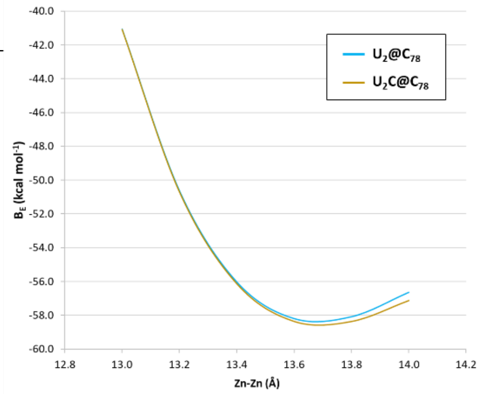

Figure S5. Energy scan and binding energies (kcal mol^{-1}) along the Zn···Zn separation maintaining porphyrins and fullerenes fixed for $U_2@D_{3h}$-C_{78} orientation **2** and $U_2C@D_{3h}$-C_{78} in the same orientation.

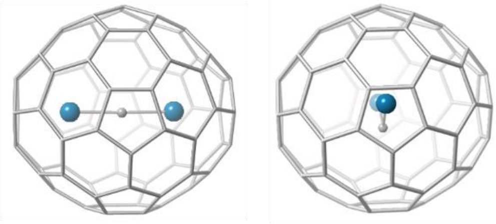

U-C-U angle (º)	178.4	128.8
U-C distance (Å)	2.028	2.025
ΔE (kcal mol^{-1})	0.00	49.84

Figure S6. U-C-U angle (º), U-C distance (Å) and relative energies (kcal mol^{-1}) for $U_2@D_{3h}$-C_{78} with the cluster in an almost linear form (this work) and in the geometry reported in ref [8].[9]

Supplementary References

1. C. Fuertes-Espinosa, A. Gómez-Torres, R. Morales-Martínez, A. Rodríguez-Fortea, C. García-Simón, F. Gándara, I. Imaz, J. Juanhuix, D. Maspoch, J. M. Poblet, L. Echegoyen and X. Ribas, *Angew. Chem. Int. Ed.*, 2018, **57**, 11294-11299.
2. M. R. Cerón, F.-F. Li and L. Echegoyen, *Chem. Eur. J.*, 2013, **19**, 7410-7415.
3. C. Fuertes-Espinosa, C. García-Simón, E. Castro, M. Costas, L. Echegoyen and X. Ribas, *Chem. Eur. J.*, 2017, **23**, 3553-3557.
4. G. te Velde, F. M. Bickelhaupt, E. J. Baerends, C. Fonseca Guerra, S. J. A. Van Gisbergen, J. G. Snijders and T. Ziegler, *J. Comput. Chem.*, 2001, **22**, 931-967.
5. A. *D.* Becke, *Phys. Rev. A*, 1988, **38**, 3098-3100.
6. C. Lee, W. Yang and R. G. Parr, *Phys. Rev. B*, 1988, **37**, 785-789.
7. S. Grimme, S. Ehrlich and L. Goerigk, *J. Comput. Chem.*, 2011, **32**, 1456-1465.
8. M. Álvarez-Moreno, C. de Graaf, N. López, F. Maseras, J. M. Poblet and C. Bo, *J. Chem. Inf. Model.*, 2015, **55**, 95-103.
9. Y. Li, L. Yang, Z. Li, Q. Hou, L. Li and P. Jin, *Inorg. Chem.*, 2019, **58**, 10648-10655.